Earth Abundant Catalysts for Water Electrolysis at Low Overpotentials

By

Joseph Barforoush

Submitted to the graduate degree program in Chemical & Petroleum Engineering and the Graduate Faculty of the University of Kansas in partial fulfillment of the requirements for the degree of Doctor of Philosophy.

_____

Chair: Prof. Kevin Leonard

_____

Prof. Bala Subramaniam

_____

Prof. Trung Nguyen

_____

Prof. Mark Shiflett

_____

Prof. Xianglin Li

Date Defended: August 20, 2018

The dissertation committee for Joseph Barforoush certifies that this is the approved version of the following dissertation:

Earth Abundant Catalysts for Water Electrolysis at Low Overpotentials

_____

Chair: Prof. Kevin Leonard

Date Approved: August 31, 2018

Abstract

Water electrolysis via renewable electricity (e.g., wind, solar) provides a carbon neutral route for pure hydrogen production to fuel zero emission power generation devices, such as fuel cells. Deployment of fuel cell vehicles is growing in the US and around the world, coupled with the construction of hydrogen fueling stations, of which there are expected to be 200 hydrogen refueling stations operating in California by 2025. However, 96% of hydrogen is still produced by steam reformation of natural gas or sourced from other petroleum feedstocks. As a result, the fuel cell vehicles produce zero emissions at the tailpipe but the production of the hydrogen fuel still contributes to greenhouse gas emissions. Moreover, mature technologies essential to the sustenance of the human population, specifically the Haber-Bosch process for the production of ca. 187 million tonnes of ammonia fertilizer per year, account for the majority of hydrogen consumption. Thus, a carbon neutral route for hydrogen production from renewable feedstocks is an exigency for Earth's inhabitants to avoid the worsening of the catastrophic effects of anthropogenic climate change.

Water splitting is a technology that is hundreds of years old, yet it has still not become commercially relevant due to high capital costs and high operating costs of the electrolyzers available today. A major driver of these costs are the hydrogen evolution and oxygen evolution electrocatalysts, which are typically composed of platinum and iridium for operation in acidic electrolyte. The main objective of this doctoral work is to decrease the overpotential of the water splitting reactions by tuning the morphology of earth abundant metal catalysts.

Platinum is known to catalyze the hydrogen evolution reaction (HER) at the thermodynamic equilibrium potential, and it is most active in acidic media. However, the corrosive nature of acidic electrolyte causes degradation of non-precious metal catalysts as well as other components that the electrolyte comes into contact with. Various transition metal dichalcogenides have been

investigated as alternatives to platinum, but here we report the first nanostructured FeS_2 HER catalyst. By utilizing a hot sulfur injection synthesis and adjusting the sulfur concentration, we were able to create one-dimensional (1D) FeS_2 wires and two-dimensional (2D) FeS_2 discs, unique from the previously known three-dimensional (3D) FeS_2 cubes. We found that the catalytic activity of the nanostructured FeS_2 was highly dependent on the morphology, and the 2D FeS_2 discs had an exchange current density of the same order of magnitude as Pt in neutral electrolyte. The 2D morphology of the FeS_2 discs bears resemblance to the 2D MoS_2 catalyst which is known to have HER activity in acidic media, with the edges of the 2D nanosheet structure being the active sites.

The oxygen evolution reaction (OER) is the largest source of inefficiency in overall water splitting reaction because it is a four electron/four proton transfer reaction. NiFe oxides have emerged as highly active OER catalysts in alkaline media, surpassing the activity of even the precious metal-based catalysts, IrO_x and RuO_x. Specifically, $Ni_{0.8}$:$Fe_{0.2}$ has been shown to be the most active ratio for NiFe catalysts because above ca. 25% iron, segregation of the metals occurs. Utilizing surface interrogation mode of scanning electrochemical microscopy (SI-SECM), we measured the kinetic rate constant(s) of the active sites on crystalline $Ni_{0.8}$:$Fe_{0.2}$ and amorphous $Ni_{0.8}$:$Fe_{0.2}$. We found that the crystalline $Ni_{0.8}$:$Fe_{0.2}$, synthesized at high temperatures, had both "fast" and "slow" sites with a rate constant of 1.3 s^{-1} and 0.05 s^{-1}, respectively, while the amorphous $Ni_{0.8}$:$Fe_{0.2}$, synthesized by a low temperature (microwave-assisted) method, only had "fast" sites with a rate constant of 1.9 s^{-1}. High resolution transmission electron microscopy (HRTEM) and electron diffraction showed that the microwave-assisted $Ni_{0.8}$:$Fe_{0.2}$ was amorphous down to the five nanometer scale, indicating that low temperature synthesis is crucial for homogeneous dispersion of the metals and maximization of bimetallic active sites. Further SI-SECM studies revealed that the $Ni_{0.8}Fe_{0.2}OOH$ layered double hydroxide (LDH), a structure known to have electrolyte permeability, had an anomalously high active site density (4500 sites nm^{-2}) compared to that of the crystalline $Ni_{0.8}$:$Fe_{0.2}$ (500 sites nm^{-2}), from which it was synthesized by electrochemical conditioning. This gives evidence that electrolyte permeability allows for catalysis via subsurface sites.

The final objective of this work was to lower the overall water splitting overpotential with earth abundant metal catalysts. Current water electrolyzers utilize acidic (PEM) or alkaline configurations. However, neither of these configurations are amenable to using the FeS_2 discs and nanoamorphous $Ni_{0.8}$:$Fe_{0.2}$ oxide for overall water splitting because the former is the most active

in neutral media and the latter is most active in alkaline media. By analogy with the chlor-alkali membrane process, we utilized the K^+ form of the Nafion 117 membrane to enable water splitting with the anode in alkaline media and the cathode in neutral media, or dual-pH water splitting. With this system, we were able to achieve water splitting at 10 mA cm^{-2} under 1.6 V—a total overpotential of less than 270 mV—for a 24 h period.

Acknowledgements

It is with deep gratitude and appreciation that I acknowledge my advisor and friend, Dr. Kevin Leonard, for helping me progress to where I am today. I joined his lab with an interest in alternative fuels and no knowledge in electrochemistry. He graciously dedicated his time and effort to passing on his knowledge in the fields of electrocatalysis, materials science, and electrochemistry. Moreover, he honored my personal entrepreneurial inclinations and drew from his own past experiences to guide me on a path to pursue my aspiration. I am very grateful to have crossed paths with him.

I would also like to extend my gratitude to my Committee. Dr. Trung Van Nguyen has given me tremendous insight from an electrochemical engineer's perspective in the three courses he has taught me. I am very thankful to him for offering his course in Electrochemical Engineering, in which I felt like I was part of his research group, being included in many "cheese hole filling" discussions that deepened my understanding of electrochemical phenomena. I am privileged to have had Dr. Bala Subramaniam as an instructor for undergraduate kinetics; he has also helped me with encouraging words when I have asked for advice at times when I was unsure if I should move forward with a PhD. Through his class, Dr. Xianglin Li has helped me understand how to characterize PEM fuel cells, which has proven useful for understanding electrolyzer configurations. Although I have not taken a class with Dr. Mark Shiflett, I have attended his seminars on invoking positive change with industrial research, inspiring me to do the same. Of course, the Chemical & Petroleum Engineering Department deserves recognition as well, including but not limited to Dr. Raghunath V. Chaudhari, Dr. Michael Detamore (who is no longer at KU), Dr. Marylee Southard, Dr. Prajna Dhar, and Dr. Karen J. Nordheden who have all given me encouragement and advice throughout years at KU. I am also grateful to Dr. Shenqiang Ren and Daniel Jasion for collaborating with us on the nanostructured FeS_2 publication, as well as, Dr. Prem Thapa and

Dr. Justin Douglas for their insights, guidance, and assistance with materials characterization.

My labmates Dylan Jantz, Tess Seuferling, Yukari Yamazaki, Timothy McDonald, and Charles Shaugnessy deserve my thanks for the good company and consultation they have provided, as well as, those who worked with me as undergraduate researchers, including but not limited to Kelly Song, Laura Cummings, Maeley Brown, Danny Widrig, Tej Desai, Cal Bayer, Taylor Bahm, Lexi Hunter, and Aaron Gehrke.

I would like to acknowledge my kids, who give me a reason to do everything I can to improve the world that we are living in. My wife has supported me and graciously tolerated my, sometimes unpredictable, work schedule. Lastly, I express my appreciation to my family who has always been there for me when I needed them.

Contents

List of Figures

Chapter 1

Overview and Introduction

1.1 Importance of Hydrogen

Molecular hydrogen is a vital commodity chemical with a wide variety of applications. The uses for hydrogen as an industrial gas include applications in petroleum refining, chemical processing, pharmaceuticals, electronics, metallurgical, power generation, and food processing industries. In most cases, it is used as a reactant, for example, in the simultaneous cracking and hydrogenation (hydrocracking) of hydrocarbons to produce smaller molecules and higher hydrogen-to-carbon ratios, hydrogenolysis of hydrocarbon fuels to remove sulfur as H_2S (hydrodesulfurization), catalytic production of methanol from syngas, gas-to-liquid hydrocarbon products from syngas by the Fischer-Tropsch process, hydrogenation of adiponitrile to produce hexamethylenediamine, unsaturation of fats and oils via hydrogenation, reduction of nickel sulfate in elemental nickel production, reduction of $SiCl_4$ to silicon for epitaxial growth of silicon in semiconductor fabrication, and reduction of N_2 to ammonia for fertilizer production by the Haber-Bosch process.[7–12] However, the physical properties of hydrogen also make it useful for niche industrial applications. Extremely low viscosity (0.00892 cP at 25 °C), high specific heat (14.3 kJ kg^{-1} $°C^{-1}$ at 25 °C), and high thermal conductivity (0.019 kJ m^{-1} $°C^{-1}$ at 25 °C) makes hydrogen a superior coolant and lubricant for electrical turbine power generation systems, and it's low density (0.0899 kg m^{-3} at 25 °C) is a favorable property for weather balloon lift as well.[13] In addition, liquid hydrogen has found applications as a rocket fuel due to its high energy density (8496 MJ m^{-3} at -253 °C).[14] Thus far, this brief summary has only included established hydrogen technologies. While many of these technologies

are extremely relevant to modern industrialized living, emerging technologies, if implemented on a large-scale, hold the potential to have an even greater positive impact on society.

1.2 The Future of Hydrogen

The use of hydrogen as a fuel has largely been limited to rocket engines, for which solid state rocket fuel has become more commonplace, and the concept of hydrogen as a ubiquitous fuel in the "hydrogen economy" has been all but implemented for nearly 50 years now.[15] This is an unfortunate truth in the wake of the 4 globally hottest years on record, acidification of the oceans devastating the calcium carbonate-based coral reefs, rising sea levels due to the glacier caps melting, and the acceleration of the extinction rate of species of plants and animals, among other natural disasters of abnormal intensity; all conditions that have the potential to worsen on the current trajectory of the status quo to forge on with fossil fuel technology.[16] However, the adoption of hydrogen as a fuel, namely for fuel cells, is gaining traction, albeit slowly, with GM, Toyota, Honda, and other major automobile manufacturers releasing or preparing to release fuel cell vehicles (FCVs) to the commercial market. In addition, public transportation sectors as well as some commercial and residential buildings have implemented stationary fuel cells. These trends come as some advances in the manufacturing technology of fuel cells have been made,[17–19] but mainly as the advantages of hydrogen as a fuel over fossil fuels has become increasingly apparent, in spite of the lack of infrastructure for hydrogen fueling and generally low economic incentives. A variety of fuel cells (e.g., proton exchange membrane (PEM), solid oxide (SOFC) fuel cells) utilize hydrogen as a fuel for the anode where it is oxidized, while oxygen is reduced at the cathode, and electricity is produced with a byproduct of water and heat. This electricity generation process is far simpler than the conventional scheme of chemical energy to thermal energy to mechanical energy to electricity—the middle two steps are unnecessary in fuel cells, which makes the theoretical efficiency very high. Commercial fuel cell systems for passenger cars operate in the range of 40 - 50% and efficiency under partial load is higher than at full load—a major improvement when compared to the 25 - 30% efficiency of gasoline or diesel internal combustion engines which have the opposite load-efficiency relationship.[11] Further, the use of hydrogen fuel cells results in massive reductions in both air and noise pollution because they produce zero harmful emissions and run quietly. The

largest drawback is that with current technology, fuel cells can cost in excess of \$2000 kW^{-1}.[11] Hydrogen internal combustion engines, however, may provide an interim application for automobile hydrogen fuel. The combustion of hydrogen for transportation is also unique from conventional fuels in that the flammability limits are much wider, allowing for operation with mixtures as lean as 4% hydrogen in air; the ignition energy (0.02 MJ) is 12 times lower than that of gasoline; the detonation concentration limits are wider when confined, but the diffusion velocity is very high (2 m s^{-1}), which allows for quick dispersal in the case of a hydrogen leak; and simple water vapor constitutes the majority of hydrogen internal combustion engine emissions when the limit of the autoignition temperature is utilized (858 K) to prevent the temperature from reaching temperatures above 2300 K where nitrogen oxides form.[9], but this is estimated to require a tank that is 4 times the volume of the required size to store the same amount of energy as gasoline.[12] Cryogenic refrigeration is one way to minimize hydrogen storage volume, but less energy intensive options are also being investigated, including solid phase hydrogen storage and liquid organic hydrogen carrier (LOHC) technologies.[20–22] There is a caveat to all of the potential environmental benefits of using hydrogen as any type of fuel. That is, the source and production methods of hydrogen dictate whether there is any overall reduction in greenhouse gas emissions.

1.3 Hydrogen Production

Hydrogen is the most abundant element in the universe, but in the molecular form it does not exist in harvestable quantities in nature.[23] For this reason, hydrogen is not an energy source but a secondary energy carrier like electricity. Primary sources of energy, such as fossil fuels, nuclear, or renewable energy, are used to produce hydrogen by a wide range of different routes. Global hydrogen production is estimated at 700 billion Nm^3 per year with a market share of \$130 billion, expected to reach \$200 billion by 2025.[11] Fossil fuels are still the main source of hydrogen production with 48% from natural gas, 30% from oil, 18% from coal, and approximately 4% from electrolysis.[24] Hydrogen production from desulphurized natural gas starts with steam reformation where methane reacts with steam at 700 - 1000 °C and 3 - 25 bar, typically over a nickel catalyst, to form hydrogen and carbon monoxide. This step is followed by the water-gas shift reaction to recover more hydrogen from the carbon monoxide while producing stoichiometric quantities of CO_2, and

finally pressure swing adsorption removes most of the impurities from the hydrogen. Overall, the temperatures and pressures required make this process very energy intensive, especially considering the strong endothermicity of the first reaction ($\Delta H_{SMR,298\ K}$ = 206.1 kJ mol^{-1}). When natural gas supplies are limited, residues of crude oil and liquid hydrocarbons are common feedstocks for a similar process, starting with partial oxidation where oxygen levels are controlled in combustion of the fuels to produce a hydrogen-rich syngas. Another common hydrogen production route is coal gasification where pulverized coal is mixed with water and the mash is heated under pure oxygen to form syngas.[14] Due to economies of scale, operating conditions, and chemical hazards involved, routes from fossil fuels require centralized production facilities. As a result, many large-scale operations requiring hydrogen as a reactant produce hydrogen on-site. Ammonia synthesis plants account for 62.4% of hydrogen production and consumption. These facilities employ on-site steam reformation, consuming 3-5% of the global natural gas supply and liberating ca. 2 metric tons of CO_2 per metric ton of ammonia produced.[25] In the current hydrogen landscape, the few examples of on-site production of hydrogen at the point-of-use are mostly limited to such centralized facilities where massive amounts of greenhouse gases are also released into the earth's atmosphere. However, the technology is now available to produce hydrogen near the point-of-use on potentially any scale using only renewable feedstocks and in the absence of greenhouse gas emissions.

Water electrolysis provides a means of hydrogen production, in simplest terms, from water, electricity, and salt. Perhaps the first recorded instance of electrolytic water splitting was by Troostwijk and Deinman who showed that the application of an electric discharge causes water to decompose into "combustible air" and "life-giving air" in 1789.[26] However, it was not until Volta discovered the first battery, in the year 1800, that Nicholson and Deinman were led to use the voltaic pile in the same year to split water and specifically identify the evolved gases as hydrogen and oxygen. While water electrolysis was discovered in acidic electrolyte, the reaction was not utilized for large-scale production of hydrogen until 1888 when Lachinov devised a method for industrial electrolysis in alkaline electrolyte.[27] By 1902, 400 industrial electrolyzers were in use, and the first pressurized electrolyzer capable of producing 10,000 Nm^3 H_2 h^{-1} was developed by Zdansky and Lonza in 1948.[28] Alkaline electrolyzers are still in use today, operating in 20 - 30% KOH electrolyte with nickel-based catalysts, commonly with noble metal coatings to increase activity, separated by a diaphragm to prevent mixing of gases.[29] Issues remaining with alkaline electrolyzers

include the corrosive environment created from high KOH concentrations, the diaphragm is bulky with limited ionic conductivity causing large ohmic losses at higher current densities, the liquid electrolyte-diaphragm system makes high pressure operation difficult, significant permeability of the diaphragm to product gases makes operation under partial load dangerous, and high purity gas cannot be achieved directly out of the electrolyzer.[30,31] Following the invention of the proton exchange membrane (PEM), the PEM electrolyzer system was developed in the sixties, providing an alternative to alkaline electrolyzers. In the PEM electrolyzer, the PEM acts as a separator as well as the electrolyte. The unique properties of the PEM provide some advantages, including higher conductivity, low permeability to hydrogen allowing for high purity gas production directly from the electrolyzer, faster response time, and enhanced operation under partial load. PEM electrolyzers are also generally scalable to almost any production capacity compared to alkaline electrolysis which is better suited for high production rates.[30,32] However, there are drawbacks due to the acidic regime created by the membrane, which requires precious metal catalysts and noble metal current collectors, flow fields, and bipolar plates. Precious metal catalysts typically account for the bulk of the capital cost of the electrolyzer stack.[29,30] Earth abundant electrocatalysts have been shown to be competitive with their precious metal counterparts on the lab-scale and could be part of the answer to lowering the capital cost of electrolyzers. With substantial cost reductions, water electrolyzers could revolutionize hydrogen production with decentralized units, scaled specifically for the application, to generate hydrogen on demand at the point-of-use as it is needed.

The existing electrolyzer technologies are capable of producing 760 Nm^3 h^{-1}, enough to fill nearly 14,000 fuel cell vehicle tanks each hour, at 2.5 V or below, but the story is not complete without consideration of the electricity source used to drive the electrolysis.[30] The majority of electricity today is generated from the burning of coal, which is the largest source of anthropogenic CO_2 emissions. Coal plants have been optimized to run at up to 50% efficiency, but the remaining energy goes to waste as high temperature exhaust, except in the rare cases where the heat can be integrated with a nearby cement factory or steel mill.[33] Electricity can be generated by renewable energy sources, such as tidal, wind, and solar, with no emissions and sometimes at a load that is too large for the grid to handle. It is these sources that must be utilized to drive hydrogen production from water electrolysis for the benefits of the hydrogen economy to be fully realized.

1.4 Hydrogen Evolution

The hydrogen evolution reaction (HER) in acid is an ideal model electrocatalytic reaction with no side reactions and one product. The reaction occurs reversibly on platinum metal at the thermodynamic equilibrium potential ($E^0 = 0$ vs. NHE). As a result, a platinum wire in solution with H^+ and H_2 at unit activity and 25 °C, called the natural hydrogen electrode (NHE), or the standard hydrogen electrode (SHE), is internationally recognized as the primary reference electrode. Figure 1.1 shows an example of a classic NHE configuration in use with a Ag to AgCl oxidation reaction occurring on the other electrode.[1] The NHE, however, is not very practical as a reference electrode for most experimental applications, but other electrodes at equilibrium, such as Ag in a saturated KCl solution, are commonly used instead.

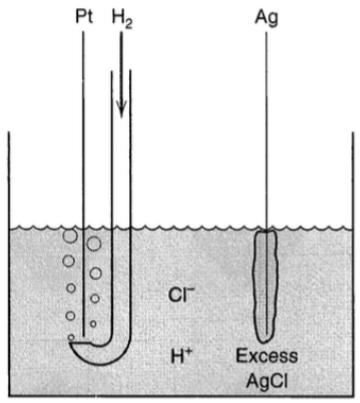

Figure 1.1. Diagram of a natural hydrogen electrode (left)—a Pt wire with H^+ and H_2 at unit activity and 25 °C, and a Ag wire coated in AgCl (right).[1]

Insight into the high activity of Pt for the HER is obtained from the plot of metal catalyst HER activity versus the free energy of adsorption of the hydrogen atom, which shows volcano-type behavior. Platinum follows the Sabatier principle in that it resides at the top of the volcano with the optimum binding energy ($\Delta G_H \approx 0$) that is neither too weak nor too strong.[34,35] It is intuitive that HER catalyst activity is strongly dependent on ΔG_H because the mechanism in acidic electrolyte consists almost entirely of proton adsorption steps. The first electron transfer-proton adsorption step, known as the Volmer step (Equation 1.1 where "S" denotes a catalytic site), is followed by either a chemical reaction with another adsorbed proton, Tafel step (Equation 1.2), or an electron transfer reaction with a solvated proton, Heyrovsky step (Equation 1.3).[36]

$$S + H^+ + e^- \rightleftharpoons S - H_{ads} \tag{1.1}$$

$$S - H_{ads} + S - H_{ads} \rightleftharpoons 2S + H_2 \tag{1.2}$$

$$S - H_{ads} + S + H^+ + e^- \rightleftharpoons 2S + H_2 \tag{1.3}$$

However, the HER in acidic electrolyte has several limitations in industrial applications, including low efficiency and short catalyst lifetime when non-precious metals are employed.[2] Alternatively, the HER can be carried out in alkaline and neutral solutions, in which hydrogen adsorption energy cannot be the sole descriptor of activity because protons could only come from the very low concentration in solution or from the dissociation of water near the electrode surface, estimated to be on the order of 10^{-3} L mol^{-1} s^{-1}.[2] Instead, water reduction (Equation 1.4, E^0 = -0.828 vs. NHE) is the dominant reaction. The mechanism is analogous to that of the acidic reaction, with the Volmer and Heyrovsky steps likely requiring catalytic dissociation of water to yield H_{ads} and OH^-.[37,38]

$$H_2O + 2e^- \rightleftharpoons H_2 + 2OH^- \tag{1.4}$$

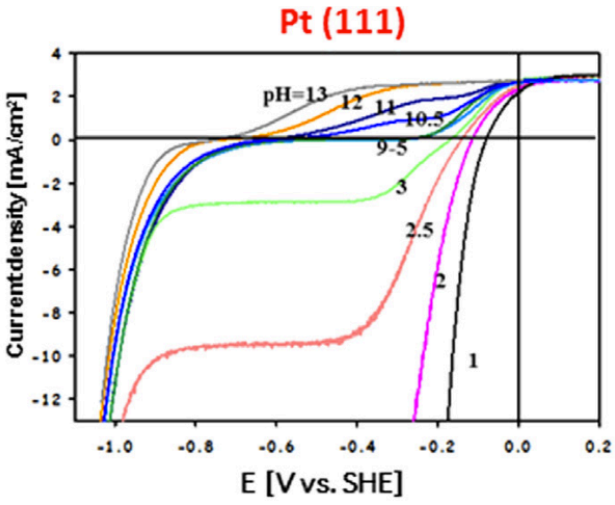

Figure 1.2. pH-dependence of the current-potential behavior of Pt(111) for the HER. The linear sweep voltammograms (LSVs) were performed at 50 mV s^{-1} while the Pt(111) disk electrode was rotating at 1600 rpm, and the pH was adjusted by adding NaOH or $HClO_4$ to 0.1 M $NaClO_4$.[2]

The alkaline HER has not been studied as extensively as the acidic HER has, and the reason for the steady decline in activity with increasing pH (Figure 1.2) is still a subject of debate. There is evidence that the water dissociation step governs the kinetics, and, in some cases, two sites are actually required for the dissociation step.[38] For example, $Ni(OH)_2$ clusters on Pt at 40 - 45% coverage were shown to dramatically increase the HER activity of bare Pt in alkaline electrolyte.[39] It follows that the oxophilicity of the $Ni(OH)_2$ is responsible for the adsorption of O atoms while the Pt provides a site for the H atoms, forming an activated water complex before the water dissociates, OH^- is released from $Ni(OH)_2$, and reaction of H_{ads} with another H_{ads} evolves H_2 from the Pt surface.[2] Further investigation of other 3d transition metal hydroxides of varying oxophilicity by Markovic and co-workers (Figure 1.3) revealed that there is also an optimum binding energy for the OH_{ads} site. The HER activity follows the trend of the oxophilicity of the metal (Ni < Co < Fe < Mn), too much of which renders the metal hydroxide a spectator due to high OH binding strength.[40] This phenomenon is consistent with Brønsted-Evans-Polanyi-type scaling relations in that the lower the water dissociation barrier is, the stronger the H/OH binding energy is, eventually leading to poisoning rather than activation of the catalyst surface. Therefore, a balance between the activation energy of the water dissociation, ΔG_H, and ΔG_{OH} must be met to produce high alkaline HER activity.

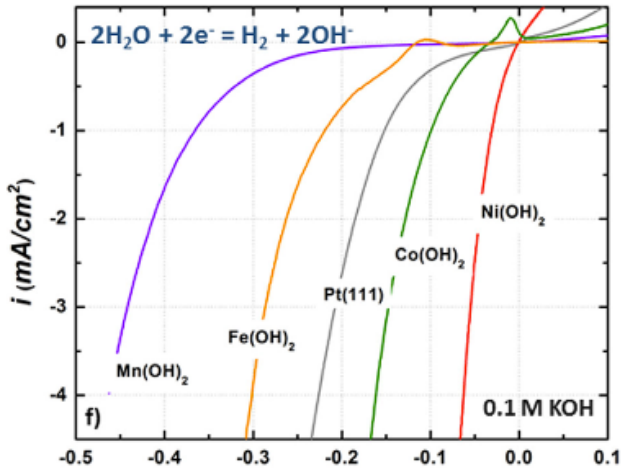

Figure 1.3. HER linear sweep voltammograms (LSVs) at 50 mV s^{-1} in 0.1 M KOH for different transition metal hydroxides coated on Pt(111) disk electrodes, rotating at 1600 rpm. The electric potential (x-axis) is reported V vs. NHE.[2]

The activity of HER catalysts across the whole pH range is highly dependent on structure.

MoS_2, an extremely important hydrodesulfurization catalyst used across the globe, has been shown to be active for the HER in acidic media. Nørskov and co-workers identified MoS_2 as an HER catalyst by the similarity of its edge sites with the active site of hydrogen evolution on the nitrogenase FeMo cofactor, the enzyme in the soil-dwelling *Azotobacter vinelandii* bacterium responsible for nitrogen fixation, and its near-zero ΔG_H.[41,42] Subsequent studies showed that MoS_2 could be made as two-dimensional nanostructures with more exposed edge sites, and the active sites could be increased even further by defect engineering, chemical exfoliation, and doping of the two-dimensional nanosheets.[36,43–45] The discovery of the HER activity of MoS_2 sparked interest in a number of other transition metal dichalcogenides (TMDs) (e.g., $NiSe_2$, $CoSe_2$, WS_2, NiS_2, CoS_2, and FeS_2) for the HER in acidic media.[46–48] In the aforementioned studies, bulk FeS_2 performed quite poorly. However, we found that when FeS_2 was created as nanostructured 2D FeS_2 discs, Pt-like activity was achieved for the HER in neutral electrolyte. We also found that the 2D FeS_2 discs had dramatically improved catalytic activity compared to nanostructured one-dimensional (1D) FeS_2 wires and three-dimensional (3D) FeS_2 cubes.[49] This finding is consistent with the increased activity found in the 2D nanosheet morphology of MoS_2. More studies on HER catalysts in neutral media are expected to be worthwhile because, if employed in an electrolyzer, substantial cost reductions could be made, stemming from the mild requirements of such a benign electrolyte (i.e. noble metals are not required to withstand contact with neutral electrolyte).

1.5 Oxygen Evolution

The oxygen evolution reaction (OER) is a four electron/four proton transfer reaction, and it is the half reaction that limits the overall water splitting efficiency. Currently, there is no material known to catalyze the OER at the thermodynamic equilibrium potential (Equation 1.5, $E^0 = 1.229$ V vs. NHE), but, historically, RuO_2 or IrO_2 have been the benchmark catalysts, employed extensively with acidic electrolyte in commercial PEM electrolyzers.

$$2H_2O \rightleftharpoons O_2 + 4H^+ + 4e^- \tag{1.5}$$

The mechanism for the OER is much more complex than that of the HER, and there are several proposed mechanisms, although definitive validation has been lacking due to the difficulty in

spectroscopically detecting intermediates.[15,50,51] Equations (1.6) – (1.9) show a well-accepted OER mechanism for acidic media, which excludes the direct recombination of adsorbed oxygen (a key step in the classic OER mechanism) because it is expected to have a high activation barrier.[52,53]

$$S + H_2O \rightleftharpoons S - OH + H^+ + e^- \tag{1.6}$$

$$S - OH \rightleftharpoons S - O + H^+ + e^- \tag{1.7}$$

$$S - O + H_2O \rightleftharpoons S - OOH + H^+ + e^- \tag{1.8}$$

$$S - OOH \rightleftharpoons S + O_2 + H^+ + e^- \tag{1.9}$$

However, a non-precious metal catalyst that is competitive with Ru or Ir-based catalysts and stable under oxidizing potentials in strong acid has yet to be reported.[54–56] Conversely, Ni-based catalysts rival the activity of RuO_2 and IrO_2 in alkaline media and have been utilized in commercial alkaline electrolyzers.[57] Similar to the HER, the dominant mechanism for the OER is different in alkaline media due to the pH-dependent availability of reactive species. The overall reaction for alkaline OER is shown in Equation 1.10 (E^0 = 0.401 V vs. NHE), and Equations (1.11) – (1.14) show the corresponding mechanism for OER in alkaline media.[50]

$$4OH^- \rightleftharpoons O_2 + 2H_2O + 4e^- \tag{1.10}$$

$$S + OH^- \rightleftharpoons S - OH + e^- \tag{1.11}$$

$$S - OH + OH^- \rightleftharpoons S - O + H_2O + e^- \tag{1.12}$$

$$S - O + OH^- \rightleftharpoons S - OOH + e^- \tag{1.13}$$

$$S - OOH + OH^- \rightleftharpoons S + O_2 + H_2O + e^- \tag{1.14}$$

Rossmeisl and co-workers performed density functional theory (DFT) calculations on a wide range of metal oxide OER catalysts and found that there was a universal scaling relation between the binding energy of OH and OOH, key intermediates in both the acidic and alkaline mechanisms. Figure 1.4 shows the linear scaling relation between the adsorption energy of OOH, ΔE_{OOH}, and the adsorption energy of OH, ΔE_{OH}, for perovskites, rutiles, anatase, Mn_xO_y, Co_3O_4, and NiO oxides, which dictates that $\Delta E_{OOH} = \Delta E_{OH} + 3.20$ eV.[3] The red star on Figure 1.4 represents the binding energies for a thermodynamically ideal catalyst, characterized by having the difference in free energy of each mechanistic step equal to E^0 at standard conditions. In other words, each charge transfer step for an ideal catalyst should have a free energy change of 1.23 V, amounting to $\Delta E_{OOH} = \Delta E_{OH} + 2.46$ eV because OOH and OH are separated by two H^+/e^- transfer steps.[3] Rossmeisl concluded that this scaling relation provides a lower limit of the OER overpotential (deviation of the applied potential from the thermodynamic equilibrium potential — a quantity thought to be directly related to the rate-deterimining step when effects from mass transfer limitations and ohmic losses are absent) as (3.2 - 2.46 eV)/$2e^-$, which comes to a limit of 0.2 - 0.4 V overpotential when the standard deviation of Figure 1.4 is taken into consideration.[3,50] This estimated lower limit is surprisingly close to the limit of the overpotentials reported for the OER.

Among the most active OER catalysts, NiFe-based materials have achieved some of the lowest overpotentials reported for the OER, in the range of 200 mV at 10 mA cm^{-2}, outperforming Ir and Ru-based electrocatalysts.[58–62] Ni is always found in combination with Fe in the earth's crust, and Fe impurities are common in Ni metal. The strong affinity of Ni and Fe, lead to the discovery of NiFe-based OER catalysts when Edison and Junger found that the Fe impurities in $Ni(OH)_2$ of Ni-based positive electrodes in alkaline batteries decreased capacity and cycle life. This anomaly prompted further studies, revealing that the poisoning effect was due to the lowering of the OER potential, which became lower with increasing levels of Fe impurities.[58] Since this discovery, a wide range of synthesis techniques have been employed to improve the activity of NiFe-based alkaline OER catalysts, including mechanical alloying, electrodepostion of mixed metal salt solutions, and high temperature annealing to form NiFe oxides.[58] The morphology and the ratio of nickel-to-

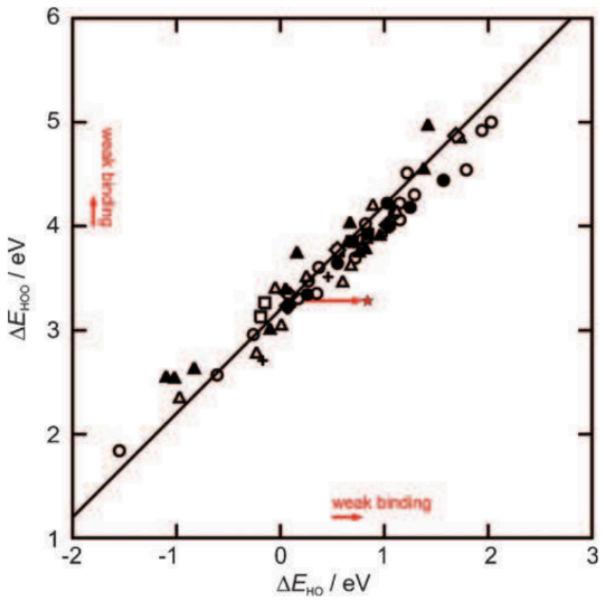

Figure 1.4. Adsorption energy of OOH vs. adsorption energy of OH for perovskites (circle), rutiles (triangle), anatase (diamond), Mn_xO_y (square), Co_3O_4 (plus sign), and NiO oxides, based on density functional theory (DFT) calculations. The hollow symbols represent adsorption energies for clean surfaces, and the solid shapes represent adsorption energies for surfaces with high coverage. The red star indicates the adsorption energies of an ideal OER catalyst.[3]

iron has been shown to govern OER activity. Fe content above ca. 25% results in segregation of the metals, leading to low active site densities.[62,63] In recent years, numerous reports of the layered double hydroxide (LDH) class of NiFe materials as OER catalysts have emerged. LDHs are composed of positively charged layers, balanced by permeation of anions from electrolyte into the interlayer, allowing for anomalously high active site densities.[58,64,65] However, there are several reports of amorphous NiFe OER catalysts, synthesized at low temperatures, outperforming the crystalline NiFe LDH catalysts.[59,62,65,66] Using the surface interrogation mode of scanning electrochemical microscopy (SI-SECM), we found that our microwave-assisted synthesis of nanoamorphous ($Ni_{0.8}$,$Fe_{0.2}$) yielded a catalyst with only one "fast" site while the crystalline NiFe LDH had a "fast" site and a slow site.[62,64] Transmission electron microscopy (TEM) on our ($Ni_{0.8}$,$Fe_{0.2}$) catalyst revealed that it is truly amorphous, down to the 5 nm scale, giving evidence that homogeneous dispersion of the Ni and Fe is critical for high OER activity.

1.6 Polymer Electrolyte Membrane

In 1959, the use of an ion exchange polymer to conduct the entire current in a battery cell was reported by Grubb at the General Electric Company Research Laboratory.[67] However, a polymer electrolyte stable under the oxidizing conditions at the anode of an electrolyzer was not known until Grot at E. I. DuPont Company discovered the Nafion ionomer.[4,68] The Nafion ionomer is a perfluorosulfonic acid (PFSA) synthesized by copolymerization of a perfluorinated vinyl ether comonomer with tetrafluoroethylene (TFE), and it has excellent proton conductivity as well as high chemical and mechanical stability. The hydrated structure, based on small-angle X-ray scattering (SAXS) spectra, in Figure 1.5 shows an arrangement of ionic clusters with channels in between, where water can pass through.[4] The —SO_3^--lined channels allow for proton conduction through the membrane while excluding hydroxyl ions.

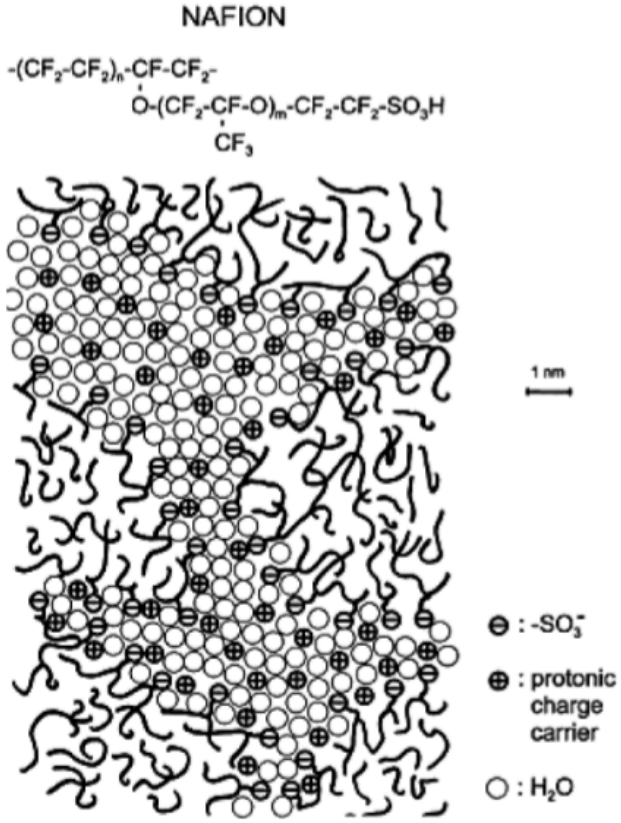

Figure 1.5. Diagram made by Kreuer of a hydrated Nafion membrane based on small-angle X-ray scattering (SAXS) spectra by Gebel.[4]

Proton conduction can occur through the vehicular mechanism, where a hydrated proton ($H^+(H_2O)_x$)

passes through a channel, due to the difference in electrochemical potential, carrying water molecules with it via electroosmotic drag (Figure 1.6, top arrows). Alternatively, the Grotthus-type mechanism, where the positive-charged proton hops from one negative-charged site (i.e. —SO_3^-) to the next via the breaking and forming of hydrogen bonds (Figure 1.6, bottom arrows), is also possible.[5] The dominant mechanism of proton transport is dependent on the type of proton exchange membrane (PEM) and the operating conditions (e.g., temperature, level of hydration), but, in general, the predominant mechanism for hydrated sulfonic acid-attached PEMs (e.g., PFSAs, sulfonated poly(ether ether ketone) (SPEEK), sulfonated polysulfone (SPSf)) is vehicular-type.[69]

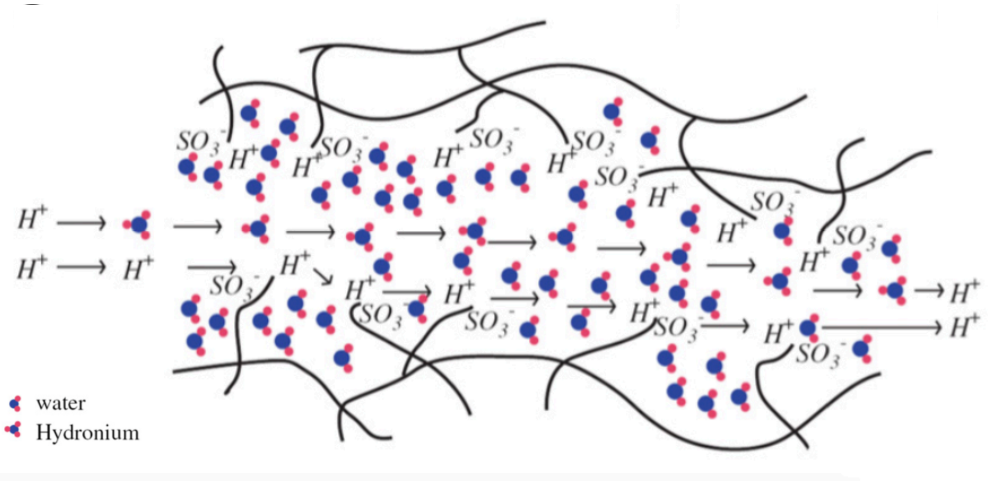

Figure 1.6. Schematic of the vehicular mechanism (upper set of arrows) and the Grotthus mechanism (lower set of arrows) of proton transport through a PEM.[5]

General Electric developed the first PEM fuel cell for the NASA Gemini missions, and the first PEM electrolyzer was created shortly after in 1966.[6,70] In a PEM electrolyzer (Figure 1.7), water is fed to the anode side where it oxidized at the electrocatalyst layer to produce oxygen and protons. The PEM facilitates the transfer of protons from the anode side to the electrocatalyst layer on the cathode side where the protons are reduced with electrons from water oxidation to evolve hydrogen. Because of the participation of the PEM in the reaction, the active area of the anode electrocatalyst is limited to areas where there is contact between the PEM, the electrocatalyst, and water, i.e. the triple phase boundary (TPB), and the cathode side requires contact between the PEM and the electrocatalyst.[71] Electrolyzers are especially useful for space applications because of the abundance of solar energy and the efficiency of generating hydrogen and oxygen from water. Electrolysis has been used extensively in space for producing oxygen for environmental control life

support systems and extravehicular activity, and hydrogen for energy storage and propulsion.[72] PEM water electrolysis has also proved useful for similar purposes in submarine applications,[6] however, it was not until the PFSA membrane was adapted to suit the chlor-alkali process that the PEM became industrially relevant.

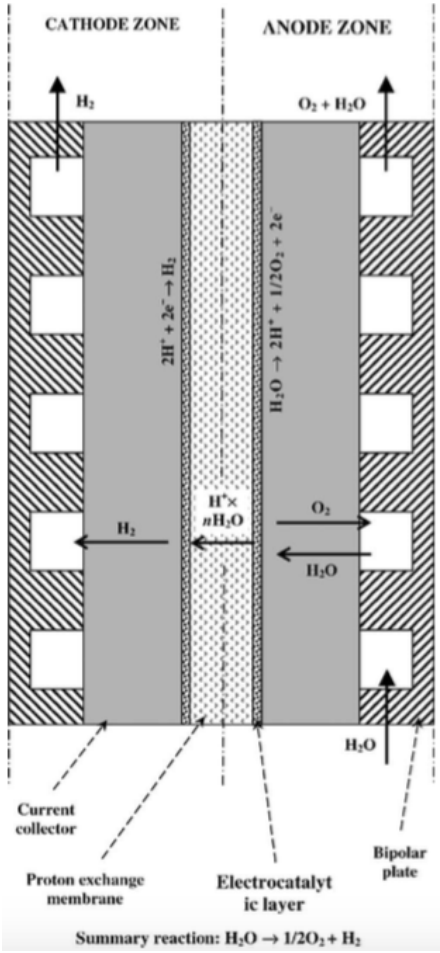

Figure 1.7. Schematic of the general PEM electrolysis cell.[6]

In 1975, the Asahi chemical company in Japan developed the chlor-alkali membrane electrolysis process to replace the hazardous mercury cell process.[71] For typical PFSA membranes, the precursor is a thermoplastic —SO_2F, which is easily extruded into sheets. The —SO_2F sheet is then treated with concentrated aqueous acid solution to convert it to the —SO_3H form, known as the PEM. However, the sulfonyl fluoride form can also be converted to other forms, such as —SO_3Na by treatment with NaOH.[4] In membrane brine electrolysis, saturated brine is fed to the anode side where chloride ions are oxidized to evolve chlorine gas (Equation 1.15, E^0=1.358 V vs. NHE) while

the —SO_3Na membrane allows sodium ions to cross over to the cathode side. Water is fed to the cathode side where hydrogen evolution (Equation 1.16, E^0=-0.828 V vs. NHE) occurs and the generated hydroxyl ions, unable to cross the —SO_3Na membrane, react with the sodium ions to produce sodium hydroxide.

$$2Cl^- \rightleftharpoons Cl_2 + 2e^- \tag{1.15}$$

$$2H_2O + 2e^- \rightleftharpoons H_2 + 2OH^- \tag{1.16}$$

The membrane prevents cross-contamination of the gases and electrolytes, greatly reducing product separation costs. Currently, more than half of the world production capacity of chlorine, 76 million tonnes Cl per year, is produced by membrane brine electrolysis, and a bilayer sodium form of perfluorinated membrane is used with sulfonyl and carboxylate groups to reduce backflow of hydroxyl ions from the cathode to the anode.[71] In other words, the membrane in brine electrolysis allows for operation with the two half cells maintained at different pHs. We have found that application of this method to membrane water electrolysis enables operation with the anode (e.g. nanoamorphous ($Ni_{0.8}$,$Fe_{0.2}$) oxide) in alkaline solution and the cathode (FeS_2 discs) in neutral solution, which dramatically reduces the overpotential required for overall water splitting.

Chapter 2

Low-Dimensional Hyperthin FeS_2 Nanostructures for Efficient and Stable Hydrogen Evolution Electrocatalysis

2.1 Abstract

We report a scalable, solution-processing method for synthesizing low-dimensional hyperthin FeS_2 nanostructures, and we show that 2D FeS_2 disc nanostructures are an efficient and stable hydrogen evolution electrocatalyst. By changing the Fe:S ratio in the precursor solution, we were able to preferentially synthesize either 1D wire or 2D disc nanostructures. The 2D FeS_2 disc structure has the highest electrocatalytic activity for the hydrogen evolution reaction, comparable to platinum in neutral pH conditions. The ability of the FeS_2 nanostructures to generate hydrogen was confirmed by scanning electrochemical microscopy, and the 2D disc nanostructures were able to generate hydrogen for over 125 h.

2.2 Introduction

A key green energy initiative is the discovery of efficient, stable, and elemental abundant electrocatalysts for the water splitting reactions (i.e., the hydrogen evolution reaction (HER) and the oxygen evolution reaction (OER)).[73–75] Water splitting with HER and OER electrocatalysts play a vital role in converting solar energy into chemical energy via artificial photosynthesis and also provides a pathway to use water (as opposed to natural gas) as a feedstock for hydrogen production.[76–78] Nanostructured transition-metal chalcogenides have previously been studied as HER electrocatalysts.[45,46,79–81] In particular, two-dimensional (2D) MoS_2 nanosheets are effective HER catalysts under acidic conditions,[45,82] and it has been discussed that the HER activity correlates with the number of edge sites on the MoS_2 and/or the hopping efficiency of electrons in the vertical direction.[83,84] Although other transition-metal chalcogenides have also been studied as HER catalysts (e.g., WS_2, NiS_2, CoS_2, $NiSe_2$, and $CoSe_2$),[46,48] there have been only limited reports on the catalytic activity of FeS_2,[46,47] and none have shown high efficiency for FeS_2. In order to improve the electrocatalytic activity of earth-abundant FeS_2, we report a novel synthesis technique for the creation of hyperthin 1D and 2D FeS_2 nanostructures, which we term "wires" and "discs", respectively. We show that the 2D FeS_2 disc nanostructure has high catalytic activity for the HER, very similar to Pt, and is stable in neutral pH conditions.

Many different nanostructured morphologies of iron sulfides have previously been identified.[85,86] However, reports of low dimensional iron sulfide nanostructures with atomic layer thickness have been rare and were typically seen as an intermediate.[87–89] Previous methods for producing iron sulfides with atomic layer thickness have relied on chemical vapor deposition (CVD), electrodeposition, techniques reqnuiring high temperature sulfurization, and/or a brute force cleavage.[90–93]

2.3 Catalyst Synthesis

Here we utilize a solution hot-injection method, analogous to a previously reported iron sulfide synthesis,[89] to create unique hyperthin iron sulfide nanostructures with atomic layer thickness. In the first step of the synthesis, an octadecylamine (ODA) ligand was added to a Fe^{2+} solution, which formed 3-5 nm iron nanoparticles as seen in the transmission electron microscopy, TEM, images (Figure 2.1a,e). The ODA ligand acts as both a reducing agent for the Fe^{2+} (eqn 2.1) and as a

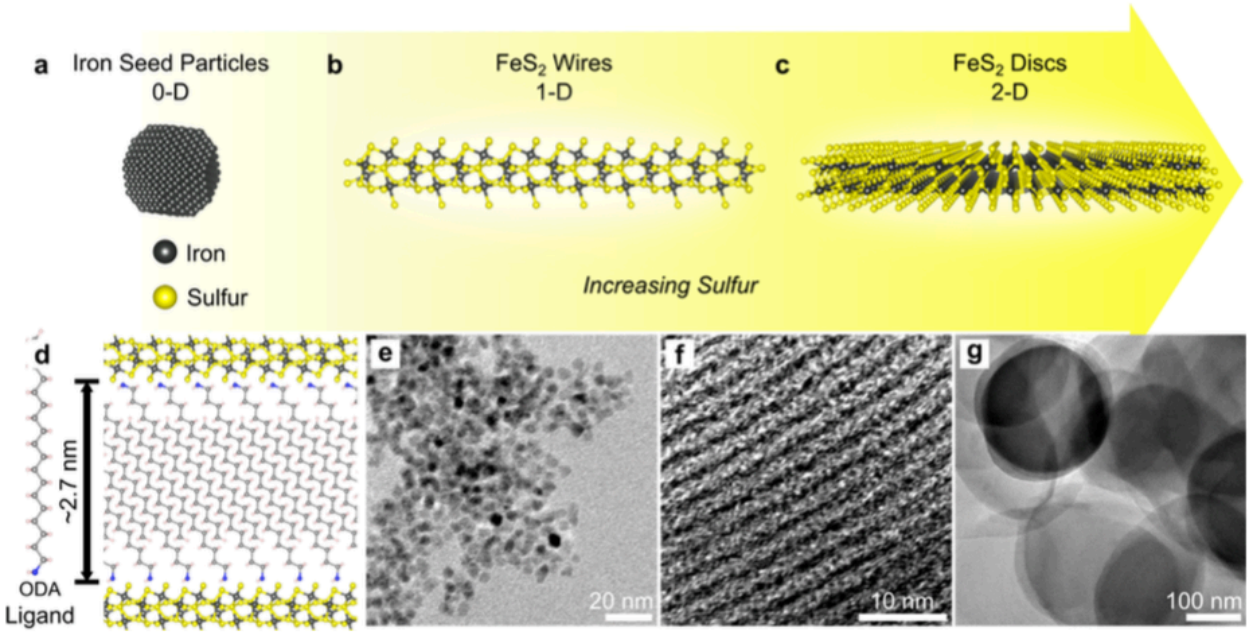

Figure 2.1. Schematic representation and TEM images of the 1D and 2D FeS_2 structure formation. (a, e) Fe^0 nanoparticles that are formed in the absence of sulfur. (b, f) FeS_2 wires formed from 1:6 Fe:S precursor solution. (c, g) FeS_2 discs formed in the 1:24 Fe:S precursor. (d) Schematic of 2.7 nm wide ligand interstitial layer that separates both wires and discs to form their respective bulk structures.

capping layer on the subseqnuent nanocrystal formation. Next, upon injection of sulfur, the iron seed particles oxidize to form Fe^{2+} and S_x^{2-} moieties (eqn 2.2) and these species form the FeS_2 nanostructures via eqns 2.3 and 2.4.

$$Fe^{2+} + 2e^- \rightarrow Fe^0 \tag{2.1}$$

$$Fe^0 + S_x \rightarrow Fe^{2+} + S_x^{2-} \tag{2.2}$$

$$Fe^{2+} + S_x^{2-} \rightarrow FeS + S_{x-1} \tag{2.3}$$

$$FeS + S_x^{2-} \rightarrow FeS_2 + S_{x-1}^{2-} \tag{2.4}$$

It was found that low-dimensional structural formation could be tuned through adjustments of the initial sulfur concentration with two primary low dimensional FeS_2 nanostructures being

observed. Changing the Fe:S ratio present in the precursor solutions formed either distinct wire or disc nanostructures, as seen in Figure 2.1. We determined that a 1:6 Fe:S ratio yields wires (Figure 2.1b,f) uniformly separated by a tightly packed layer of ligand (Figure 2.1d) with a spacing of approximately 2.7 nm. Increasing the Fe:S ratio to 1:24 results in the formation of discs (Figure 2.1c,g) which appear in a stack of thin sheets also separated by a ligand layer.

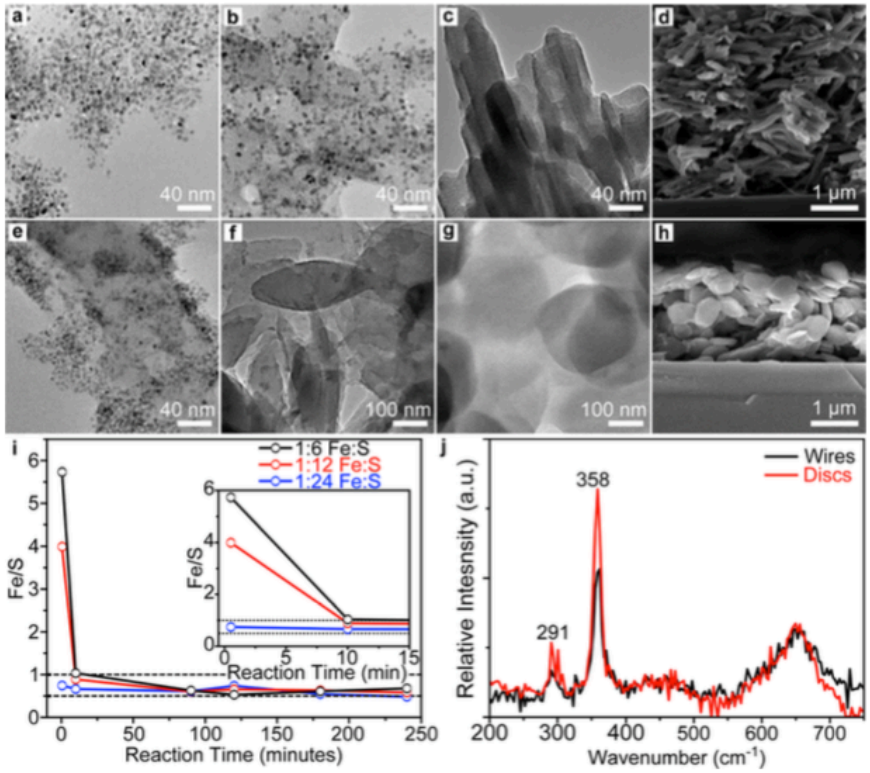

Figure 2.2. Time-dependent TEM characterization is shown for the wires (a-c) and discs (e-g) taken at 0.5, 5, and 240 min, respectively. SEM characterization of the final wire (d) and disc (h) formations cast on Si substrates. Time-dependent EDS measurements (i) are shown with the inset focusing on the first 15 min of the reaction. The plot of the Raman spectroscopy data (j) is to establish phase identification.

The kinetics of the wire and disc reactions were tracked through (1) time-dependent growth patterns monitored by TEM (Figure 2.2); (2) energy-dispersive X-ray spectroscopy (EDS) measurements (Figure 2.2i), which monitored the rate at which the Fe:S stoichiometry changed; and (3) UV-vis-IR spectra (Figure 2.5), which showed the changes in the relative peak heights of the FeS_2 characteristic set of absorbance peaks with respect to reaction time. The transition to FeS_2 was kinetically different between the wire and disc structures. The wire reaction (Figure 2.2a-c) occurred relatively slowly, with the iron seed particles still present for several minutes into the reaction. Examination of the disc reaction (Figure 2.2e-g) revealed faster kinetics with initial disc

formation occurring within seconds of the injection and the seed particles being consumed minutes earlier than the wires. The EDS measurements correlate well with both the TEM and absorbance data. The wires reached the desired 1:2 stoichiometry after 30-60 min and maintained that stoichiometry for the duration of the reaction. The 1:24 Fe:S precursor ratio (discs) showed a faster conversion. Within 30 s, disc formations were observed, and 10 min into the reaction, the discs reached a 1:2 Fe:S ratio. The scanning electron microscopy (SEM) characterization of the final wire structure (Figure 2.2d) showed the bulk wires forming long bundled strands with lengths well over a micron which come together to form a porous sponge-like structure held together by ligand-ligand interactions. The SEM image of the final disc structure (Figure 2.2h) also showed the stacking of discs to form larger structures with a range of diameters from 300 to 800 nm that most likely are connected by ligand-ligand interactions.

2.4 Materials Characterization

Raman spectroscopy was used to further elucidate structure and phase identification (Figure 2.2j). Both the wire and disc structures share a characteristic set of Raman peaks at 291 and 358 cm^{-1}.[91,94] The combination of the EDS data and ordered nanostructures within TEM images led to the conclusion that these peaks correspond to an ordered FeS_2 structure. The thinness of these materials may not allow for the more typical Raman active modes[95,96] of the usual FeS_2 phases (e.g., pyrite, marcasite) nor of the other typical $Fe_{1-x}S$ phases. X-ray diffraction (XRD, Figure 2.6) confirmed the presence of Fe nanoparticles in the early stages but exhibited no discernible phase in the final products, potentially due to the thinness of the material leading to insufficient scattering volume.

2.5 Electrochemical Characterization

The HER electrocatalytic activity of the nanostructured FeS_2 (drop-casted on a glassy carbon electrode) was measured via linear sweep voltammetry (LSV) at 1 mV/s in 0.1 M pH 7 phosphate buffer solution (PBS) (see Supporting Information for experimental details). Figure 2.3a (solid lines) shows the capacitance and iR-corrected LSVs for the champion FeS_2 1D wires, 2D discs, 3D cubes (TEM for the 3D FeS_2 cubes shown in Figure 2.8b) along with a blank glassy carbon electrode and Pt electrode. By synthesizing 2D FeS_2 nanostructures, we were able to shift the onset

potential to very near the thermodynamic potential for hydrogen evolution (0 V vs RHE) indicative of exceptionally high electrocatalytic activity. In fact, these novel 2D FeS_2 nanostructures have an overpotential less than 50 mV larger than that of Pt. Triplicates of the LSV experiments obtained from separate batches of the FeS_2 1D wires, 2D discs, and 3D cubes (Figure 2.8a) show good reproducibility between samples with variances attributed to variability in electrode fabrication.

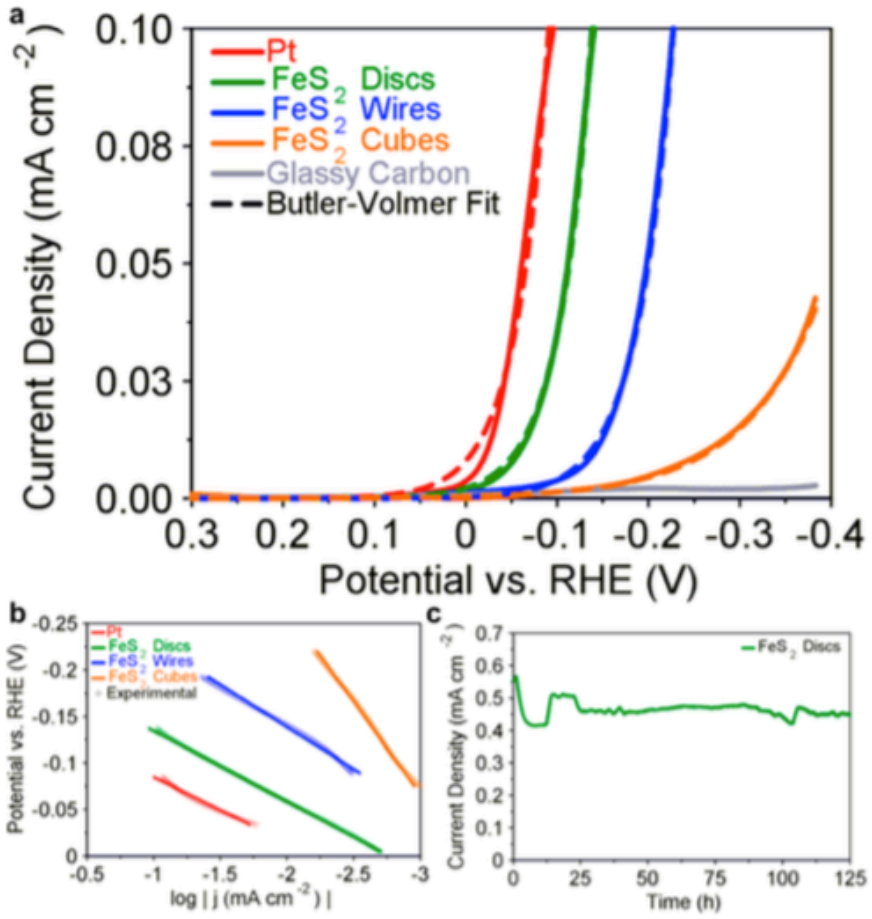

Figure 2.3. Electrochemical characterization of FeS_2 discs, wires, and cubes in 0.1 M pH 7 phosphate buffer solution (PBS) for the hydrogen evolution reaction. (a) Experimental linear sweep voltammograms at 1 mV/s (solid lines) for the champion FeS_2 discs, wires, cubes coated on glassy carbon along with a bare Pt electrode, and a bare glassy carbon electrode. Also shown are the corresponding best-fit single-electron Butler-Volmer equations (dashed lines) for each electrode. (b) Tafel plot showing the experimental data in the Tafel region (circle markers) with the corresponding Tafel slopes (solid lines) for Pt, FeS_2 discs, wires, and cubes. (c) Current density vs time profile for a 125 h constant potential (-0.14 V vs RHE) stability test for the FeS_2 discs under continuous stirring.

To quantify the electrocatalytic activity, the pseudosteady-state measurements were fit to the single-electron transfer Butler-Volmer equation (dashed lines, Figure 2.3a) assuming no mass-transfer effects (equation 2.5). This allowed for accurate exchange current densities and transfer

coefficients to be obtained for each structure. It should be noted that at this pH and scan rate, the mass-transfer limited regime is reached at much lower currents than typically seen at faster scan rates (Figure 2.10) or at lower pH.[97] From the Butler-Volmer equation, the exchange current density, which is a measure of kinetics for the hydrogen evolution reaction,[1] for the FeS_2 discs, wires, and cubes were determined to be 2.2, 0.32, and 0.41 μA cm^{-2}, respectively, whereas Pt had an exchange current density of 8.0 μA cm^{-2}. This shows that only the 2D FeS_2 disc nanostructures had an exchange current density on the same order of magnitude as Pt. A secondary calculation of the exchange current densities and transfer coefficients were obtained from Tafel analysis (Figure 2.3b). The Tafel plot yielded exchange current densities of 6.3, 1.7, 0.30, and 0.47 μA cm^{-2} for Pt and the FeS_2 discs, wires, and cubes, respectively. All of the exchange current densities as calculated via the Tafel plot are within 25% of those values calculated with the Bulter-Volmer equation. Transfer coefficients and Tafel slopes for each electrode are shown in Supporting Information Table S2.14. Similar transfer coefficients and Tafel slopes between the 2D FeS_2 disc structure and Pt suggest that the 2D FeS_2 structure has a Pt-like HER mechanism in neutral pH.

To determine the stability of the FeS_2 discs, a constant potential of -0.14 V versus RHE was applied for over 125 h in 0.1 M pH 7 PBS while vigorously stirring, and the reduction current was measured as a function of time. Figure 2.3c shows that the reduction current did not change significantly over the 125 h experiment. This suggests that, by maintaining reducing conditions (i.e., negative potentials) sufficient to evolve hydrogen, the FeS_2 discs catalyst is stable for generating hydrogen from water under neutral pH conditions. The turnover freqnuency (TOF) was calculated from equation 2.6 using the data presented in Figure 2.3c and the electrochemical surface area, which was calculated from double-layer capacitance measurements (see Supporting Information for details). The TOFs of the FeS_2 discs and the Pt electrode were determined to be 149 electrons h^{-1} and 644 electrons h^{-1} under the same conditions (Figure 2.11), with the FeS_2 discs having more than double the electrochemical surface area than the Pt electrode.

To verify that hydrogen was evolving from the surface of the 2D FeS_2 discs, an HER electrochemical reactivity map was obtained via scanning electrochemical microscopy (SECM, Figure 2.4). SECM is a powerful technique for imaging the reactivity of electrocatalytic surfaces and for studying electro- chemical reactions.[98–100] Figure 2.4a shows the schematic for obtaining a hydrogen evolution electrochemical reactivity map. Here the catalytic electrode was held at a negative

potential sufficient to evolve hydrogen, and a 200 μm Pt SECM tip electrode was held at a positive potential sufficient to oxidize any hydrogen present in solution. The SECM tip electrode was placed ca. 100 μm above the catalyst electrode and was scanned across the catalyst surface while the tip current was recorded as a function of tip position. Areas where hydrogen is being generated by the catalyst electrode will produce an oxidation current on the SECM tip electrode at that position.

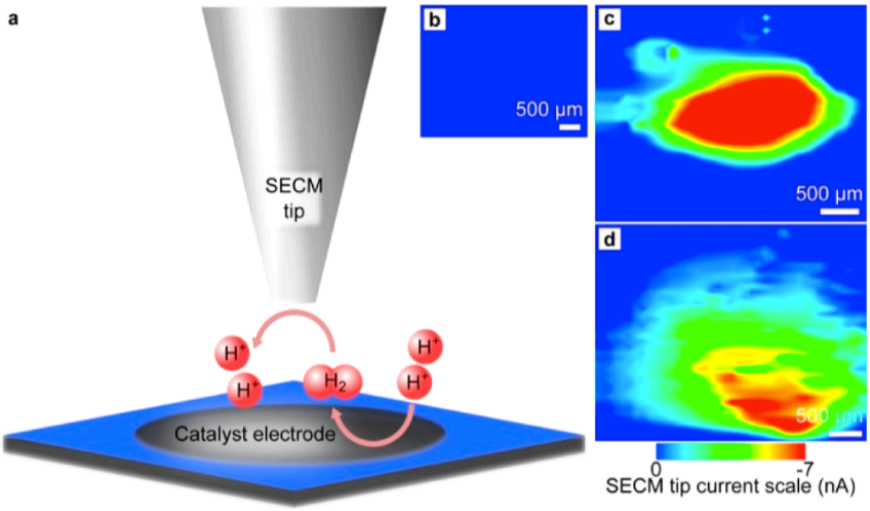

Figure 2.4. Hydrogen evolution electrochemical reactivity maps obtained via scanning electrochemical microscopy (SECM). (a) Schematic of the SECM experiment showing hydrogen collection on the SECM tip electrode. (b) The reactivity map for a bare glassy carbon electrode. (c, d) Electrochemical reactivity maps for the HER on Pt and FeS_2 discs on glassy carbon, respectively.

HER electrochemical reactivity maps were obtained on the Pt electrode, the 2D FeS_2 discs coated on glassy carbon, and a bare glassy carbon electrode (Figure 2.4b-d). Both the Pt (Figure 2.4c) and the 2D FeS_2 discs-coated electrode (Figure 2.4d) shows oxidation currents (reds, yellows, and greens) on the SECM tip electrode, indicative of hydrogen existing in solution over each electrode. For comparison, Figure 2.4b shows no hydrogen in solution for the bare glassy carbon electrode operated at the same potential at which Figure 2.4c was generated. Thus, via these SECM electrochemical reactivity maps, we can conclude that the FeS_2 discs catalyst is indeed generating hydrogen gas.

Substrate generation/tip collection (SG/TC) SECM was used to estimate the Faradaic efficiency for hydrogen generation (Figure 2.13). In this experiment, a 200 μm Pt tip electrode was positioned over a 200 μm Au substrate electrode coated with FeS_2 discs, and linear sweep voltammetry was performed on the FeS_2 electrode and the Pt tip electrode collected the evolved hydrogen as a

function of potential (see Supporting Information for details). Using the SG/TC SECM technique, we estimate the faradaic efficiency of the FeS_2 discs for hydrogen evolution to be 92 ± 8%.

2.6 Conclusion

In summary, we report a novel synthesis method to create 2D FeS_2 nanostructures, which significantly improve the electrocatalytic performance of earth-abundant FeS_2 for the HER. It was found that the morphology and stoichiometry of the FeS_2 could be tuned by the initial sulfur concentration. The 1D FeS_2 wires and the 2D FeS_2 discs showed higher electrocatalytic activity compared to the conventional 3D FeS_2 cubes for the HER under neutral pH conditions. In fact, the 2D FeS_2 materials displayed excellent electrochemical activity similar to platinum with high exchange current densities and an onset potential for hydrogen evolution near the thermodynamic potential. The 2D FeS_2 discs also proved to be remarkably stable, demonstrating the ability to generate hydrogen for over 125 h when under reducing conditions. Using SECM, we verified that hydrogen was being generated from both the Pt and FeS_2 discs electrodes but not from a bare glassy carbon electrode.

2.7 Acknowledgements

This work was previously published in ACS Catalysis:
Jasion D, Barforoush JM, Qiao Q, Zhu Y, Ren S, Leonard KC. Low-dimensional hyperthin FeS2 nanostructures for efficient and stable hydrogen evolution electrocatalysis. ACS Catalysis. 2015;5(11):6653-6657.

2.8 Supporting Information

2.8.1 Materials and Methods

Chemicals

FeI_2 (Sigma-Aldrich, anhydrous, 99.99%), sulfur powder (Sigma-Aldrich, Colloidal), carbon black (Alfa-Aesar, acetylene, 100% compressed, 99.9%), monobasic dihydrate sodium phosphate (Acros Organics, 99%), dibasic sodium phosphate (Acros Organics, anhydrous, ACS Reagent)(dimethylaminomethyl)ferroc

(Alfa Aesar, 98+%), octadecylamine (Acros Organics, technical grade, 90%), diphenyl ether (Acros Organics, 99%), chloroform (BDH, Anhydrous), methanol (Fischer Chemical, Certified ACS), tetrachloroethylene (Sigma-Aldrich, ACS) were all used as received.

Wire and Disc synthesis

To make the FeS_2 wires, 0.5 mmol of FeI_2 and 1 mL of phenyl ether was added to a septa sealed vial in a N_2 flushed glovebox. This mixture was sonicated to form a uniform slurry, approximately 1 hour. In a round bottom flask 12 g of ODA was added and degassed and backfilled with argon. The flask was then heated to 120 °C, degassed and backfilled with argon again, and allowed to cool to 80 °C. The FeI_2 precursor solution was injected into the flask containing ODA and heated back to 120 °C and then left to stir for 1 hour to allow the precursor to decompose. In a separate flask, 128 mg of sulfur and 5 mL of phenyl ether was added and then degassed and backfilled with argon. This flask was heated to 70 °C and left to stir for 1 hour. After 1 hour, the sulfur solution was rapidly injected into the Fe-ODA solution and left to react at 120 °C for 4 hours. The solution was allowed to cool to 100 °C before injection of 10 mL of chloroform to prevent the solution from congealing and then was transferred to centrifuge tubes, topped off with methanol, and centrifuged at 4000 rpm for 7 minutes. The supernatant was poured off and an additional 5 mL of chloroform and 40 mL of methanol was added, and the solution was mixed and centrifuged again. This step was repeated two more times resulting in a fluffy black solid that was suspended in chloroform and stored under nitrogen. The same procedure is used to make discs except only 0.125 mmol of FeI_2 was used. The average yield of the 2 syntheses is roughly around 70%, without the consideration of the mass loss during the cleaning process. The FeS_2 cubes were synthesized using a previously reported method.[89]

Materials Characterization

UV–Vis absorbance spectra were taken on a UV-3600 Shimadzu UV–Vis–NIR spectrophotometer. X-ray powder diffraction was done at room temperature using monochromatic Cu-Kα radiation on a Bruker proteum diffraction system equipped with Helios multilayer optics, and APEX II CCD detector and a Bruker MicroStar microfocus rotation anode X-ray source operating at 45 kV and 60 mA. Powders were suspended in Paratone N oil and placed into a nylon loop and mounted on

a goniometer head. Transmission electron microscope (TEM) images were obtained using a field emission FEI Tecnai F20 Xt. Energy dispersive X-ray (EDS) was done using an EDAX EDS with SiLi detector. Scanning electron microscope (SEM) images were obtained using a LEO 1550 field emission SEM. Fourier transform infrared spectroscopy (FTIR) was performed using a Nicolet 6700. Raman spectroscopy was performed using a Witec alpha 300 with a 633 nm wavelength laser.

Electrode Fabrication

A suspension was made by combining 5 mg carbon black, 200 μL of 5 wt% Nafion solution (Fuel Cell Earth), and 1 mL of 50 mg/mL of either the FeS_2 wires or discs suspended in chloroform. Because of the difference in conductivity and particle size between the wires/discs and the cubes, the FeS_2 cubes suspension was fabricated by combining 5 mg carbon black, 100 μL of 5 wt% Nafion solution, and 500 μL of FeS_2 cubes suspended in chloroform. Each nanostructure suspension was sonicated for 15 min then <10 μL were dropcast on a 3 mm diameter glassy carbon electrode (CH Instruments) and allowed to dry for 15 min before testing.

SECM tip electrode fabrication

A laser capillary pipet puller (Model P-2000, Sutter Instruments, USA), quartz capillaries (1 mm O.D., 0.3 mm I.D., 7.5 cm in length, Sutter Instruments, USA), 200 μm diameter Pt wire (Electron Microscopy Sciences 99.95% Pt wire), conductive silver epoxy (Circuit Works, USA), and silver connection wire (30 AWG, Belden, USA) were utilized in the fabrication of 200 μm SECM tip electrodes. MicroCloth polishing disks (Buehler, Canada), alumina micropolish (1 μm, 0.3 μm, Buehler, Canada), and MicroCut 1200 grit silicon carbide grinding paper (P2500, Buehler, Canada) were utilized to polish SECM tips before experiments.

Microdisk Pt electrodes 200 μm in diameter were fabricated for the SECM tip. The 200 μm Pt wire was centered in the quartz capillary before sealing the capillary to the wire and pulling to a tip with a laser capillary pipet puller (Sutter P- 2000). Course polishing of the electrode tip with 1200 grit silicon carbide grinding paper was performed before fine polishing with 1 μm and 0.3 μm alumina micropolish, consecutively. Silver connection wire lightly coated with silver epoxy was inserted into the open end of the capillary tip electrode such that the silver epoxy was connecting the silver connection wire and the Pt wire. The SECM tip electrode was allowed to dry in a Model

30GC Lab Oven (Quincy Lab Inc) at 100 °C for 20 min before using.

SECM instrumentation

All reactivity maps were performed in a custom-built SECM including the following components from Newport: Vision Isostation air table (VIS2436-IG2-125A), faraday cage for air table, XPS Motion Controller/Driver with XPS-DRVP1 driver boards, 3-axis motion stage (VP-25XL- XYZL), 2 tilt stage motors (LTA-HS), and a Series 37 tilt stage. The SECM components were operated from an iMac computer via custom designed LabVIEW software while electrochemical measurements were collected via CH Instruments potentiostat (CHI730E).

Electrochemical Characterization

Electrochemical measurements were performed in a glass cell with a simple 3-electrode configuration and carried out in a 0.1 M pH 7 phosphate buffer solution (PBS) bubbled with argon for 5 min before use. The 0.1 M PBS was made by combining 4 mL of 1 M NaH_2PO_4 and 6 mL of 1 M Na_2HPO_4 and diluting with 90 mL of deionized Milli-Q water. The electrochemical measurements used either the FeS_2 coated 3 mm glassy carbon electrode, or a bare 3 mm glassy carbon electrode, or a bare 2 mm Pt electrode (CH Instruments) as the working electrode, a Pt wire (CH Instruments) as the counter electrode, and an Ag/AgCl electrode with porous Teflon tip (CH Instruments) as the reference electrode; however, the experiments were reported using the reversible hydrogen electrode as the reference potential. Linear sweep voltammetry (LSV) experiments were performed at 1 mV s^{-1} with a CH660E potentiostat (CH Instruments). All reported LSVs were corrected for double-layer capacitance and uncompensated resistance. The FeS_2 discs stability test along with the Pt TOF calculations were performed by utilizing chronoamperometry at an applied potential of -0.14 V vs RHE, with stirring provided by a magnetic stir bar to overcome mass transfer limitations. Time average data was recorded with each data point corresponding to an average current over 5 minutes.

The scanning electrochemical microscopy (SECM) reactivity mapping experiments were performed in a Teflon cell using either the FeS_2 discs coated 3 mm glassy carbon electrode, or a bare 3 mm glassy carbon electrode, or a bare 2 mm Pt electrode as the substrate, a 200 μm Pt ultra-microelectrode (UME) as the SECM tip, a 200 μm Pt wire (Electron Microscopy Instruments) as

the counter electrode, and an Ag/AgCl electrode with porous Teflon tip as the reference electrode with 0.1 M PBS, bubbled with argon for 10 min, as the electrolyte. The SECM tip electrode was positioned approximately 100 μm away from the substrate electrode before scanning. Scanning was performed with the substrate electrode at a negative potential sufficient to produce hydrogen while the SECM tip electrode was held at a positive potential sufficient to collect hydrogen. A 666.67 μm/s scanning speed was utilized with 100 μm steps over a 3500 μm x 3500 μm area for the Pt substrate electrode, or a 4000 μm x 4000 μm area for the FeS_2 discs coated glassy carbon and bare glassy carbon substrate electrodes. The SECM substrate generation / tip collection (SG/TC) experiments were performed in a Teflon cell with an FeS_2 discs coated 200 μm Au ultramicroelectrode (UME) as the substrate, a 200 μm Pt UME as the SECM tip, a 200 μm Pt wire (Electron Microscopy Instruments) as the counter electrode, and an Ag/AgCl electrode with porous Teflon tip as the reference electrode with 0.1 M PBS 0.5 mM (dimethylaminomethyl)ferrocene (DMAMFc), bubbled with argon for 10 min, as the electrolyte, and scan rate of 10 mV/s.

2.8.2 Supporting Results and Discussion

Materials Characterization

It should be noted that this low temperature phase could not be characterized as a standard phase such as pyrite or marcasite because of its atomic layer thickness. As such, standard characterization methods of these 1D and 2D structures yielded results that are different than the 3D high temperature phases. UV-Vis-IR measurements were taken of aliquots of wire and disc reactions at 0.5, 5, 10, 30, 90, and 240 minutes. Initially peaks are not readily apparent, but after reaction times greater than 1 minute the characteristic peaks appear at 320, 430, 530, 660, and 700 nm in both the wire (Fig. 2.5a) and the disc (Fig. 2.5b) reactions.[101,102] Optically the 2D growth of the discs causes rapid peak formation with little difference between scans at earlier and later reaction times. The 1D growth of the wires shows slower peak formation, and the resulting spectra is similar to those previously reported when investing growth of other pyrite structures where the wires were an intermediate stage.[89] In the early stages of the wire reaction, the shorter wavelengths dominate the spectra and have the highest relative intensities. However, as the reaction progresses, the peaks at 660 and 700 nm proceed to become the dominant peaks with the 700 nm peak appearing as a

lower intensity shoulder. The absorbance spectra stabilize when the 700 nm shoulder eclipses the 660 nm peak achieving the highest maximum relative intensity of all the characteristic peaks.

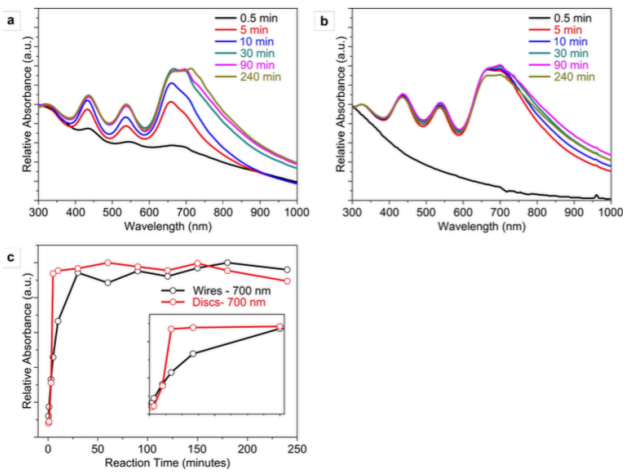

Figure 2.5. Time dependent absorbance spectra and EDS data. UV-Vis-IR is shown in (a) and (b) for wires and discs, respectively. In (c) growth of the peak at 700 nm was tracked over the course of the reaction with the inset focusing on the first 30 minutes to illustrate the relative changes.

For clarity, the growth of the 700 nm absorbance peak over the course of the reaction was plotted (Fig. 2.5c) and shows a strong correlation with the EDS data monitoring stoichiometry. The fact that the 700 nm peak grows in and does not appear to shift as it grows suggests a structural (i.e. stoichiometry) change instead of a size dependent shift in peak absorbance because of confinement. Additionally, the rate and time at which the 700 nm peak reaches its maximum could be used as an in-situ method for characterizing wires or discs formation as well as reaction progress, respectively.

Characterization by XRD shown in Fig. 2.6a-c was used to determine crystal structure and structural evolution during the course of the reaction. Initially, it was found that crystalline iron particles had formed prior to the injection of the sulfur, and persisted for the first few minutes of the reaction. The match to iron oxide (Fig. 2.6a) is a result of exposure of these small particles to open air during the measurement. Further along in the reaction, the iron oxide peaks disappear and what is left is mostly noise with small peaks observed that do not match with the typical 1:2 Fe:S structures of iron pyrite or marcasite. Numerous other Fe_xS_y XRD patterns were investigated but none matched appropriately. This may be caused by the limitations of the XRD when scanning particles with atomic layer dimensions. In addition, as the low-dimensional FeS_2 hyperthin nanostructured materials are susceptible to the irradiation damage (primarily the oxidation issue)

during the XRD measurement, it does not serve as a reliable source to characterize the FeS_2 in this study.

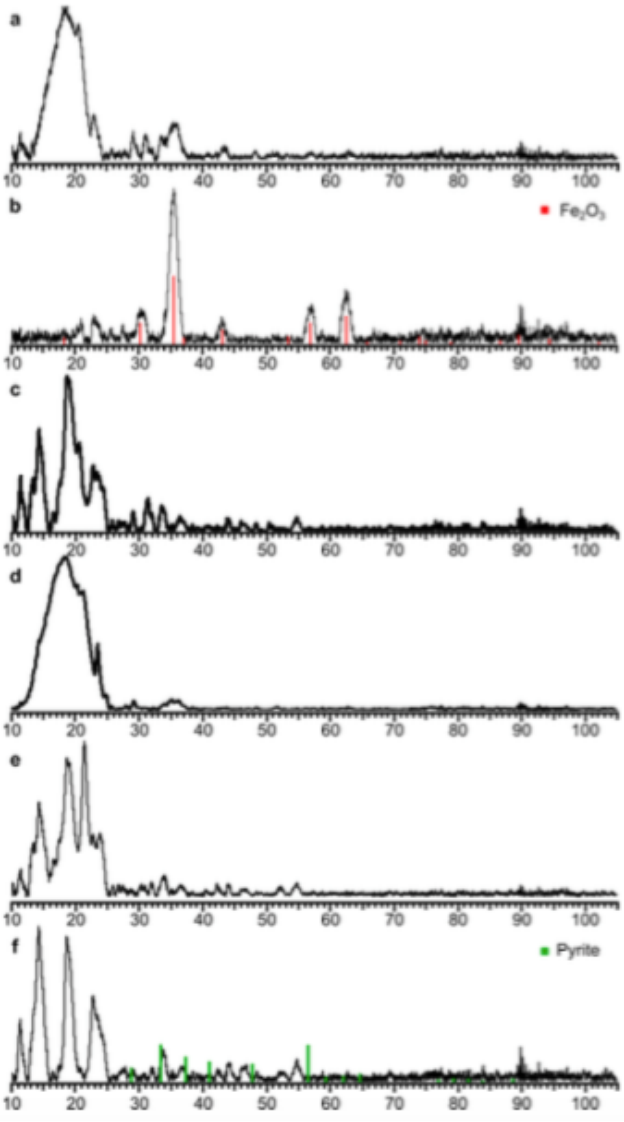

Figure 2.6. XRD data used to characterize the resulting nanostructures. XRD was taken of aliquots of wire and disc reactions at (a,b) 1 min, (c,d) 30 min, and (e,f) 240 min during the reactions. The red peaks correspond to Maghemite, Fe_2O_3 (00-004-0755) and the green peaks correspond to Pyrite, FeS_2 (00-001-1295).

TEM images of crystalline FeS_2 discs are shown in Figure 2.7. In Figure 2.7a, a low magnification image shows a FeS_2 disc with 1 μm diameter. Select area electron diffraction (SAED) pattern was taken from the red-circled area to confirm its crystallinity, as shown in the inset. High resolution TEM image of a FeS_2 disc is shown in Figure 2.7b. FFT of the squared area (inset) shows characteristic diffraction peaks of the (020), (110), and (200) planes from marcasite FeS_2,

indicating the image was taken from its [001] direction.

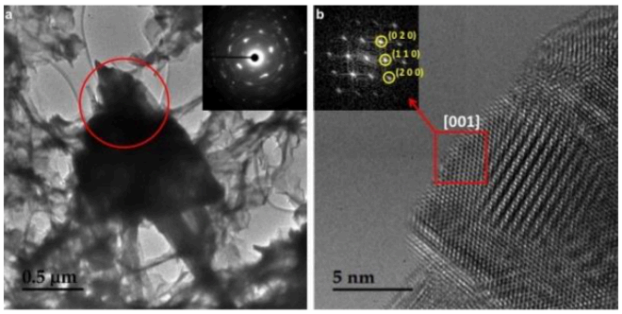

Figure 2.7. TEM images of crystalline FeS_2 discs. A FeS_2 disc with 1 μm diameter is shown in (a), red circle indicates the area where SAED pattern (inset) was taken. (b) High resolution TEM image of the FeS_2 disc observed from its [001] direction, FFT of the red-squared area (inset) shows diffraction peaks from (020), (110) and (200) planes.

Electrochemical Characterization

Equation 2.5 is an approximate form of the single-electron transfer Butler-Volmer Equation4 assuming an irreversible reaction with no mass transfer effects and a large overpotential. The equation describes the relation between the current density, j, and the overpotential, η, which is equivalent to the electrode potential versus RHE. The exchange current density, j_0, and the transfer coefficient, α, are the two kinetic parameters that were regressed from the LSV data, F is the Faraday constant, R is the universal gas constant, and T is temperature.

$$j = j_0 e^{-\frac{\alpha \eta F}{RT}} \tag{2.5}$$

As stated in the main text, triplicates of the LSV experiments were obtained from separate batches of the FeS_2 1D wires, 2D discs, and 3D cubes as shown in Fig. 2.8a. While the champion data from each set was reported in the main text, good reproducibility was obtained with no overlap between the worst 2D discs and best 1D wires, and no overlap between the worst 1D wires and best 3D cubes. Differences between samples were attributed to variability in electrode fabrication. Fig. 2.8b shows the TEM image of the 3D FeS_2 cubes to compare to the 1D wire and 2D disc structures.

We also demonstrated that high stability of these catalysts can be obtained when held under reducing conditions to evolve hydrogen. However, exposure of the FeS_2 nanostructures to oxi-

dizing potentials causes deactivation. Thus, it should be noted that the catalytic activity of the FeS_2 nanostructures decreases between scans when multiple cyclic voltammetry experiments are performed in the range of +0.3 to -0.3 V vs RHE on the same electrode.

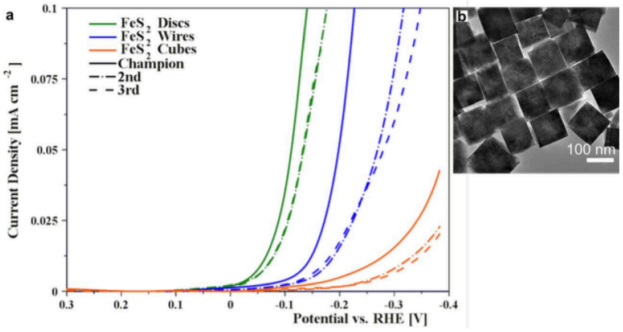

Figure 2.8. (a) Experimental linear sweep voltammograms for three different batches of FeS_2 discs, wires, and cubes coated on glassy carbon in 0.1 M pH 7 PBS using the convention of negative potentials to the right and reduction currents as positive. Each LSV shown is from a freshly fabricated FeS_2 electrode. (b) TEM image of the 3D cubes is shown for comparison to wire and disc structures.

For all electrochemical measurements, uncompensated resistance measurements were made via the "iR Comp" function on the CHI 660E Potentiostat software. The potential of all LSVs were then corrected for the uncompensated resistance. Measurements of uncompensated resistance in the samples were in the range of 100 - 520 Ω. Double-layer capacitance was also corrected for by subtracting background current (or current density) obtained from an extrapolated CV performed in the potential region before the onset of hydrogen evolution. Figure 2.9a shows the raw experimental data with no capacitance or iR correction for the data shown in Figure 2.3a in the main text, and Figure 2.9b shows the raw experimental data with no capacitance or iR correction for the data shown in Figure 2.8a.

As stated in the main text, linear sweep voltammograms (LSVs) of the FeS_2 nanoparticles were carried out at 1 mV/s so that a pseudo-steady state current could be reached at each potential. In Figure 2.10a, it can be seen that the system becomes mass transfer limited at modest current densities, but both the Pt and the FeS_2 disc reach the mass transfer limited regime at similar current densities. The mass transfer limited regime for Pt at 50 mV/s (Figure 2.10b) occurs at much higher current densities than for Pt at 1 mV/s because of the transients and steeper concentration gradients occurring from a faster scan rate. Figure 2.10c shows the LSVs with current density normalized by scan rate to illustrate the dependence of current on scan rate.

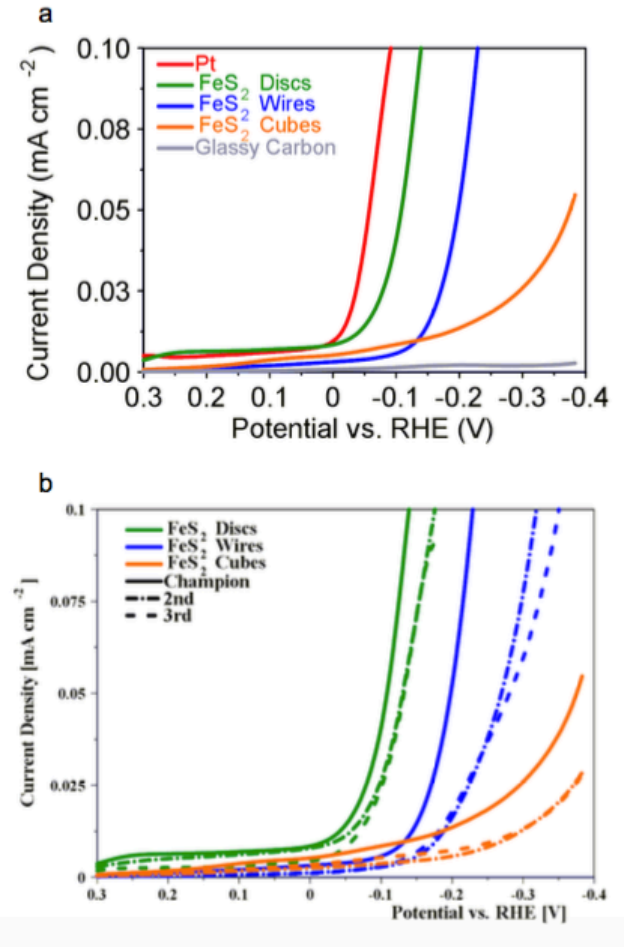

Figure 2.9. (a) Raw experimental linear sweep voltammograms with no capacitance or iR correction for the champion Pt, glassy carbon, and FeS_2 discs, wires, and cubes in 0.1 M pH 7 PBS using the convention of negative potentials to the right and reduction currents as positive. Capacitance and iR corrected data is shown in Figure 2.3a of the main text. (b) Raw experimental linear sweep voltammograms with no capacitance or iR correction for three different batches of FeS_2 discs, wires, and cubes coated on glassy carbon in 0.1 M pH 7 PBS using the convention of negative potentials to the right and reduction currents as positive. Capacitance and iR corrected data shown in Figure 2.8a.

The turnover frequency (TOF) was calculated with Equation 2.6.

$$TOF = \frac{iN_{Avo}}{A_{EC}FN} \tag{2.6}$$

Where i is the current, N_{Avo} is Avogadro's constant, A_{EC} is the electrochemical surface area, F is Faraday's constant, and N is approximated as 10^{15} atoms cm^{-2}. The electrochemical surface area was determined from standard active surface area calculations based on capacitance assuming 20 μF cm^{-2} as described above. The surface area was 4.8 and 1.0 cm^2 for the FeS_2 discs and Pt, respectively. The roughness factor (electrochemical surface area / geometric area) was found to be

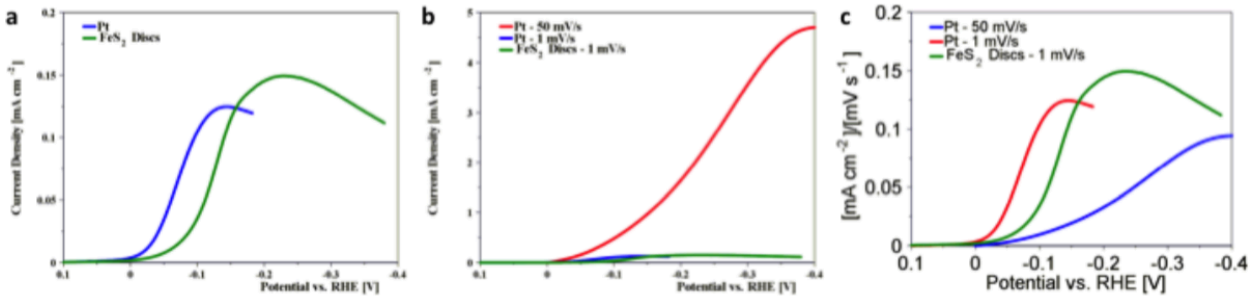

Figure 2.10. (a) Linear Sweep Voltammograms (LSVs) of Pt and FeS_2 Discs at a scan rate of 1 mV/s showing the mass-transfer limited regime (b) LSVs in (a) overlaid with a LSV of Pt at a scan rate of 50 mV/s (c) LSVs in (b) with the current density normalized by scan rate.

68 for the FeS_2 discs and 31 for Pt. The raw data from which the current, i , was obtained can be seen in Figure 2.11.

Similar measurements of the electrochemical surface area were also obtained for the wires and cubes. The wires had an electrochemical surface area of 2.3 cm^2 and the cubes had an electrochemical surface area of 0.56 cm^2. This corresponds to roughness factors of 33 and 8, respectively. Figure 2.12 shows the surface area normalized current as a function of potential.

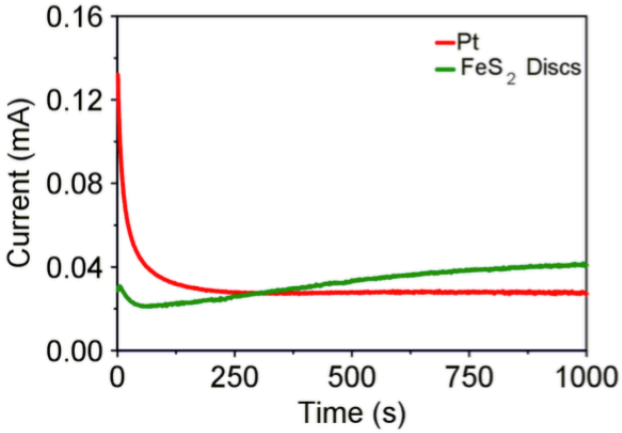

Figure 2.11. Current vs. Time plots for Pt and FeS_2 discs in stirred 0.1 M pH 7 phosphate buffer held at a constant potential of -0.14 V vs. RHE.

The Faradaic efficiency of hydrogen evolution on the FeS_2 discs was estimated from a SECM substrate generation / tip collection (SG/TC) experiment (Figure 2.13). In this experiment a 200 μm Pt tip electrode was positioned over a 200 μm Au electrode coated with FeS_2 disc substrate electrode. Linear sweep voltammetry was performed on the FeS_2 electrode and the Pt tip electrode collected the evolved hydrogen as a function of potential. However, the first step in performing

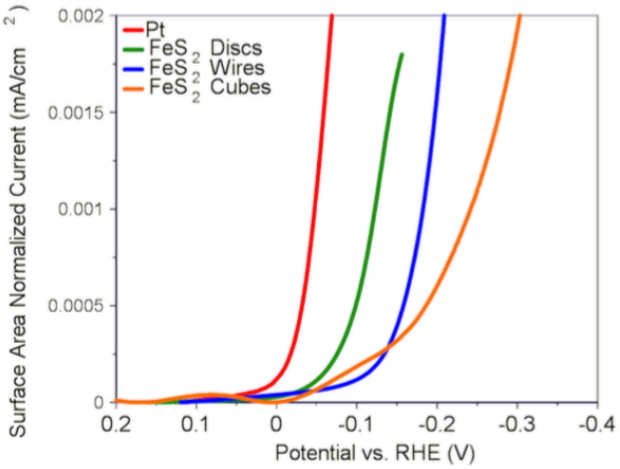

Figure 2.12. Electrochemical surface area normalized linear sweep voltammograms of Pt, and FeS_2 discs, wires, and cubes in 0.1 M pH 7 phosphate buffer solution (PBS) for the hydrogen evolution reaction at 1 mV/s.

SG/TC SECM to obtain the faradaic efficiency for hydrogen evolution is to determine the maximum collection efficiency using an outer-sphere redox mediator. The maximum collection efficiency can be under 100% because of misalignment of the tip to the substrate.

The redox mediator used to determine the theoretical maximum collection efficiency was (dimethylaminomethyl)ferrocene, DMAMFc, ($E^{1/2}$ 0.35 V vs. Ag/AgCl). However, the FeS_2 discs were found to deactivate under oxidizing potentials required to approach, align the tip and substrate, and perform the $DMAMFc^+$ SG/TC SECM (Figure 2.13a). Thus, a quick approach and map were required, resulting in misalignment of the substrate and the SECM tip. This resulted in a maximum collection efficiency, for $DMAMFc/DMAMFc^+$, of 1.6%. Figure 2.13b shows the $DMAMFc/DMAMFc^+$ SG/TC SECM data corrected for the collection efficiency. Also the large tip/substrate distance caused a delay in the collection of $DMAMFc^+$, which is corrected for in Figure 2.13b.

The raw experimental data for the hydrogen SG/TC SECM is shown in Figure 2.13c. Figure 2.13d shows the hydrogen SG/TC data corrected for the maximum collection efficiency of the DMAMFc SG/TC experiment. In addition the large tip/substrate distance caused a delay in hydrogen collection by the SECM tip due to a large diffusion distance between the tip and substrate, as was also the case for the $DMAMFc^+$ collection. Figure 2.13d also corrects for capacitance as described above. Due to the low collection efficiency it is difficult to exactly quantify the

faradaic efficiency of hydrogen because small variations in the collection efficiency of DMAMFc propagate through in calculating the Faradaic efficiency of hydrogen. However using this method we determined an estimate of hydrogen Faradaic efficiency of the FeS_2 discs to be 92 ± 8%.

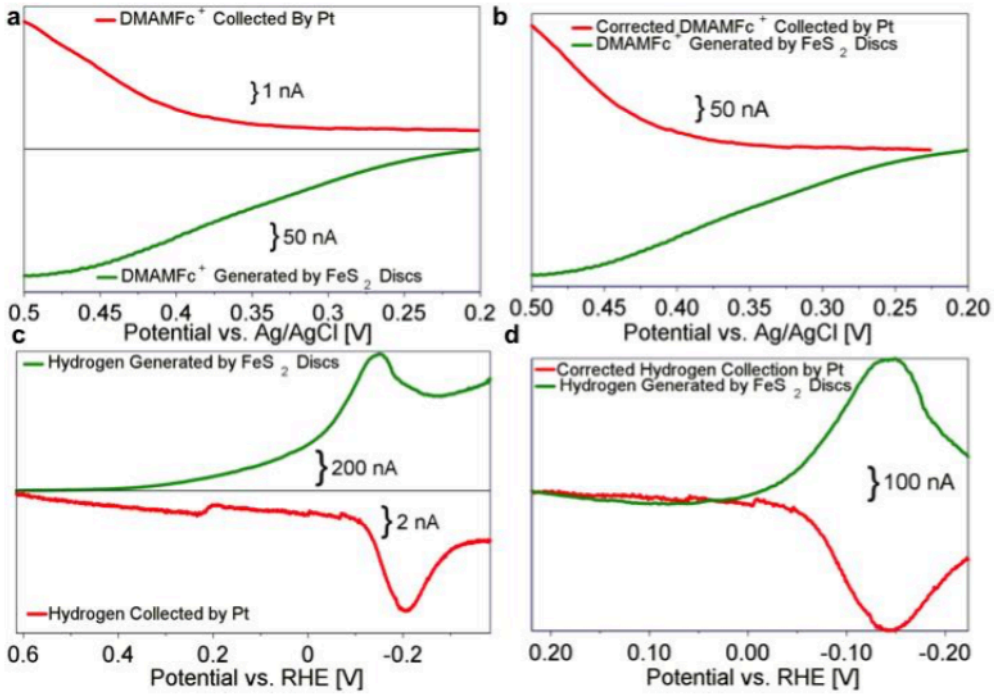

Figure 2.13. SECM substrate generation / tip collection (SG/TC) experiments with an FeS_2 discs coated 200 μm Au ultramicroelectrode (UME) as the substrate and a 200 μm Pt UME as the SECM tip. (a) $DMAMFc^+$ SG/TC raw data (b) $DMAMFc^+$ SG/TC corrected data – the FeS_2 discs current was corrected for capacitance and the Pt current was corrected for capacitance, scaled to the collection efficiency (1.6%), and the Pt potential was shifted to account for delay due to diffusion. (c) Hydrogen SG/TC raw data (d) Hydrogen SG/TC corrected data – the FeS_2 discs current was corrected for capacitance and the Pt current was corrected for capacitance, scaled to the $DMAMFc^+$ collection efficiency, and the Pt potential was shifted to account for delay due to diffusion.

	Tafel Slope			Butler-Volmer	
	Slope [mV decade^{-1}]	j^0 [µA cm^{-2}]	α	j^0 [µA cm^{-2}]	α
Discs	76	1.7	0.76	2.2	0.71
Wires	91	0.30	0.64	0.32	0.65
Cubes	200	0.47	0.29	0.41	0.31
Pt	71	6.3	0.82	8.0	0.71

Figure 2.14. Kinetic parameters obtained from the Tafel analysis and Bulter-Volmer Equations for Pt and the FeS2 Discs, Wires and Cubes.

2.9 Appendix

Earth abundant catalysts, such as transition metal dichalcogenides, may have insufficient conductivity for electrocatalysis. FeS_2 pyrite is a semiconductor, and the 1D FeS_2 wires, 2D FeS_2 discs, and 3D FeS_2 cubes all required addition of carbon to ensure that the current measured was due to electrocatalytic reaction and not influenced by resistance of the catalyst. Figure 2.15 shows a cyclic voltammogram (CV) of the FeS_2 discs without any conductive agents (blue line), exemplifying how resistance current can obscure the performance of the catalyst. Initially, activated carbon powder was added to the catalyst suspension (such that the suspension was 8 wt% activated carbon) before dropcasting the catalyst on the glassy carbon electrode. However, the CV still exhibited substantial resistive current (Figure 2.15, black line) and the catalyst commonly flaked off of the glassy carbon into the electrolyte during experiments. In the next iteration, acetylene carbon black was mixed in with the catalyst suspension because of it's higher surface area and conductivity, and 5 wt% Nafion solution was added to help bind the FeS_2 discs to the carbon black and the electrode. A CV of a sample from the 8 wt% carbon black, 15 wt% Nafion FeS_2 discs suspension (Figure 2.15, red line) shows a sharp onset of current (after the thermodynamic potential for water reduction, E^0=-0.617 V vs Ag/AgCl), indicative of an electrocatalytic reaction. The same recipe was found to be effective for the FeS_2 wires suspension as well, but the difference in particle size and conductivity of the FeS_2 cubes required double the carbon black content (20 wt% carbon black).

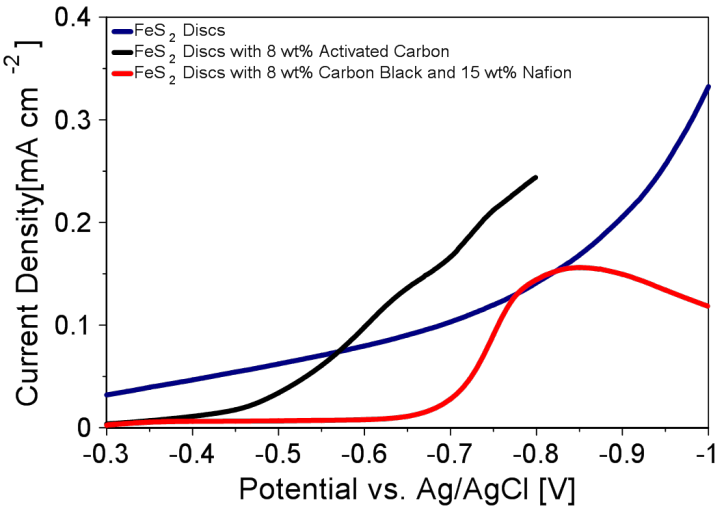

Figure 2.15. Cyclic voltammograms showing the decrease in resistive current of the FeS_2 discs with the addition of conductive agents.

Chapter 3

Microwave-assisted synthesis of a nanoamorphous ($Ni_{0.8}$,$Fe_{0.2}$) oxide oxygen-evolving electrocatalyst containing only "fast" sites

3.1 Abstract

Nickel-iron oxyhydroxides ($Ni_{0.8}Fe_{0.2}OOH$) are non-precious metal electrocatalysts for the oxygen evolution reaction (OER) that have high efficiency in alkaline media. It has been suggested that the layered-double hydroxide (LDH) crystal structure of $Ni_{0.8}Fe_{0.2}OOH$ contains two types of catalytic sites, "fast" Fe sites and "slow" Ni sites, which may limit the overall activity because only 20% of the catalytic surface is highly active. Herein, we report a facile microwave-assisted synthesis route of creating a nanoamorphous nickel-iron oxide electrocatalyst that contains only "fast" catalytic sites. Benchmarking experiments on flat electrodes (roughness factors <1.4) showed that the microwave-assisted, nanoamorphous ($Ni_{0.8}$,$Fe_{0.2}$) oxide had a low OER overpotential of 286 mV at a current density of 10 mA cm^{-2}. We measured the kinetic rate constant of the active sites directly with the surface interrogation mode of scanning electrochemical microscopy (SI-SECM). We show that the microwave-assisted, nanoamorphous ($Ni_{0.8}$,$Fe_{0.2}$) oxide has only one type of catalytic site with an

OER kinetic rate constant of 1.9 s^{-1} per site. We compared this to a crystalline $Ni_{0.8}Fe_{0.2}OOH$ that was synthesized via electrochemical conditioning of crystalline $Ni_{0.8}$:$Fe_{0.2}$ oxide, and verified that the $Ni_{0.8}Fe_{0.2}OOH$ contained two types of catalytic sites – "fast" sites with an OER rate constant of 1.3 s^{-1} per site and "slow" sites with a OER rate constant of 0.05 s^{-1} per site. The percentage of "fast" sites in the crystalline $Ni_{0.8}Fe_{0.2}OOH$ was well matched to the total iron atom content, while 100% of the sites were "fast" in the microwave-assisted, nanoamorphous ($Ni_{0.8}$,$Fe_{0.2}$) oxide.

3.2 Introduction

The development of efficient, earth-abundant electrocatalysts for the oxygen evolution reaction (OER) is of great importance to solar fuel production, because the OER is the half reaction that limits the overall efficency.[73,103,104] Developing catalysts for the OER is especially challenging since the oxidation of water to oxygen occurs through a complex four-electron/four-proton transfer[3] and many materials require a significant overpotential to drive the catalysis.[105] Traditionally, the best catalysts for the OER have been composed of the noble metals R_u and Ir.[50,106,107] However, since the discovery that iron impurities can improve the OER activity of nickel oxide electrocatalysts,[108,109] nickel-iron oxyhydroxides ($Ni_{0.8}Fe_{0.2}OOH$), specifically the layered double hydroxide (LDH) structure of $Ni_{0.8}Fe_{0.2}OOH$, have emerged as promising non-precious metal OER electrocatalysts in alkaline media and can rival the performance of iridium oxides.[60,61,110–127]

Experimental analysis of nickel to iron ratios has shown that approximately a $Ni_{0.8}$:$Fe_{0.2}$ ratio provides optimum catalytic performance.[60,112,113,121,128,129] This optimum ratio has been supported by a recent study by Bell and co-workers, which coupled X-ray absorption spectroscopy (XAS) with density functional theory (DFT) calculations.[63] segregation occurs and an inactive γ-FeOOH phase is formed.[63] In addition, DFT calculations from this study showed that the isolated iron sites within the $Ni_{0.8}Fe_{0.2}OOH$ matrix are highly active for the OER, while Ni sites in $Ni_{0.8}Fe_{0.2}OOH$ matrix are not active for the oxidation of water.[63] The existence of "fast" Fe sites and "slow" Ni sites in $Ni_{0.8}Fe_{0.2}OOH$ was recently verified experimentally by Bard and co-workers.[130] The Bard study used the surface interrogation mode of scanning electrochemical microscopy (SI-SECM) to probe the kinetics of the active sites on iron, nickel, and nickel-iron (oxy)hydroxides.[130] It is known that insights into the intrinsic activity of a catalyst can be obtained via SI-SECM, which mea-

sures the active site density and the kinetic rate constants of catalyst sites via an electrochemical titration.[130–133] In Bard's study, they observed that two types of catalytic sites existed for $Ni_{0.8}Fe_{0.2}OOH$; "fast" sites with a kinetic rate constant of 1.70 s^{-1} per site and "slow" sites with a kinetic rate constant of 0.056 s^{-1} per site.[130] Bard also showed that the percentage of "fast" sites matched well with the iron atom content in the $Ni_{0.8}Fe_{0.2}OOH$ matrix, providing further experimental evidence for the existence of both "fast" and "slow" sites in $Ni_{0.8}Fe_{0.2}OOH$. However, this finding implies that only 20% of the catalytic surface is highly active, and it may be possible to further improve the OER performance of nickel-iron electrocatalysts if more of the surface could be made active.

In addition to LDH $Ni_{0.8}Fe_{0.2}OOH$, there is extensive experimental evidence that amorphous materials can have exceptionally high electrocatalytic activity for the OER.[134–140] In fact, a recent report from Vojvodic, Sargent and co-workers showed that amorphous, homogeneously-dispersed multimetal oxygen-evolving electrocatalysts exhibited some of the best OER performance yet to be reported.[66] However, it is not well understood why these amorphous and homogeneously-dispersed materials exhibit such high cataltyic activity, nor is it well understood if amorphous structures also exhibit both "fast" and "slow" catalytic sites.

Herein, we set out to develop a catalytically active, well-dispersed, nanoamorphous (Ni,Fe) oxide for use as an OER electrocatalyst in which we can control the Ni:Fe ratio, and determine if amorphous structures give rise to only "fast" catalytic sites. To accomplish this, we developed a microwave-assisted synthesis route for creating nanoamorphous (Ni,Fe) oxide structures. Microwave synthesis routes[141] have been previously used to form nanostructures of iron oxides,[142–144] but to the best of our knowledge microwave synthesis routes of nickel-iron OER catalysts have not been previously reported. We compared the electrochemical activity of this microwave-assisted, nanoamorphous (Ni,Fe) oxide material to a $Ni_{0.8}Fe_{0.2}OOH$ that we synthesized via an electrochemical conditioning of crystalline $Ni_{0.8}$:$Fe_{0.2}$ oxide.[122] To measure the kinetics of the active sites directly, we utilized SI-SECM via a masked-electrode technique. Our findings show that on flat electrodes (roughness factor <1.4), the microwave-assisted, nanoamorphous (Ni,Fe) oxide material had a lower overpotential for the OER compared to the crystal-derived oxyhydroxide. Our SI-SECM experiments on the crystal-derived $Ni_{0.8}Fe_{0.2}OOH$ showed the existence of "fast" and "slow" sites (kinetic rate constants of 1.3 s^{-1} and 0.05 s^{-1}, respectively) and the percentage of fast

sites (7%) matched well with the iron-metal content. These results are in very good agreement with the study recently performed by Bard and co-workers.[130] However, SI-SECM experiments on the nanoamorphous ($Ni_{0.8}$,$Fe_{0.2}$) structure showed only one type of site, and the kinetic rate constant of this site (1.9 s^{-1}) matched well with the kinetics of the "fast" site on the crystal-derived $Ni_{0.8}Fe_{0.2}OOH$. This finding suggests that well-dispersed, amorphous materials may have higher catalytic activity because they exhibit only the "fast" catalytic sites.

3.3 Materials and Methods

3.3.1 Chemicals

Iron (III) nitrate nonahydrate (98%+, ACS Reagent, Acros), nickel (II) nitrate hexahydrate (99%, Fisher Scientific), iridium (III) chloride (99.99%, Alfa Aesar), sodium hydroxide (¿97%, Fisher Scientific), ethylene glycol (99.8%, anhydrous, Sigma Aldrich), sodium bicarbonate (Fisher Scientific), potassium hydroxide (85%, Acros Organics), iron (III) sulfate hydrate (Reagent Grade, Alfa Aesar), triethanolamine (97%, Acros Organics) were all used as received without additional purification.

3.3.2 Catalyst Synthesis

Crystalline-derived catalyst.

Crystalline thin-films of $Ni_{0.8}$:$Fe_{0.2}$ oxide were made similar to those previously reported.[145] Briefly, two solutions, one of 0.02 M $Ni(NO_3)_2 \cdot 6H_2O$ and the other of 0.02 M $Fe(NO_3)_3 \cdot 9H_2O$, were prepared separately in ethylene glycol and subsequently mixed in an 8:2 ratio. The solution was dropcast and annealed on fluorine-doped tin oxide (FTO) coated glass (Sigma-Aldrich) to create the $Ni_{0.8}$:$Fe_{0.2}$ oxide as described in Supporting Information. The oxide was then electrochemically conditioned by applying an oxidation current of ca. 10 mA cm^{-2} for 1 hour, as has been previously described.[122]

Nanoamorphous microwave-assisted catalysts.

First, a nanoamorphous Fe catalyst was synthesized using a sol-gel method similar to a previously reported method with some modifications.[146,147] Briefly, 8.08 grams of $Fe(NO_3)_3 \cdot 9H_2O$ was dis-

solved in 100 mL of 18.2 MΩ water. Separately, 1.99 grams of $NaHCO_3$ was dissolved in 100 mL of 18.2 MΩ water. Both solutions were sonicated until fully dissolved. The $Fe(NO_3)_3 \cdot 9H_2O$ was placed in a 250 mL Erlenmeyer flask with a Teflon stir bar and placed on a stir plate. The $NaHCO_3$ was placed in a burette and was used to titrate at a rate of 2 - 3 drops per second to achieve a rate of 2.5 - 3 mL/min rate while rapidly stirring the $Fe(NO_3)_3$ solution. The suspension underwent a gradual color change from orange to deep red at the end. The total titration time was about 40 - 45 minutes, and the solution continued to stir for one hour after titration. This suspension was then placed in Nalgene bottles to be microwaved. The solution was microwaved for about two minutes, with swirling every 15 - 20 seconds to mix the contents, in a conventional 1050 W microwave (Rival). After two minutes of microwaving, the solution had begun to boil with bubbles on the sides of the bottles. To form the nanoamorphous Ni catalyst, this procedure was repeated by replacing the $Fe(NO_3)_3 \cdot 9H_2O$ with 5.82 grams of $Ni(NO_3)_2 \cdot 6H_2O$. After microwaving the nickel suspension, some separation occurred. To form the nanoamorphous mixed-metal catalysts, this procedure was repeated except the $Ni(NO_3)_2 \cdot 6H_2O$ and $Fe(NO_3)_3 \cdot 9H_2O$ were mixed to create two additional solutions at 1:1 and 8:2 molar ratios, respectively. These solutions were titrated and microwaved as described above. Some separation also occurred in the nanoamorphous mixed-metal suspensions. Electrodes were made by dropcasting the suspensions, both with and without the microwave step, on FTO-coated glass and were dried at 70 °C as described in the Supporting Information. After dropcasting, the samples were gently rinsed with 18.2 MΩ water to remove any material that was not well adhered to the surface. This left a nearly transparent film of the nanoamorphous Ni_{1-x}:Fe_x catalyst on the FTO-coated glass. Additionally, the microwave-assisted nanoamorphous $Ni_{0.8}$:$Fe_{0.2}$ was deposited via electrophoretic deposition on FTO-coated glass to compare to the dropcast samples on FTO. The nanoamorphous $Ni_{0.8}$:$Fe_{0.2}$ was also electrophoretically deposited onto a glassy carbon rotating disc electrode (RDE) for benchmarking, and solution-derived (non-microwaved) and microwave-assisted $Ni_{0.8}$:$Fe_{0.2}$ were dropcast on a glassy carbon RDE for comparison. Electrophoretic deposition was performed by applying -5 V to the working electrode for 10 minutes in a two electrode system with a Ti counter electrode.

3.3.3 Materials Characterization

Scanning electron microscope (SEM) images and Energy Dispersive X-Ray Spectrometry (EDS) images were obtained using a FEI Versa 3D Dual Beam SEM. X-ray Diffraction (XRD) data were collected on a Bruker D8 Discover with DaVinci diffractometer, in the standard Bragg-Brentano para-focusing configuration utilizing sealed tube CuKα radiation ($\gamma = 1.5418$ $\mathring{A}$) operated at 40kV and 40mA. The sample was mounted using a zero background holder (ZBH) on a horizontal sample stage for an 830 mm diameter goniometer equipped with a 1D Lynxeye detector. Data were collected using a step width of 0.02° and step time of 0.3 s with a 2θ range of 20.0° - 100.0°. X-ray photoelectron spectroscopy (XPS, Physical Electronics, Inc USA) was used to obtain binding energies of the C 1s, O 1s, Fe 2p, and Ni 2p orbitals using a monochromatic Al X-ray source. The adventitious carbon 1S binding energies for all XPS measurements were taken to be 284.8 eV.

3.3.4 Electrochemical characterization

Cyclic voltammetry (CV) was performed on the catalyst coated FTO electrodes in a custom Teflon cell with a holding place for a Ag/AgCl reference electrode with porous Teflon tip (CH Instruments). The size of all FTO glass working electrodes was 0.49 cm^2, except for those used in the non-microwaved vs microwaved comparison (See Figure 3.1c), which were 0.97 cm^2. A 200 μm Pt wire (Electron Microscopy Instruments) was used as the counter electrode, and the CV experiments were performed in 1 M NaOH. All electrochemical measurements were obtained via a CH Instruments (Austin, TX) potentiostat.

Benchmarking experiments (i.e. cyclic voltammetry, chronopotentiometry, chronoamperometry) were performed on a catalyst coated glassy carbon custom rotating disc electrode (RDE), 0.071 cm^2, in a glass cell with a Ag/AgCl reference electrode with porous Teflon tip (CH Instruments) and a Pt counter electrode (CH Instruments). All RDE experiments were operated at 1600 rpm in 1 M NaOH.

The SECM Instrumentation utilized for the surface interrogation experiments was described previously.[148] Before each SECM experiment, the 2 M NaOH ca. 50 mM Fe(III)-TEA (E^0 = -1.05 V vs Ag/AgCl in 2 M NaOH) solution (synthesis described in Supporting Information) was bubbled with argon for 10 minutes. The experiments were carried out in a custom Teflon cell holding the

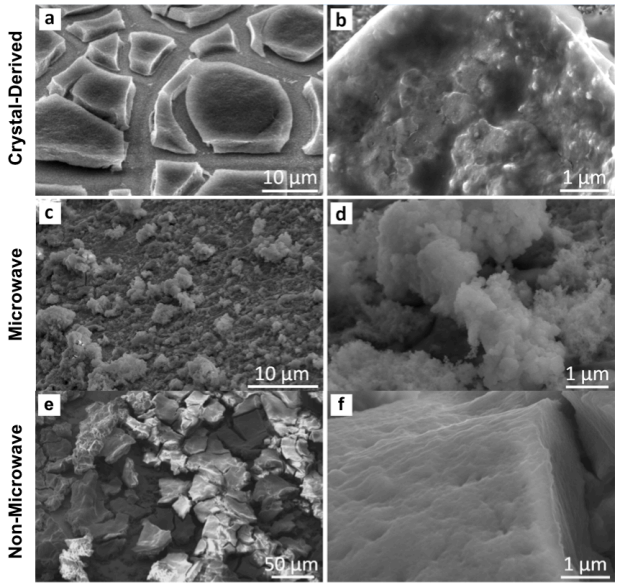

Figure 3.1. Scanning Electron Microscopy (SEM) images of the crystal- derived (a and b), microwave-assisted (c and d), and solution-derived (non-microwaved) (e and f) $Ni_{0.8}$:$Fe_{0.2}$ catalysts deposited on FTO-coated glass.

masked crystal-derived oxyhydroxide or microwave-assisted nanoamorphous $Ni_{0.8}$:$Fe_{0.2}$ on FTO glass substrate as the working electrode, a 200 μm Pt wire (Electron Microscopy Instruments) as the counter electrode, and a Ag/AgCl electrode with porous Teflon tip (CH Instruments) as the reference electrode. The SECM tip, a glassy carbon (GC) ultramicroelectrode, a = 29 μm (fabrication described in the Supporting Information), was held at -1.1 V vs Ag/AgCl while it was approached to the approximate location of hole in the masked substrate until a current enhancement of 0.4 was reached (Supporting Information Figure 3.10). Electrochemical reactivity maps, ranging in size from 200 – 1600 μm x 200 – 1600 μm, were performed, with step sizes ranging from 10 – 40 μm and a sample interval of 2 s, until the location of the hole was apparent (Supporting Information Figure 3.11). The GC tip was positioned near the hole and re-approached to a current enhancement of 0.3 before moving the GC tip directly over the hole. For the surface interrogation experiment, a potential step with a 20 s duration was performed on the catalyst with 0.383 V overpotential. Immediately following, the substrate was brought to open circuit for a delay time ranging from 0 – 2000 ms before a potential step was applied to the GC tip electrode at -1.1 V vs Ag/AgCl with pulse width of 180 s. Finite element analysis simulations were performed with COMSOL Multiphysics v. 5.2 (additional details provided in Supporting Information).

3.4 Results and Discussion

3.4.1 Materials Synthesis

Scheme 1 compares the synthesis routes of the nanoamorphous (Ni,Fe) oxide using our newly reported microwave-assisted technique, to the synthesis route of the crystal-derived $Ni_{0.8}Fe_{0.2}OOH$. Both techniques start with iron nitrate and nickel nitrate precursors. To fabricate the crystal-derived $Ni_{0.8}Fe_{0.2}OOH$, we utilized a previously reported method where Fe-doped NiO rock salt structures are converted to nickel-iron oxyhydroxides via electrochemical conditioning.[122] The rock salt structure (see XRD analysis under Materials Characterization) was fabricated by depositing solutions of these nitrate salts in ethylene glycol on a fluorine-doped tin oxide (FTO) coated glass substrate, followed by annealing in air at 525 °C for 3 hours.[143] To fabricate the nanoamorphous structure, we needed to devise a method that allowed us to control the Ni:Fe ratio and form the oxide structure without excessive heating to avoid crystallization and segregation. To accomplish this, we used a titration technique to form nickel-iron carbonates, and then applied a microwave-heating step to decompose the carbonate and form an amorphous oxide structure. For example, when an aqueous solution containing $Fe(NO_3)_3$ is titrated with $NaHCO_3$, the iron and carbonate ions will form iron (III) bicarbonate (Equation 3.1, which spontaneously decomposes to iron (III) carbonate as a precipitate (Equation 3.2) (See XPS analysis under Materials Characterization). Iron (III) carbonate is inactive for the OER, but it decomposes further to produce the active iron oxide (Equation 3.3) at temperatures below 100 °C.[149] We utilized the microwave-heating step to force the decomposition of the carbonate species to the oxide species while still in solution, so that the crystallization and segregation do not occur.

$$Fe^{3+} + 3HCO_3^- \rightarrow Fe(HCO_3)_3 \tag{3.1}$$

$$2Fe(HCO_3)_3 \rightarrow Fe_2(CO_3)_3 + 3CO_2 + 3H_2O \tag{3.2}$$

$$Fe_2(CO3)_3 \rightarrow \text{iron oxides} + 3CO_2 \tag{3.3}$$

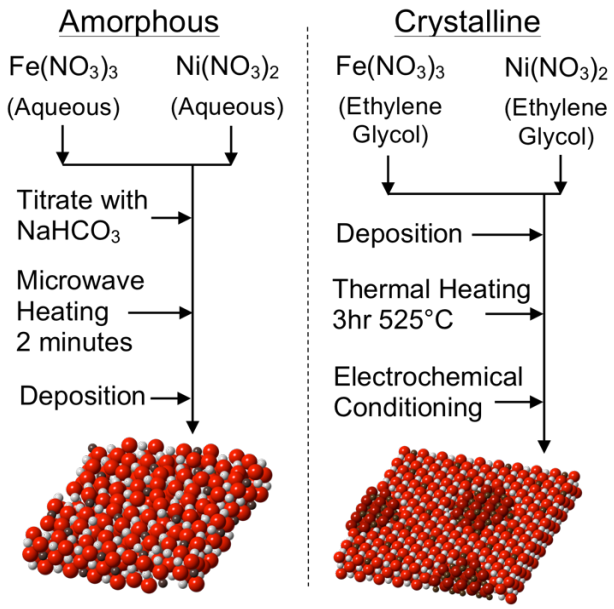

Figure 3.2. Synthesis sequence of nanoamorphous $Ni_{0.8}$:$Fe_{0.2}$ oxide (left) and crystal-derived $Ni_{0.8}$:$Fe_{0.2}$ oxyhydroxide (right).

3.4.2 Materials Characterization

SEM images of the crystal-derived $Ni_{0.8}$:$Fe_{0.2}$ prior to electrochemical conditioning (Figure 3.1a) show a catalyst layer with some catalyst cracking occurring due to the annealing step. This formed macroparticles ca. 10's of μm in size. These macroparticles have some porosity and are not single crystals (Figure 3.1b). EDS measurements show a uniform distribution of Fe and Ni in these macroparticles (Supporting Information Figure 3.18), and show that the nickel to iron ratio is approximately $Ni_{0.8}$:$Fe_{0.2}$. SEM images of the solution-derived (non-microwaved) structure (Figures 3.1e and 3.1f) show uniform macroparticles of ca. 50-100 μm in size. These macroparticles are fairly smooth with little surface variation. When the microwave-heating step was applied, the structure changes into an amorphous network, presumably from the release of CO_2 that occurs during the decomposition of the carbonate species (Figures 3.1c and 3.1d). EDS measurements on the microwave-assisted structure also show uniform distribution of Fe and Ni and an approximate nickel to iron ratio of $Ni_{0.8}$:$Fe_{0.2}$ (Supporting Information Figure 3.19).

High resolution transmission electron microscopy (HRTEM) images (Figure 3.3) show that the microwave-assisted $Ni_{0.8}$:$Fe_{0.2}$ is not a collection of individual particles but it is a nanoamorphous network. Complete absence of crystalline order is seen even at the 5 nanometer scale (Figure

3.3d). Electron diffractograms (Figure 3.3, inlays) show no diffraction spots, indicating that our microwave-assisted $Ni_{0.8}$:$Fe_{0.2}$ is indeed nanoamorphous. XRD (Figure 3.4a) on the crystal-derived $Ni_{0.8}$:$Fe_{0.2}$ oxide prior to electrochemical conditioning shows the NiO rock-salt structure in addition to Fe_3O_4. Segregation of iron and nickel has been previously reported on nickel-iron samples that have molar ratios very near to the 25% iron segregation limit.[63,130] XRD on the microwave-assisted structure shows an amorphous structure with no iron oxide, nickel oxide, or oxyhydroxide peaks visible, confirming that this material is amorphous. The only diffraction peaks observed are those of $NaNO_3$ which is a remnant of the titration of $Fe(NO_3)_3$ or $Ni(NO_3)_2$ with $NaHCO_3$. The $NaNO_3$ crystals can be seen on SEM images of un-rinsed XPS was performed on the crystal-derived $Ni_{0.8}$:$Fe_{0.2}$ oxide prior to conditioning (Figures 3.4b-e, top spectrum), electrochemically conditioned crystal-derived $Ni_{0.8}$:$Fe_{0.2}$ oxyhydroxide (Figures 3.4b-e, second spectrum), solution-derived (non-microwaved) $Ni_{0.8}$:$Fe_{0.2}$ (Figures 3.4b-e, third spectrum), and microwave-assisted nanoamorphous $Ni_{0.8}$:$Fe_{0.2}$ (Figures 3.4b-e, bottom spectrum). On the crystal-derived sample prior to conditioning, the Fe $2p^{3/2}$ binding energy was 711 eV, which is consistent with the binding energy for Fe_3O_4.[150] Three separate O 1S peaks are visible at binding energies of 528.8 eV, 530.0 eV, and 531.6 eV. The 528.8 eV peak is consistent with iron oxides and/or hydroxide species, and the 530 eV and 531.6 eV peaks are consistent with nickel oxide and/or hydroxide species.[127] The Ni $2p^{3/2}$ binding energies were 854.5 eV and 856.5 eV. The 854.5 eV peak is consistent with NiO, and the 856.5 eV peak is consistent with NiO or nickel hydroxide.[127] The multiple oxygen and nickel peaks confirm that some segregation occurs during the synthesis of the crystal-derived structure prior to conditioning as also shown with the XRD data. The electrochemically conditioned crystal-derived sample shows similar characteristic peaks, and the two separate O 1S peaks suggest that segregation still exists in the crystalline nickel-iron oxyhydroxide structure.

On the microwave-assisted structure, the Ni $2p^{3/2}$ binding energy was 855.9 eV, indicative of $Ni(OH)_2$ or NiOOH.[127] The single O 1S peak at a binding energy of 531.2 eV is indicative of nickel oxide, nickel hydroxide, or iron hydroxide species.[150,151] The Fe $2p^{3/2}$ binding energy of 711.1 eV is also indicative of an iron binding energy in a hydroxide structure.[151]61 However, the solution-derived (non-microwaved) binding energies contain a crucial difference when compared to that of the microwave-assisted. On the non-microwaved sample, there is a C 1s binding energy at 289.2 eV, which is not present on the microwave-assisted structure. The 289.2 eV peak is consistent

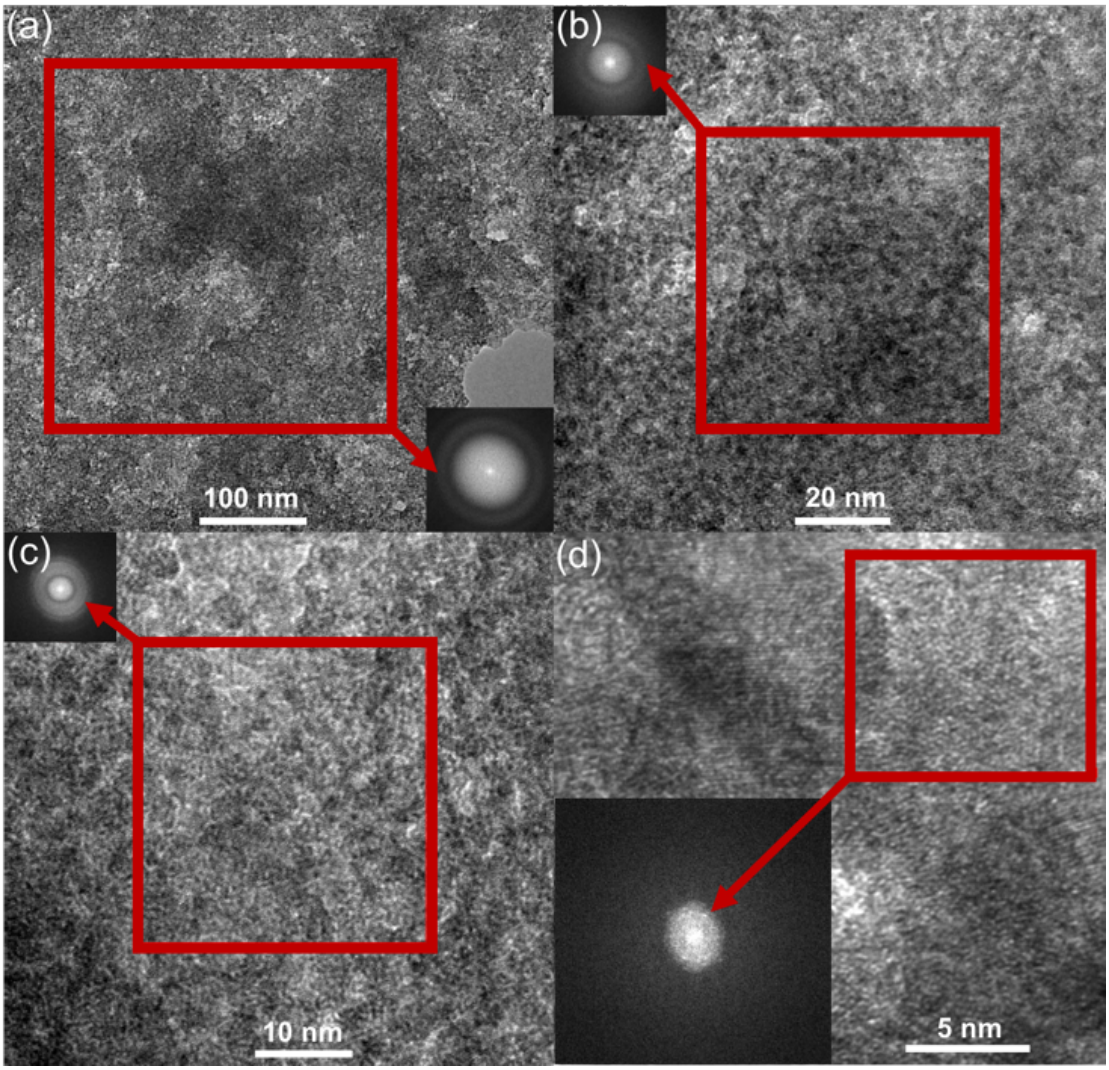

Figure 3.3. High resolution transmission electron microscopy (HRTEM) images of the microwave-assisted nanoamorphous $Ni_{0.8}$:$Fe_{0.2}$ (a–d) with the corresponding electron diffractograms (inlays).

with a carbonate peak,[149] which gives strong evidence to support the formation of an inactive iron carbonate species in the initial steps of the synthesis preceding the microwave step. In addition, this XPS data is further evidence that the microwave-assisted synthesis is able to create a nickel-iron structure with no measurable segregation of iron.

3.4.3 Electrochemical Characterization

Rotating disc electrode (RDE) cyclic voltammograms of solution-derived (non-microwaved) and microwave-assisted $Ni_{0.8}$:$Fe_{0.2}$ on a glassy carbon electrode, along with bare glassy carbon are shown in Figure 3.5a. Here the utility of the microwaving step is apparent. The activity of the

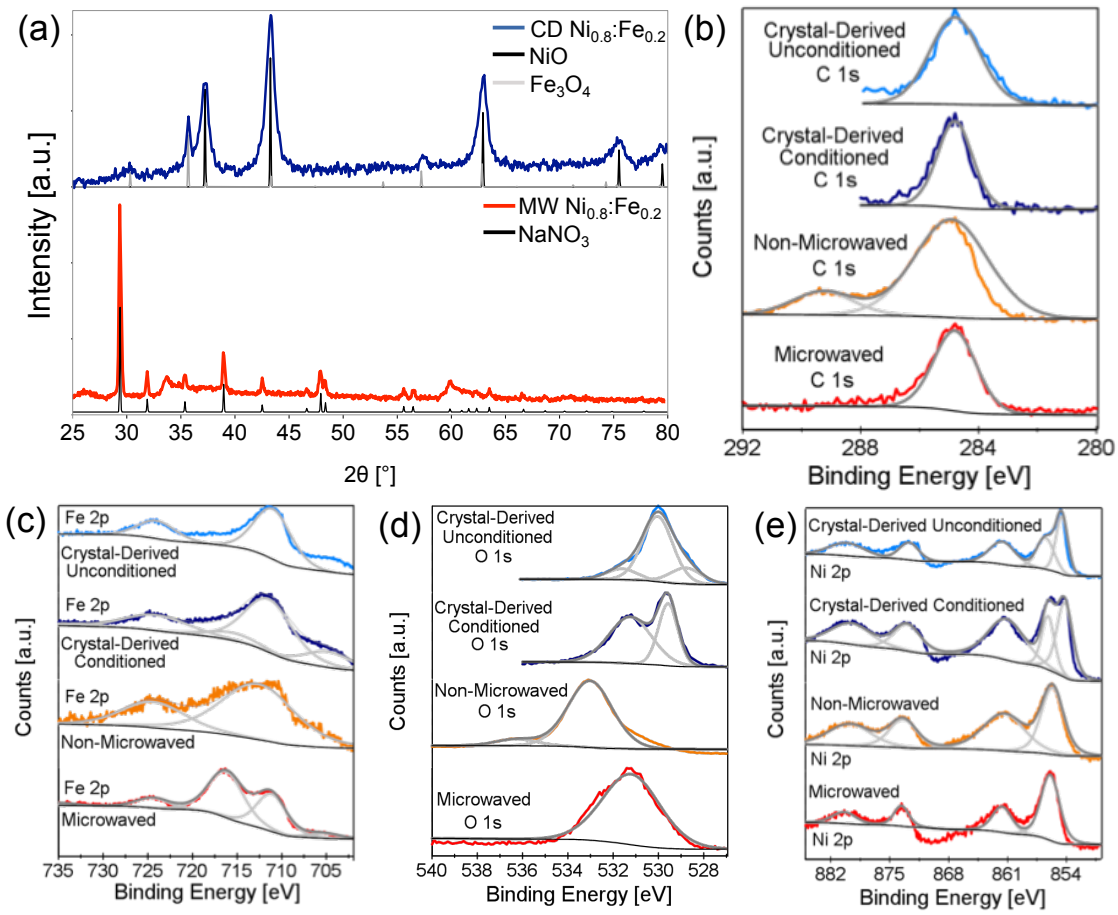

Figure 3.4. X-ray diffraction of crystal-derived $Ni_{0.8}$:$Fe_{0.2}$ oxide prior to electrochemical conditioning and microwave-assisted nano- amorphous $Ni_{0.8}$:$Fe_{0.2}$ powders (a). X-ray photoelectron spectroscopy of the crystal-derived $Ni_{0.8}$:$Fe_{0.2}$ oxide prior to conditioning (b–e, top spectrum), electrochemically conditioned crystal-derived $Ni_{0.8}$:$Fe_{0.2}$ oxyhydroxide (b–e, second spectrum), solution-derived (non-micro- waved) $Ni_{0.8}$:$Fe_{0.2}$ (b–e, third spectrum), and microwave-assisted nanoamorphous $Ni_{0.8}$:$Fe_{0.2}$ (b–e, bottom spectrum).

non-microwaved (i.e. carbonate) material over the bare glassy carbon is marginal. However, the catalytic activity of microwave-assisted structure shows a dramatic improvement compared to the non-microwaved structure. We also utilized two deposition techniques to apply the microwave-assisted sample to the GC electrode, electrophoretic deposition and dropcasting (MW-E and MW-D, respectively), and found that electrophoretic deposition (electrodeposition) provided better catalyst coverage and higher catalytic activity, with the MW-E electrode reaching 100 mA cm^{-2} at 369 mV overpotential. To further demonstrate the utility of the microwave-step, we compared the catalytic activity of non-microwaved and microwave-assisted structures of mixed-metal Ni_{1-x}:Fe_x with different Ni:Fe ratios (representative cyclic voltammograms are shown in Figure 3.5b). We

observed that the non-microwaved samples containing Fe (Fe, Ni:Fe, and $Ni_{0.8}$:$Fe_{0.2}$) did not have any significant catalytic activity for the OER, nor did we observe the $Ni(OH)_2$/NiOOH redox peaks typically found in Ni:Fe oxyhydroxides[60,121] for these samples (Supporting Information Figure 3.12 and 3.13). For all of the Ni_{1-x}:Fe_x microwave-assisted structures, we observed the $Ni(OH)_2$/NiOOH redox peaks (See Supporting Information Figure 3.14) and a large oxidation current indicative of catalytic activity for the OER. The solution-derived and microwave-assisted samples that only contained Ni also exhibited both of these characteristics. Since we made no attempt to purify the Ni precursors, we attribute the relatively high activity of the Ni-only samples to Fe impurities that may be present.[109,121] Triplicate cyclic voltammetry measurements from different synthesis batches show good reproducibility for all microwave-assisted structures (Supporting Information Figure 3.15). To compare the MW-E and MW-D $Ni_{0.8}$:$Fe_{0.2}$ to the crystal-derived $Ni_{0.8}$:$Fe_{0.2}$ oxyhydroxide and crystalline IrO_x, cyclic voltammograms were performed with all samples deposited onto FTO-coated glass (Figure 3.5c). Both the microwave-assisted and crystal-derived samples show the $Ni(OH)_2$/NiOOH redox peaks and the large oxidation current indicative of catalytic activity for the OER. The IrO_x sample also shows a small wave, which may be attributed to a Ir^{IV}/Ir^{V} transition,[132] prior to the onset of the large oxidation wave indicative of catalytic activity for the OER. The static cyclic voltammetry measurements showed that MW-E $Ni_{0.8}$:$Fe_{0.2}$ electrode has an overpotential ca. 100 mV less than that of the crystal-derived $Ni_{0.8}$:$Fe_{0.2}$ and ca. 200 mV less than that of crystalline IrO_x.

In order to determine if the increase in catalytic activity of the microwave-assisted electrodeposited $Ni_{0.8}$:$Fe_{0.2}$ samples was due to an increase in the electrochemical surface area (ECSA), the double layer capacitance was measured via cyclic voltammetry (Supporting Information Figures 3.16 and 3.17). We measured similar and very low roughness factors on both the crystalline $Ni_{0.8}Fe_{0.2}OOH$ and the microwave-assisted nanoamorphous $Ni_{0.8}$:$Fe_{0.2}$ structures, 1.2 and 1.4, respectively. Reliable estimation of the ECSA of a catalyst can be difficult and subjective, but based on these measurements, it cannot be conclusively stated that a change in the ECSA is the reason for the increase in electrocatalytic performance of the microwave-assisted structure. In addition, we measured a slightly higher mass loading with the crystal-derived sample having 120 $\pm$ 20 μg cm^{-2} and the microwave-assisted sample having 60 $\pm$ 20 μg cm^{-2}. This suggests that the increased electrocatalytic activity of the microwave-assisted structure is not simply due to an increase in the

ECSA or an increase in the mass loading.

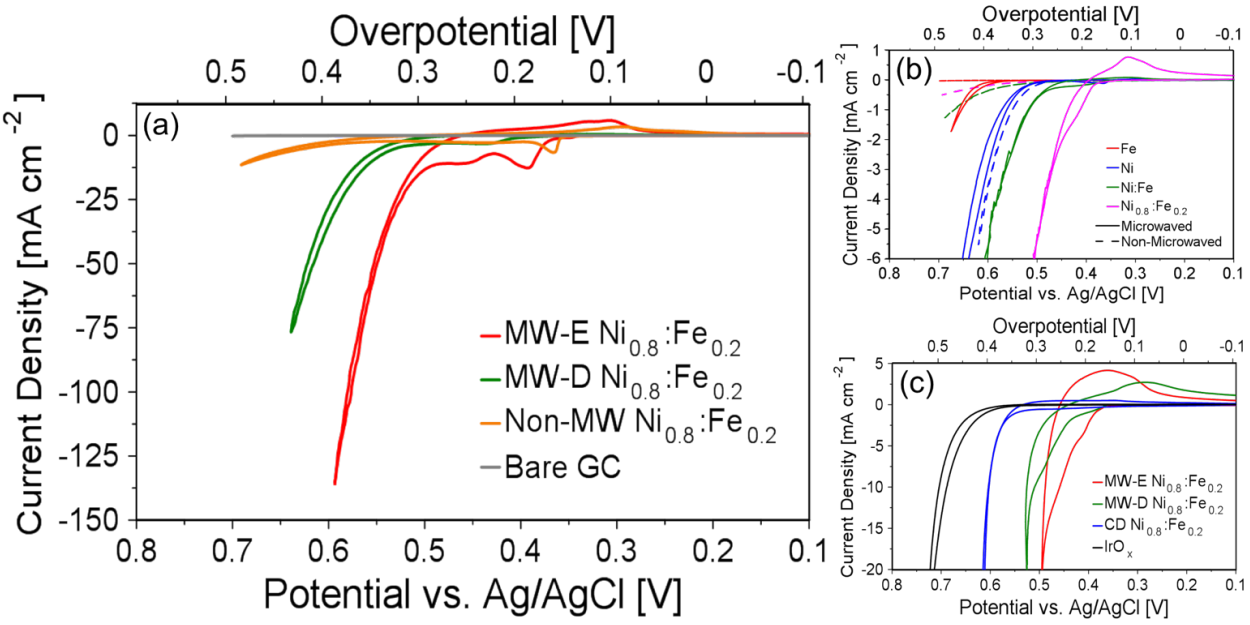

Figure 3.5. Rotating disc electrode cyclic voltammograms of microwave-assisted electrodeposited (MW-E) and dropcast (MW-D) nanoamorphous $Ni_{0.8}$:$Fe_{0.2}$, with solution-derived (Non-MW) $Ni_{0.8}$:$Fe_{0.2}$ on a glassy carbon (GC) electrode at 10 mV s^{-1} (a). Static cyclic voltammograms of solution-derived (non-microwaved) and microwave-assisted Ni1 x:Fex on FTO glass at 1 mV s^{-1} (b). Static cyclic voltammograms of MW-E and MW-D nanoamorphous $Ni_{0.8}$:$Fe_{0.2}$ along with crystal-derived (CD) $Ni_{0.8}$:$Fe_{0.2}$ oxyhydroxide and crystalline IrO_x on FTO glass at 50 mV s^{-1} (c). All experiments were performed in 1 M NaOH and are corrected for uncompensated resistance (R_u).

While, the microwave-assisted $Ni_{0.8}$:$Fe_{0.2}$ sample showed an OER overpotential of 250 mV at 10 mA cm^{-2}, overpotentials obtained from Figure 3.5c are not at steady-state. This makes comparison difficult due to transient concentration gradients that occur in static cyclic voltammetry experiments. Thus, the overpotential was obtained under steady-state conditions to benchmark the electrocatalytic activity for the OER as articulated by Jaramillo (Figure 3.6).[105] The steady-state currents from 30 s chronoamperometry experiments (Figure 3.6, squares) and the steady-state overpotentials from 30 s chronopotentiometry experiments (Figure 3.6, circles) agree well with the RDE cyclic voltammetry curve (Figure 3.6, solid line). The microwave-assisted nanoamorphous electrodeposited $Ni_{0.8}$:$Fe_{0.2}$ sample had a low overpotential for the OER at 286 mV for 10 mA cm^{-2} (geometric area), where the overpotential at t=0 was taken from the chronopentiometry curve at 30 s. This value is among the lowest overpotentials reported on "flat" electrodes (Supporting Information Table 3.9). A 2 hour chronopotentiometry experiment at 10 mA cm^{-2} was also conducted to assess the stability of the catalyst. After two hours of applying an overpotential sufficient to

produce a current density of 10 mA cm^{-2}, the required overpotential increased only slightly to 315 mV (Figure 3.6, inlay).

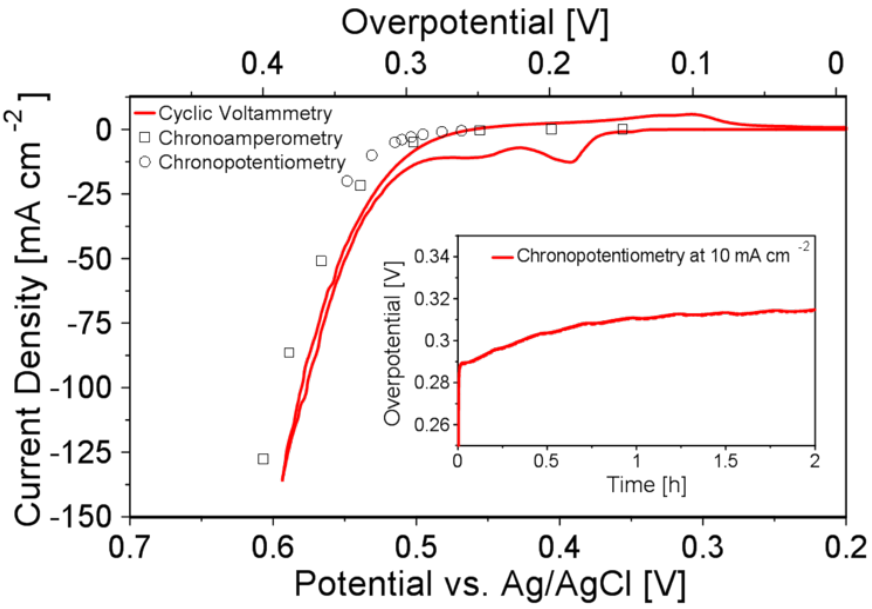

Figure 3.6. Cyclic voltammogram at 10 mV s^{-1} (solid line), steady-state currents from 30 s chronoamperometry experiments (squares), and steady-state potentials from 30 s chronopotentiometry experiments (circles) on microwave-assisted nanoamorphous $Ni_{0.8}$:$Fe_{0.2}$ electrodeposited on a glassy carbon rotating disc electrode (RDE). 2 h chronopotentiometry experiment at 10 mA cm^2 with the microwave- assisted nanoamorphous $Ni_{0.8}$:$Fe_{0.2}$ electrodeposited on a glassy carbon RDE (inlay). All RDE experiments were operated at 1600 rpm in 1 M NaOH and corrected for R_u.

3.4.4 Surface-interrogation scanning electrochemical microscopy

In order to determine if the reason for the increased activity of the microwave-assisted, nanoamorphous ($Ni_{0.8}$,$Fe_{0.2}$) structure was due to an increased percentage of "fast" catalytic sites, we performed surface interrogation scanning electrochemical microscopy (SI-SECM) on both the nanoamorphous and crystalline samples. Traditionally, SI-SECM involves two ultramicroelectrodes (UMEs) of the same size aligned such that analyte produced from one of the electrodes (tip or substrate) is quantified via electrochemical detection without the analyte ever escaping the tip/substrate gap.[133] The standard use of size-matched UMEs requires that one of the UME surfaces be composed of the electrocatalytic material to be analyzed. Justification of this technique is difficult if the preliminary studies (i.e. cyclic voltammetry) of the catalytic material are better suited on conductive supports (i.e. FTO-coated glass), which are not easily created as UME surfaces. To circumvent this problem,

we introduce a masking technique to create pseudo-UME surfaces from large (a 500 μm) substrates. A 12.5 μm thick Teflon fluorinated ethylene propylene (FEP) film with a voided center ([effective] radius a = 31 and 37 μm for crystal-derived $Ni_{0.8}$:$Fe_{0.2}$ and microwave-assisted $Ni_{0.8}$:$Fe_{0.2}$ samples, respectively, as shown in Supporting Information Figure 3.11) was heat-bonded to the electrodes to yield a pseudo-UME substrate suitable to perform SI-SECM. A glassy carbon UME (radius a = 29 μm) was crafted similar in procedure to that described elsewhere.[132] The redox mediator employed for the SI-SECM titration was an iron(III)-triethanolamine (Fe(III)-TEA) complex (E^0 = -1.05 V vs Ag/AgCl in 2 M NaOH, Supporting Information Figure 3.21).[130,132] To conduct the SI-SECM experiment, the tip was aligned with the substrate and approached to a tip/substrate gap of ca. 7 μm above the FEP mask. The surface interrogation mode involved two steps (Scheme 3.7). A potential pulse, E_{sub} (0.383 V overpotential) was first applied to the substrate to generate surface-active Ni^{IV} and/or Fe^{IV} species,[130] while the tip was held at a potential near open circuit potential (OCP) for a characteristic time, t_{step} (20 s). Subsequently, the substrate electrode was switched to OCP, and after a delay time, t_{delay} (varied from 0 to 2000 ms), the potential of the tip was stepped to E_{tip} (-1.1 V vs Ag/AgCl) to introduce the titrant, Fe(II)-TEA (Equation 3.4).

$$Fe(III) - TEA + e^- \rightarrow Fe(II) - TEA \tag{3.4}$$

$$Fe(II) - TEA + S^* \rightarrow Fe(III) - TEA + S \tag{3.5}$$

When the Ni^{III}, Ni^{IV} and/or Fe^{IV} surface-active species (S^*) are present, the titration of the surface species back to Ni^{II} and/or Fe^{III} produces positive feedback current on the tip until all surface-active species on the substrate are consumed (Equation 3.5).[130] In this experiment, when the substrate was switched to OCP these surface species participated solely in water oxidation until the potential of the tip was stepped to E_{tip} after t_{delay} (Equations 3.6 and 3.7). By titrating the surface species remaining after different delay times, concentration-time profiles were obtained, allowing for the extraction of the pseudo-first order rate constant of water oxidation by the catalytic sites of the substrate.

$$Fe^{IV} + H_2O \rightarrow Fe(III) - TEA + OH_{(ads)} \cdot + H^+ \tag{3.6}$$

$$Ni^{IV} + H_2O \rightarrow Ni^{III} + OH_{(ads)} \cdot + H^+ \tag{3.7}$$

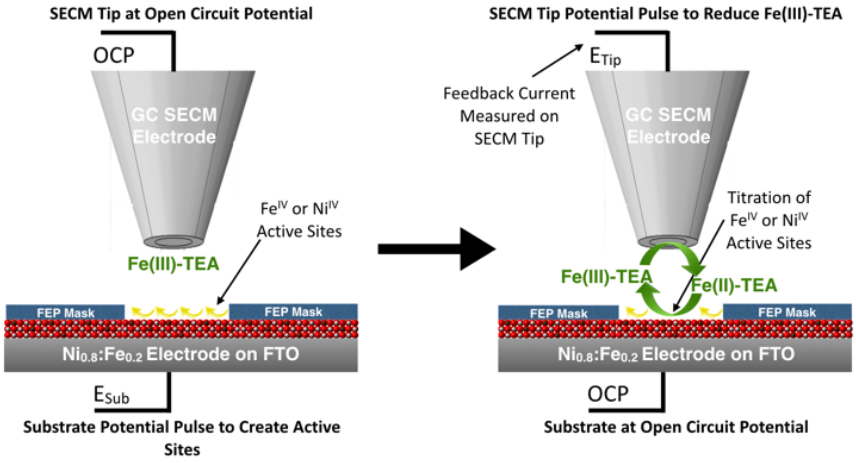

Figure 3.7. SI-SECM experimental sequence. First (left) a potential pulse is applied to the catalytic substrate to create active sites. Second (right) a potential pulse is applied to the SECM tip after a delay time (while the catalytic substrate is at open-circuit) to generate reactive Fe(II)–TEA which titrates the active sites on the catalytic substrate.

To obtain the concentration profiles (Figure 3.8a,c) from the current-time data, the surface charge densities at each t_{delay} were first quantified by integrating the net current (difference of measured current and negative feedback current).[130] The SI-SECM negative feedback trace (black line, Figure 3.8) was simulated via finite element analysis in COMSOL Multiphysics (details provided in Supporting Information).

The resulting concentration-time profiles (Figures 3.8b and 3.8d-e) were used to extract the pseudo-first order rate constant(s) of each material. The crystal-derived $Ni_{0.8}$:$Fe_{0.2}$ oxyhydroxide showed showed a sharp decrease in the number of active sites at very short delay times (less than 0.1 s), followed by a gradual decrease in the number of active sites at long delay times (greater than 0.1 s). This is indicative of the existence of two types of catalytic sites as previously demonstrated by Bard and co-workers.[130] The "fast" and "slow" sites on the crystal-derived $Ni_{0.8}$:$Fe_{0.2}$ oxyhydroxide had rate constants of 1.3 s^{-1} and 0.05 s^{-1}, respectively, which is in very good agreement with the Bard study which measured 1.70 s^{-1} and 0.056 s^{-1}, respectively. However, the microwave-assisted nanoamorphous $Ni_{0.8}$:$Fe_{0.2}$ structure only showed a sharp decrease in the number of active sites at all times indicative of only one type of catalytic site. We measured a kinetic rate of 1.9 s^{-1}, indicating that the microwave-assisted nanoamorphous $Ni_{0.8}$:$Fe_{0.2}$ structure has only "fast"

sites. We calculated the total active site density of the crystal-derived $Ni_{0.8}$:$Fe_{0.2}$ oxyhydroxide and microwave-assisted nanoamorphous $Ni_{0.8}$:$Fe_{0.2}$ to be 145 mC cm^{-2} and 81 mC cm^{-2}, respectively, using the y-intercept of the concentration-time regression lines. The microwave-assisted sample had 100% fast sites while the crystal-derived sample had only 7% fast sites and 93% slow sites, roughly correlating to the ratio of Fe to Ni in the sample. This matched well with the total iron atom content (20%), and the lower percentage of fast sites can be attributed to the segregation that was observed in the XRD and XPS measurements for the crystalline oxyhydroxide structure.

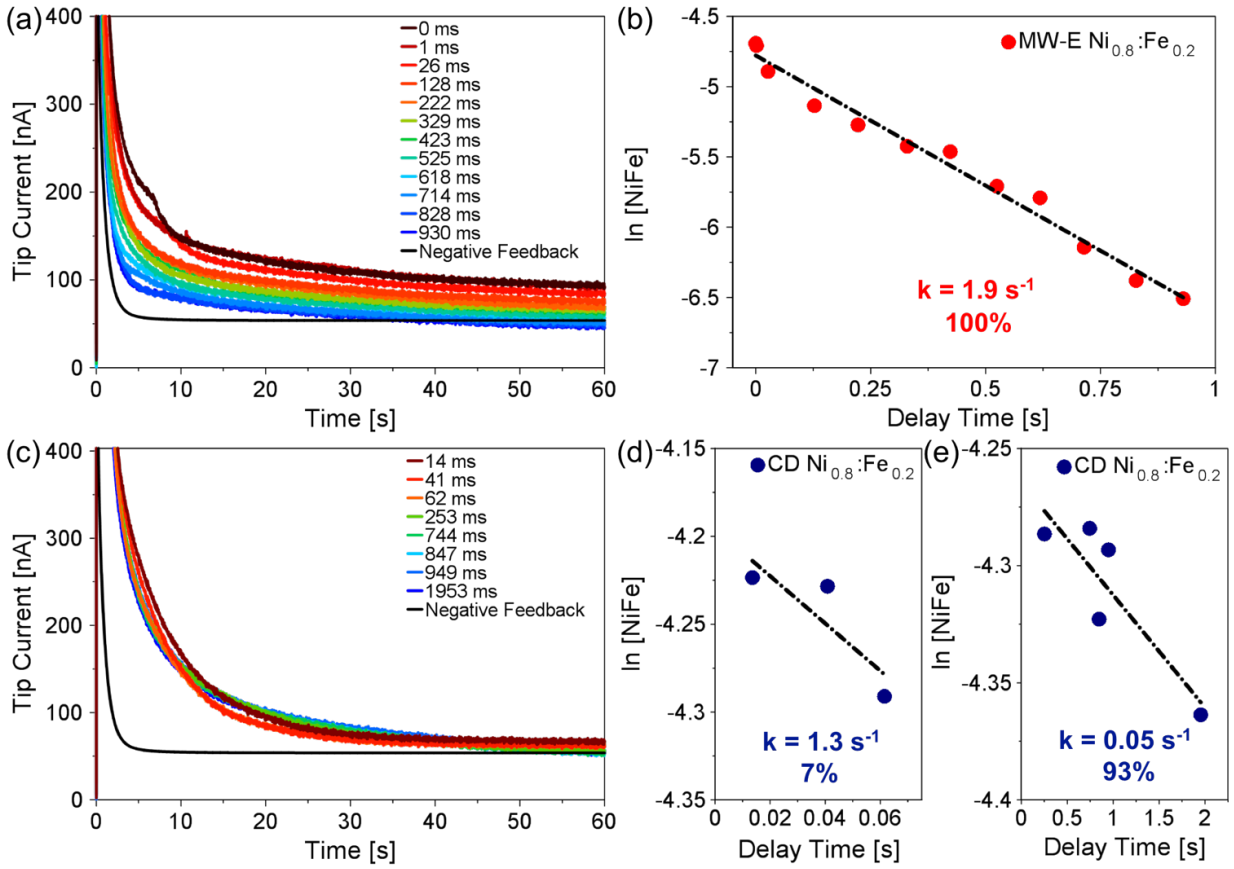

Figure 3.8. Surface interrogation chronoamperograms performed with microwave-assisted nanoamorphous $Ni_{0.8}$:$Fe_{0.2}$ (a) and electrochemically conditioned crystal-derived $Ni_{0.8}$:$Fe_{0.2}$ oxyhydroxide (c) in 2 M NaOH ca. 50 mM Fe(III)–TEA showing positive feedback after the application of 0.383 V overpotential to the catalyst and a subsequent delay time, varied from 0–2000 ms. Regression of pseudo-first order rate constants of the OER on the activated sites of the microwave-assisted nanoamorphous $Ni_{0.8}$:$Fe_{0.2}$ (b) and electrochemically conditioned crystal-derived $Ni_{0.8}$:$Fe_{0.2}$ oxyhydroxide (d and e).

3.5 Conclusions

Here we report a microwave-assisted synthesis method to create mixed-metal nanoamorphous nickel-iron catalysts for the OER. We observed that on flat electrodes (roughness factor <1.4), the OER electrocatalytic activity was higher on the microwave-assisted, nanoamorphous $Ni_{0.8}$:$Fe_{0.2}$ structure compared to the crystal-derived $Ni_{0.8}$:$Fe_{0.2}$ oxyhydroxide. By benchmarking the microwave-assisted, nanoamorphous structure, we determined that it had a very low overpotential of 286 mV at 10 mA cm^{-2}. We measured the kinetics of the active sites of both the crystal-derived and microwave-assisted $Ni_{0.8}$:$Fe_{0.2}$ samples directly using the surface interrogation mode of scanning electrochemical microscopy (SI-SECM). We determined that the microwave-assisted structure contained all "fast" sites with rate constant 1.9 s^{-1}, and the crystal-derived structure contained 7% "fast" sites with rate constant 1.3 s^{-1} and 93% slow sites with a rate constant of 0.05 s^{-1}. This finding, is experimental evidence that developing synthesis methods to maximize the uniformity of amorphous structures is advantageous for the development of highly efficient Ni-Fe catalysts for electrochemical water oxidation.

3.6 Acknowledgements

This work was previously published in Journal of Materials Chemistry A:
Barforoush JM, Jantz DT, Seuferling TE, Song KR, Cummings LC, Leonard KC. Microwave-assisted synthesis of a nanoamorphous ($Ni_{0.8}$,$Fe_{0.2}$) oxide oxygen-evolving electrocatalyst containing only "fast" sites. Journal of Materials Chemistry A. 2017;5(23):11661–11670.

3.7 Supporting Materials and Methods

3.7.1 Electrode Fabrication

Drop-cast Thin Films

FTO glass sheets (Sigma Aldrich) cut to 0.5-inch squares were cleaned by washing with soap, deionized water, and ethanol. The FTO pieces were placed in a beaker with ethanol and sonicated for 10 minutes. The slides were dried at room temperature for about 5 minutes. Then, using a

micropipette, approximately 250 μL of solution was dropped onto each square in the most even thin layer possible. The slides were then placed into an oven at 135 °C for about 30 minutes. This was repeated once more for a second coating. After coating the FTO glass, the crystalline thin-film samples were fired in air at 500 °C for 3 hours with a 1 °C min^{-1} ramp rate. For each sample, a 2-3 mm edge of coating was scraped off and copper wire tape (Electron Microscopy Sciences) was placed on and scored.

Drop-cast solution-derived and microwave-assisted films:

FTO glass sheets were cut and cleaned as described above. Using a micropipette, approximately 250 μL of the suspension was dropped onto each square in the most even thin layer possible. The slides were then placed into an oven at 70 °C for about 30 minutes. This was repeated once more for a second coating. No additional annealing was applied to the electrode. For suspensions where separation occurred, the suspension was pipetted from the bottom of the container.

Masked Substrate:

The substrate in the scanning electrochemical microscopy (SECM) experiment was a catalyst sample drop-cast on FTO glass (Sigma-Aldrich) and masked to create a pseudo-ultramicroelectrode suitable for surface interrogation mode of SECM. To make the mask, a 2 cm x 2 cm square of Teflon FEP Film (50A, American Durafilm) was taped to a Teflon block, which was fixed in the clamp of a CNC Mill. A hole was drilled in the FEP film with a 100 μm diameter drill bit (One Piece, Drill Bits Unlimited). The FEP film mask was placed over the catalyst-coated FTO glass with the hole centered and the excess FEP film trimmed off. The masked substrate was placed in the furnace above 271 °C for 30 minutes to allow the FEP film to heat-bond to the substrate.

Glassy Carbon Ultramicroelectrode:

The glassy carbon (GC) ultramicroelectrode utilized as the SECM tip was fabricated similar to the procedure previously reported with some modifications.[132] A 1 cm GC rod (type 2, 1 mm diameter, Alfa Aesar) was electrochemically etched in 4 M KOH by submersing half of the rod and applying 5 V using a graphite counter electrode for 500 s. Subsequently, the rod was flipped and the other end of the rod was electrochemically etched in the same manner. The etching process

was repeated, alternating the end of the rod and lowering the etch time as needed, until a sharp GC needle was obtained. The GC needle was rinsed with acetone and deionized water and allowed to dry completely. A silver connection wire (30 AWG, Belden, USA) coated with conductive silver epoxy (Circuit Works, USA) was inserted into one end of a borosilicate glass capillary (1 mm O.D., 0.5 mm I.D., Sutter Instruments, USA). The other end of the borosilicate glass capillary was filled with silver epoxy and the etched GC needle with one end coated in silver epoxy was inserted. The conductive wire was pushed against the GC needle inside the capillary to ensure good electrical contact. The silver epoxy in the electrode was dried in the oven at 120 °C for 30 minutes with the GC tip pointing upwards. The GC tip was completely coated in epoxy (1C&EPKC, Loctite Hysol) and dried in the oven with the GC tip pointing upwards at 120 °C, removing the electrode to recoat/remold the epoxy every 20 s until sufficiently coated. Finally, the electrode was dried in the oven at 120 °C for 2 hours to hasten the curing of the epoxy. After the epoxy was fully cured, the tip of the electrode was polished with MicroCloth polishing disks (Beuhler, Canada) until a GC disc was visible. The electrode tip was also sharpened with the MicroCloth polishing disc until the desired RG was reached. Before experimentation, the GC disc was polished with alumina micropolish (1 μm, Beuhler, Canada) until it possessed a mirror-like surface.

3.7.2 Synthesis

Redox Mediator:

The Fe(III)-TEA solution was prepared according to a previously reported procedure.[132] Briefly, 3.2 g of NaOH were added to 10 mL of deionized water while stirring and cooling in a 25 °C water bath. Separately, 20 mL of deionized water was bubbled with argon in a round-bottom flask for 5 minutes. While stirring, 214.4 mg of $Fe_2(SO_4)_3 \cdot xH_2O$ were added to the round-bottom flask. 104 μL of triethanolamine (TEA) were added dropwise to the round-bottom flask. The NaOH solution was added dropwise to the Fe(III) + ligand solution and the volume was adjusted to 40 mL with deionized water.

3.7.3 Crystalline IrO_x:

The crystalline thin-films of IrO_x were made similar to the crystalline-derived $Ni_{0.8}$:$Fe_{0.2}$ described in the main paper. Briefly, a solution of 0.02 M $IrCl_3$ was prepared in ethylene glycol, and the solution was drop-cast and annealed on FTO coated glass (further details can be found in Electrode Fabrication section).

	$\eta_{t=0}$ [mV] (10 mA cm^{-2})	$\eta_{t=2h}$ [mV] (10 mA cm^{-2})	η_{CV}[mV] (10 mA cm^{-2})	η_{CV} [mV] (100 mA cm^{-2})	j_g, [mA cm^{-2}] (η=0.35 V)	j_s, [mA cm-2] (η=0.35 V)	Roughness Factor
This Study	**286**	**315**	**250**	**369**	**61.5**	**55.2**	**1.4**
IrO_x[2]	320 ± 40	1050 ± 20	-	-	42 ± 13	0.4 ± 0.2	105
$NiFeO_x$[2]	350 ± 10	380 ± 20	-	-	15 ± 6	3 ± 2	6
LDH $Ni_{0.9}Fe_{0.1}O_x$[3]	-	-	336	-	-	-	-
Electrodeposited NiFe (40% Fe)[4]	280	-	-	-	-	20 (at 0.3 V)	2-6
LDH NiFe on Graphene Oxide[5]	-	-	221	-	-	-	-
Fractal NiFe[6]	-	-	-	300	-	-	-
Amorphous Ni-Fe oxyhydroxide[7]	300	-	-	-	-	-	-
Pulse-Electrodeposited Ni–Fe (Oxy)hydroxide[8]	-	-	250	-	-	-	-
Laser Ablation $Ni_{0.22}Fe_{0.78}$ LDH[9]	280	-	-	-	-	-	-

Figure 3.9. Performance comparisons between the results of this study and other recent studies on (Ni,Fe) electrocatalysts for the oxygen evolution reaction.

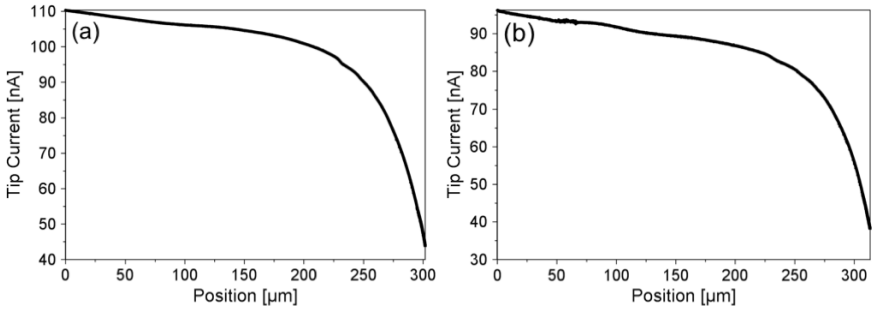

Figure 3.10. Examples of negative feedback approach curves for imaging and surface interrogation scanning electrochemical microscopy (SI-SECM). Negative feedback approach curve for SI-SECM experiments with glassy carbon ultramicroelectrode tip and masked crystal-derived $Ni_{0.8}$:$Fe_{0.2}$ (a) and microwave-assisted $Ni_{0.8}$:$Fe_{0.2}$ (b) on FTO glass substrate.

3.7.4 Details on COMSOL Multiphysics Simulations

COMSOL (COMSOL Multiphysics v. 5.2) simulations were performed to obtain the negative feedback current for the SI-SECM experiments. In COMSOL a 2D axial-symmetric domain was created to simulate the actual size of our SECM tip electrode, the size and thickness of the masked catalyst electrode, and the tip/substrate distance as described in the main paper (Figure 3.24).

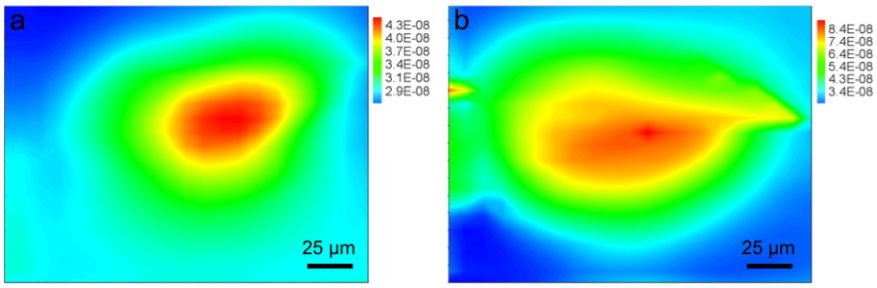

Figure 3.11. Electrochemical imaging maps for surface interrogation scanning electrochemical microscopy. Map of the hole in the mask on crystal-derived $Ni_{0.8}$:$Fe_{0.2}$ (a) and microwave-assisted $Ni_{0.8}$:$Fe_{0.2}$ (b) on FTO glass substrate generated using a glassy carbon ultramicroelectrode tip with Fe(III)/Fe(II)-TEA redox couple. High reduction current is represented as red, revealing the location of the mask hole, and low reduction current is shown as blue.

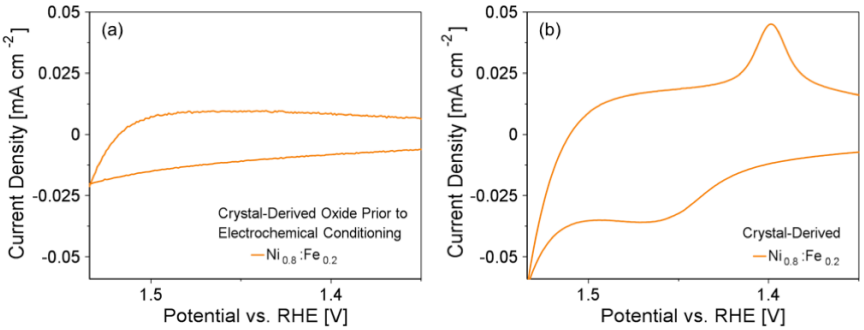

Figure 3.12. Cyclic voltammograms (CVs) of the crystal-derived $Ni_{0.8}$:$Fe_{0.2}$ before (a) and after (b) applying an electrochemical conditioning oxidation current of ca. 10 mA for 1 h to create an oxyhydroxide morphology with characteristic peaks appearing in the CVs between 1.45 and 1.5 V vs RHE. The CV after electrochemical conditioning is a magnified view of the crystal-derived CV presented in Figure 3.4a of the main text.

Two separate edge meshes were used, (1) on the SECM tip boundary, and (2) on the catalyst electrode boundary extending up and halfway across the FEP mask. These edge meshes had a maximum element size of 0.5 μm and a minimum element size of 0.05 μm. A free triangular mesh was used for the solution using COMSOL's built-in "fine" element size, which was calibrated for fluid dynamics. Figure 3.22 shows 2D axial-symmetric geometry with the mesh used for these simulations.

The COMSOL Electroanalysis module was used to simulate the SECM tip current during the surface interrogation experiment. This module couples Fick's Law of Diffusion with the Butler-Volmer Equation to obtain the concentration of the oxidized and reduced species in solution, as well as the current on the electro-active boundary as a function of applied potential. Since the reduction of Fe(III)-TEA to Fe(II)-TEA is a fast outer-sphere, one-electron transfer, we used 1

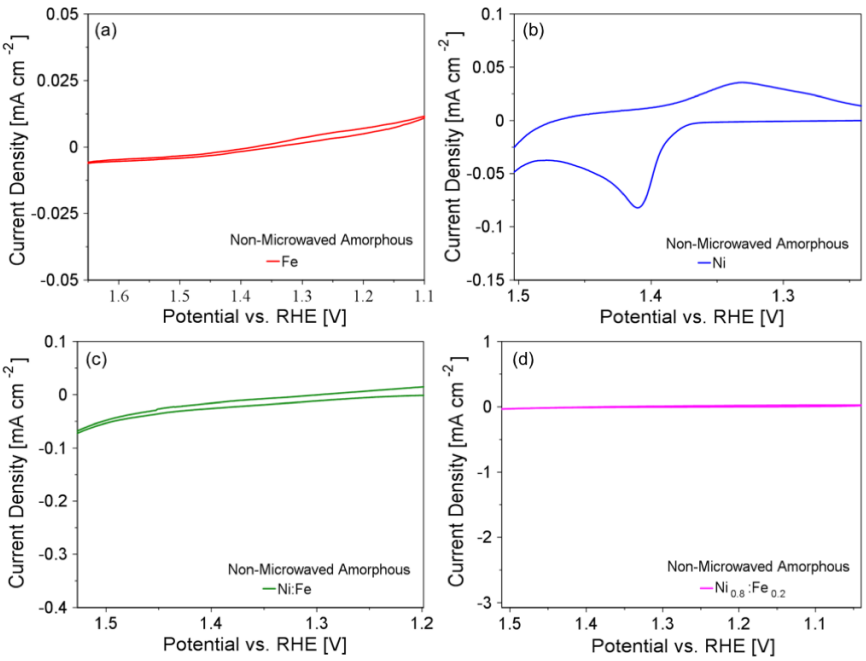

Figure 3.13. Cyclic voltammograms (CVs) of the solution-derived Fe (a), Ni (b), Ni:Fe (c), and $Ni_{0.8}$:$Fe_{0.2}$ (d) on FTO-coated glass. Each CV was taken from Figure 3.1a of the main text and magnified to the region where the Ni^{II}/Ni^{III} peaks would be visible. The Ni is the only one of our solution-derived materials to show the characteristic oxyhydroxide peaks before microwaving.

cm/s as the electron-transfer kinetic rate constant and $\alpha = 0.5$ for the transfer coefficient. The diffusion coefficient for both the Fe(III)-TEA and Fe(II)-TEA species was 2E-6 cm^2/s as previously reported.[132] The tip potential in our simulations was exactly as it was in our experiment. The tip/substrate distance was 7 microns above the surface of the FEP mask. The initial concentration of redox mediator, Fe(III)-TEA, used was 28 mM for the crystal-derived $Ni_{0.8}$:$Fe_{0.2}$ and 65 mM for the microwave-assisted $Ni_{0.8}$:$Fe_{0.2}$ (different concentrations of redox mediator were attributed to evaporative losses of solution from argon bubbling in between experiments).

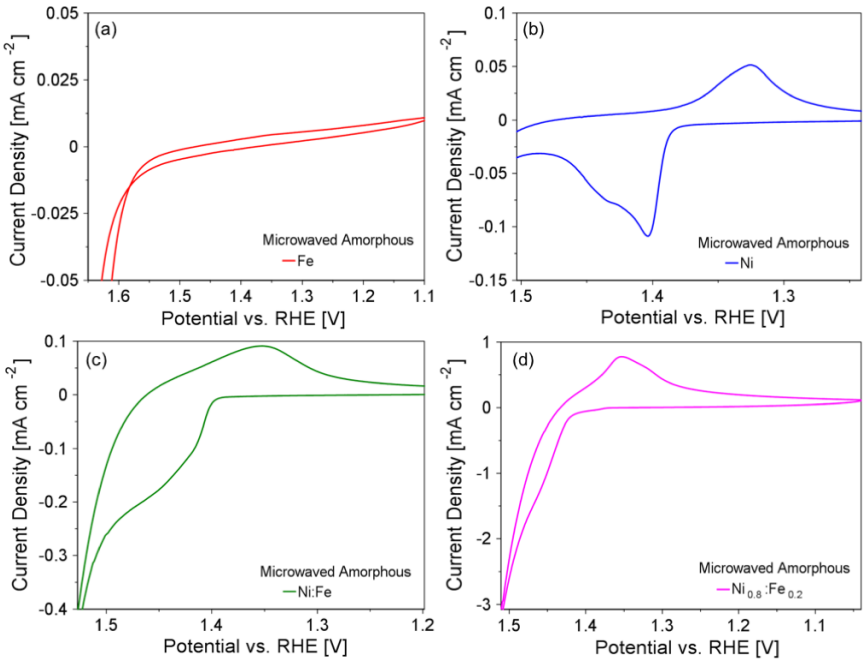

Figure 3.14. Cyclic voltammograms (CVs) of the microwave-assisted Fe (a), Ni (b), Ni:Fe (c), and $Ni_{0.8}$:$Fe_{0.2}$ (d). Each CV was taken from Figure 3.1a of the main text and magnified to the region where the Ni^{II}/Ni^{III} peaks are visible. As expected, the Fe is the only one of our microwave-assisted materials to lack the characteristic peaks.

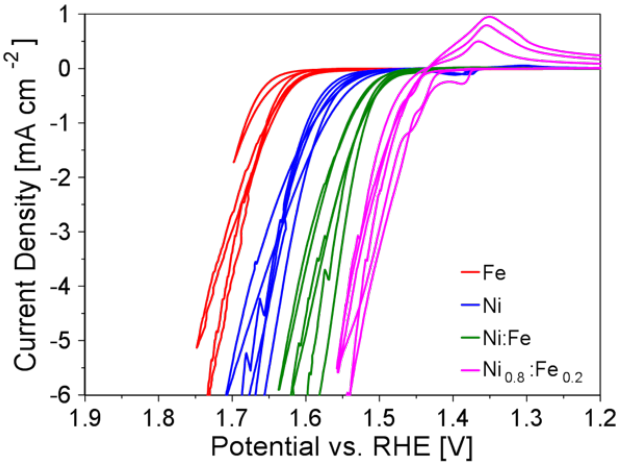

Figure 3.15. Experimental cyclic voltammograms (CVs) in 1 M NaOH at a scan rate of 1 mV s^{-1} not corrected for R_u for three different batches of microwave-assisted Fe, Ni, Ni:Fe, and $Ni_{0.8}$:$Fe_{0.2}$ coated on FTO glass using the convention of reduction currents as positive and negative potentials to the right. Each CV shown is from a freshly fabricated microwave-assisted metal/mixed metal (oxy)hydroxide.

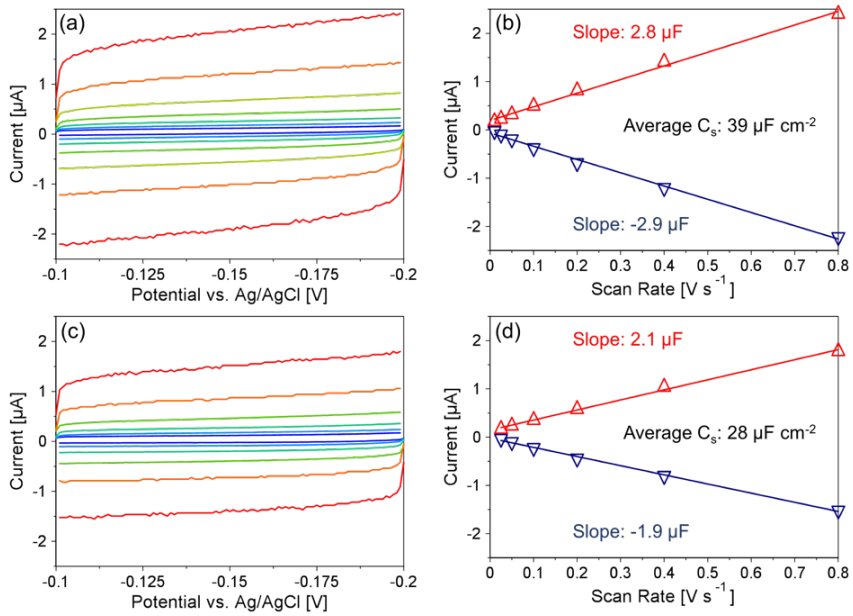

Figure 3.16. Double-layer capacitance measurements via cyclic voltammetry on microwave-assisted $Ni_{0.8}$:$Fe_{0.2}$ electrodeposited on glassy carbon (a) and bare glassy carbon (c) in 1 M NaOH at various scan rates where non-faradaic current occurs. Current vs scan rate for microwave-assisted $Ni_{0.8}$:$Fe_{0.2}$ electrodeposited on glassy carbon (b) and bare glassy carbon (d) with regression lines next to the corresponding double layer capacitance values and the average specific capacitance, C_s.

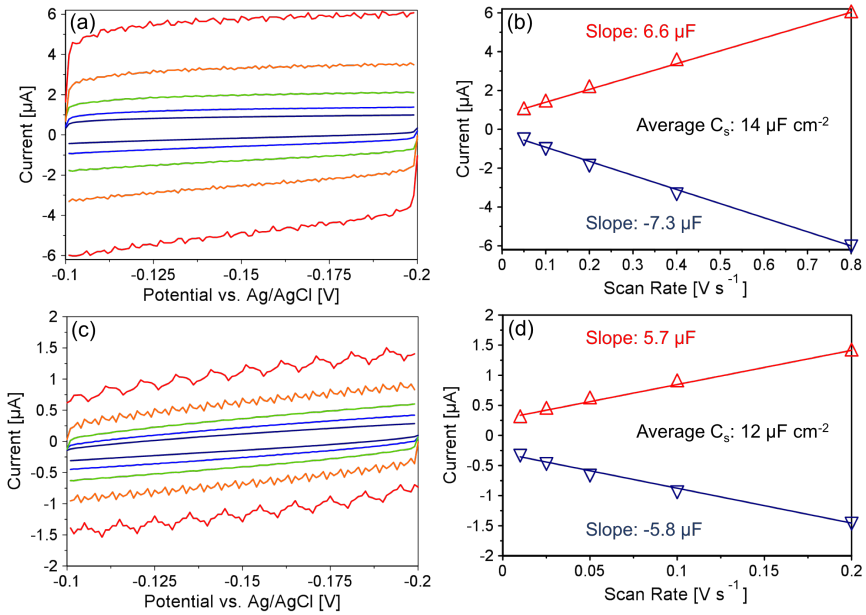

Figure 3.17. Double-layer capacitance measurements via cyclic voltammetry on crystal-derived $Ni_{0.8}$:$Fe_{0.2}$ oxyhydroxide on FTO-coated glass (a) and bare FTO-coated glass (c) in 1 M NaOH at various scan rates where non-faradaic current occurs. Current vs scan rate for crystal-derived $Ni_{0.8}$:$Fe_{0.2}$ oxyhydroxide on FTO-coated glass (b) and bare FTO-coated glass (d) with regression lines next to the corresponding double layer capacitance values and the average specific capacitance, C_s.

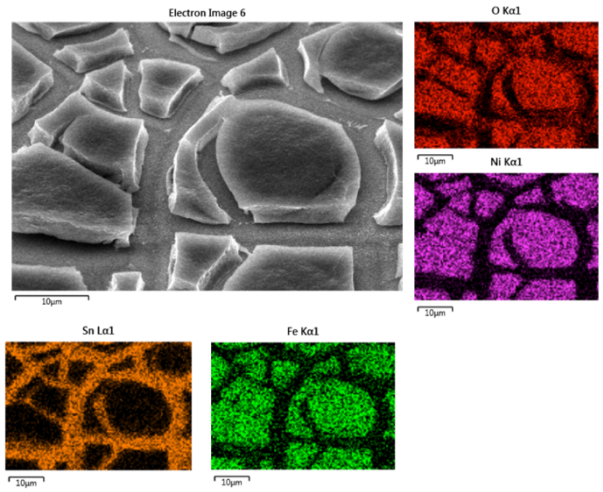

Figure 3.18. SEM and corresponding EDS images of crystal-derived $Ni_{0.8}$:$Fe_{0.2}$ sample prior to electrochemical conditioning step. Shown is the uniform distribution of Fe and Ni along with the Sn of the sub-layer due to the FTO coated glass substrate.

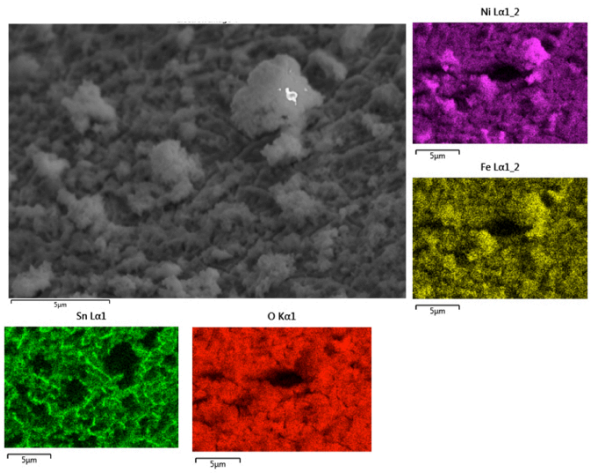

Figure 3.19. SEM and corresponding EDS images of microwave-assisted, nanoamorphous $Ni_{0.8}$:$Fe_{0.2}$ sample electrophoretically deposited on a FTO coated glass substrate. Shown is the uniform distribution of Fe and Ni along with the Sn of the sub-layer due to the FTO coated glass substrate.

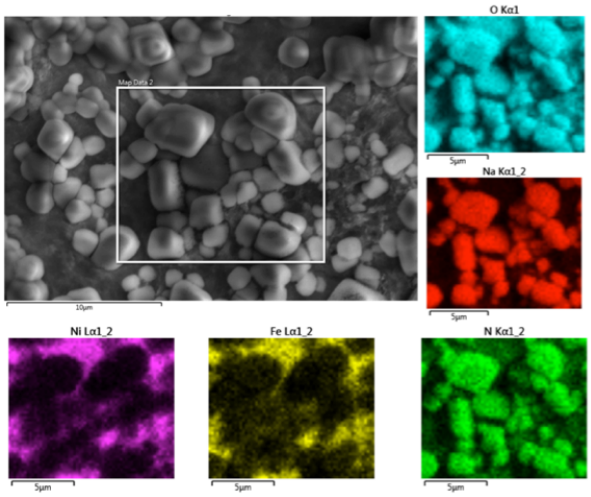

Figure 3.20. SEM and corresponding EDS images of the microwave-assisted $Ni_{0.8}$:$Fe_{0.2}$ sample without the rinsing step. Shown are the $NaNO_3$ crystal that are a result of titration of $NaHCO_3$ with Fe or Ni NO3. These $NaNO_3$ crystals are also present in the XRD patterns of the microwave-assisted samples.

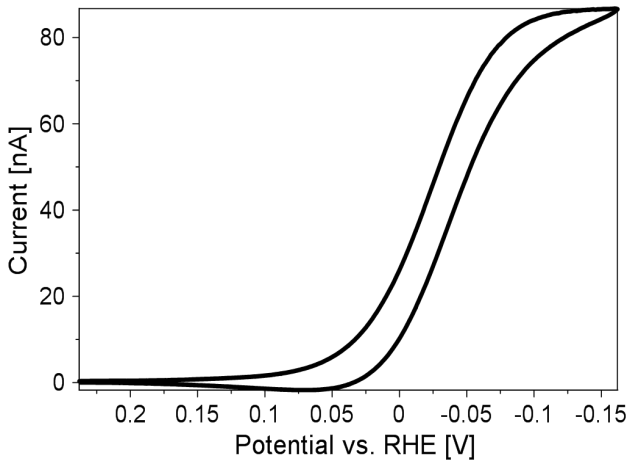

Figure 3.21. Redox mediator, ca. 50 mM Fe(III)-TEA, cyclic voltammogram (CV) at 10 mV s^{-1} in 2 M NaOH with a glassy carbon ultramicroelectrode.

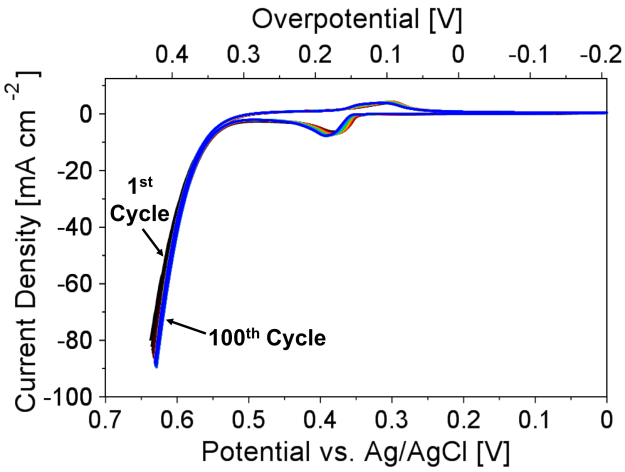

Figure 3.22. 100 cyclic voltammetry (CV) cycles at 50 mV s^{-1} on microwave-assisted nanoamorphous $Ni_{0.8}$:$Fe_{0.2}$ electrodeposited on a glassy carbon electrode in 1 M NaOH and corrected for R_u showing no significant change in activity with each successive cycle.

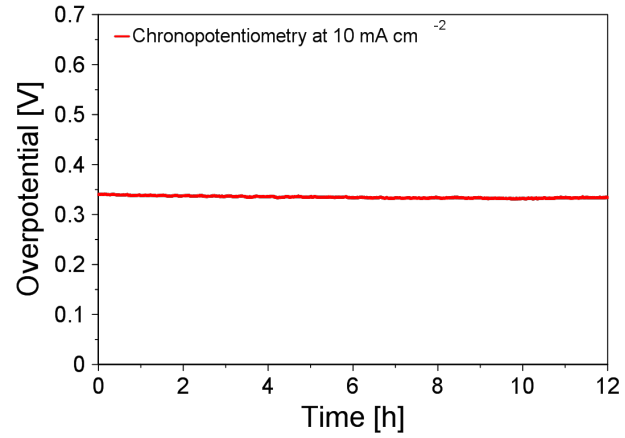

Figure 3.23. 12 h chronopotentiometry experiment at 10 mA cm^{-2} with microwave-assisted nanoamorphous $Ni_{0.8}$:$Fe_{0.2}$ electrodeposited on a glassy carbon RDE at 1600 rpm in 1 M NaOH and corrected for R_u showing stable oxygen production with an overpotential of 0.33 V at 12 h.

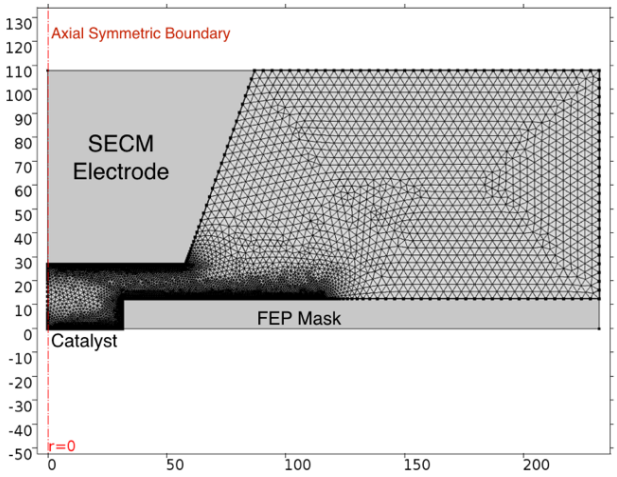

Figure 3.24. COMSOL 2D axial-symmetric domain and corresponding mesh used for SI-SECM simulations.

3.8 Appendix

The synthesis for the microwave-assisted nanoamorphous $Ni_{0.8}$:$Fe_{0.2}$ oxide yields a suspension in which separation occurs, resulting in a reddish brown layer (containing the catalyst) beneath a green layer (Figure 3.25). Different combinations of these two layers were used for dropcasting on fluorine doped tin oxide (FTO) glass to determine the most efficient way of depositing the catalyst from solution. Using a pipette, bottom layer:top layer ratios of 60:40, 70:30, 90:10, and 100:0 were dropcast onto FTO glass, and the samples were tested using cyclic voltammetry (CV). There was no apparent advantage in using one ratio over the other so the bottom layer was used in all of the depositions.

Figure 3.25. Nanoamorphous $Ni_{0.8}$:$Fe_{0.2}$ oxide in solution after the microwave-assisted heating step in 125 mL Nalgene bottles.

Dip-coating was investigated as an alternative to drop-casting nanoamorphous $Ni_{0.8}$:$Fe_{0.2}$ oxide on FTO glass. Using the CNC mill, clean FTO glass was dipped into catalyst solution and removed at a controlled rate. The catalyst suspension would not adhere well the FTO glass when it was removed from the catalyst solution; whereas, drop-casting on FTO glass allowed the catalyst solution to dry onto the electrode and provide sufficient adhesion for electrochemical characterization.

Different methods of drying the drop-cast nanoamorphous $Ni_{0.8}$:$Fe_{0.2}$ oxide on FTO were also investigated, including drying in the oven at 70 °C and 120 °C, air overnight, and UV lamp. At 120 °C, the coating would be thicker around the edges and absent in the center, possibly due to drying too quickly, and the UV lamp did not produce consistent results. Oven drying at 70 °C gave identical results to air drying overnight, so oven drying at 70 °C was used to dry drop-cast samples.

Voltage and electrodeposition time were varied to find the optimum conditions for electrodeposition. Electrodeposition at -2 volts was insufficient to form a catalyst layer on the FTO glass while -5 V formed a catalyst layer. Based on cyclic voltammograms (CVs), samples electrodeposited at -10 V did not show better performance than those electrodeposited at -5 V. Electrodeposition at -5 V was performed over 5, 10, 15, 20, 30, and 60 minute time periods. Samples prepared from 5 minutes of electrodeposition showed poor performance compared to those prepared from 10 minutes of electrodeposition, indicating insufficient catalyst coverage. Longer electrodeposition times, such as 30 minutes and 60 minutes, also produced samples with poor coverage.

Chapter 4

Insights into the Active Electrocatalytic Areas of Layered Double Hydroxide and Amorphous Nickel–Iron Oxide Oxygen Evolution Electrocatalysts

4.1 Abstract

Layered double hydroxide (LDH) and amorphous nickel-iron (oxy)hydroxides ($Ni_{1-x}Fe_xOOH$) are emerging catalysts for the electrochemical oxygen evolution reaction (OER). It is still unresolved if the layered two-dimensional (2D) structure allows for active catalytic sites to exist below the traditional electrode/electrolyte interface. Herein, we utilized the surface interrogation mode of scanning electrochemical microscopy (SI-SECM) to directly measure active site densities *in-situ*. We determined that $Ni_{0.8}Fe_{0.2}OOH$ LDH showed a 10-fold increase in the active site density compared to rock salt $Ni_{0.8}$:$Fe_{0.2}$ oxide, giving direct evidence that water and hydroxide in the interlayer are able to create stable Ni^{IV}/Fe^{IV} active species at layers below the electrode/electrolyte interface. This result suggests that electrolyte permeability of the 2D LDH structure is a major contributor

for its increased catalytic activity. Amorphous $Ni_{0.8}$:$Fe_{0.2}$ oxide also exhibits an anomalously high active site density and higher activity than $Ni_{0.8}Fe_{0.2}OOH$ LDH.

4.2 Introduction

Designing efficient, earth-abundant, and stable electrocatalysts for the oxygen evolution reaction (OER) is paramount to the electrochemical production of carbon neutral fuels, because the OER is the half reaction that limits the overall efficiency due to the complexity of the four electron/four proton transfer event.[152–157] Historically, the most effective catalysts for the OER have been composed of the precious metals, Ru and Ir.[158–160] However, in recent years nickel-iron (oxy)hydroxides ($Ni_{1-x}Fe_xOOH$), specifically the layered double hydroxide (LDH) structure of $Ni_{1-x}Fe_xOOH$, have emerged as non-precious metal electrocatalysts with competitive performance to precious metal counterparts in alkaline media.[161–177]

LDHs are layered two-dimensional (2D) materials with each layer in the LDH made up of two intercalated metal hydroxide sub-layers[178–183]. It is known that, due to the layered 2D structure, $Ni_{1-x}Fe_xOOH$ LDHs are permeable to aqueous electrolytes allowing for water and hydroxide ions to access layers below the electrode/electrolyte interface.[184–187] It has been shown that the water molecules can desorb at elevated temperatures, indicative of the freedom of translational movement of this interfacial water.[179–181,185] This movement of water and hydroxide anions into and out of the interlayer has been suggested as an important factor in the high activity of catalytic LDHs for the OER.[186,187] Recently, there has been significant interest in 2D materials and layered 2D materials for electrocatalysis.[188–193] Understanding the role of interlayer water and hydroxide in OER catalysis would greatly aid in the development and design of layered 2D electrocatalysts. However, it is still uncertain if these water molecules and hydroxide ions in the interlayer can participate in OER electrocatalysis. The difficulty in determining the role of interlayer hydroxide ions arises from the fact that nickel (oxy)hydroxides undergo a redox transition from non-conducting Ni^{II} species to conducting $Ni^{III/IV}$ species during OER electrocatalysis, which makes traditional electrochemical surface area (ECSA) measurements via voltammetry impossible.

In order to determine the degree to which the 3D structure of $Ni_{1-x}Fe_xOOH$ LDH is catalytically active for the OER, one needs an accurate measurement of the number of sites that can

participate in catalysis. If the active site density of the catalyst is higher than the atomic surface density (e.g. 20 sites nm^{-2}), one can conclude that the electrolyte permeability allows for sub-surface layers to participate in electrochemical reactions. Accurately measuring the active site density is also imperative for measuring the turnover frequency (TOF)—a crucial metric for direct comparison of catalysts. The active site density of the $Ni_{1-x}Fe_xOOH$ LDH structure, for example, may be approximated indirectly by integrating the $Ni^{III/II}$ redox wave. Boettcher and co-workers have shown good agreement between the integration of the $Ni^{III/II}$ redox wave and catalytic activity for the OER, indicating that the 3D structure does indeed participate it catalysis.[194–196] However, traditional voltammetry uses the same electrode to produce and detect the $Ni^{III/II}$ transition, which is often bordering or nearly overlapping the catalytic water oxidation wave. Thus, for some materials, it may be difficult to accurately determine the active site density with voltammetry. Alternatively, active site density can be calculated from the electrochemical surface area (ECSA), which is a measurement of the surface roughness or the surface area exposed to the electrolyte. Typically, ECSA measurements are made by determining the double layer capacitance of the electrode. Cyclic voltammetry (CV) and electrochemical impedance spectroscopy (EIS) are known methods to measure double layer capacitance, however these techniques may not be accurate for every catalyst system.[175,194,197–199] For example, ECSA measurements obtained from CV are especially troublesome on nickel (oxy)hydroxide-based materials due to the Ni^{II} species being electrically insulating.[194] Moreover, even with accurate double layer capacitance measurements, a capacitance per unit true surface area must be assumed to calculate ECSA.[200] The capacitance per unit true surface area is dependent on the oxide surface and electrolyte, and values in the range of 20 and 140 $\mu F\ cm^{-2}$ are commonly assumed, although there is not an established basis for this assumption.[200–202] All of these factors may result in difficulties in obtaining accurate active site density measurements.

To circumvent these problems and determine if the 3D structure of $Ni_{1-x}Fe_xOOH$ LDH is a major contributing factor for its high OER activity, we utilized the surface interrogation mode of scanning electrochemical microscopy (SI-SECM) to directly measure the active site density without the uncertainty associated with ECSA measurements and assumptions for indirect measurements of active site density (Scheme 4.1). SI-SECM, originally pioneered by Bard and Rodríguez-López, is a technique through which insights into the intrinsic activity of a catalyst can be obtained via an

electrochemical titration that measures the active site density of a catalyst.[55,175,203–211]. Recently, Bard and co-workers used SI-SECM to probe the active site densities of iron, nickel, and nickel-iron (oxy)hydroxides, and they found that the 80% Ni 20% Fe oxide material had two discrete surface sites identified as "fast" and "slow" sites.[212] More recent SI-SECM studies on other systems, such as photo-assisted water oxidation on a hematite surface, have also revealed the existence of discrete sites with different rate constants on the same catalyst surface.[213,214] In addition, Bard observed that the nickel and nickel-iron (oxy)hydroxides have very high active site densities, more than one order of magnitude higher than those observed on IrO_x[204] or on a Co OER catalyst.[203] Bard suggested that such a densely packed active site density cannot be attributed simply to the surface roughness or porosity of the catalysts, but that the layered structure of these (oxy)hydroxides allows for electron transport from the bulk material to the solution interface through holes that may also participate in surface catalysis.[212] However, no direct comparisons were made in Bard's original study to provide certainty that sub-surface sites participate in catalysis.

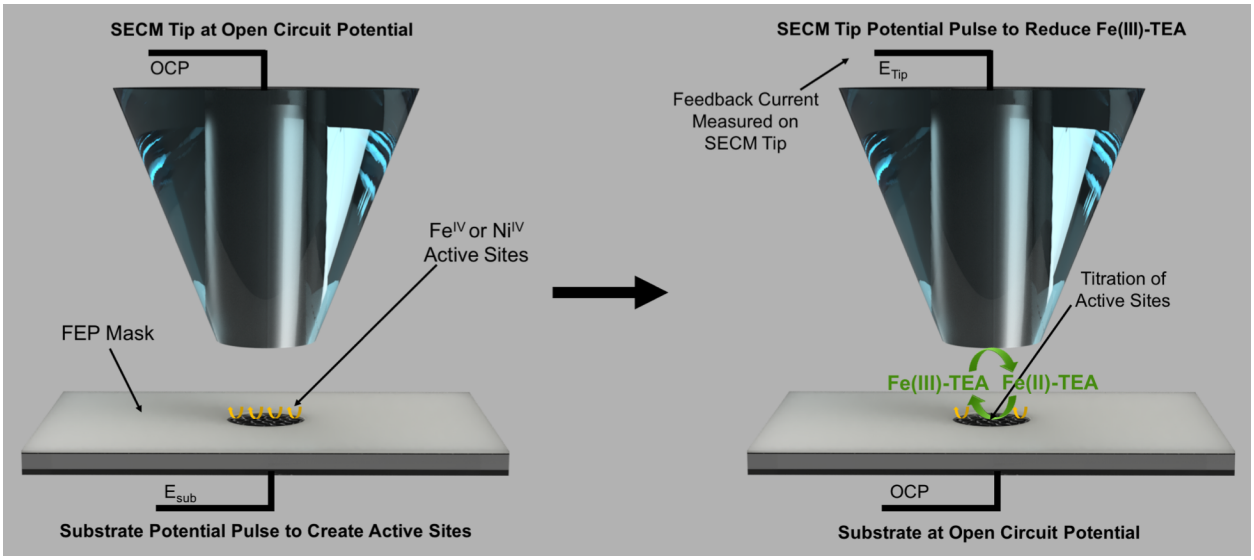

Figure 4.1. Schematic describing the SI-SECM experiment. First, a potential is applied to the catalytic electrode to generate active sites while the SECM tip electrode is at open circuit (left). Next, a potential pulse is applied to the SECM tip electrode to generate the redox active titrant (Fe(II)-TEA) while the catalytic electrode is at open circuit (right). The active site density can be measured by the feedback current measured on the SECM tip electrode.

In order to make a direct comparison between different crystal structures, which have the same morphology, we utilized SI-SECM to compare the active site density of a rock salt $Ni_{0.8}$:$Fe_{0.2}$ oxide (XRD shown in Figure 4.8 with a $Ni_{0.8}Fe_{0.2}OOH$ LDH, where the $Ni_{0.8}Fe_{0.2}OOH$ LDH was

synthesized via electrochemical conditioning of the rock salt $Ni_{0.8}$:$Fe_{0.2}$ oxide.[215] If the electrolyte permeability of the LDH structure plays a role in catalysis, we would expect the LDH structure to have a higher active site density than the rock salt structure even though their morphologies are the same. In addition to the $Ni_{1-x}Fe_xOOH$ LDH structure, a number of highly active amorphous oxide catalysts for the OER have emerged,[175,216–230] including a report from Vojvodic, Sargent, and co-workers of homogeneously dispersed multimetal oxygen-evolving electrocatalysts that are among the best performing OER catalysts reported.[231] In a previous study, our group reported a microwave-assisted synthesis technique to create a nanoamorphous $Ni_{0.8}$:$Fe_{0.2}$ oxide structure, which had an overpotential of 286 mV at 10 mA cm^{-2} on a glassy carbon support electrode.[175] However, it is not known if electrolyte permeability contributes to the high OER activity of these amorphous structures either.

4.3 Materials and Methods

4.4 Electrochemical Characterization

The OER activity of the three $Ni_{0.8}$:$Fe_{0.2}$ oxide materials having the same chemical compositions and mass loadings but different crystal structures were measured via cyclic voltammetry (Figure 4.2). The $Ni_{0.8}$:$Fe_{0.2}$ ratio was chosen because the 80:20 ratio has been established as the optimum for nickel-iron oxide electrocatalysts.[60,113,170,207,220,232] It is known that by applying a simple electrochemical conditioning step, the rock salt $Ni_{0.8}$:$Fe_{0.2}$ structure is converted to a $Ni_{0.8}Fe_{0.2}OOH$ LDH structure.[215] This provides two different crystal structures with the same morphology, allowing for direct comparisons to be made. Comparing the $Ni_{0.8}Fe_{0.2}OOH$ LDH to the rock salt $Ni_{0.8}$:$Fe_{0.2}$, the utility of a layered structure is quite apparent. The $Ni_{0.8}Fe_{0.2}OOH$ LDH structure has an overpotential nearly 100 mV less than that of the rock salt $Ni_{0.8}$:$Fe_{0.2}$ monolayer structure at 20 mA cm^{-2}. At 10 mA cm^{-2}, the amorphous $Ni_{0.8}$:$Fe_{0.2}$ oxide, $Ni_{0.8}Fe_{0.2}OOH$ LDH, rock salt $Ni_{0.8}$:$Fe_{0.2}$ oxide, and IrO_x had overpotentials of 303 mV, 396 mV, 453 mV, and 481 mV, respectively.

We performed double layer capacitance measurements via cyclic voltammetry (CV) to demonstrate the futility of this technique for obtaining accurate surface area measurements on nickel

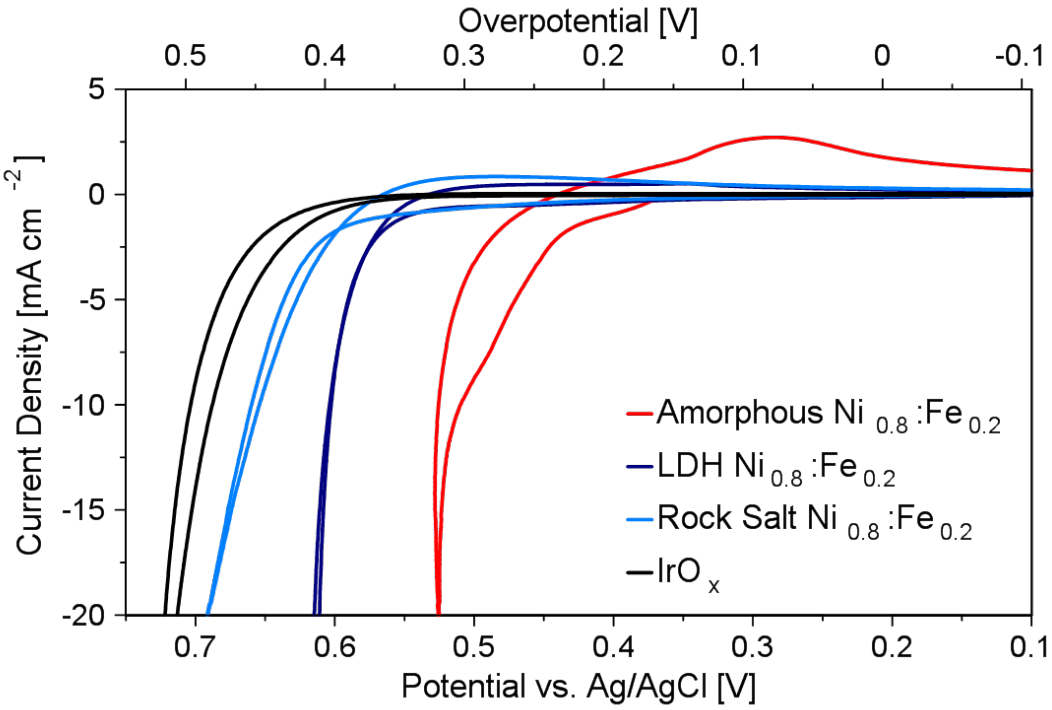

Figure 4.2. Cyclic voltammograms of amorphous $Ni_{0.8}$:$Fe_{0.2}$, $Ni_{0.8}Fe_{0.2}$OOH LDH, rock salt $Ni_{0.8}$:$Fe_{0.2}$, and crystalline IrO_x on fluorine doped tin oxide (FTO) glass in 1 M NaOH at 50 mV s^{-1} and corrected for uncompensated resistance, R_u.

(oxy)hydroxide-based materials (Figure 4.3). The rock salt $Ni_{0.8}$:$Fe_{0.2}$ oxide, $Ni_{0.8}Fe_{0.2}$OOH LDH, and amorphous $Ni_{0.8}$:$Fe_{0.2}$ oxide all had capacitance values (11, 14, and 11 μF cm^{-2}) similar to that of the underlying FTO glass (12 μF cm^{-2}), consistent with the report by Boettcher that double layer capacitance CVs taken on nickel-iron (oxy)hydroxides typically only measure the capacitance of the underlying support.[194] The IrO_x supported on FTO glass had a capacitance of 270 μF cm^{-2}, resulting in a roughness factor of ca. 22.5. This is the expected order of magnitude of capacitance for a catalyst supported on FTO glass.

4.4.1 Surface Interrogation Scanning Electrochemical Microscopy

To gain insight into the dramatic increase in OER activity when utilizing a $Ni_{0.8}Fe_{0.2}$OOH LDH structure instead of the rock salt $Ni_{0.8}$:$Fe_{0.2}$ structure, we performed surface interrogation scanning electrochemical microscopy (SI-SECM). In the SI-SECM experiment, we utilized a glassy carbon ultramicroelectrode (UME), a = 29 μm, as the SECM tip positioned within close proximity of a masked pseudo-UME substrate, made up of amorphous $Ni_{0.8}$:$Fe_{0.2}$, $Ni_{0.8}Fe_{0.2}$OOH LDH, rock salt

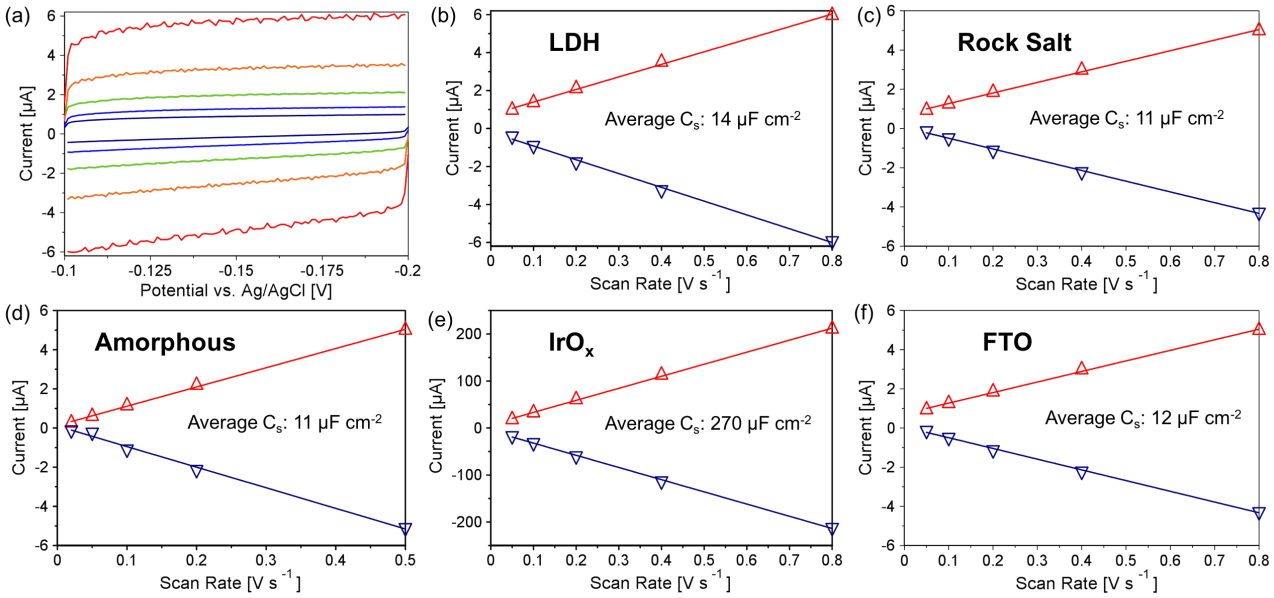

Figure 4.3. (a) Double layer capacitance measurements via cyclic voltammetry on $Ni_{0.8}Fe_{0.2}OOH$ LDH. Current vs scan rate with regression lines and the corresponding double layer capacitance values for (b) $Ni_{0.8}Fe_{0.2}OOH$ LDH, (c) rock salt $Ni_{0.8}$:$Fe_{0.2}$, (d) amorphous $Ni_{0.8}$:$Fe_{0.2}$, (e) crystalline IrO_x, and (f) bare FTO glass.

$Ni_{0.8}$:$Fe_{0.2}$, or IrO_x on FTO-coated glass. Fabricating a masked pseudo-UME is critical for the success of this experiment. Typical SI-SECM experiments involve the use of two equally sized UMEs.[233] However, due to the high annealing temperature required to create the oxide materials (500 ^{o}C), a conventional glassy carbon UME would not be suitable for this experiment. By masking the catalyst on FTO-coated glass, we can perform SI-SECM on this unique set of materials.

The surface interrogation experiments involved an initial potential pulse, E_{sub} (varied from -0.207 to 0.468 V overpotential), applied to the substrate to form surface-active species, while the tip electrode was held at a potential near open circuit potential (OCP) for a characteristic time, t_{step} (20 s). Following t_{step}, the substrate electrode was switched to open circuit potential and the titrant, Fe(II)-TEA, was generated by stepping the tip potential, E_{tip}, to -1.1 V vs Ag/AgCl. At E_{sub} sufficient to form surface-active species (Ni^{III}, Fe^{IV}, and/or Ni^{IV} for the $Ni_{0.8}$:$Fe_{0.2}$ catalysts)[212], positive feedback current was measured on the tip in the subsequent step until the titration of surface-active species was complete (Scheme 4.1).

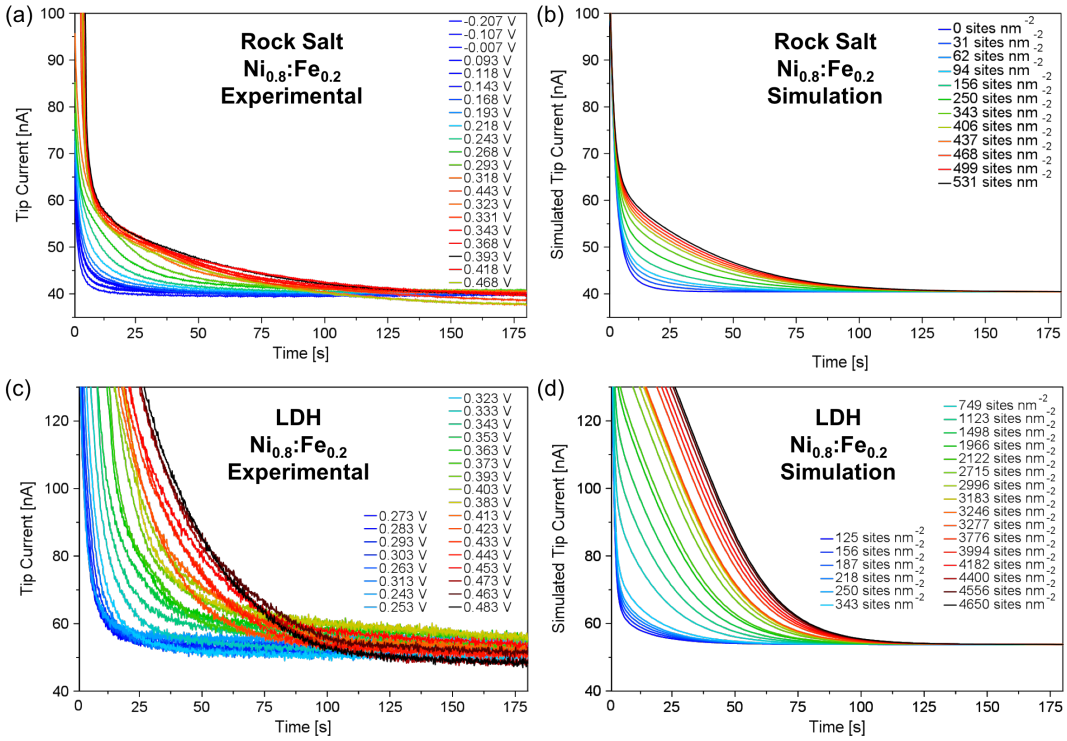

Figure 4.4. Surface interrogation chronoamperograms performed in 2 M NaOH ca. 50 mM Fe(III)-TEA. (a,c) Experimental chronoamperograms and (b,d) COMSOL simulated chronoamperograms showing positive feedback at elevated potentials of rock salt $Ni_{0.8}$:$Fe_{0.2}$ and $Ni_{0.8}Fe_{0.2}OOH$ LDH on FTO glass.

4.5 Results and Discussion

To quantify the active site densities, and to provide insights into the differences in the shape of the current-time profiles, the SI-SECM experiment was simulated via finite element analysis in COMSOL Multiphysics (details provided in Supporting Information). The physics of the simulation included Butler-Volmer one-electron transfer at the SECM tip (Equation 1), Fick's diffusion of Fe(II)-TEA from the tip to the substrate, the surface reaction of Fe(II)-TEA with surface-active species (Equation 2), and Fick's diffusion of Fe(III)-TEA back to the tip electrode. The only adjustable parameters in our simulation were the rate constant of the surface reaction, k_{sr}, and the active site density, Γ; all other parameters were obtained from experiment.

$$Fe(III) - TEA + e^{-} \rightarrow Fe(II) - TEA \tag{4.1}$$

$$Fe(II) - TEA + S^{*} \rightarrow Fe(III) - TEA + S \tag{4.2}$$

Keeping k_{sr} constant for each sample, increasing the total active site density on the substrate resulted in higher levels of positive feedback measured on the tip current. We determined the active site density on the catalyst substrate as a function of potential by performing a least-squares fit between the experimental and simulated data. There is good agreement between experimental and simulated SI-SECM data for all four catalysts (Figure 4.4, Figure 4.11, and Figure 4.12), which demonstrates the reliability of measuring active site densities with these simulations. It should be noted that the experimental tip current and simulated tip current are actual values without any normalizations or corrections.

Figure 4.5 shows the dependence of active site density on E_{sub}. The surface interrogation of nickel-iron (oxy)hydroxides is an overall two-electron titration, with the $Ni^{III/II}$ transition occurring first followed by the $Ni^{IV/III}$ transition, overlapped with the $Fe^{IV/III}$ transition.[212] The surface interrogation of iridium oxide is only a single-electron transfer corresponding to the $Ir^{V/IV}$ transition.[204] We measured the active site density of both rock salt $Ni_{0.8}$:$Fe_{0.2}$ and IrO_x to be ca. 500 sites nm^{-2}. As described in Supporting Information, the crystalline IrO_x sample was fabricated in the same method as the rock salt $Ni_{0.8}$:$Fe_{0.2}$. There are several outcomes from this measurement. First, a site density of 500 sites nm^{-2} for the IrO_x results in a surface roughness measurement of

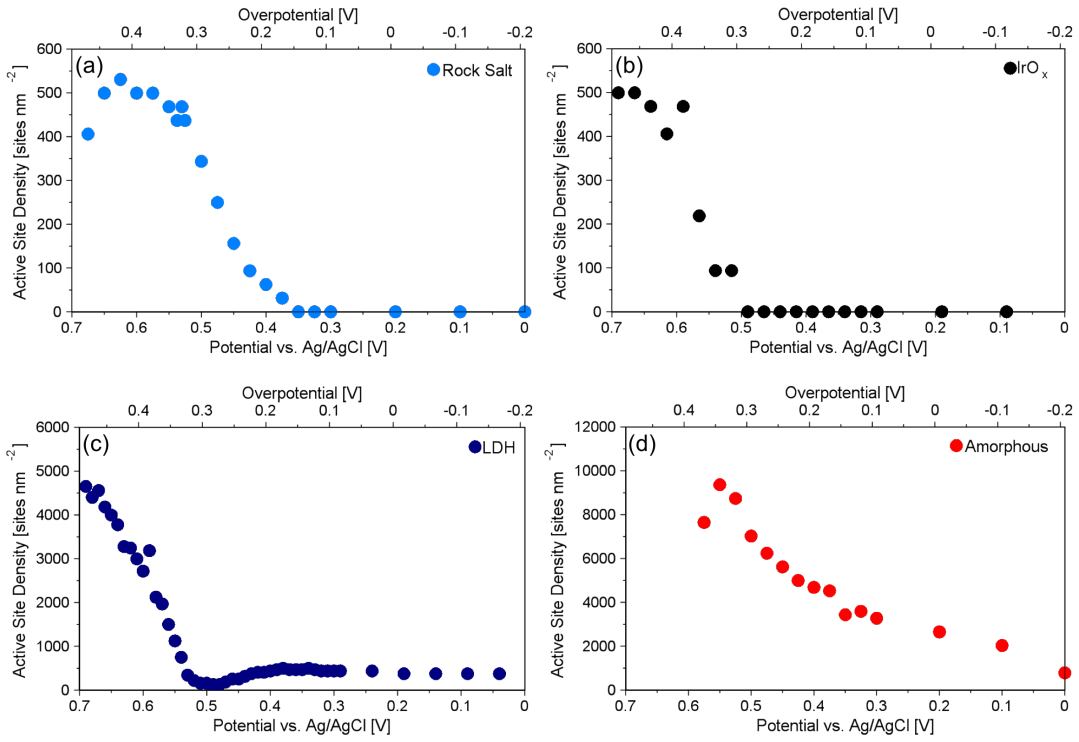

Figure 4.5. Active site density measured via SI-SECM as a function of catalyst potential for (a) rock salt $Ni_{0.8}$:$Fe_{0.2}$, (b) crystalline IrO_x, (c) $Ni_{0.8}Fe_{0.2}OOH$ LDH, and (d) amorphous $Ni_{0.8}$:$Fe_{0.2}$.

ca. 25, assuming that there are ca. 20 metal atoms per nm^2. This is in very good agreement with our double layer capacitance measurements shown in Figure 4.3, where we measured a roughness factor of 22.5 for IrO_x, implying that SI-SECM gives accurate measurements of the total number of active sites exposed to the electrolyte. Second, the rock salt $Ni_{0.8}$:$Fe_{0.2}$ oxide and the IrO_x have the same active site density and they were derived from the same synthesis method, which suggests that the morphology of the oxide is a major contributing factor to the active site density. Third, there is not good agreement between the double layer capacitance measurements and the SI-SECM measurements for the $Ni_{0.8}$:$Fe_{0.2}$ oxide, which confirms that double layer capacitance is not suitable for measuring the ECSA of nickel (oxy)hydroxide-based materials. However, SI-SECM can measure the active site density as a function of potential, and it is a useful tool in obtaining accurate electrochemical surface area results at potentials where catalysis is occurring.

The redox active site densities of the $Ni_{0.8}Fe_{0.2}OOH$ LDH and amorphous $Ni_{0.8}$:$Fe_{0.2}$ were determined to be 4500 and 9000 sites nm^{-2}, respectively—ca. one order of magnitude higher than that of either the rock salt $Ni_{0.8}$:$Fe_{0.2}$ oxide or the IrO_x. Several additional conclusions can be

made from this measurement. The LDH $Ni_{0.8}$:$Fe_{0.2}$ structure was fabricated by applying a simple electrochemical conditioning step to the rock salt structure to ensure that the LDH structure had the same morphology as both the IrO_x and rock salt samples, but the LDH structure has ca. 10 times the active site density, as measured by SI-SECM. This shows that the electrolyte permeability of $Ni_{1-x}Fe_xOOH$ LDH allows for stable Ni^{IV}/Fe^{IV} to be formed on surfaces below the traditional electrode/electrolyte interface. If the LDH structure was not permeable to the electrolyte, then we should have observed the same active site density for the rock salt structure due to the similar morphology between the samples. Our measurements show that these sub-surface Ni^{IV}/Fe^{IV} sites can be effectively titrated by Fe(II)-TEA (Scheme 4.6). While there are two possible pathways for this to occur, we postulate that $Ni_{0.8}Fe_{0.2}OOH$ LDH is permeable to water and hydroxide ions but not permeable to the bulky Fe(II)-TEA species. This implies that electron/hole transport between Ni^{IV}/Fe^{IV} species from the bulk of the LDH material to Fe(II)-TEA species at the solution interface[212] occurs due to the conductivity of LDH at OER potentials. The second possibility is that $Ni_{0.8}Fe_{0.2}OOH$ LDH is permeable to many dissolved species including the bulky Fe(III/II)-TEA. In this case, electron transfer would occur at the subsurface layers and Fe(III/II)-TEA would need to diffuse both into and out of the LDH structure. However, via our finite elemental analysis simulations, we have evidence that Fe(II)-TEA does not permeate to the sub-surface layers. These simulations allow us to calculate the k_{sr} for each of the three materials, which we determined to be 1×10^{-3}, 2×10^{-3}, and 1×10^{-3} m^3 mol^{-1} s^{-1} for the IrO_x, rock salt $Ni_{0.8}$:$Fe_{0.2}$ oxide, and $Ni_{0.8}Fe_{0.2}OOH$ LDH, respectively. If Fe(II)-TEA was indeed permeating into the LDH structure, then we would have expected a much smaller k_{sr} value due to the mass transfer effects of diffusing into and out of the LDH structure. In addition, our measurements show that this electrolyte permeability phenomena does not occur in the rock salt structure of $Ni_{0.8}$:$Fe_{0.2}$ oxide. This gives further credence to the notion that the electrolyte permeability of the $Ni_{0.8}Fe_{0.2}OOH$ LDH is a major cause of its increased electrocataltyic activity for the OER. It is still uncertain, however, exactly how these sub-surface sites participate in the OER. We postulate two possible mechanisms. One possibility is that the LDH structure is also permeable to dissolved O_2—oxygen evolution occurs on these sub-surface layers and O_2 diffuses through the interlayers to the surface.[234] The second possibility is that O_2 does not diffuse through the layers, and it is electron/hole hopping that is responsible for the increased oxygen evolution activity.

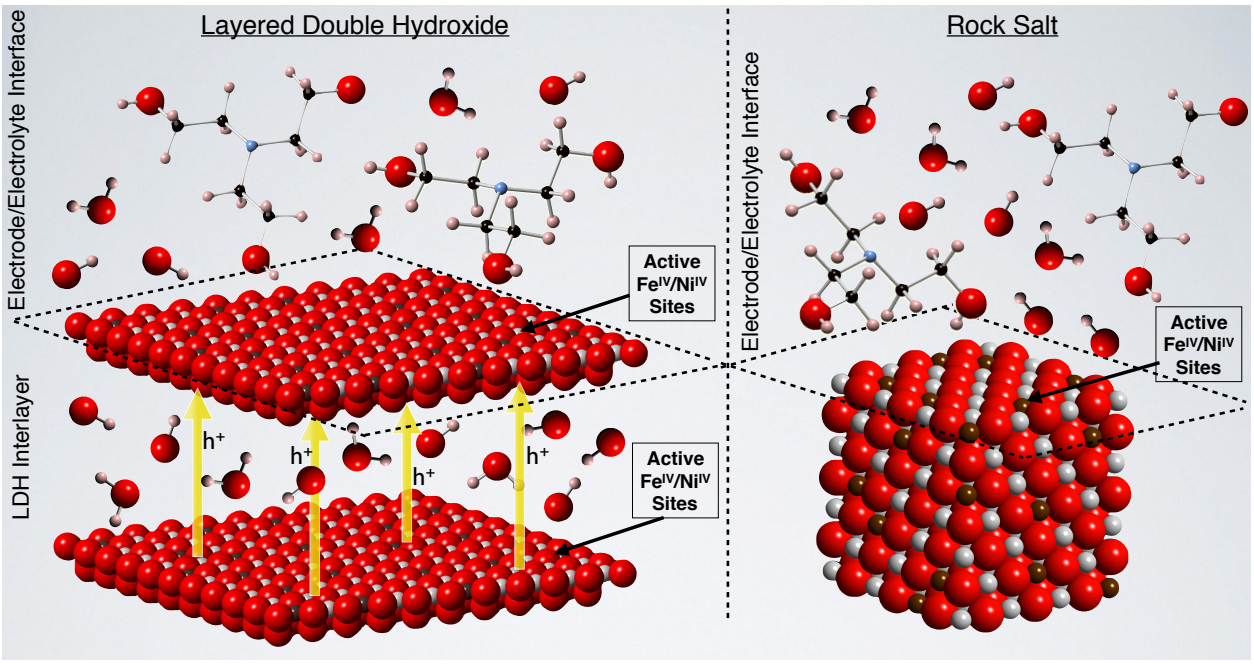

Figure 4.6. Schematic depicting the $Ni_{1-x}Fe_xOOH$ LDH structure (left) and the rock salt nickel-iron oxide structure (right). The LDH structure allows water and hydroxide permeation to the interlayer, which can create active Ni^{IV}/Fe^{IV} below the traditional electrode/electrolyte interface, while the LDH structure is not permeable to Fe(II)-TEA. Active Ni^{IV}/Fe^{IV} sites are only created at the electrode/electrolyte interface on the rock salt structure.

While catalysis on sub-surface layers appears to be enabled by the ability of oxyhydroxides to incorporate water into the interlayers,[199,235,236] the amorphous $Ni_{0.8}$:$Fe_{0.2}$ structure also showed very high active site densities. Given that the amorphous structure shows an anomalously high active site density, we postulate that the amorphous structure, too, has some electrolyte permeability. In addition, we measured a slower k_{sr}, 1×10^{-4} m^3 mol^{-1} s^{-1}, on the amorphous structure compared to the LDH structure, indicative of an additional mass transfer effect during the Fe(II)-TEA titration due to a higher degree of macroscopic porosity (also evident in the SEM, Figure 4.7).

Some further insights can be obtained from the potential-dependence of active site density shown in Figure 4.5. The rock salt $Ni_{0.8}$:$Fe_{0.2}$ follows the potential-dependence of active site density found by Bard and co-workers with an 80% Ni 20% Fe oxide material, where both materials begin the $Ni^{IV/III}$, $Fe^{IV/III}$, and $Ni^{III/II}$ transitions near 0.4 V vs Ag/AgCl and attain a total active site density of ca. 500 sites nm^{-2} at 0.5 V vs Ag/AgCl.[212] The $Ni_{0.8}Fe_{0.2}OOH$ LDH has a delayed onset of increased active site density compared to the rock salt $Ni_{0.8}$:$Fe_{0.2}$, but the total active site density of the $Ni_{0.8}Fe_{0.2}OOH$ LDH is an order of magnitude higher than that of the rock salt

$Ni_{0.8}$:$Fe_{0.2}$. This may suggest that the $Ni_{0.8}Fe_{0.2}OOH$ LDH is undergoing an additional transition to the ion permeable state from 0.4 to 0.5 V vs Ag/AgCl, allowing for the anomolously high active site density. The amorphous $Ni_{0.8}$:$Fe_{0.2}$, however, has an onset at less positive potentials than the $Ni_{0.8}Fe_{0.2}OOH$ LDH. One could speculate that this is due to a combination of an early onset of the $Ni^{IV/III}$, $Fe^{IV/III}$, and $Ni^{III/II}$ transitions and some transition to an ion permeable state. An overlap of these two transitions may account for the gradual increase of active site density starting at low oxidizing potentials. Thus, we attribute the increased performance of the amorphous structure to the increased number of catalytic sites (twice as many as the LDH structure used in our study), as well as the homogeneous dispersion, which allowed for only "fast" sites to exist instead of a mixture of "fast" and "slow" sites, as our group previously reported.[175]

4.6 Conclusions

Here we report that SI-SECM can be used to obtain accurate active site densities of nickel (oxy)hydroxide-based materials where ECSA measurements via double layer capacitance are unreliable. We also measured very similar active site densities (500 sites nm^{-2}) for the rock salt $Ni_{0.8}$:$Fe_{0.2}$ and IrO_x which were prepared via the same method and have the same morphology. This shows, as expected, that morphology dictates active site density. However, $Ni_{0.8}Fe_{0.2}OOH$ LDH prepared from rock salt $Ni_{0.8}$:$Fe_{0.2}$ had an active site density approximately one order of magnitude higher (4500 sites nm^{-2}). This anomalously high active site density was attributed to the electrolyte permeability of $Ni_{0.8}Fe_{0.2}OOH$ LDH, which allows for water and OH^- ions to access sub-surface layers and the formation of active Ni^{IV}/Fe^{IV} sites below the traditional electrode/electrolyte interface. In addition, our results strongly suggest that during OER electrocatalysis, electrolyte permeability allows for active sites below the electrode/electrolyte interface to be utilized, but it is still unclear if O_2 is formed at these sites directly and diffuses through the LDH layers, or if electron/hole transport is responsible for forming O_2 only at the surface. In any event, the sub-surface layers are crucial in the electrocatalytic activity of $Ni_{0.8}Fe_{0.2}OOH$ LDH and possibly other layered 2D materials that are electrolyte permeable.

4.7 Acknowledgements

This work was previously published in ACS Applied Energy Materials:
Barforoush JM, Seuferling TE, Jantz DT, Song KR, Leonard KC. Insights into the Active Electrocatalytic Areas of Layered Double Hydroxide and Amorphous Nickel-Iron Oxide Oxygen Evolution Electrocatalysts. ACS Applied Energy Materials. 2018;1(4):1415-1423.

4.8 Supporting Information

4.8.1 Materials and Methods

Chemicals

Ethylene glycol (99.8%, anhydrous, Sigma Aldrich), iridium(III) chloride (99.99%, Alfa Aesar), iron(III) nitrate nonahydrate (98%+, ACS Reagent, Acros), iron(III) sulfate hydrate (Reagent Grade, Alfa Aesar), nickel(II) nitrate hexahydrate (99%, Fisher Scientific), potassium hydroxide (85%, Acros Organics), sodium bicarbonate (Fisher Scientific), sodium hydroxide (>97%, Fisher Scientific), triethanolamine (97%, Acros Organics) were all used as received without additional purification.

Synthesis

Redox Mediator

The Fe(III)-TEA solution was prepared following a previously reported procedure.[175,204] Briefly, 3.2 g of NaOH was added to 10 mL of deionized water in a stirred beaker cooled by a room temperature water bath. In a round-bottom flask, 20 mL of deionized water was bubbled with argon while stirring. After 5 minutes, 214.4 mg of $Fe_2(SO_4)_3 \cdot xH_2O$ was added to the round-bottom flask, and 104 μL of triethanolamine (TEA) was added dropwise to the round-bottom flask. The NaOH solution was added dropwise to the Fe(III) + ligand solution before adding deionized water to bring the total volume to 40 mL.

$Ni_{0.8}$:$Fe_{0.2}$ Catalysts

Rock Salt and LDH: Thin films of crystalline $Ni_{0.8}$:$Fe_{0.2}$ were made according to a previously reported procedure.[175,206] A 0.02 M $Ni(NO_3)_2 \cdot 6\,H_2O$ ethylene glycol solution was mixed with a 0.02 M $Fe(NO_3)_3 \cdot 9\,H_2O$ ethylene glycol solution at an 8:2 ratio, dropcast on fluorine-doped tin oxide (FTO) coated glass (Sigma-Aldrich), and annealed to create the rock salt $Ni_{0.8}$:$Fe_{0.2}$ structure at a mass loading of 120 ± 20 μg cm^{-2}. The rock salt was electrochemically conditioned by applying an oxidation current of ca. 10 mA cm^{-2} for 1 hour to form the $Ni_{0.8}Fe_{0.2}OOH$ LDH structure, as described previously.[215] Crystalline IrO_x was prepared following the same procedure for rock salt $Ni_{0.8}$:$Fe_{0.2}$, substituting the nickel and iron nitrate precursors for 0.02 M $IrCl_3$ in ethylene glycol.

Amorphous: The microwave-assisted synthesis of amorphous $Ni_{0.8}$:$Fe_{0.2}$ was reported previously.[175] Briefly, 4 mmol of $Fe(NO_3)_3 \cdot 9\,H_2O$ and 16 mmol of $NiNO_3 \cdot 6\,H_2O$ were dissolved in 100 mL of 18.2 MΩ water in an Erlenmeyer flask. A separate solution was made by dissolving 1.99 g $NaHCO_3$ in 100 mL of 18.2 MΩ water. The Ni-Fe solution was titrated with the $NaHCO_3$ solution at ca. 2.5 - 3 mL min^{-1} while rapidly stirring. The resulting deep red suspension was allowed to stir for one hour after titration. Finally, the suspension was transferred to Nalgene bottles and microwaved for ca. two minutes. The suspensions were dropcast on FTO-coated glass and dried at 70 °C to create amorphous $Ni_{0.8}$:$Fe_{0.2}$ electrodes with a mass loading of 60 ± 20 μg cm^{-2}.

4.8.2 Electrode Fabrication

Masked Substrate

The catalyst sample dropcast on FTO glass was masked to create a pseudo-ultramicroelectrode substrate for the surface interrogation mode of scanning electrochemical microscopy (SI-SECM). The general masking procedure was reported previously.[175] Briefly, three holes were drilled, 500 μm apart in a line, in the center of a 2 cm x 2 cm square of Teflon FEP Film (50A, American Durafilm) with a 100 μm diameter drill bit (One Piece, Drill Bits Unlimited) in a CNC mill. The FEP film mask was placed over the catalyst sample dropcast on FTO glass, centering the three holes. The FEP film mask was heat-bonded to the substrate by placing in the furnace above 271 °C for 30 minutes.

Glassy Carbon Ultramicroelectrode

The fabrication of the glassy carbon (GC) ultramicroelectrode utilized as the SECM tip was reported previously.[175,212] A 1 cm GC rod (type 2, 1 mm diameter, Alfa Aesar) was electrochemically etched, one end at a time, in 4 M KOH with a graphite counter electrode by applying 5 V for 500 s. The etching process was repeated, lowering the etch time as needed, until a sharp GC needle formed. Acetone and deionized water were used to rinse the GC needle before allowing it to dry completely. One end of a borosilicate glass capillary (1 mm O.D., 0.5 mm I.D., Sutter Instruments, USA) was filled with conductive silver epoxy (Circuit Works, USA) and the etched GC needle, with one end coated in silver epoxy, was inserted. A silver connection wire (30 AWG, Belden, USA) coated with conductive silver epoxy (Circuit Works, USA) was inserted into the other end of the borosilicate glass capillary and pushed against the GC needle inside the capillary to ensure good electrical contact. The silver epoxy in the electrode was dried at 120 °C for 30 minutes. Epoxy (1C&EPKC, Loctite Hysol) was used to completely coat the GC tip, and the epoxy coated electrode was dried in the oven at 120 °C with the GC tip pointing up. Every 20 s, the epoxy was recoated/remolded to achieve a sufficient epoxy coat with the desired shape, and the epoxy was allowed to fully cure. The tip of the epoxy coated electrode was polished with MicroCloth polishing disks (Beuhler, Canada) until a GC disc was visible. A MicroCloth polishing disc was also used to sharpen the electrode tip to adjust the RG. The GC disc was polished with alumina micropolish (1 μm, Beuhler, Canada) to render a smooth surface for experimentation.

4.8.3 Electrochemical Characterization

The catalyst coated FTO electrodes were characterized via cyclic voltammetry (CV) in 1 M NaOH in a custom Teflon cell with a Ag/AgCl reference electrode with porous Teflon tip (CH Instruments) and a 200 μm Pt wire (Electron Microscopy Instruments) as the counter electrode. The FTO glass working electrodes were 0.49 cm^2. All CV data was obtained via a CH Instruments (Austin, TX) potentiostat.

The instrumentation for the surface interrogation SECM (SI-SECM) experiments was described previously.[207] The 2 M NaOH ca. 50 mM Fe(III)-TEA (E^0 = -1.05 V vs. Ag/AgCl in 2 M NaOH) solution was bubbled with argon for 10 minutes prior to each SECM experiment. Experiments on

the masked catalyst coated FTO glass samples were performed in a custom Teflon cell with the catalyst coated FTO glass substrate as the working electrode, a Ag/AgCl electrode with porous Teflon tip (CH Instruments) as the reference electrode, and a 200 μm Pt wire (Electron Microscopy Instruments) as the counter electrode. The SECM tip, a glassy carbon (GC) ultramicroelectrode, a = 29 μm, was held at -1.2 V vs Ag/AgCl while it was approached to an insulating portion of the masked substrate until a current enhancement of 0.3 was reached (Figure 4.9). Electrochemical reactivity maps, ranging in size from 500 – 1400 μm x 500 – 1400 μm, were performed, with step sizes ranging from 25 – 50 μm and sample intervals ranging from 2 - 4 s, until the hole was located (Figure 4.10). The GC tip was aligned with the hole and re-approached to position the tip in close proximity to the substrate. For the surface interrogation experiment, a potential step with a 20 s duration was performed on the catalyst with potentials ranging between 0 – 0.675 V vs Ag/AgCl. Immediately following, the substrate was brought to open circuit and a potential step was applied to the GC tip electrode at -1.2 V vs Ag/AgCl with pulse width of 180 s. All finite element analysis simulations were performed with COMSOL Multiphysics v. 5.2.

4.8.4 Details on COMSOL Multiphysics Simulations

COMSOL (COMSOL Multiphysics v. 5.2) simulations were performed to obtain the active site density of the catalysts, Γ, and the kinetic rate constant of the surface reaction. The COMSOL geometry and mesh for simulation of surface interrogation scanning electrochemical microscopy (SI-SECM) on a masked substrate were described previously.[175] Briefly, a 2D axial-symmetric domain was created to simulate the actual size of our SECM tip electrode, the size and thickness of the masked catalyst electrode, and the tip/substrate distance as shown in Figure 4.14a. The roughness of the substrate electrode is incorporated into the experimental tip current via feedback from the substrate during the approach curve (Figure 4.9), allowing for the use of the calculated tip/substrate distance with a flat substrate to simulate the SI-SECM experiment. Different edge meshes with a maximum element size of 0.5 μm and a minimum element size of 0.05 μm were used for the SECM tip boundary and the boundary on the catalyst electrode extending partially along the FEP mask. A free triangular mesh with COMSOL's built-in "fine" element size, calibrated for fluid dynamics, was used for the simulation.

The SECM tip current in the surface interrogation experiment was simulated via the COMSOL

Electroanalysis module. This module obtains the concentration of the oxidized and reduced species in solution and the current on the electro-active boundary as a function of applied potential by coupling the Butler-Volmer Equation with Fick's Law of Diffusion. We assumed an electron-transfer rate constant of 1 cm s^{-1} and a transfer coefficient of $\alpha = 0.5$ for the reduction of Fe(III)-TEA to Fe(II)-TEA because it is a fast outer-sphere, one electron transfer reaction. The diffusion coefficient for both Fe(III)-TEA and Fe(II)-TEA was previously reported as 2×10^{-6} cm^2 s^{-1}.[204] The exact tip potential used in our experiment was used in our simulations. The tip/substrate distance was determined by fitting the experimental negative feedback current with simulations. The COMSOL Surface Reactions physics in the Chemical Reaction Engineering Module was used to model the reaction of the Fe(II)-TEA with the surface-active species. The rate of titration of the surface-active species was as shown in Equation 4.3.

$$r_{sr} = -k_{sr} C_{Fe^{II},0} C_{S^*} \tag{4.3}$$

where k_{sr} is the kinetic rate constant of the surface titration, $C_{Fe^{II},0}$ is the concentration of Fe(II)-TEA at the catalyst surface, and C_{S^*} is the surface concentration of active sites. To account for Fe(II)-TEA converting back to Fe(III)-TEA after the titration step, a flux boundary condition in the Electroanalysis physics was used at the catalyst surface. The inward flux of both Fe(II)-TEA, $N_{Fe^{II}}$, and Fe(III)-TEA, $N_{Fe^{III}}$, are shown in Equations 4.4 and 4.5.

$$N_{Fe^{II}} = -k_{sr} C_{Fe^{II},0} C_{S^*} \tag{4.4}$$

$$N_{Fe^{III}} = k_{sr} C_{Fe^{II},0} C_{S^*} \tag{4.5}$$

In order to quantify the active site density, the COMSOL simulation was performed with different initial surface concentrations of active sites, S^*. Increasing the initial active site density concentration would increase the positive feedback measured on the tip electrode as shown in the main paper. We determined k_{sr} to be 2×10^{-3}, 1×10^{-3}, 1×10^{-3}, and 1×10^{-4} m^3 mol^{-1} s^{-1} for the rock salt $Ni_{0.8}$:$Fe_{0.2}$, crystalline IrO_x, $Ni_{0.8}Fe_{0.2}OOH$ LDH, and amorphous $Ni_{0.8}$:$Fe_{0.2}$ samples, respectively. Active site densities as a function of potential were found by performing a least-squares

analysis between the experimental and simulated data. Figure 4.14c-d is an example COMSOL simulation for $Ni_{0.8}Fe_{0.2}OOH$ LDH showing the concentration of Fe(II)-TEA at 0.2 s, 0.8 s, and 25 s.

4.8.5 Supporting Figures

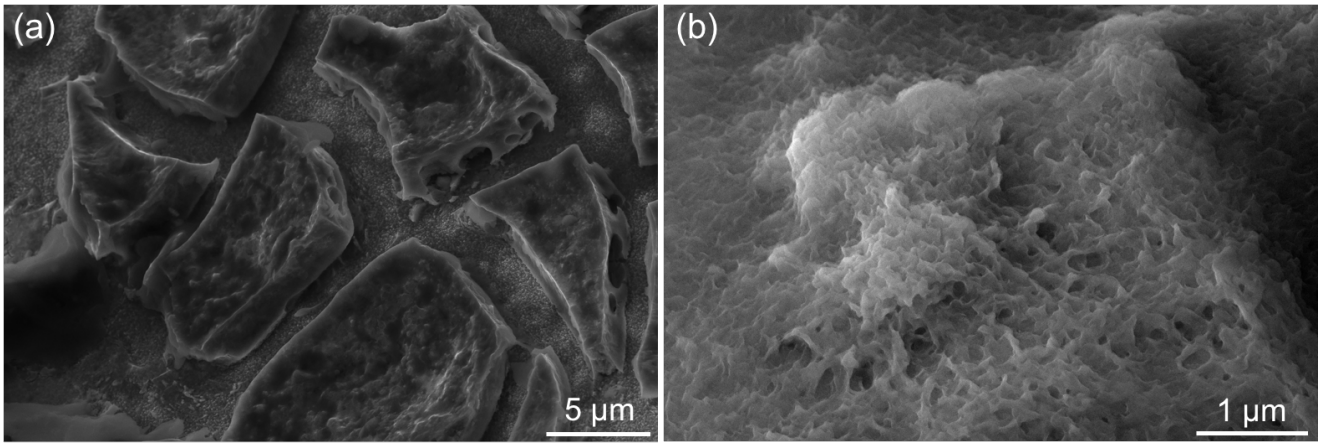

Figure 4.7. Scanning electron microscopy (SEM) images of (a) $Ni_{0.8}Fe_{0.2}OOH$ LDH and (b) amorphous $Ni_{0.8}$:$Fe_{0.2}$.

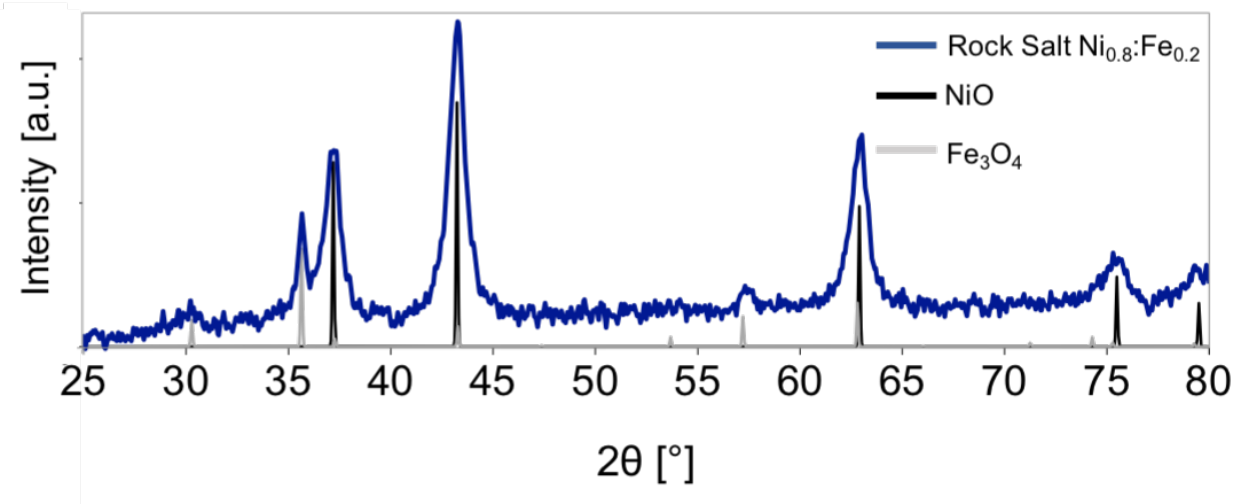

Figure 4.8. X-ray diffraction (XRD) pattern of rock salt $Ni_{0.8}$:$Fe_{0.2}$ oxide.

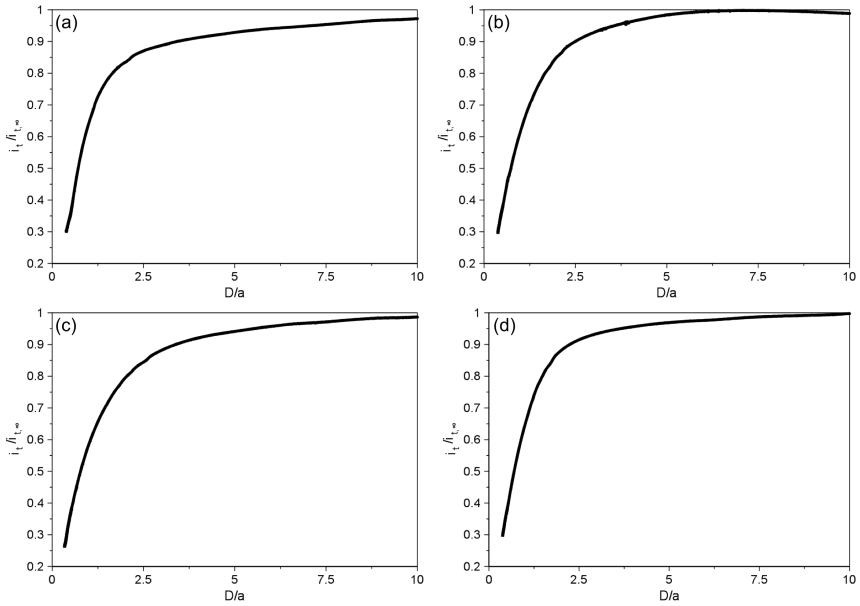

Figure 4.9. Scanning electrochemical microscopy negative feedback approach curves for imaging and surface interrogation (SI-SECM). Negative feedback approach curves for SI-SECM experiments with glassy carbon ultramicroelectrode tip and masked (a) rock salt $Ni_{0.8}$:$Fe_{0.2}$, (b) crystalline IrO_x, (c) $Ni_{0.8}Fe_{0.2}$OOH LDH , and (d) amorphous $Ni_{0.8}$:$Fe_{0.2}$ on FTO glass substrate.

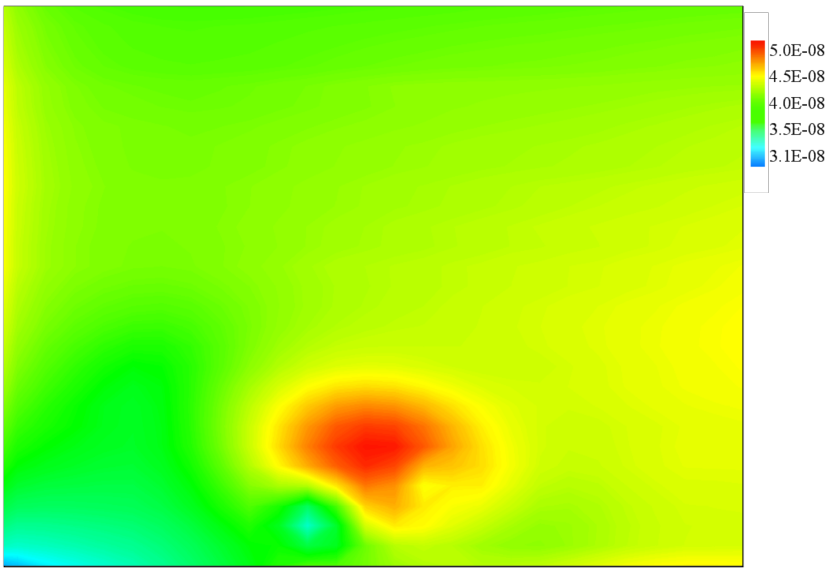

Figure 4.10. Example of an electrochemical imaging map for surface interrogation scanning electrochemical microscopy (SI-SECM). Map of the hole in the mask on amorphous $Ni_{0.8}$:$Fe_{0.2}$ on FTO glass substrate obtained using a glassy carbon ultramicroelectrode tip with Fe(III)/Fe(II)-TEA redox couple. Red represents high reduction current, indicative of the location of the hole in the mask, and blue represents low reduction current. The values reported in the legend are in units of amperes.

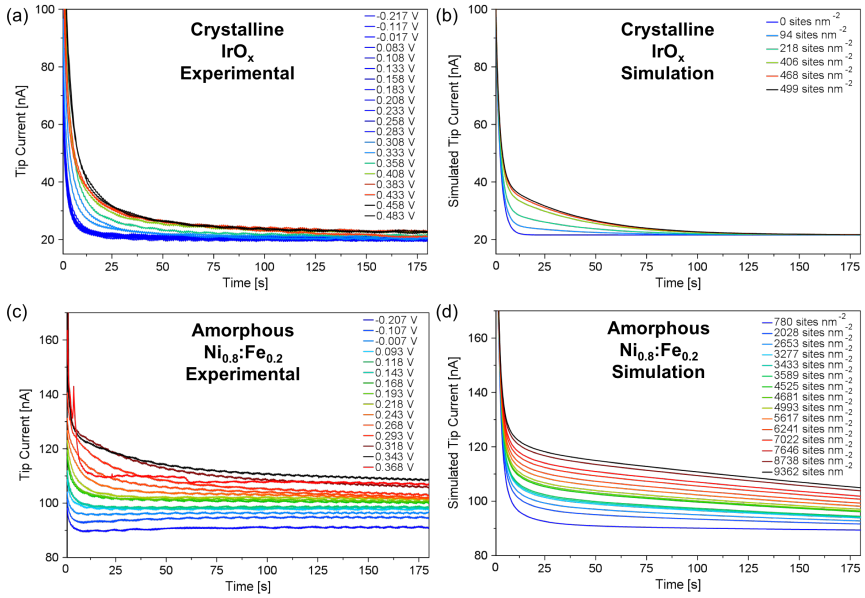

Figure 4.11. Surface interrogation chronoamperograms performed in 2 M NaOH ca. 50 mM Fe(III)-TEA. (a,c) Experimental chronoamperograms and (b,d) COMSOL simulated chronoamperograms showing positive feedback at elevated potentials of crystalline IrO_x and amorphous $Ni_{0.8}$:$Fe_{0.2}$ on FTO glass.

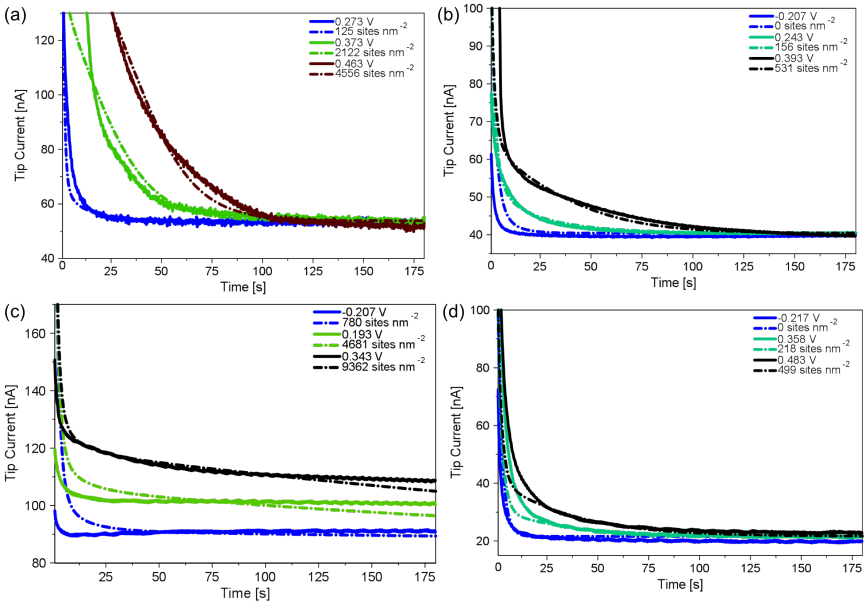

Figure 4.12. Comparison of experimental (solid lines) and COMSOL simulated (dashed lines) surface interrogation chronoamperograms for (a) $Ni_{0.8}Fe_{0.2}OOH$ LDH, (b) rock salt $Ni_{0.8}$:$Fe_{0.2}$, (c) amorphous $Ni_{0.8}$:$Fe_{0.2}$, and (d) crystalline IrO_x on FTO glass.

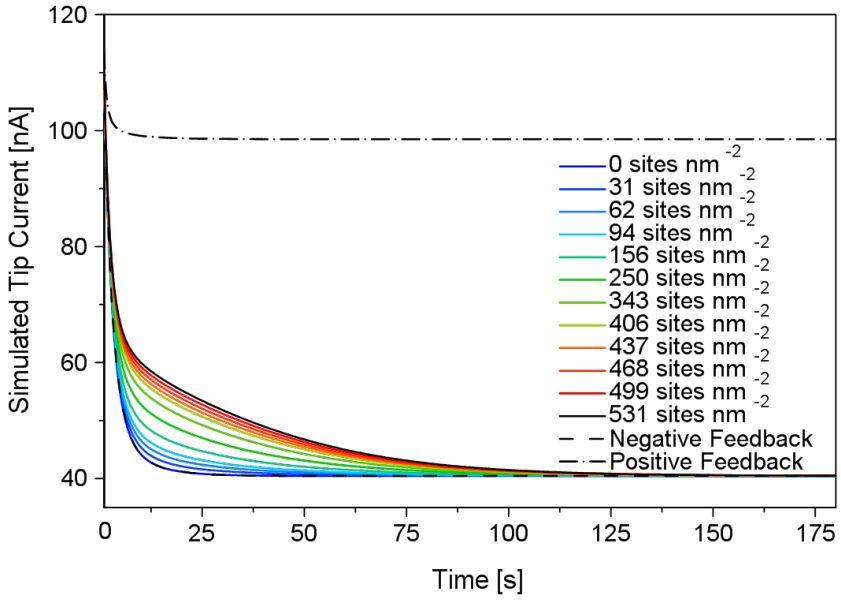

Figure 4.13. COMSOL simulated surface interrogation chronoamperograms (CAs) of rock salt $Ni_{0.8}$:$Fe_{0.2}$ showing the negative feedback and positive feedback boundaries. The negative feedback boundary is consistent with the CA for 0 sites nm^{-2}, and the positive feedback boundary is outside the range of the surface interrogation CAs.

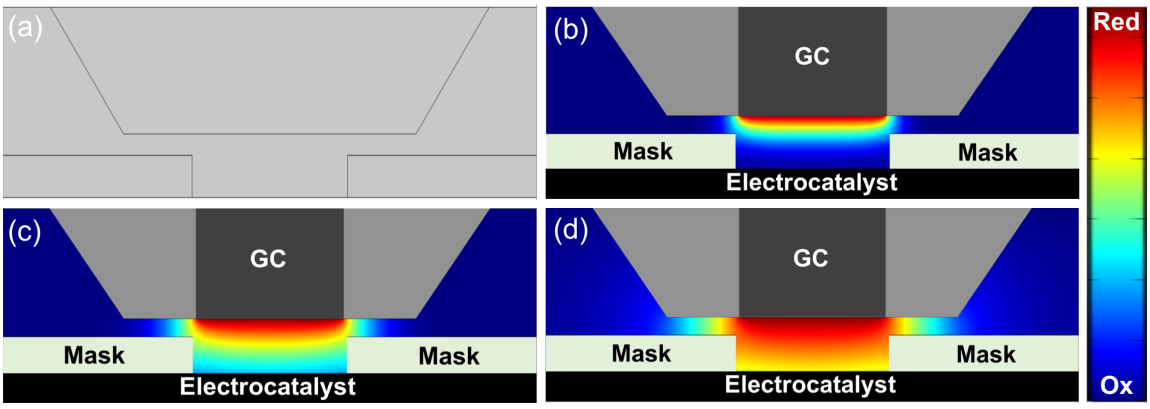

Figure 4.14. Example COMSOL simulation for surface interrogation scanning electrochemical microscopy (SI-SECM) on $Ni_{0.8}Fe_{0.2}OOH$ LDH showing the (a) geometry constructed for the COMSOL simulation, and the concentration profiles for the Fe(III)/Fe(II)-TEA redox couple at (b) 0.2 s, (c) 0.8 s, and (d) 25 s after bringing the catalyst to open circuit potential.

4.9 Appendix

A material suitable for masking the catalyst substrate must be an insulator, prevent electrolyte leakage over the course of the experiment (8-12 hours), and withstand the 2 M NaOH solution in which the surface interrogation scanning electrochemical microscopy (SI-SECM) experiment was performed. Teflon polytetrafluoroethylene (PTFE) tape was the initial choice for masking. Several tools for punching a ca. 100 μm hole in the PTFE tape were used, including a 26 gauge needle, a razor blade, and a quartz glass capillary pulled to a sharp point. The pulled capillary, which consistently yielded the smallest holes compared to the other tools, was made from a 0.30 mm ID x 1 mm OD quartz capillary in a Model P-2000 with the settings: H=850, F=1, V=50, D=100, and P=175. The PTFE tape was stretched in both directions, and stretched again after punching a small hole in the tape. Wearing gloves, the mask was pressed down onto the electrode surface. To determine the approximate size of the hole, cyclic voltammetry was performed on the masked electrode in a 0.5 mM ferrocenemethanol 0.1 M $NaNO_3$ solution. In many cases, only a linear current-potential relationship was observed, attributed to the hydrophobicity of the PTFE preventing the aqueous electrolyte from going into the small hole and causing resistive current. Although SECM was successfully performed on a PTFE masked substrate electrode, the reproducibility of the PTFE mask was quite poor—a robust mask was needed.

Poly(methyl methacrylate) (PMMA) was investigated as an alternative to the PTFE mask. A drop of glycol from a 100 μm pipette tip in an ultrasonic printer was used to maintain a void in the PMMA film, which was applied to the substrate electrode by pipetting a PMMA-saturated tetrachloroethylene solution. The PMMA-masked electrode was heated at 100 °C for one hour and allowed to cure overnight. 1, 3, and 4 coats of PMMA were tried, and in all cases the electrolyte seeped underneath the edges of the PMMA during cyclic voltammetry.

Parafilm masking was also performed using a technique similar to the PTFE masking technique. A parafilm square was stretched very thin and a pulled glass capillary, oriented vertically in a clamp, was used to punch a hole. The parafilm mask was then pushed over the substrate electrode using the wax paper on the back of pre-packaged parafilm. In addition, a heat gun was used to seal the parafilm to the electrode and remove any air bubbles. The parafilm mask, however, was not able to prevent electrolyte leakage over the whole duration of the SECM experiments.

Kapton FN film, 25.4 μm thick, with one side coated with Teflon fluorinated ethylene propylene (FEP) was investigated next. The concept was that a heat gun or oven could be used to heat bond the FEP side of the film to the substrate electrode. However, the Kapton film was too rigid to allow sufficient contact between the FEP and the substrate electrode without compression. Compression by a metal clamp allowed for heat bonding in the oven, but this method was impractical for catalyst coated electrodes.

Finally, Teflon FEP 12.7 μm film was employed for masking. Micro-drill bits were used to drill the hole(s) in the film as described in 3.6.1 and 4.7.2. At any temperature above the melting point of the FEP film, 271 °C, oven heating provided ample adhesion between the film and the substrate electrode. Crystalline catalyst-coated substrate electrodes were suitable for masking while less uniform coatings would often introduce new holes into the mask during the heat bonding process. For samples with less uniform coatings (i.e. nanoamorphous $Ni_{0.8}$:$Fe_{0.2}$ oxide), the bare FTO glass electrode was masked before electrodeposition of the catalyst solution into the holes.

Chapter 5

Intelligent Scanning Electrochemical Microscopy Tip and Substrate Control Utilizing Fuzzy Logic

5.1 Abstract

In this paper, we present a technique to intelligently control the motion of Scanning Electrochemical Microscopy (SECM) tip electrodes and automatically align SECM tip electrodes to the substrate with no user interaction. This intelligent method utilizes a custom fuzzy logic algorithm to control the motion of the tip electrode and automate tip/substrate alignment. The fuzzy logic control algorithm rapidly obtains SECM approach curves via a variable speed approach and automatically stops the tip electrode at a preprogrammed tip/substrate distance without "crashing" the tip electrode into the substrate. The fuzzy logic algorithm automatically adjusts the speed of the electrode based on the tip size, the enhancement of the tip current, and the distance that the tip electrode is from a user defined setpoint. We validated that both positive feedback and negative feedback approach curves obtained using the fuzzy logic algorithm matched well with simulated approach curves for both large microelectrodes (sometimes used for Surface-Interrogation SECM, a = 175 mm) and for conventional SECM ultramicroelectrodes (a = 4.2 mm). The ability to automatically stop the tip electrode is crucial for the automated sample tilt adjustment protocol.

This ability allows us to automate the interactive process of (1) approaching the tip to the substrate, (2) scanning the tip across the substrate to measure the tip/substrate tilt, (3) correcting for the tip/substrate tilt. We demonstrated that this tip/substrate alignment protocol allows us to obtain highly resolved constant-height SECM images over large areas with ease.

5.2 Introduction

Scanning Electrochemical Microscopy (SECM) is an electro- chemical scanning probe technique that is frequently used to study homogeneous[237–239] and heterogeneous[98,240,241] reaction mechanisms, biological systems[242–246], electrocatalysts[247,248], semi-conductor surfaces[145,249], reaction intermediates[130–133,250–252], and topographical and reactivity imaging[100,253–255], among many others[114,256–266]. There are two main challenges that the SECM operator typically faces when performing SECM experiments: (1) Approaching the SECM tip electrode sufficiently close to the substrate of interest without "crashing" the tip into the substrate. (2) Obtaining precise tip/substrate alignment.

It is critical that the SECM tip electrode is in very close proximity (less than one tip radius) to the substrate for all modes of SECM[258]. For example, in positive feedback mode, a small tip/substrate distance increases mass transfer to the tip electrode so that fast kinetics can be measured accurately[257]. Small tip substrate distances also allow for interrogating surface adsorbed intermediates of catalytic reactions[131]. However, if the SECM tip is not stopped at just the right moment during the approach, the tip electrode can "crash" into the substrate causing damage to both electrodes.

With SECM, it is also imperative to have the tip and substrate highly aligned (i.e., the substrate cannot be tilted relative to the tip). If the tip electrode and substrate electrode do not have excellent alignment during the approach, small tip/substrate distances cannot be obtained because the glass sheath surrounding the tip electrode will contact the substrate before the needed tip/substrate distance is reached.

Tip/substrate alignment is even more important when obtaining chemical reactivity images. The chemical-reactivity imaging mode of SECM is able to measure areas of higher chemical activity on a surface. However, obtaining high quality chemical reactivity images over large areas is

challenging because the tip current not only depends on the electroactivity of the substrate, but it is also dependent on the tip/substrate distance. Thus, poorly aligned samples will show spots with either artificially high or low electroactivity simply due to poor substrate alignment[257]. In addition, performing tip/substrate alignment with SECM can be time intensive and can prove challenging when the substrate tilt is adjusted manually. This is because numerous iterations are required to align the tip and the substrate, and manual setscrews, which are typically used to adjust the sample stage, are difficult to adjust for fine tip/substrate adjustment.

One method to circumvent poor tip/substrate alignment during imaging is to use the constant-current imaging mode[267–271]. In the constant-current imaging mode, the SECM experiment is operated with an outer-sphere redox mediator (such as ferrocenemethanol) in solution. In this mode, one is able to measure the morphology of a conductive electrode because the SECM tip is placed within the feedback distance, i.e. a tip/substrate distance that produces an enhancement of the tip current. Since the current of the SECM tip is controlled by the tip/substrate distance, if the instrument continually adjusts the height of the SECM tip in order to maintain a constant current throughout the experiment, the morphology of the substrate can be mapped by measuring the changes in the tip height as the tip is scanned across the substrate of interest. However, the drawback of the constant-current imaging mode is that it cannot be used to measure electrochemical activity; it can only be used to obtain morphological information. In addition, hybrid techniques also exist where the tip distance can be controlled independent of the electrochemical measurement (e.g. SECM-AFM[272–275], SECM-SICM[246,276], and Shear Force SECM[277,278]). However, simple yet intelligent control of SECM tip electrodes are still needed, and would complement both traditional and hybrid SECM techniques.

In this manuscript, we present a new computer algorithm and motion control system that provides intelligent control for approaching SECM tips to the substrate, and automatically corrects any tip/substrate tilt. To do this, we developed a fuzzy logic control algorithm, which varies the speed of the tip electrode depending on the electrode size and the tip/substrate distance. More importantly, the algorithm stops the tip electrode once a pre-programmed setpoint has been reached to avoid crashing the tip into the substrate. The ability to automatically stop the tip allows us to automate the iterative alignment process and achieve precise tip/substrate alignment without any user interaction. In addition, the fuzzy logic algorithm is able to obtain approach curves

faster than traditional constant-speed approach curves. The approach curves are faster because the algorithm approaches the tip at greater speeds when the tip is far from the substrate, and then automatically slows the electrode when small tip/substrate distances are obtained. Also, this technique automatically alternates between using coarse and fine motion controllers depending on the tip/substrate distance. Here we demonstrate the functionality of this fuzzy logic control algorithm to approach both large and conventional UMEs under both positive feedback and negative feedback[131,257,279,280]. We also demonstrate an automated tilt adjustment algorithm, which utilizes our fuzzy logic algorithm and dramatically enhances the quality of constant-height SECM chemical reactivity images.

5.3 Experimental

5.3.1 Chemicals

All solutions were prepared with deionized Milli-Q water, and the chemicals purchased from the following were used as received: ferrocenemethanol (FcMeOH, 97%) from Sigma-Aldrich, sodium nitrate ($NaNO_3$, 99%) from Fisher Scientific, (dimethylaminomethyl) ferrocene (DMAMFc, 98+%) from Alfa Aesar, N,N,N',N'-tetramethyl-p-phenylenediamine (TMPD) hydrochloride from Cayman Chemical Company, and perchloric acid ($HClO_4$, ACS Reagent, ca. 70% solution in water) from Acros Organics.

5.3.2 SECM Instrumentation

All SECM experiments were performed with our custom-built SECM (Fig. 5.14 and 5.15. For the motion control, two separate systems are utilized to achieve both coarse and fine control. The coarse substrate control is performed with a Newport VP-25XL-XYZ, which moves the substrate electrode into close proximity of the SECM tip. This stage is able to move in the X, Y, and Z directions and has a total range of 25 mm with a minimum increment motion of 10 nm in each direction. This coarse control allows us to position the SECM tip close to the substrate before engaging the fine nanopositioner control. For the fine tip control, we use a highly- precise 3-axis piezo controller (Newport NPXYZ100SG-D) with a feedback system to eliminate any hysteresis in the piezo control. This nanopositioner is able to move in the X, Y, and Z directions and has a

travel range of 100 mm and a resolution of 0.4 nm. The tilt adjustment was performed using a Newport Series 37 tilt stage along with 2 tilt stage motors (Newport LTA-HS). The entire system, including the bi-potentiostat (CH Instruments 730E), is computer-controlled using custom software built with LabVIEW. The custom LabVIEW software is capable of performing cyclic voltammetry, chronoamperometry, amperometric i-t, linear approach curves, fuzzy logic-based approach curves, tilt adjustments, and electrochemical reactivity mapping. The custom LabVIEW software is also able to automate many SECM routines by allowing the user to set up a series of experiments to be carried out sequentially.

5.3.3 Fuzzy Logic Algorithm

The fuzzy logic algorithm was built using National Instruments' (Austin, TX) LabVIEW Fuzzy System Designer toolkit. This toolkit allows the programmer to create linguistic variables, linguistic terms, membership functions and rule base via a graphical user interface (GUI) (details provided in Supplementary Materials). We used three linguistic variables for the inputs and one linguistic variable for the output. The input linguistic variables were tip size (i.e. radius of the tip), enhancement factor (i.e. the ratio of the tip current to the tip current at infinite distance from the substrate), and setpoint difference (i.e. the difference between the measured enhancement factor and the user-entered enhancement factor at which to stop the SECM tip electrode). The output linguistic variable was step size (i.e. the size of the step to move the SECM tip electrode towards the substrate). The output variable, step size, is directly related to the speed of the approach curve because this process is repeated in a continuous loop with a specified loop duration.

5.3.4 Electrode Fabrication

Details on all electrode fabrication are provided in Supplementary Materials. Briefly, a borosilicate glass capillary (1 mm O.D., 0.5 mm I.D., Sutter Instruments, USA) and 10 mm Pt-wire (0.01 mm, 99.9% Pure, Hard, Goodfellow, Cambridge, England) were rinsed with deionized water and allowed to air dry. A small section of Pt- wire (3 cm) was threaded and centered into the quartz capillary. The capillary-wire assembly was secured to a laser puller (Model P-2000, Sutter Instruments, USA). The UME fabrication procedure required three steps: stretching, sealing, and pulling. To stretch and thin the capillary, a four-line program was run (Heat: 300, Filament: 4, Velocity: 14, Delay:

120, Pull: 0) followed by a single-line break (Heat: 0, Filament: 4, Velocity: 14, Delay: 120, Pull: 0). Without removing the assembly, the sealing step was performed by blocking the slight pulling force (at Pull: 0) with razor blades placed between the bearing and the capillary clamp on each side of the puller. A single line program (Heat: 320, Filament: 4, Velocity: 12, Delay: 120, Pull: 0) was manually run and repeated eight times at intervals of five seconds. To pull the electrodes, the razor blades were removed and the sealing program was allowed to run automatically, with one heating cycle followed by a clean split (0.6 seconds to complete) resulting in two sealed UMEs of approximately equal size. The UMEs were polished on a MicroCloth disk (Beuhler, Canada) with alumina micropolish (0.05 mm, Beuhler, Canada) in a slight side-to-side movement, ensuring no pressure was applied on the tip.

5.3.5 Printing "KU" Slide

The gold "KU" was printed on a glass microscope slide (Fisher Scientific). An acid bath of 10% perchloric acid was used to clean the surfaces of the slides overnight. The gold "KU" was printed with ink made from bright brushing gold (Alfa Aesar) diluted with tetrachloroethylene in a 5:4 ratio (BBG:TCE). The printing was performed by a Sonoplot GIX Microplotter Desktop printer, utilizing piezoelectric dispensing to pump the ink onto the slide. To create the design of the "KU," Sonoplot SonoDraw software was used. Once the "KU" was printed, the ink was fired in a vented box furnace (Barnstead Thermolyne 48000) at 525 °C for an 8 hour dwell following a 1 C/min ramp rate to set the gold.

5.4 Results and Discussion

5.4.1 Control Algorithm

While many control mechanisms have been utilized for motion control (e.g. PID)[281], we utilized a fuzzy logic algorithm because it is highly efficient and an easy-to-implement control strategy. With fuzzy logic, one describes the control strategy qualitatively (as opposed to numerically), and the controller uses a rule base, which is a series of "if . . . then" statements, to determine the output of the controller. To create a fuzzy logic control strategy, one needs to define linguistic variables, linguistic terms, and membership functions for the inputs (tip size, tip current, and setpoint) and

output (tip speed), as well as the rule-based linguistic control strategy. As opposed to Boolean logic where events are in either one set or another, fuzzy logic allows for events to have partial membership in multiple sets[281]. Thus, one single algorithm can be used for any size electrode and under both positive and negative feedback.

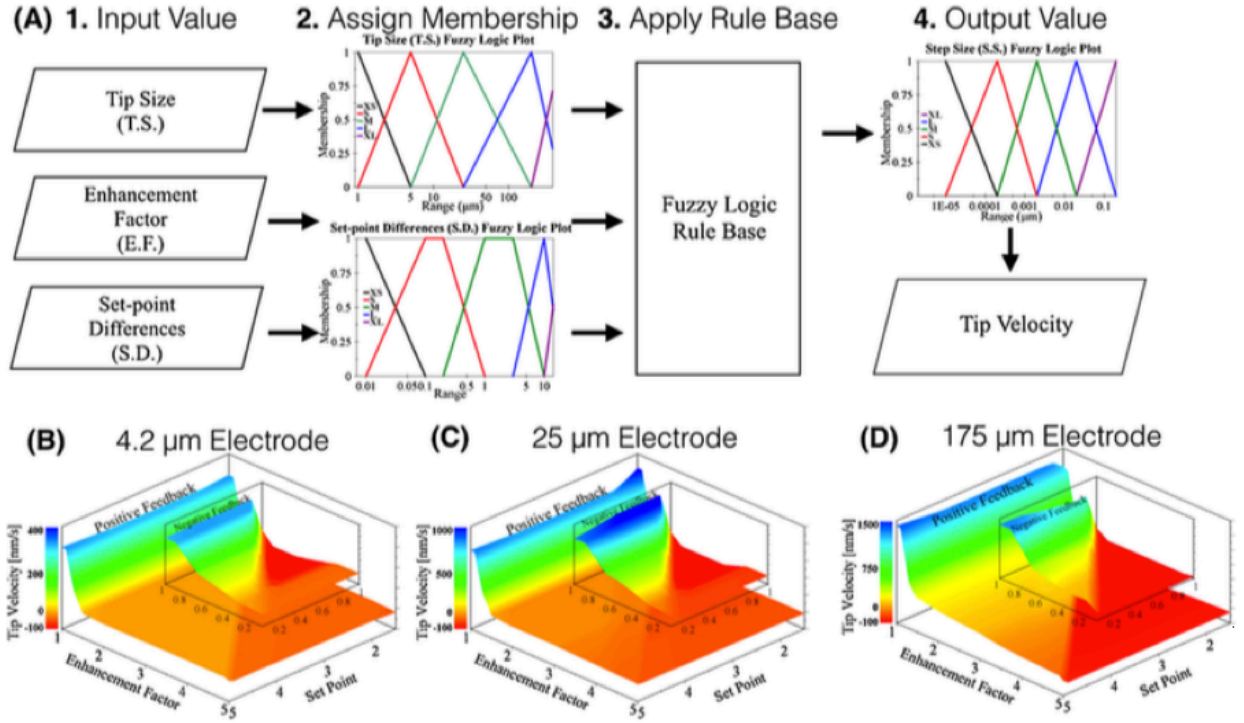

Figure 5.1. (A) SECM fuzzy logic process flow chart detailing the membership functions controlling each input and output parameter (tip size, present enhancement factor (Fig. 5.6), setpoint difference). (B-D) The resulting tip velocity plots for both positive and negative feedback generated from the fuzzy logic algorithm as a function of the enhancement factor and setpoint for three different tip sizes.

Each of the input and output linguistic variables has distinct linguistic terms (e.g., extra-small, small, medium, large, and extra-large). Each of these linguistic terms is defined using membership functions (Fig. 5.1A), which represent the degree of membership that each of the linguistic variables has with its corresponding linguistic terms. For example, from the Tip Size Fuzzy Logic Plot in Fig. 5.1A, a tip size of 10 mm would have a 40% membership in "Medium Tip Size" and a 60% membership in "Small Tip Size."

We chose three inputs for our fuzzy logic control strategy to control the speed of the tip approaching the substrate. The first input variable was tip size, which has five possible memberships, extra-small, small, medium, large, and extra-large. On average, the larger the tip size, the faster

the speed of the approach curves. The second input was enhancement factor, which is defined as the tip current divided by the tip current at infinite distance from the substrate. The enhancement factor linguistic variable has nine possible memberships (Fig. 5.6) covering large and small tip substrate distances for both positive and negative feedback. On average, when the tip/substrate distance is small (i.e., the enhancement factor is large) the speed of the approach is slow, and when the tip/substrate distance is large the speed of the approach is fast. The third linguistic term is setpoint difference, which is defined as the difference in the enhancement factor compared to a desired enhancement factor set by the user. As with the enhancement factor, when the set-point difference is large, the approach speed is fast, when the set-point difference is small, the approach speed is slow, and when the set-point difference is zero the tip stops.

The implementation of the control algorithm is described in Fig. 5.1A. First, the algorithm takes the three input linguistic variables and assigns them membership to one or more linguistic terms (e.g. extra-small, small, medium, large, extra-large) based on the membership functions. Once each of the input linguistic variables is assigned membership, the step size output is determined via the "if . . . then" rule base shown in Table 5.5. The rule base was created via a trial and error method. We found that the best way to stop the tip electrode at the user-entered setpoint was to weight the rules where the set-point difference was extra-small more heavily. We also found that weighting the rules where the tip approaches the slowest more heavily gave us better control of the tip. Thus, rules where the tip size is extra-small, setpoint difference is extra-small, or the enhancement factor is extra-large are weighted more than the other rules.

The final output of the fuzzy logic algorithm gives the velocity of the SECM tip based on the three input variables, as shown by the flow chart in Fig. 1A. Fig. 1B-D show the tip velocity as calculated from our fuzzy logic algorithm under both positive and negative feedback as a function of the enhancement factor and setpoint for three different tip sizes. These three figures illustrate that the tip velocity decreases with (1) decreasing tip size, (2) increasing enhancement factor, and (3) decreasing difference between the setpoint and the enhancement factor. The fuzzy logic algorithm stops the tip when the enhancement factor equals the setpoint and reverses the tip if the enhancement factor exceeds the setpoint.

5.4.2 SECM Approach Curves

To demonstrate how well the fuzzy logic algorithm generates approach curves, Fig. 5.2 compares positive feedback approach curves using the conventional "constant-speed" method with the fuzzy logic algorithm for a 4.2 mm diameter electrode in a 0.5 mM ferrocenemethanol solution (with 0.1 M $NaNO_3$ supporting electrolyte) with a 2mm diameter Pt substrate electrode. Fig. 2A shows the tip current versus tip/substrate distance for the constant-speed approach, the fuzzy logic approach, a simulated approach using COMSOL, and a theory-based approach curve (Eq. (S1)). Both the constant-speed approach curve and the fuzzy logic approach curve fit the simulated and theoretical approach curves very well. We obtained a tip/substrate distance of 700 nm (enhancement factor of 2.8) with the constant-speed method, and by utilizing the fuzzy logic algorithm we obtained a closer tip/substrate distance of 580nm (enhancement factor of 3.5). Fig. 2B shows the tip displacement and tip speed as a function of time for the fuzzy logic approach curve and the constant-speed approach curve. By utilizing the fuzzy logic control algorithm, the user has more control, precision, and adaptability as compared to the conventional constant-speed approach. In these experiments, the fuzzy logic algorithm was able to complete the approach curve ca. 3 times faster because it is able to approach faster at larger tip/substrate distances and automatically slow down and stop once a desired tip/ substrate distance is achieved. In addition to being faster, the fuzzy-logic algorithm can automatically stop the tip electrode at small tip/substrate distances without crashing the tip into the substrate.

We also demonstrate that our fuzzy-logic algorithm can be used for many different SECM modes as described in Supplementary Materials. We are also able to utilize the same fuzzy logic algorithm to obtain negative feedback approach curves as demonstrated in Fig. 5.7a, which shows a 4.2 mm diameter UME reaching a tip/substrate distance of 580 nm under negative feedback conditions. The fuzzy logic algorithm also produced a positive feedback approach curve to an enhancement factor of 10 with a larger 175mm electrode (Fig. 5.9c), typically used for Surface Interrogation SECM. We used our fuzzy logic algorithm to approach surfaces so that substrate generation/tip collection (SG/TC) could be performed both on masked substrates (Fig. 5.10b), and for "tip-to-tip" measurements (Fig. 5.10c). For these SG/TC SECM experiments, we employed the hydrogen evolution reaction on Pt as a model system. We masked a 2 mm diameter Pt substrate with a Teflon

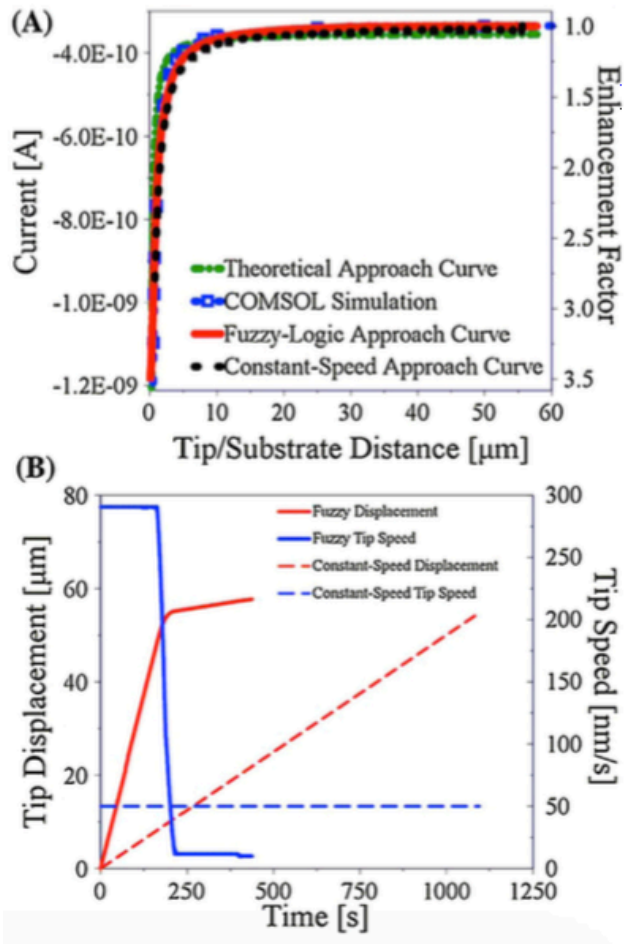

Figure 5.2. (A) SECM approach curves using the fuzzy logic algorithm with a 4.2 mm Pt tip electrode (RG = 10) at +0.4 V vs Ag/AgCl and a 2 mm Pt substrate electrode at +0.05 V vs Ag/AgCl in 0.5 mM FcMeOH along with the corresponding constant- speed approach curve, COMSOL simulation, and theoretical calculation. (B) Tip displacement and tip speed for the fuzzy logic and constant-speed approach curves.

film possessing a 200 mm hole. After approaching a 200 mm Pt tip electrode to the substrate (Fig. 5.10b), we obtained both low- resolution and high-resolution electrochemical reactivity maps (Fig. 5.11a-b) to locate the hole in the Teflon mask. After aligning the tip electrode over the hole in the mask, we performed SG/TC using the FcMeOH/$FcMeOH^+$ redox couple (Fig. 5.11c) followed by a SG/TC experiment where the substrate generation was via the proton reduction reaction and the tip collection was via the hydrogen oxidation reaction (Fig. 5.11d). We also performed analogous SG/TC experiments where both the tip and the substrate were 200 mm Pt electrodes (Fig. 5.12). We also demonstrate that we can use our algorithm to approach a 200 mm Au microelectrode to a 200 mm Pt microelectrode (Fig. 5.10d) to perform surface-interrogation (SI) of adsorbed hydrogen

on the Pt electrode (Fig. 5.13). We are also able to generate electrochemical reactivity maps (Fig. 5.11a-b, 5.12a, 5.13a) and cyclic measurements (Fig. 5.7c, 5.8d, 5.9d) using our custom LabVIEW software after the tip is in close proximity to the substrate.

5.4.3 Automated SECM Tip/Substrate Alignment

We utilized our fuzzy-logic control algorithm, which has the advantage of automatically stopping the electrode at a specified enhancement factor, to create an automated tip/substrate alignment protocol. Our SECM tip/substrate alignment protocol is completely automated and requires no user interaction once the user starts the sequence. In the first step in the alignment protocol, the SECM tip approaches the substrate and automatically stops at a pre-programmed enhancement factor. The protocol then scans the tip electrode in either the x or y direction across the substrate and records the current versus position. Since the current is directly related to the tip/substrate distance, scanning across the surface reveals the substrate tilt. Our algorithm automatically calculates the slope of the regression of the experimental data, and then adjusts the substrate tilt based on the slope by moving the tilt adjustment actuators. The tip electrode is then returned to the original position, and the process repeats until the substrate tilt is removed in both the x and y directions. Fig. 5.3 shows the results for correcting the substrate tilt in both the x direction (Fig. 5.3A) and the y direction (Fig. 5.3B). The algorithm repeated the process seven times to correct the tilt in the x direction and five times to correct the tilt in the y direction.

We also demonstrate how the intelligent tip/substrate alignment protocol can dramatically improve the quality of constant- height SECM images. The automated tilt adjust was performed on a glass slide on which we printed the letters “KU” in gold using an ultrasonic printer (see Supplementary Materials). The tip electrode was a 200 mm Pt tip electrode at +0.4 V vs Ag/AgCl in 0.5 mM FcMeOH. The scans shown in Fig. 5.3 were performed over the glass portion either below or to the left of the “KU.”

Fig. 5.4 shows two constant-height SECM reactivity images; Fig. 5.4A was obtained before we performed the automated tilt correction and Fig. 4B was obtained after we performed the automated tilt correction. In these images we are able to distinguish the conductive gold letters from the insulating glass because open-circuit positive feedback will occur when the tip is over the gold, but negative feedback will occur when the tip is over the glass. In Fig. 5.4A the letters

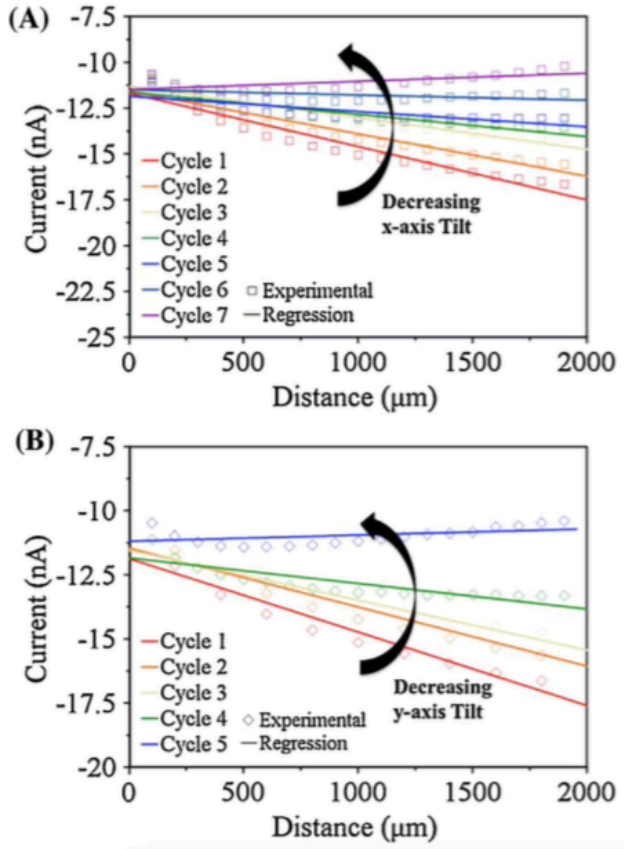

Figure 5.3. Current versus distance plots for our automated SECM tilt correction algorithm, where the SECM tip electrode is scanned across the x-axis (A) and y-axis (B). For each cycle the SECM tip electrode (1) approaches the substrate until a set enhancement factor is reached, (2) scans the SECM tip electrode across the surface, (3) adjusts the tilt of the substrate stage and returns the tip to the original position to repeat the process. The process stops once the slope of the regression line changes sign. Tip/substrate alignment within finer tolerances can be achieved by reducing the tilt adjust step size.

"KU" are barely visible due to the substrate tilt. Near the origin (bottom left hand corner) the bottom of the "K" is visible, but since the sample is tilted away in both the x and y directions (see Fig. 5.3), the image becomes faded far from the origin due to the tip no longer being in the feedback regime. Fig. 5.4B shows the positive feedback image after the substrate tilt algorithm was completed. After our automated tilt adjustment protocol, the full "KU" image is highly visible because the tip/ substrate alignment was dramatically improved.

5.5 Conclusions

We have developed a new control algorithm, which utilizes fuzzy logic, to approach SECM tip electrodes to a surface. The fuzzy logic algorithm automatically varies the speed of the approach,

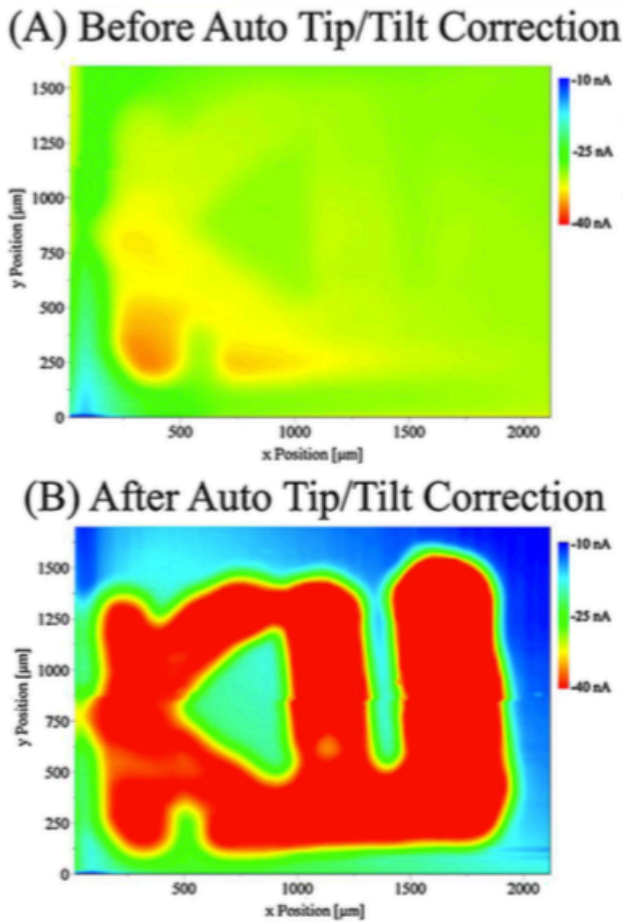

Figure 5.4. SECM positive feedback image of the letters "KU" printed in gold on a glass slide using a 200 mm Pt tip electrode at +0.4 V vs Ag/AgCl in 0.5 mM FcMeOH. (A) Positive feedback image before the automated substrate tilt algorithm was performed. (B) Positive feedback image after the automated substrate tilt algorithm was performed.

and obtains approach curves both faster and with a higher degree of accuracy compared to conventional constant- speed approach curves. With one algorithm, a wide range of tip sizes and approach methods are possible, allowing for more control and precision while substantially reducing the risk of crashing the tip into the substrate. We demonstrate that this algorithm can be used under both positive and negative feedback, and can be used to approach tips of various sizes to large substrates or other SECM tips. The capability of this fuzzy-logic algorithm to automatically stop the SECM tip electrode at a pre- programmed enhancement factor has allowed us to create an automated tip/substrate alignment protocol. This protocol utilizes both the fuzzy logic algorithm and a computer-controlled tilt adjustable stage to automatically align the tip to the substrate with no user interaction. We have demonstrated that this alignment protocol can obtain highly resolved

constant-height SECM images over large areas with ease. We anticipate that this auto-alignment protocol will be highly beneficial for obtaining many types of chemical reactivity images because removing sample tilt will eliminate variations in tip/substrate distances yielding images with higher accuracy.

5.6 Acknowledgements

This work was previously published in Electrochimica Acta:
Barforoush JM, McDonald TD, Desai TA, Widrig D, Bayer C, Brown MK, Cummings LC, Leonard KC. Intelligent Scanning Electrochemical Microscopy Tip and Substrate Control Utilizing Fuzzy Logic. Electrochimica Acta. 2016;190:713-719.

5.7 Supporting Information

5.7.1 Materials and Methods

Chemicals

All solutions were prepared with deionized Milli-Q water, and the chemicals purchased from the following were used as received: ferrocenemethanol (FcMeOH, 97%) from Sigma-Aldrich, sodium nitrate ($NaNO_3$, 99%) from Fisher Scientific, (dimethylaminomethyl) ferrocene (DMAMFc, 98+%) from Alfa Aesar, N,N,N',N'-tetramethyl-p-phenylenediamine (TMPD) hydrochloride from Cayman Chemical Company, and perchloric acid ($HClO_4$, ACS Reagent, ca. 70% solution in water) from Acros Organics.

Electrode Fabrication

Pt Microdisk Electrode Fabrication: Microdisk electrodes of two different tip diameters (ca. 200 μm and ca. 10 μm) were fabricated for the SECM experiments similar to methods previously reported[243,282]. Quartz capillaries (1 mm O.D., 0.3 mm I.D., Sutter Instruments, USA), 200 μm diameter platinum wire (Electron Microscopy Sciences 99.95% Pt wire), borosilicate glass capillaries (1 mm O.D., 0.5 mm I.D., Sutter Instruments, USA), 10 μm diameter platinum wire (0.01 mm, 99.9% Pure, Hard, Goodfellow, Cambridge, England), a laser pipet puller (Model P-2000, Sutter

Instruments, USA), standard razor blades, conductive silver epoxy (Circuit Works, USA), and silver connection wire (30 AWG, Belden, USA) were utilized to manufacture the UMEs. MicroCut 1200 grit silicon carbide grinding paper (P2500, Buehler, Canada), alumina micropolish (1 μm, 0.3 μm, 0.05 μm, Beuhler, Canada), and MicroCloth polishing disks (Beuhler, Canada) were used to polish the tips of the UMEs before experimentation.

200 μm Electrodes: The quartz capillary and 200 μm Pt-wire were rinsed with deionized water and allowed to air dry before assembly. A short (3 cm) section of Pt-wire was threaded and centered in the quartz capillary. The capillary-wire assembly was then centered and secured to the laser pipet puller. A single line program (Heat: 850, Filament: 1, Velocity: 50, Delay: 100, Pull: 225) was run so that the capillary-wire assembly split and sealed into two UMEs of approximately equal size. The UMEs were polished on MicroCut grinding paper to expose the Pt-wire at the tip. A figure eight motion was used in polishing to ensure a flat platinum disk surface. Using the 1 μm and 0.3 μm alumina micropolish and MicroCloth disks, rough patches and scratches on the UME tip were buffed out to leave a smooth, even surface. The final size of the electrode was determined to be a = 175 μm due to slight stretching of the Pt wire during fabrication.

10 μm Electrodes: The general procedure for the 10 μm capillary-wire assembly was similar to the steps outlined for the 100 μm assembly. The borosilicate glass capillary and 10 μm Pt-wire were rinsed with deionized water and allowed to air dry. A small section of Pt-wire (3 cm) was threaded and centered into the quartz capillary. The capillary-wire assembly was secured to the laser puller. The UME fabrication procedure required three steps: stretching, sealing, and pulling. To stretch and thin the capillary, a four-line program was run (Heat: 300, Filament: 4, Velocity: 14, Delay: 120, Pull: 0) followed by a single-line break (Heat: 0, Filament: 4, Velocity: 14, Delay: 120, Pull: 0). Without removing the assembly, the sealing step was performed by blocking the slight pulling force (at Pull: 0) with razor blades placed between the bearing and the capillary clamp on each side of the puller. A single line program (Heat: 320, Filament: 4, Velocity: 12, Delay: 120, Pull: 0) was manually run and repeated eight times at intervals of five seconds. To pull the electrodes, the razor blades were removed and the sealing program was allowed to run automatically, with one heating cycle followed by a clean split (0.6 seconds to complete) resulting in two sealed UMEs of approximately equal size. The UMEs were polished on a MicroCloth disk with 0.05 μm alumina micropolish in a slight side-to-side movement, ensuring no pressure was applied on the tip.

UME Completion: To complete each UME, a conductive epoxy and silver wire were applied to the open end of the capillary. Silver epoxy and hardener were mixed together. This mixture was forced into the open end of the UME through capillary action, carefully tapping the mixture into the tube. A large segment (6 cm) of silver connection wire was straightened by rolling it against a flat surface and epoxy was applied to the end of the wire before inserting into the capillary. The wire was inserted through the epoxy mixture until it met the Pt-wire. A final epoxy application to the end of the capillary ensures the silver wire is sealed into place. The UMEs were allowed to cure at room temperature in a well-ventilated area for 24 hours. Each UME was imaged with a digital compound microscope (Micromaster II Digital Microscope with Phase Contrast, Fisher Scientific, USA). A top view of each UME was generated by suspending the UME on the microscope stage with forceps (Fig. 5.7a, 5.8a, 5.9a). The images were obtained via the microscope's accompanying digital program (Micron) to capture the field of the microscope view. The contrast levels were then adjusted to improve the image clarity.

5.7.2 SECM Instrumentation and Experimentation

A custom SECM was used for these experiments (Fig. 5.14). Components include the following from Newport: 3-axis motion stage (VP-25XL-XYZL), Series 37 tilt stage, piezoelectric nanopositioner (NPXYZ100SG-D), Vision Isostation air table (VIS2436-IG2-125A), faraday cage for air table, XPS Motion Controller/Driver with XPS-DRVP1 driver boards, 2 tilt stage motors (LTA-HS), small L-mount (EQ80-I), larger L-mount (EQ80-E), Cable Management System (CMS), vertical rail and mount for nanopositioner. In addition to these components, the SECM also includes a CH Instruments potentiostat (CHI730E) and an iMac computer running custom designed LabVIEW software to control the instrument. The custom LabVIEW software is capable of performing cyclic voltammetry, chronoamperometry, amperometric i-t, linear approach curves, fuzzy logic-based approach curves and tilt adjustments, and electrochemical reactivity mapping. By inputting parameters (electrode tip size, desired setpoint difference, desired enhancement factor), the fuzzy logic approach software will dictate what speed of approach is appropriate for the system parameters at the given point, adjusting the speed and slowing down gradually as the electrode gap is lessened. For all SECM experiments except surface interrogation, a solution containing 0.5 mM of the redox mediator, FcMeOH or DMAMFc, and 0.1 M of electrolyte was utilized. For surface interrogation,

TMPD was utilized as the redox mediator in a solution of 1 M $HClO_4$.

Fuzzy Logic Algorithm:

The fuzzy logic algorithm was built using National Instrument's LabVIEW Fuzzy System Designer toolkit. This toolkit allows the programmer to create the linguistic variable, linguistic terms, membership functions and rule base via a graphical user interface (GUI). The algorithm had three linguistic variables for the inputs (tip size, enhancement factor, and setpoint difference) and one linguistic variable for the output (step size). The linguistic variables and membership functions were entered in as described in Fig. 1 of the main text. Fig. 5.6 shows the membership function for the Enhancement Factor, which was not included in Fig. 5.1 in the main text to conserve space. Table S1 contains the "if....then" rule base that governs the Fuzzy Logic Algorithm for SECM.

#	Fuzzy Logic Rules	Weight	#	Fuzzy Logic Rules	Weight
1	IF S.D. IS 'XS' AND E.F. IS 'XL' THEN S.S. IS 'XS'	1.0	14	IF E.F. IS 'XS' THEN S.S. IS 'XL'	0.1
2	IF S.D. IS 'XS' AND E.F. IS 'L' THEN S.S. IS 'XS'	1.0	15	IF T.S. IS 'XS' THEN S.S. IS 'XS'	1.0
3	IF S.D. IS 'XS' AND E.F. IS 'M' THEN S.S. IS 'XS'	1.0	16	IF T.S. IS 'S' THEN S.S. IS 'S'	0.2
4	IF S.D. IS 'XS' AND E.F. IS 'S' THEN S.S. IS 'XS'	1.0	17	IF T.S. IS 'M' THEN S.S. IS 'M'	0.1
5	IF S.D. IS 'XS' AND E.F. IS 'XS' THEN S.S. IS 'XS'	1.0	18	IF T.S. IS 'L' THEN S.S. IS 'L'	0.1
6	IF S.D. IS 'S' THEN IS 'S'	0.1	19	IF T.S. IS 'XL' THEN S.S. IS 'L'	0.1
7	IF S.D. IS 'M' THEN S.S. IS 'M'	0.1	20	IF T.S. IS 'M' AND S.D. IS 'XS' THEN S.S. IS 'XS'	1.0
8	IF S.D. IS 'L' THEN S.S. IS 'L'	0.1	21	IF T.S. IS 'L' AND S.D. IS 'XS' THEN S.S. IS 'XS'	1.0
9	IF S.D. IS 'XL' THEN S.S. IS 'XL'	0.1	22	IF T.S. IS 'XL' AND S.D. IS 'XS' THEN S.S. IS 'XS'	1.0
10	IF E.F. IS 'XL' THEN S.S. IS 'XS'	1.0	23	IF E.F. IS '-S' THEN S.S. IS 'L'	0.1
11	IF E.F. IS 'L' THEN S.S. IS 'S'	0.1	24	IF E.F. IS '-M' THEN S.S. IS 'M'	0.1
12	IF E.F. IS 'M' THEN S.S. IS 'M'	0.1	25	IF E.F. IS '-L' THEN S.S. IS 'S'	0.1
13	IF E.F. IS 'S' THEN S.S. IS 'L'	0.1	26	IF E.F. IS '-XL' THEN S.S. IS 'XS'	1.0

Figure 5.5. Fuzzy Logic Rule Table listing all of the rules in the Fuzzy Logic Control Algorithm and the corresponding weights. Abbreviations: S.D. – Setpoint Difference, E.F. – Enhancement Factor, S.S. – Step Size, T.S. – Tip Size.

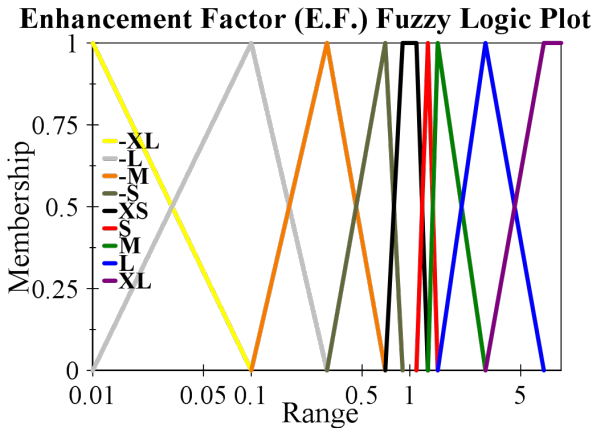

Figure 5.6. Enhancement Factor Membership Function, a supplement to Fig. 5.1 in the main text.

Positive Feedback/Negative Feedback:

For positive feedback mode, the SECM tip electrode was positioned over a conductive portion of the substrate. Starting at a distance sufficient to measure current in the absence of any appreciable feedback effects, a potential of 0.37 V vs. Ag/AgCl was applied to the tip and a potential of 0.05 V vs. Ag/AgCl was applied to the substrate electrode for solutions containing FcMeOH as the redox mediator, or a potential of 0.5 V vs. Ag/AgCl was applied to the tip and a potential of 0.2 V vs. Ag/AgCl was applied to the substrate for solutions containing DMAMFc as the redox mediator, or a potential of 0.85 vs. Ag/AgCl was applied to the tip and a potential of 0.3 V vs. Ag/AgCl was applied to the substrate for solutions containing TMPD as the redox mediator, and the tip was approached towards the substrate until an enhancement factor of at least 2.0 was reached. For negative feedback mode, the SECM tip electrode was positioned over an insulating portion of the substrate. The tip was approached to the substrate in the same manner as in positive feedback except the approach was stopped at an enhancement factor of at most 0.4. Fig. 2A in the main text includes a Theoretical Approach Curve generated from Equation 5.1[282]. Equation 5.1 is applicable to ultramicroelectrodes with RG = 10.

$$\frac{i_t}{i_{t,\infty}} = 0.7449932 + \frac{0.7582943}{D} + 0.2353042e^{\frac{-1.683087}{D}} \tag{5.1}$$

Where i_t is the SECM tip current, $i_{t,\infty}$ is the SECM tip current at infinite distance from the substrate, and D is the distance between the SECM tip and substrate.

Substrate Generation/Tip Collection:

For Substrate Generation/Tip Collection (SG/TC) experiments, pH 7 0.1 M phosphate buffer solution (PBS) with 0.5 mM redox mediator was utilized to allow for SG/TC of the redox couple and H^+/H_2 with the same solution. The redox mediator for the masked experiment was FcMeOH, and the redox mediator for the tip-to-tip experiment was DMAMFc.

Masked: The masked substrate was prepared by stretching a piece of Teflon tape in longitudinal and latitudinal directions and poking a 200 μm diameter hole before firmly pressing onto the surface of 2 mm Pt electrode such that the hole is exposing a 200 μm diameter portion of the Pt. The 200 μm Pt SECM tip electrode was approached to the substrate utilizing negative feedback, and

a low-resolution map was performed to determine the location of the hole in the mask. Then, a high-resolution map was performed to obtain a more detailed perspective of the exposed Pt. The mapping was performed by scanning the SECM tip across the substrate while applying a potential of 0.37 V vs. Ag/AgCl to the tip and a potential of 0.05 V vs. Ag/AgCl to the substrate, exploiting the redox reaction of FcMeOH/$FcMeOH^+$. Utilizing the relative coordinates of the hole in the high-resolution map, the tip was centered over the exposed Pt. For SG/TC of FcMeOH/$FcMeOH^+$, the tip was held at 0.05 V vs. Ag/AgCl while the substrate was swept from 0.05 to 0.37 V vs. Ag/AgCl at 1 mV/s. For SG/TC of H^+/H_2, the tip was held at 0.1 V vs. Ag/AgCl while the substrate was swept from -0.5 to -0.7 V vs. Ag/AgCl at 1 mV/s.

Tip-to-Tip: For Tip-to-Tip, the 200 μm Pt SECM tip electrode was positioned over the 200 μm Pt substrate electrode, and the tip was approached to the substrate utilizing negative feedback or positive feedback depending on whether the tip was positioned over the glass or the Pt of the 200 μm Pt substrate electrode. Mapping was performed by scanning the SECM tip across the substrate electrode while applying a potential of 0.5 V vs. Ag/AgCl to the tip and a potential of 0.2 V vs. Ag/AgCl to the substrate, exploiting the redox reaction of DMAMFc. Utilizing the relative coordinates of the Pt substrate electrode in the map, the tip was centered over the substrate. For SG/TC of DMAMFc/$DMAMFc^+$, the tip was held at 0.2 V vs. Ag/AgCl while the substrate was swept from 0.2 to 0.5 V vs. Ag/AgCl at 1 mV/s. For SG/TC of H^+/H_2, the tip was held at 0.1 V vs. Ag/AgCl while the substrate was swept from -0.4 to -0.8 V vs. Ag/AgCl.

Surface Interrogation:

Surface Interrogation (SI) was performed in the tip-to-tip configuration described under the Substrate Generation/Tip Collection section with a 200 μm Au electrode as the SECM tip and a 200 μm Pt electrode as the substrate electrode. After the approach, mapping was performed by scanning the SECM tip across the substrate electrode while applying a potential of 0.85 V vs. Ag/AgCl to the tip and a potential of 0.3 V vs. Ag/AgCl to the substrate, exploiting the redox reaction of TMPD/$TMPD^+$. Utilizing the relative coordinates of the Pt substrate electrode in the map, the tip was centered over the substrate. In all SI experiments, the potential of the tip was swept from 0.6 to 0.85 V vs. Ag/AgCl at 0.5 mV/s. For the negative feedback linear sweep voltammogram (LSV), the substrate electrode remained at open circuit potential (OCP) throughout the experiment. For

the positive feedback LSV, the substrate electrode remained at 0.3 V vs. Ag/AgCl throughout the experiment. For the SI LSVs, the substrate was scanned from 0.22 to -0.18 V vs. Ag/AgCl at 2 mV/s to acquire H_{ads} before sweeping the potential of the tip electrode. A delay of 20 s was utilized for the Short Delay SI LSV, and a delay of 200 s was utilized for the Long Delay SI LSV.

5.7.3 COMSOL Multiphysics Simulations

In order to analyze the SECM approach curves and cyclic voltammograms, COMSOL Multiphysics simulation software was used to fit the experimental results. A two-dimensional axial symmetric geometry of the SECM tip electrode and substrate counter electrode system with electrolyte solution was constructed for conducting these simulations. A mesh was then assigned to this geometry, concentrating calculations on and around the surface reaction sites. Once the geometry and mesh were complete, the physics packages were loaded, including Transport of Dilute Species and Electroanalysis. The Transport of Dilute Species physics solves the reactive species concentrations by means of the equations from Fick's laws of diffusion. Coupled with the species transport is the Electroanalysis physics package, which incorporates the Butler-Volmer equation of electrochemical reaction kinetics. Since the concentrations from the transport physics are coupled with the concentrations in the Butler-Volmer equations, these equations must be solved simultaneously by numerical methods. All SECM simulations were performed in the stationary mode, and all cyclic voltammetry measurements were in the time-dependent mode. For the simulations used in this manuscript, the diffusion coefficient of both the oxidized and reduced forms of FcMeOH were taken to be 7.1 x 10^{-6} cm^2 s^{-1}, and E^0 for the oxidation of FcMeOH was taken to be 0.218 V vs Ag/AgCl. The kinetic rate constant, k^0, was taken to be 0.20 cm s^{-1}.

5.7.4 Supplementary Results and Discussion

Positive Feedback/Negative Feedback:

Fig. 5.7 shows an optical image of the 4.2 μm SECM Pt tip electrode and the experimental and COMSOL simulated results of a negative feedback approach and positive feedback cyclic voltammograms (CVs). The positive feedback approach curves and tip displacement/tip speed plots for the same system are presented in Fig. 5.2 in the main text. All experiments were performed

in aqueous 0.5 mM FcMeOH with 0.1 M $NaNO_3$. For both the positive feedback and negative feedback approach curves, the 4.2 μm Pt tip electrode was held at +0.4 V vs Ag/AgCl. For the positive feedback CVs, the 2 mm Pt substrate electrode was held at +0.05 V vs Ag/AgCl. Fig. 5.8 and 5.9 contain the analogous data sets for 6.2 μm and 175 μm diameter SECM Pt tip electrodes, respectively.

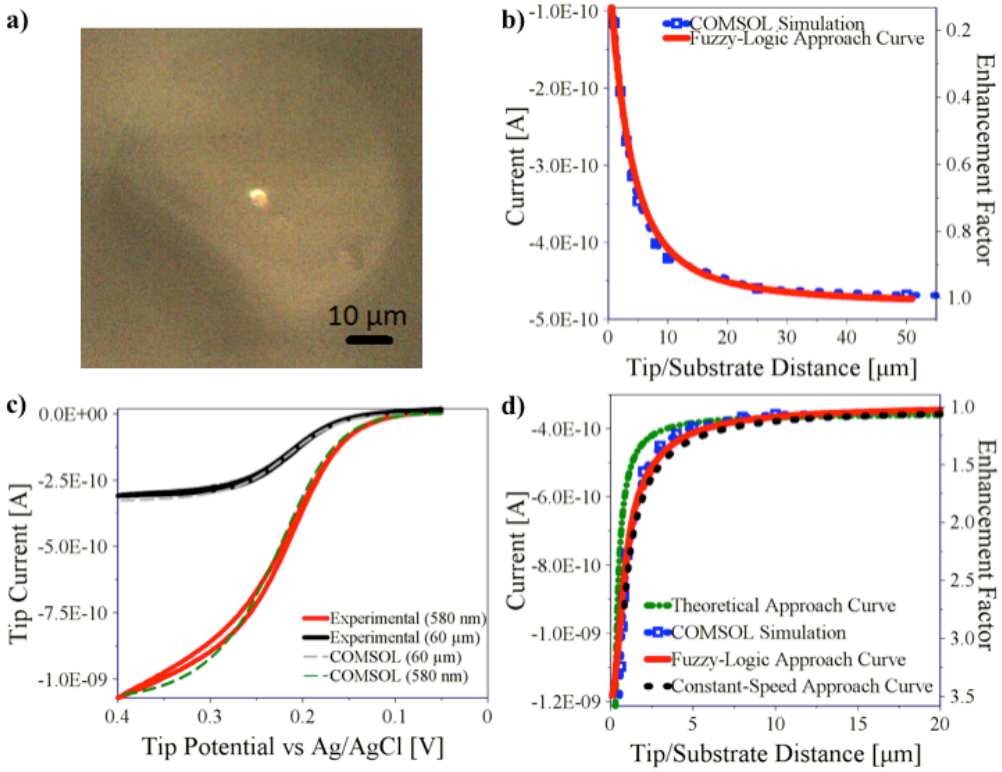

Figure 5.7. Supplementary figures for experiments with the 4.2 μm diameter SECM electrode tip. a) Optical microscope image of 4.2 μm diameter SECM electrode tip. b) Negative feedback SECM approach curve using the fuzzy logic algorithm with a 4.2 μm Pt tip electrode at 0.4 V vs Ag/AgCl in 0.5 mM FcMeOH and glass substrate along with the corresponding COMSOL simulation. c) Cyclic voltammograms showing both the experimental data and COMSOL simulations for FcMeOH oxidation for the 4.2 μm Pt UME at tip/substrate distances of 60 μm and 580 nm under positive feedback. d) Positive feedback SECM approach curve (from Fig. 5.2A) zoomed to 20 μm.

Approach curves from the remaining SECM experiments performed are shown in Fig. 5.10. As expected, a negative feedback response occurred when the SECM tip electrode was over an insulating portion of the substrate, and a positive feedback response occurred when the SECM tip electrode was over a conducting portion of the substrate. Some fluctuations in current were observed when the SECM tip electrode was not yet within a distance where feedback could be observed. These fluctuations in current could be due to some form of convective effect from the

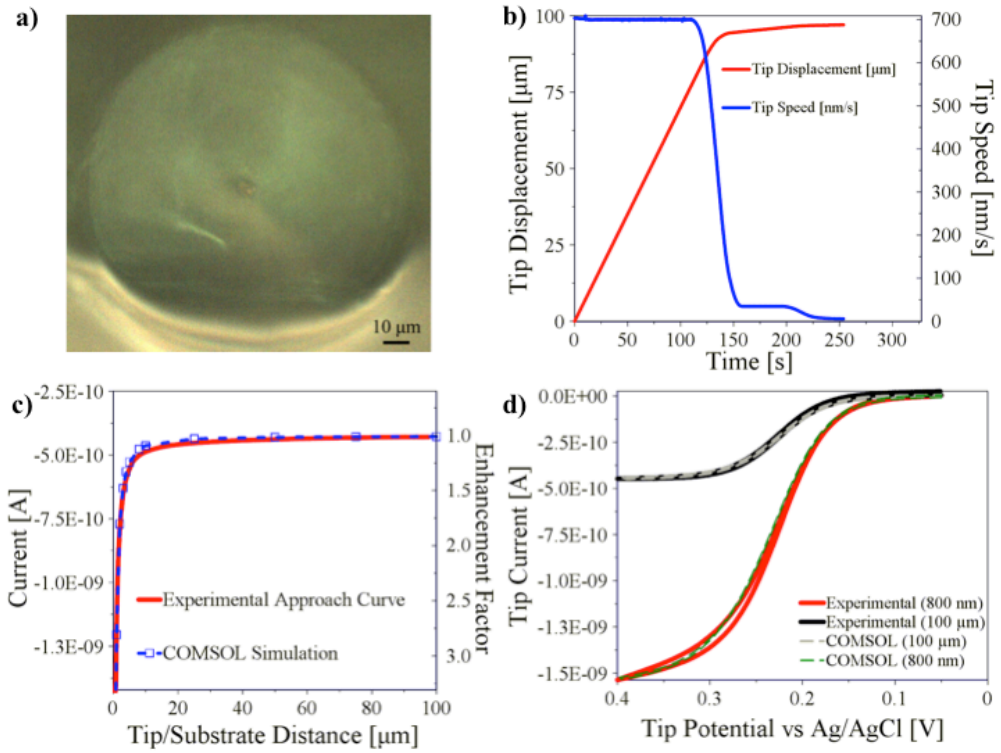

Figure 5.8. Supplementary figures for experiments with the 6.2 μm diameter SECM electrode tip. a) Optical microscope image of 6.2 μm diameter SECM electrode tip. b) Tip displacement and tip speed for the fuzzy logic approach curve. c) SECM approach curve using the fuzzy logic algorithm with a 6.2 μm Pt tip electrode at 0.4 V vs Ag/AgCl and a 2 mm Pt substrate electrode at 0.05 V vs. Ag/AgCl in 0.5 mM FcMeOH along with the corresponding COMSOL simulation. d) Cyclic voltammograms showing both the experimental data and COMSOL simulations for FcMeOH oxidation for the 6.2 μm Pt UME at tip/substrate distances of 100 μm and 800 nm under positive feedback.

electrode moving through the fluid.

Substrate Generation/Tip Collection:

Masked: After the fuzzy logic algorithm is used to approach the tip towards the substrate (Fig. 5.10b), the next step in obtaining a SG/TC experiment is to perform a constant-height SECM map to position the tip electrode over the hole in Teflon mask. The low-resolution map (Fig. 5.11a) spanned an area much larger than the hole in the Teflon mask. This course mapping revealed the location of the hole, as well as the topography of the Teflon surrounding the hole, so that a high-resolution map could be centered on the exposed electrode, greatly reducing the mapping time. The high-resolution map (Fig. 5.11b) shows that the hole is elongated with a maximum length of ca. 200 μm and a minimum length of ca. 100 μm. With the relative coordinates from

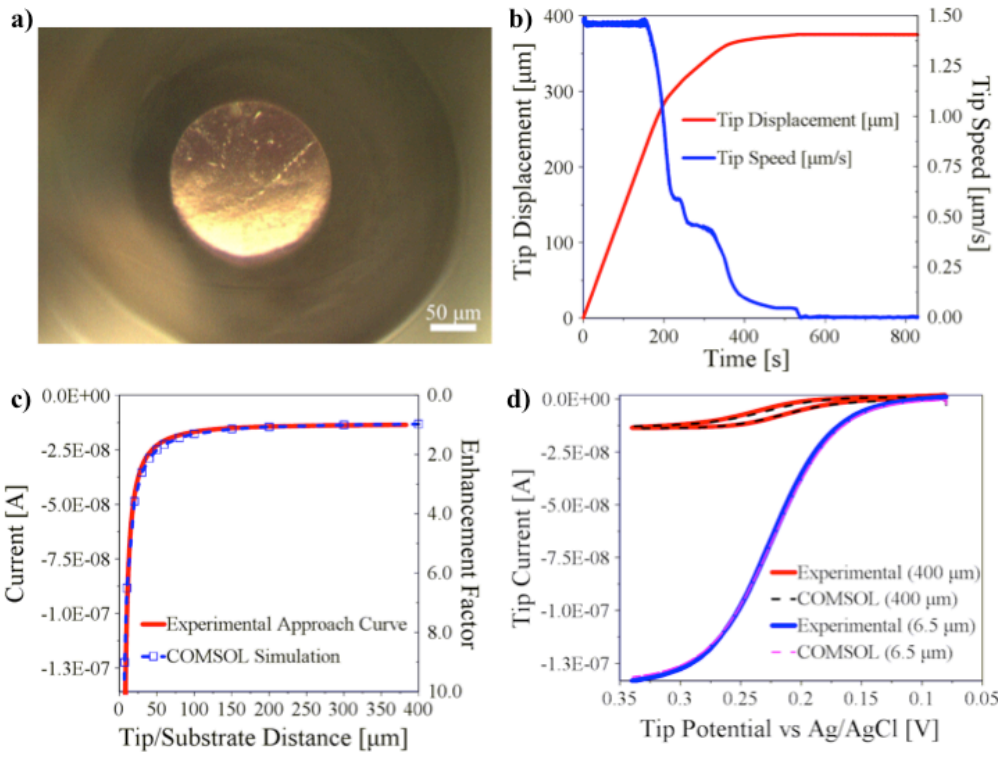

Figure 5.9. Supplementary figures for experiments with the 175 μm diameter SECM electrode tip. a) Optical microscope images of the 175 μm diameter SECM electrode tip. b) Tip displacement and tip speed for the fuzzy logic approach curve. c) SECM approach curve using the fuzzy logic algorithm with the 175 μm Pt tip electrode at +0.4 V vs Ag/AgCl and a 2 mm Pt substrate electrode at +0.05 V vs Ag/AgCl in 0.5 mM FcMeOH along with the corresponding COMSOL simulation d) Cyclic voltammogram and corresponding COMSOL simulation at tip/substrate distances of 400 μm and 6.5 μm.

the high-resolution map, the SECM tip was centered over the exposed portion of the substrate electrode and SG/TC was performed with FcMeOH/FcMeOH$^+$. Performing SG/TC with a redox couple, such as FcMeOH/FcMeOH$^+$, provides a good standard for comparison because SG/TC will be most successful with a simple outer sphere, one-electron transfer reaction. Thus, maximum collection efficiency (peak tip current/peak substrate current) for a given electrode alignment can be obtained from the results of SG/TC with FcMeOH/FcMeOH$^+$. Based on Fig. 5.11c, the maximum collection efficiency was 87%. Fig. 5.11d shows SG/TC of H^+/H_2, corrected for resistance and capacitance, with 79% tip collection. When scaled to the maximum collection efficiency, 91% of the H2 generated by the substrate was collected with the tip.

Tip-to-Tip: Again, after the fuzzy logic algorithm is used to approach the tip towards the substrate (Fig. 5.10c), the next step is to perform a constant-height SECM map to determine the position of the tip. The map in Fig. 5.12a shows high current concentrated in a circular area with ca.

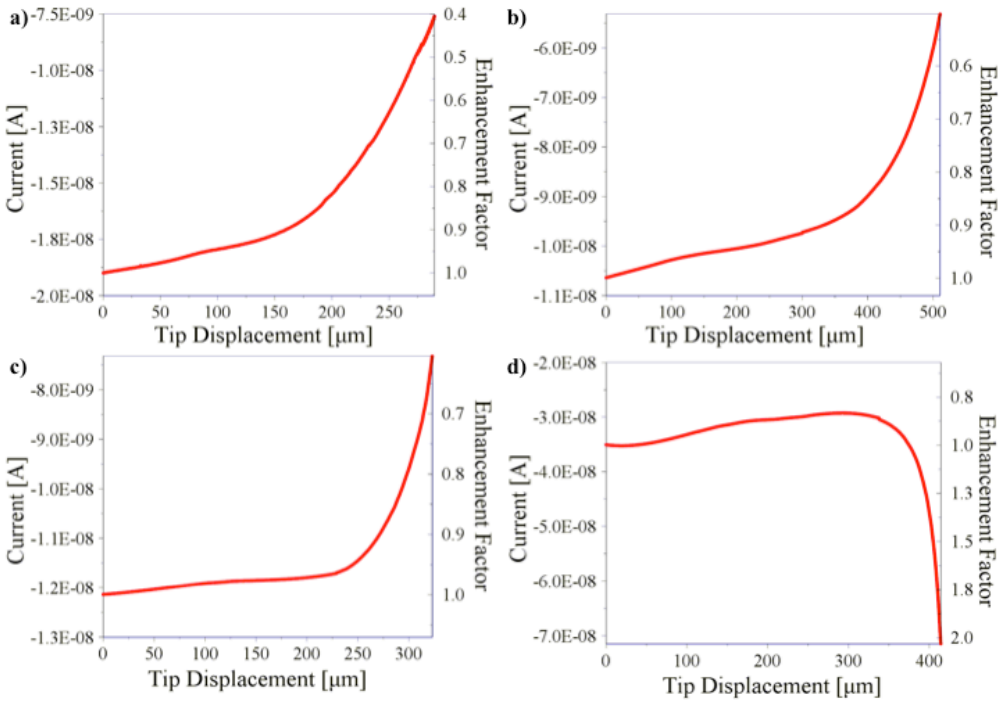

Figure 5.10. Examples of positive and negative feedback approach curves for Imaging, SG/TC and SI-SECM. a) Initial NF approach curve for tip/tilt adjustments for SECM imaging of KU slide (200 μm Pt tip electrode approaching towards a glass substrate in 0.5 mM FcMeOH). b) NF Approach curve for SC/TC SECM experiments with a 200 μm Pt SECM tip electrode approaching towards a Teflon-masked 2 mm diameter Pt substrate. c) NF Approach curve for SG/TC SECM experiments with 200 μm Pt substrate and 200 μm Pt SECM tip electrode in Tip-to-Tip configuration. d) PF Approach curve for SI SECM experiments with 200 μm Pt substrate and 200 μm Au SECM tip electrode in Tip-to-Tip configuration.

100 μm diameter and low current everywhere else, as expected. The relative coordinates from this map were utilized to center the SECM tip electrode over the substrate electrode to perform SG/TC. Collection efficiency of the SG/TC of FcMeOH/FcMeOH$^+$ was taken as the maximum collection efficiency as explained in the Masked section. Fig. 5.12b shows SG/TC of FcMeOH/FcMeOH$^+$, giving a maximum collection efficiency of 93%. Fig. 5.12c shows SG/TC of H^+/H_2, corrected for resistance and capacitance, with a tip collection of 71%, 76% when scaled to the maximum collection efficiency.

Surface Interrogation:

As with the Tip-to-Tip SG/TC experiments, in order to perform SI-SECM, we used the fuzzy logic control algorithm to approach the tip to the substrate (Fig. 5.10d) and then generated a constant-height SECM reactivity map. Fig. 5.13a shows the map, generated with the TMPD/TMPD$^+$

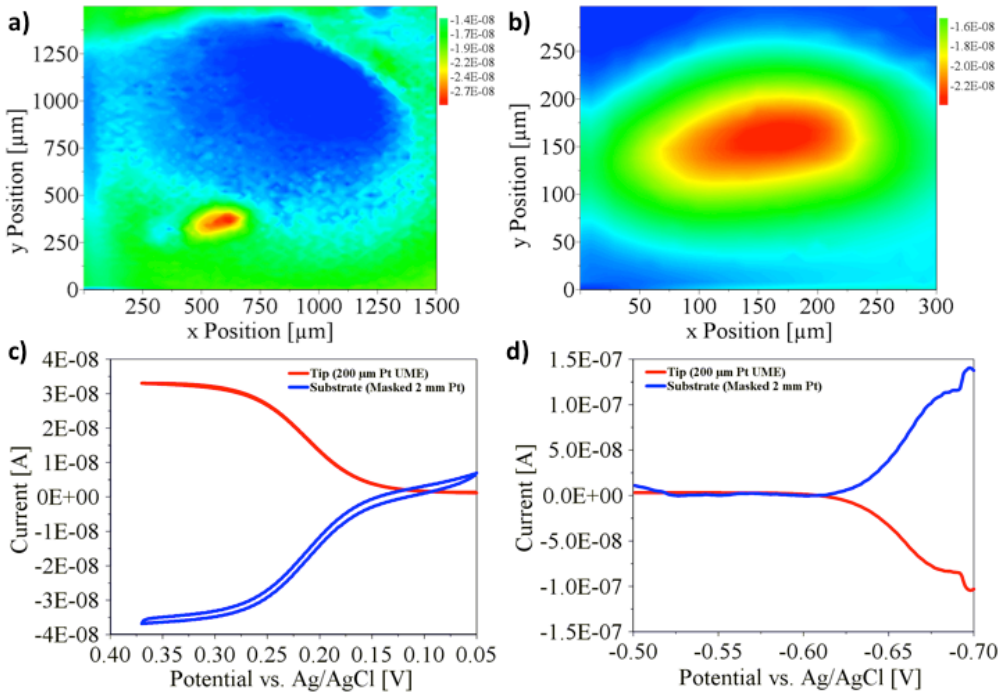

Figure 5.11. Experiments for Masked SG/TC performed in 0.5 mM FcMeOH 0.1 M PBS. a) Low resolution map of the hole in the Teflon mask, generated with the FcMeOH/FcMeOH$^+$ redox couple. b) High resolution map of the hole in the Teflon Mask, generated with the FcMeOH/FcMeOH$^+$ redox couple. c) SG/TC of FcMeOH/FcMeOH$^+$ with a collection efficiency of 87%. d) SG/TC of the H^+/H_2 with 79% tip collection of hydrogen generated by the substrate.

redox couple, utilized to position the 200 μm Au SECM tip electrode over the 200 μm Pt substrate electrode. As expected, the negative feedback (NF) linear sweep voltammogram (LSV, Fig. 5.13b) was nearly a flat line, the positive feedback (PF) LSV (Fig. 5.13b) was an elongated reduction wave. The SI experiment (Fig. 5.13b) showed a reduction wave initially when the TMPD$^+$ was titrating the H_{ads} on the Pt surface, returning to a flat line in the latter portion of the scan when all of the H_{ads} was consumed. From Fig. 5.13b, it can be seen that a shorter delay time causes a longer positive feedback response in the SI LSV, which corresponds to a higher concentration of H_{ads} on the substrate at the initiation of the SI LSV.

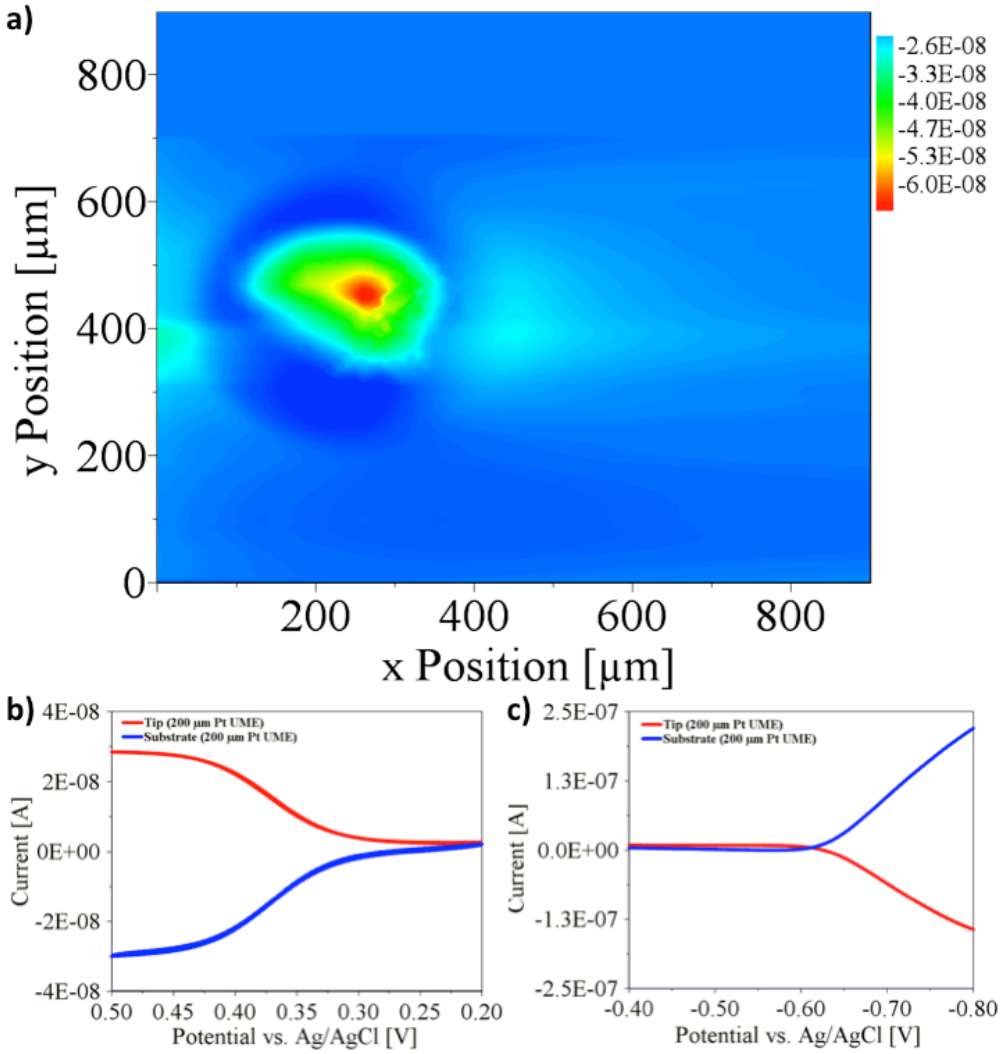

Figure 5.12. Experiments for Tip-to-Tip SG/TC performed in 0.5 mM DMAMFc 0.1 M PBS. a) Map of the 200 μm Pt substrate, generated with the DMAMFc/DMAMFc$^+$ redox couple. b) SG/TC of DMAMFc/DMAMFc$^+$ with a collection efficiency of 93%. d) SG/TC of the H^+/H_2 with 76% tip collection of hydrogen generated by the substrate.

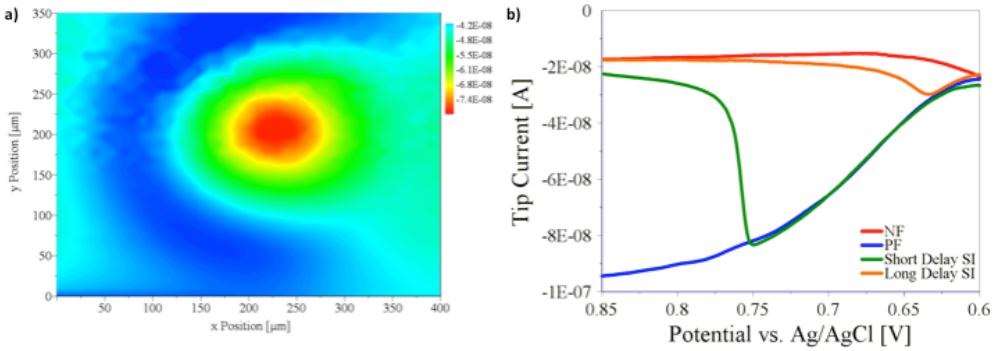

Figure 5.13. Experiments for Surface Interrogation performed in 0.5 mM TMPD 1 M $HClO_4$. a) Map of the 200 μm Pt substrate, generated with the TMPD/TMPD$^+$ redox couple. b) LSVs showing NF, PF, SI with a Short Delay, and SI with a Long Delay.

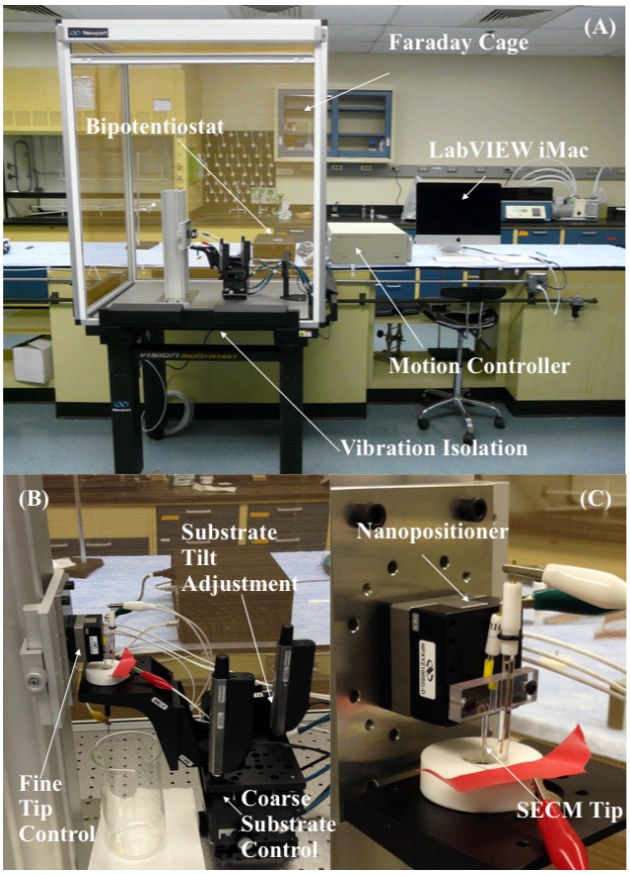

Figure 5.14. (A) Custom-made Scanning Electrochemical Microscope (SECM); (B) Newport multi-axis motion controller stages; (C) piezoelectric nanopositioner for SECM electrode tip.

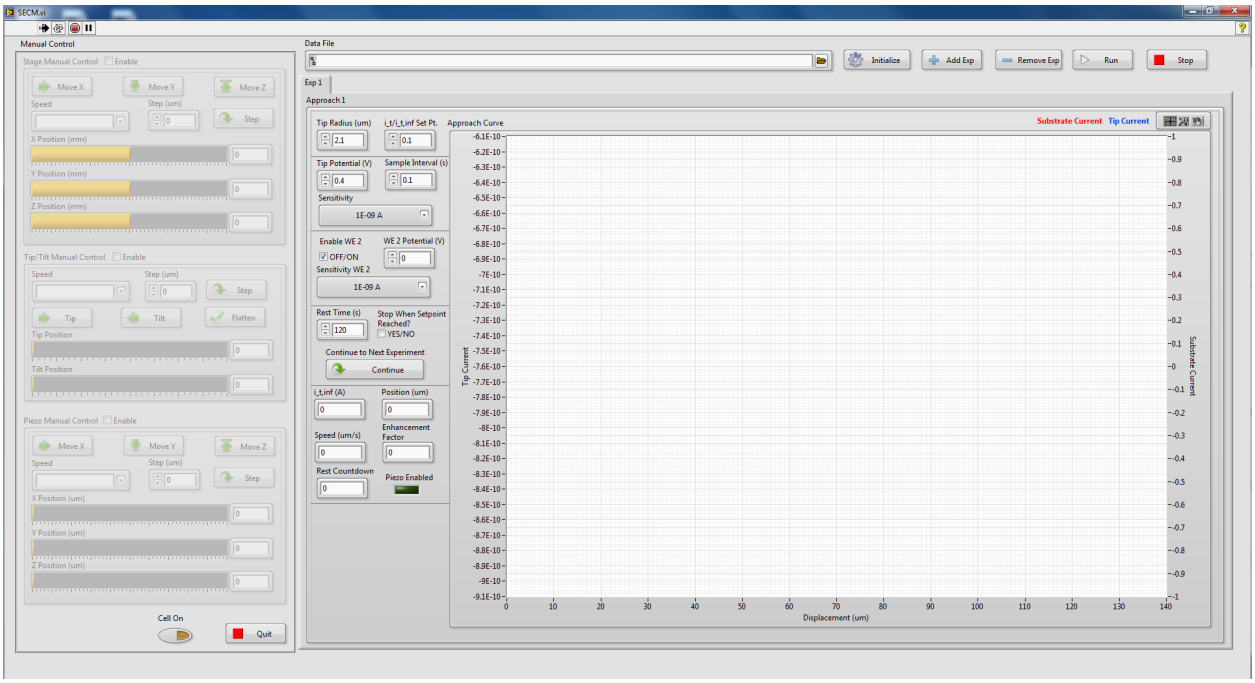

Figure 5.15. Custom Scanning Electrochemical Microscopy (SECM) Labview user interface. User inputs set for a Positive Feedback Approach Curve with a 4.2 μm diameter Pt SECM tip in 0.5 mM FcMeOH.

Chapter 6

Dual-pH Water Splitting

6.1 Abstract

Here we report a system which can perform water splitting where the hydrogen evolution reaction (HER) and oxygen evolution reaction (OER) occur at different pH values. This is enabled by the use of a neutralized Nafion membrane which allows for cations to cross the membrane and promote ionic conductivity and allow for different pHs to be on either side of the membrane. We show that this device can split water with a Pt HER catalysts at pH 7 and a $Ni_{0.8}$:$Fe_{0.2}$ oxide OER catalysts at pH 14 with an initial cell potential of 1.1 V. We also have shown the dual pH system can enable non-precious metal catalysts to split water at 1.6 V for a sustained period of 24 hours.

6.2 Introduction

Water electrolysis has been studied for over 100 years as a means to create renewable fuels and chemicals. Water electrolysis comprises two half-reactions—the hydrogen evolution reaction (HER) and the oxygen evolution reaction (OER)—which, when operated simultaneously, splits water into its elemental components, H_2 and O_2. The efficiency of conventional water electrolysis is inherently limited by the fact that acidic media is preferred for the HER, while alkaline media is preferred for the OER. This is a result of both kinetic and thermodynamic limitations. For example, in acidic media, hydrogen is formed via the two electron reduction of two protons (E^0 = 0.0 V vs SHE), while in neutral or basic media hydrogen is formed via the two electron reduction of water (E^0 =

-0.83 V vs SHE). Conversely, in basic media oxygen is evolved by the four electron oxidation of four OH^- ions ($E^0 = +0.40$ V vs SHE), while water oxidation produces oxygen in neutral or acidic media ($E^0 = +1.23$ V vs SHE). Moreover, the kinetics of the hydrogen evolution reaction have been shown to be two orders of magnitude slower in alkaline electrolyte (pH = 13) compared to acidic electrolyte (pH = 0).[283–285].

In addition to the effect of operating pH on the thermodynamics and kinetics of the water splitting reactions, pH also dictates the types of catalysts that can be utilized. For the HER, operating in acidic media typically requires platinum catalysts for long term stability, however, MoS_2 catalysts have recently been shown to be effective in acidic environments on the lab scale.[286,287] In neutral media, Ni-based catalysts, as well as transition metal dichalcogenides (TMDs), are stable and have similar activity to precious metal HER catalysts.[49,288–290] For the OER, high activity is also attainable in acidic electrolyte, however, platinum group metals (e.g., Ir, Ru) are required to avoid catalyst degradation during operation.[54,56,291] Alkaline electrolytes allow for the utilization of various oxides of nickel and iron, specifically nickel-iron layered double hydroxides (LDHs), which have far exceeded the activity of their precious metal counterparts.[62,65,292,293] Thus, a water splitting system able to operate with HER and OER catalysts in two different pH environments simultaneously, would provide significant advances in water electrolysis by reducing the total water splitting overpotential and enabling the use of new combinations of HER and OER catalysts in a water splitting cell.

Commercial water splitting devices are based on either alkaline or proton exchange membrane (PEM) technologies, which only operate in a single pH environment. However, the chlor-alkali process (for producing chlorine and NaOH) utilizes membrane electrolysis in which a cation exchange membrane is used, and the pH of the medium is different on the cathode and anode sides of the membrane. Inspired by this technology, we set out to determine the feasibility and advantages of performing water splitting where the OER and HER occur at different pHs using a cation exchange membrane.

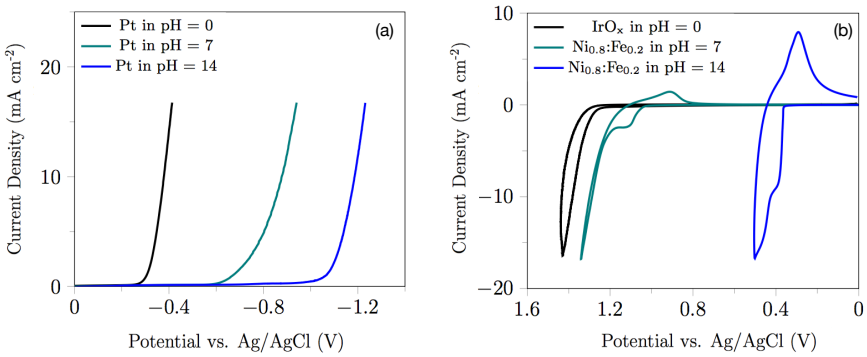

Figure 6.1. Cyclic voltammetry showing the onset potential for the HER on a Pt disk electrode (a) and OER on IrOx and $Ni_{0.8}$:$Fe_{0.2}$ oxide on FTO glass electrode (b) in pH 0 (black, 0.3 M H_3PO_4), pH 7 (teal, 1 M potassium phosphate buffer (KBS)), and pH 14 (blue, 1 M KOH) at a scan rate of 10 mV s^{-1}.

6.3 Effect of pH on the Water Splitting Reactions

To demonstrate how the onset potentials change for the HER, we performed voltammetry on a Pt electrode in pH 14, pH 7, and pH 0 media (Fig. 6.1a). Here, the utility of performing the HER in acidic media is obvious. The onset potential in acidic media is very near the thermodynamic potential for proton reduction (-0.197 V vs Ag/AgCl), while the onset shifts more negative in higher pH media. The opposite effect is observed for the OER. Here, the onset potential in basic media is a few hundred millivolts over the thermodynamic potential for OH^- oxidation (+0.20 vs. Ag/AgCl) and the onset shifts more positive with decreasing pH. Ideally, from a cell potential point of view, one would like perform the HER in strong acid and the OER in strong base. However, the strong acid will protonate the cation exchange membrane and there are safety concerns due to the exothermic reactions that occur from the mixing of strong acids and bases. An alternative, but still effective method would be to perform the OER in strong base and the HER in neutral pH. Based on the data shown in Figure 6.1, a basic/neutral dual-pH water splitting system should initially split water ca. 400 mV lower than in pure alkaline media (due to the lower HER potential afforded in pH 7 compared to pH 14), and ca. 800 mV lower than in pH 7 media (due to the lower OER potential afforded in pH 14 compared to pH 7), and ca. 400 mV lower than in pure acidic media (due to the differences in both the HER and OER).

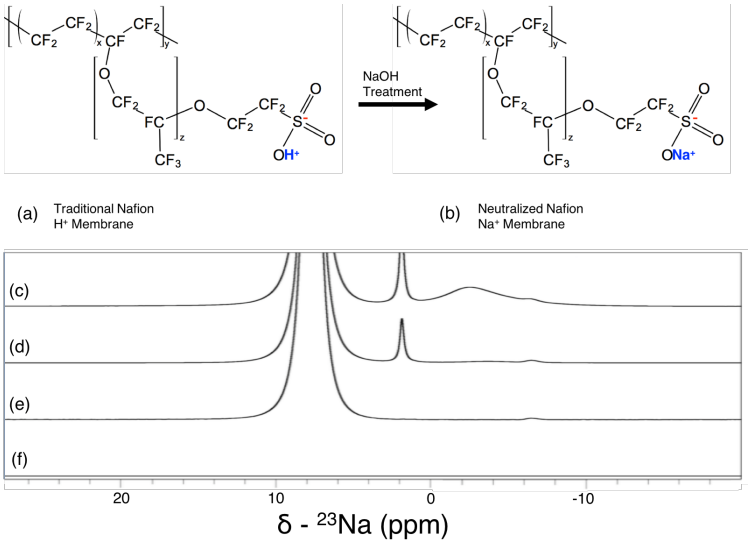

Figure 6.2. Schematic of the standard Nafion polymer (a) and the Na^+ neutralized Nafion membrane (b). 1D ^{23}Na magic angle spinning (MAS) nuclear magnetic resonance (NMR) spectra of a Na^+-neutralized Nafion 117 membrane copacked with NaCl/KBR mixture (c), standard Nafion 117 membrane copacked with NaCl/KBr (d), NaCl/KBr mixture (e), and empty rotor (f).

6.4 Neutralization of the Nafion 117 Membrane

The cation exchange membranes that we utilized were Na^+ and K^+-neutralized Nafion 117 membranes. Here the protons on the membrane (shown in blue in Figure 6.2a) are substituted with either Na^+ or K^+ ions (shown in blue in Figure 6.2b) by heating in 3 M NaOH or KOH at 100 °C. 1D ^{23}Na MAS NMR spectra show an additional peak at ca. -3 ppm (Fig. 6.2c) showing that the Na^+ ions are strongly bound to the sulfonate group on the Nafion membrane, and the total percentage of Na^+-neutralized sites is ca. 86.4% ± 9.8% (details provided in supporting information).

6.5 Dual-pH Water Splitting Results and Discussion

Once the membrane was converted to the neutralized form, we performed voltammetry using Pt as the electrode for the HER and $Ni_{0.8}$:$Fe_{0.2}$ oxide as the electrode for the OER in a two-electrode system for overall water splitting (Fig. 6.3). Consistent with our three-electrode experiments, we observed an onset for water splitting at 1.9 V for pH 7, 1.5 V for pH 14, and 1.1 V for our dual-pH system. Thus, our dual-pH system has an initial onset potential 400 mV lower than an alkaline system and 800 mV lower than the pH 7 system. However, the water splitting overpotential in the

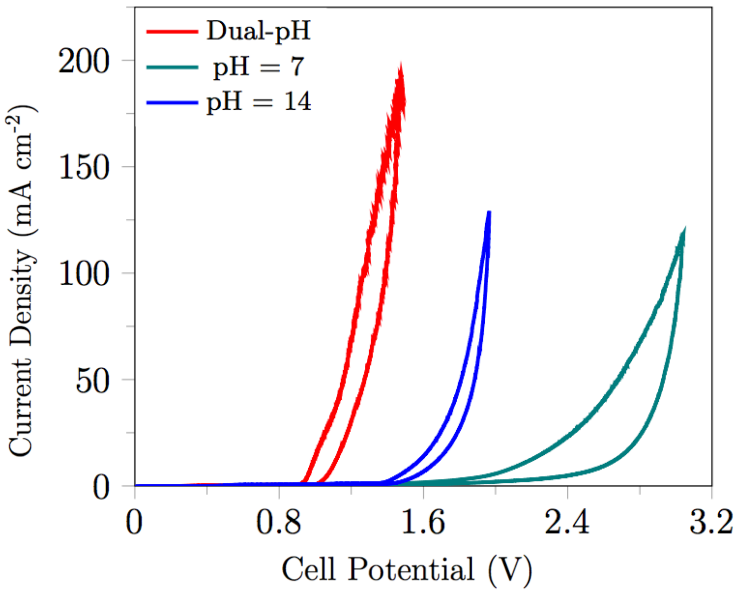

Figure 6.3. Cyclic voltammetry showing the onset potential for water splitting with a Pt HER catalyst and a $Ni_{0.8}$:$Fe_{0.2}$ oxide OER catalyst in pH 7 (teal), pH 14 (blue), and the dual-pH system (red) at a scan rate of 10 mV s^{-1} while the Pt disk electrode was rotated at 1600 rpm and the $Ni_{0.8}$:$Fe_{0.2}$ oxide on FTO glass electrode compartment was vigorously stirred.

dual-pH system will increase from local pH change at the cathode surface due to the production of OH^- ions.

Immediately, one notices that the initial onset potential for the dual-pH system (1.1 V) is lower than the thermodynamic potential for water splitting (1.23 V). While this may seem counterintuitive, it is well-known that the half-reactions for the water splitting reactions are pH dependent. For example, on the OER side (as mentioned above), the standard potential for OH^- oxidation is +0.4 V vs SHE. While we are not at equilibrium in this system, the equilibrium potential for water reduction at pH 7 is -0.417 vs SHE (-0.83 V + $7 \cdot 0.059$ V). Adding these potentials together gives a cell potential of ca. 0.82 V, valid before any net faradaic current occurs, and since our OER catalyst has an overpotential of 0.3 V and the HER catalyst operates near the thermodynamic potential, our expected initial onset potential is 1.1 V—exactly as we measured. This is also consistent with our three electrode experiments where the HER occurs at ca. -0.6 V vs Ag/AgCl, and the OER occurs at ca. +0.5 V vs Ag/AgCl—resulting in a total cell potential of 1.1 V. Production of OH^- on the cathode side will result in a change in overpotential due to local pH change at the electrode surface. The rate at which the pH changes will depend on the kinetics of the potassium phosphate buffer reactions relative to the rate of water reduction.

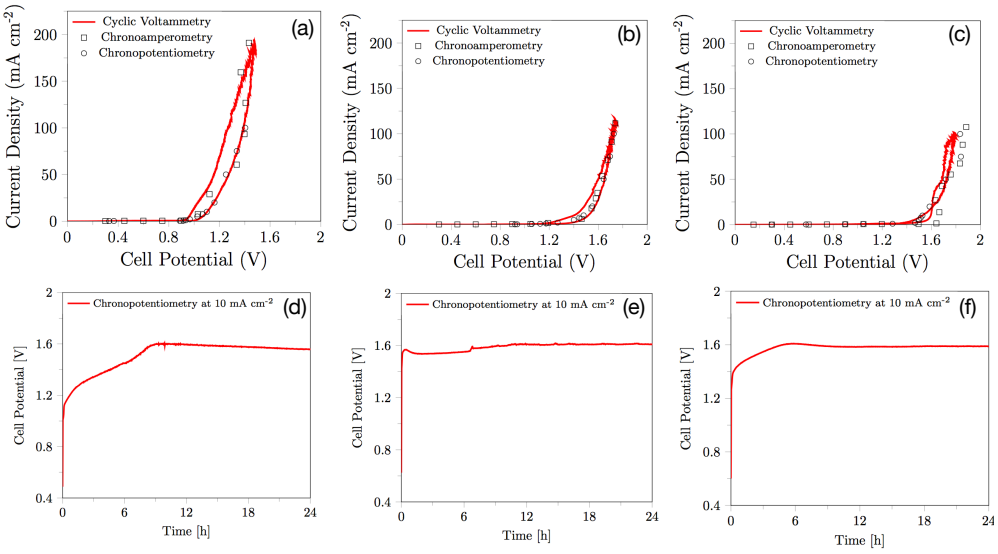

Figure 6.4. Dual-pH water splitting. Pt:$Ni_{0.8}$:$Fe_{0.2}$ (a) and (d). Ni:$Ni_{0.8}$:$Fe_{0.2}$ (b) and (e). FeS_2:$Ni_{0.8}$:$Fe_{0.2}$ (c) and (f)

One of the advantages of the dual-pH water splitting is that it enables the use of non-precious metal catalysts. Figure 6.4 shows the following HER:OER catalysts, Pt:$Ni_{0.8}$:$Fe_{0.2}$, Ni:$Ni_{0.8}$:$Fe_{0.2}$, and FeS_2:$Ni_{0.8}$:$Fe_{0.2}$. Here we observed that the non-precious metal catalysts can enable water splitting at a cell voltage under 1.6 V. 24 hour constant current measurements also show that all three systems can sustain total water splitting under 1.6 V at 10 mA cm^{-2}.

6.6 Conclusions

Here, we have demonstrated for the first time a dual-pH water splitting system which operates at incredibly low cell potentials and enables the use of non-precious metal catalysts. By neutralizing a Nafion membrane, we allow for K^+ ions to cross the membrane to promote ionic conductivity while allowing for the pH of the system to remain different on each side of the membrane. This allows for each half reaction to operate under their optimal conditions and dramatically lowers the total water splitting overpotential. Further investigation is required to understand how fast the local pH at the cathode surface will change in the presence of the potassium phosphate buffer. The phosphate buffer will be consumed by the OH^- ions produced at the cathode surface. As more OH^- is produced, the buffer will be consumed to the point that it will no longer have an effect on the pH, and the local pH at the cathode surface will increase at a faster rate, causing the water

splitting overpotential to increase substantially. For this reason, a batch dual-pH electrolysis cell is not feasible. A continuous dual-pH cell in which fresh buffered electrolyte is added is a possibility. However, an economic analysis is required to determine if the decrease in overpotential for the dual-pH system, compared to the alkaline system, outweighs the cost of adding fresh buffered electrolyte continuously.

Chapter 7

Conclusions and Future Work

7.1 Conclusion

The recurring theme of the preceding chapters is the activity of a nanostructured catalyst is strongly dependent on its morphology. By tuning the initial sulfur concentration, the airfree hot sulfur injection synthesis of nanostructured FeS_2 yielded 1D FeS_2 wires, 2D FeS_2 discs, or 3D FeS_2 cubes. We found that the HER activity of the 2D FeS_2 discs was superior compared to the 1D FeS_2 wires and 3D FeS_2 cubes. In fact, the overpotential of the 2D FeS_2 discs was within 50 mV of that of Pt in neutral media, and the exchange current densities were of the same order of magnitude. This may be due to the high edge site density of the 100 nm discs and the thinness of the discs, allowing for shorter electron hopping distances. However, further investigation is required to test these hypotheses. Scanning electrochemical microscopy using a nanoelectrode (an electrode with a diameter on the order of nanometers) can be used to map the HER activity over a single disc because the resolution of SECM is determined by the size of the electrode. This technique will be utilized to determine if the edge site of the FeS_2 disc is the active site for the HER, analogous to the active edge site on MoS_2 nanosheets. In addition, the synthesis conditions (e.g. temperature, pressure) can be modified to adjust the thickness of the discs to study the effect of the thickness of the discs on the catalytic activity.

The activity of the oxygen evolution catalysts reported herein is also strongly dependent on morphology. The nanoamorphous $Ni_{0.8}$:$Fe_{0.2}$ structure synthesized via a low-temperature microwave-assisted synthesis has remarkably higher activity than the rock salt $Ni_{0.8}$:$Fe_{0.2}$ structure. Surface

interrogation mode of scanning electrochemical microscopy (SI-SECM) revealed that the rock salt $Ni_{0.8}$:$Fe_{0.2}$ had two types of sites, a "slow" site with a rate constant of 0.05 s^{-1} and a "fast" site with a rate constant of 1.3 s^{-1}, while there was only "fast" sites with a rate constant of 1.9 s^{-1} on the nanoamorphous $Ni_{0.8}$:$Fe_{0.2}$ structure. The rock salt $Ni_{0.8}$:$Fe_{0.2}$ was synthesized at high temperature (500 °C) compared to the the nanoamorphous $Ni_{0.8}$:$Fe_{0.2}$ synthesis, which only involves a 2 minute microwave-heating step. High resolution transmission electron microscopy (HRTEM) and electron diffraction showed that the low-temperature microwave-assisted synthesis yielded a nanoamorphous material with no order down to the 5 nanometer scale. This gives evidence that homogeneous dispersion of the metals in a bimetallic catalyst is paramount to maximizing the number of bimetallic (i.e. fast) active sites; whereas, high temperature synthesis is likely to result is segregation of the metals, reducing the number of bimetallic sites.

Further conclusions on the effect of morphology on catalytic activity can be drawn from comparisons of the rock salt $Ni_{0.8}$:$Fe_{0.2}$ structure with other materials. Using SI-SECM, we determined the active site density of rock salt $Ni_{0.8}$:$Fe_{0.2}$ and crystalline IrO_x. Both catalysts had the same active site density (500 sites nm^{-2}), which is on the order of what is expected due to the roughness of the materials. However, when the rock salt $Ni_{0.8}$:$Fe_{0.2}$ is electrochemically conditioned to form the $Ni_{0.8}Fe_{0.2}OOH$ layered double hydroxide (LDH), the active site density is increased by approximately an order of magnitude. It is known that the LDH structure of $Ni_{1-x}Fe_xOOH$ has electrolyte permeability, but prior to this work, it was unclear if the permeability allows for subsurface active sites to participate in catalysis. The anomalously high active site density (4500 sites nm^{-2}) implies that the subsurface active sites do indeed participate in catalysis.

The 2D FeS_2 discs HER catalyst and the nanoamorphous $Ni_{0.8}$:$Fe_{0.2}$ OER catalyst reported herein present an opportunity to lower the overall water splitting overpotential and reduce the capital costs of an electrolyzer, yet they also pose a unique challenge: the FeS_2 discs are active in neutral media and the nanoamorphous $Ni_{0.8}$:$Fe_{0.2}$ oxide is active in alkaline media. Analogous to the chlor-alkali membrane cell, we have shown that the K^+ form of the Nafion 117 membrane can be utilized to split water with the cathode and anode in a different pH environments. The result is a substantial decrease in the overall water splitting overpotential. This phenomenon requires further investigation to determine the role of the open circuit potential across the membrane in the overpotential, **and to understand how long the phosphate buffer will prevent local**

pH changes at the cathode surface. However, it is apparent that the availability of reactants (i.e. H_2O for $H_2O + 2e^- \rightarrow H_2 + 2OH^-$ and OH^- for $4OH^- \rightarrow O_2 + 2H_2O + 4e^-$) does enhance the rates of reaction, as it does for either the cathode or the anode when operating in neutral or alkaline media, respectively.

7.2 Future Work

In order to assess the commercialization potential of the dual-pH system, we must first demonstrate that a relevant current density can be attained with the FeS_2 discs and the nanoamorphous $Ni_{0.8}$:$Fe_{0.2}$ oxide. To reach the current densities required for commercial electrolysis, 1 A cm^{-2}, the catalysts must be applied to a support to maximize utilization of the nanoparticle surface areas. In commercial PEM electrolyzers, the supported catalyst must be pressed evenly in a thin layer over the PEM surface because the reaction will only occur at the three phase boundary (TPB) between the membrane, catalyst, and reactant (i.e. proton). In our dual-pH system, the membrane only provides ionic conductivity, it does not facilitate transfer of reactant to the catalyst surface. Due to this difference, we will investigate a wide range of low-cost carbon materials (e.g. carbon paper, carbon cloth, and fleece) as high surface area catalyst supports, whereas traditional PEM electrolyzers require more expensive, dispersible carbon support materials (e.g. carbon nanotubes (CNTs), carbon nanofibers (CNFs), and carbon blacks).[294,295]

The properties that are most important for our catalyst support are surface area, conductivity, and chemical stability. Carbon supports that may be suitable for our application include carbon nanofoam (Figure 7.1a,b), non-woven carbon veil (Figure 7.1c,d), and activated carbon cloth. We will evaluate all properties of these carbon supports for use in electrochemical water splitting. BET surface area measurements will be performed on all carbon materials and those which have a surface area greater than 300 m^2/g will be prioritized. Electrical resistivity measurements will also be performed. Carbons having resistances less than 0.1 Ω·cm are preferred. If the resistance of a carbon is greater than 0.1 Ω·cm, the application of a conducting agent (e.g. HSF54 Y-Shield) will be applied to determine if the resistivity can be decreased while still maintaining the surface area target. Finally, the carbon materials will be exposed to both neutral and alkaline electrolytes under an applied potential for one week to verify chemical stability under water splitting conditions.

The synthesis of the FeS_2 discs and nanoamorphous $Ni_{0.8}$:$Fe_{0.2}$ oxide produce suspensions of the catalysts (catalyst inks), enabling the facile application to a carbon support. However, there are several methods of applying the catalysts to the support, and using the correct method to obtain the optimum catalyst coverage is imperative to the success of the device. We will investigate different application methods, including dip-coating, drop-casting, and electrophoretic deposition. The carbon cloth can be dip-coated in the catalyst ink by immersing the cloth into the ink and withdrawing it at a controlled rate. Drop-casting will be performed by pipetting the catalyst ink onto the support and allowing it to dry under controlled conditions. Electrophoretic deposition will be performed in a two electrode system with a titanium counter electrode and applying a potential to the carbon electrode. Further experimentation with electrophoretic deposition techniques and variables, such as stirring, agitation, coating time, and applied voltage may be required to ensure even catalyst coating. For each deposition method, the supported catalysts will be tested individually in a stirred 3 electrode system. Voltammetry, chronopotentiometry at 1 A cm-2, and multi-potential step experiments will be performed on the catalyst to determine activity and stability of the supported catalyst. A potential problem is the catalyst flaking off of the support under flow conditions. Rapid stirring will provide preliminary simulation of flow conditions. The application of conductive or ionic binders (e.g., Nafion solution) to the supported catalyst may help to strongly bind the catalyst to the support. Finally, supported OER and HER catalysts will be employed in our two compartment cell separated by the K^+ form of Nafion 117 membrane at 1 A cm^{-2} for one week to compare the performance to the best reported cell voltage in literature, 1 A cm^{-2} at about 1.55 V.[30]

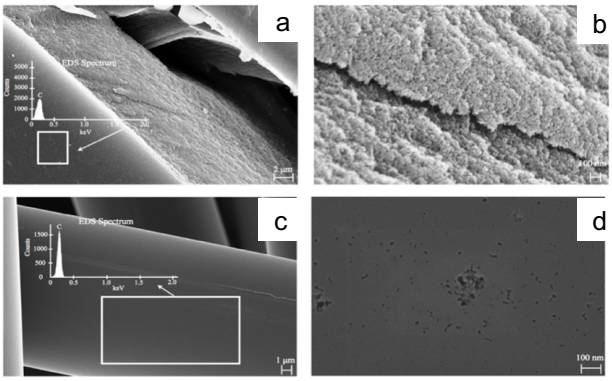

Figure 7.1. Scanning electron micrographs of possible high surface area carbon supports—carbon nanofoam from Marketech International (a,b) and non-woven carbon veil from Hollingsworth and Vose (c,d).

In order to apply our dual-pH technology to an electrolyzer, we envision utilizing a general bipolar stack design, similar to that of a PEM electrolyzer, but with a few important differences. First, instead of the acidic form of the membrane, a neutralized membrane will separate the cathode and anode compartment. The neutralized membrane will maintain the pH gradient between the cathode and anode in each cell, provide ionic conductivity between the cells, and keep the product gases separate. Second, in a traditional PEM electrolyzer, the supported catalyst layers are hot pressed directly onto the PEM surface. However, our design will utilize catalysts deposited on high surface area supports, separate from the membrane—the gap between the high surface area supports and the membrane will be made as small as possible to minimize the added solution overpotential and take advantage of the high conductivity of the membrane. Our system does not need to transfer reactants (i.e. protons) from the cathode to the anode because we are using a neutralized membrane (the ionic charge carrier is K^+ which is not a reactant). Thus, the active surface area of the catalyst is not limited by the three phase boundary (TPB) between the membrane, catalyst, and reactant, as it is in traditional PEM electrolyzers. As long as the catalysts are in good electrical contact with the bipolar plates or end plates, the active surface area is only limited by the surface area of the support, which can be extremely high for carbon materials, such as activated carbon cloth. In PEM electrolyzers, water is typically only circulated through the anode compartments of each cell to hydrate the PEM, provide liquid reactants, and facilitate the removal of product oxygen. The circulating water is made acidic by contact with the highly acidic PEM, requiring precious metal catalysts and noble metal current collectors, flow fields, and bipolar plates.[296] In our dual-pH electrolyzer, alkaline electrolyte will circulate through the anode compartments of each cell, but neutral electrolyte will also circulate through the cathode compartments. Since our electrolyzer will not have an acidic electrolyte to exacerbate the oxidizing conditions, it will allow for the utilization of low-cost materials such as high surface area carbons and earth abundant metals throughout the stack.

A single cell stack will be fabricated from titanium endplates with EDPM gaskets and the membrane sandwiched between the supported catalysts as a proof-of-concept device. Flow fields will be machined in the titanium endplates. The endplates will each have an inlet and outlet for the corresponding electrolytes. The stack is to be operated with the endplates perpendicular to the horizon and the inlet ports positioned at the lowest point possible so that the electrolyte will

travel upwards through each corresponding compartment, fully wetting the supported catalyst, hydrating the K^+ membrane, and expelling bubbles from the catalyst surface, before exiting the stack from the same endplate that it entered. The flow of electrolyte will be controlled by an adjustable pump fed by a heated electrolyte reservoir to simulate the operating temperature of a large electrolyzer stack (80 °C). The exiting electrolyte will pass through a gas/liquid separator, and the gas will travel through a silica gel column to remove the humidity before passing through a flow meter into a collection tank for sampling. The single cell dual-pH electrolyzer stack will be characterized by operation at 1 A cm^{-2} for one week and the cell potential will compared to the state-of-the-art from the literature (1 A cm^{-2} at 1.55 V).[30] After the dual-pH configuration is validated, the electrochemical performance of the dual-pH electrolyzer will be characterized with endplates made of different types of stainless steel. Stainless steel endplates would significantly reduce the cost of the stack because the titanium plates can account for up to 30% of a PEM electrolyzer stack cost.[297] We will characterize the stainless steel endplates with SEM and XPS before and after 1 week experiments at 1 A cm^{-2} to determine the degree of corrosion. If the stainless steel endplates are susceptible to an unacceptable rate of corrosion under operating conditions, then alternatives, such as nickel-plated steels will be investigated. However, it is anticipated that the neutralized membrane will be less susceptible to poisoning from metal cations than the traditional PEM because the neutralized membrane does not facilitate the reaction. Chronopotentiometry studies for extended periods of time, as well as responsiveness ramp up time and partial load testing will be performed to identify the limits of operation and stability for the device. Further studies will test how liquid recirculation rate, operating temperature, pressure, and type of neutralized membrane affect the performance of the device. It is anticipated that in commercial operation, the catholyte and anolyte may need to be concentrated and recycled to the anode side because OH^- will be consumed on the anode side with OH^- being produced on the cathode side and the OH^- will not cross the neutralized membrane. However, a similar recycling operation is done in brine electrolysis and it is not expected to impede the utility of the dual-pH electrolyzer. The flow rate and purity of the product gases will also be evaluated. It is important that the outlet gases be analyzed via gas chromatography (GC) to determine purity of the gases produced and ensure that there is not crossover occurring to the extent that the lower flammability limit (4 mol% H_2 in O_2) is breached.[298] Gas crossover does not only lead to safety concerns, but it also causes inefficiency

due to spontaneous recombination of the hydrogen and oxygen.

References

[1] Bard AJ, Faulkner LR, Leddy J, Zoski CG. *Electrochemical methods: fundamentals and applications*, vol. 2. wiley New York. 1980.

[2] Strmcnik D, Lopes PP, Genorio B, Stamenkovic VR, Markovic NM. Design principles for hydrogen evolution reaction catalyst materials. *Nano Energy*. 2016;29:29–36.

[3] Man IC, Su HY, Calle-Vallejo F, Hansen HA, Martínez JI, Inoglu NG, Kitchin J, Jaramillo TF, Nørskov JK, Rossmeisl J. Universality in oxygen evolution electrocatalysis on oxide surfaces. *ChemCatChem*. 2011;3(7):1159–1165.

[4] Mauritz KA, Moore RB. State of understanding of Nafion. *Chemical reviews*. 2004; 104(10):4535–4586.

[5] Peighambardoust SJ, Rowshanzamir S, Amjadi M. Review of the proton exchange membranes for fuel cell applications. *International journal of hydrogen energy*. 2010;35(17):9349–9384.

[6] Grigoriev S, Porembsky V, Fateev V. Pure hydrogen production by PEM electrolysis for hydrogen energy. *International Journal of Hydrogen Energy*. 2006;31(2):171–175.

[7] Ramachandran R, Menon RK. An overview of industrial uses of hydrogen. *International Journal of Hydrogen Energy*. 1998;23(7):593–598.

[8] Muradov N. Low to near-zero CO2 production of hydrogen from fossil fuels: Status and perspectives. *International Journal of Hydrogen Energy*. 2017;42(20):14058–14088.

[9] Balat M. Potential importance of hydrogen as a future solution to environmental and transportation problems. *International journal of hydrogen energy*. 2008;33(15):4013–4029.

[10] Winter CJ. Hydrogen energy—abundant, efficient, clean: a debate over the energy-system-of-change. *International Journal of hydrogen energy*. 2009;34(14):S1–S52.

[11] Ball M, Wietschel M. The future of hydrogen–opportunities and challenges. *International journal of hydrogen energy*. 2009;34(2):615–627.

[12] Sharma S, Ghoshal SK. Hydrogen the future transportation fuel: from production to applications. *Renewable and sustainable energy reviews*. 2015;43:1151–1158.

[13] Abbasi T, Abbasi S. 'Renewable'hydrogen: prospects and challenges. *Renewable and Sustainable Energy Reviews*. 2011;15(6):3034–3040.

[14] Cipriani G, Di Dio V, Genduso F, La Cascia D, Liga R, Miceli R, Galluzzo GR. Perspective on hydrogen energy carrier and its automotive applications. *International Journal of Hydrogen Energy*. 2014;39(16):8482–8494.

[15] Bockris JOM. The hydrogen economy: its history. *International Journal of Hydrogen Energy*. 2013;38(6):2579–2588.

[16] Chivian E, Bernstein A. *Sustaining life: how human health depends on biodiversity*. Oxford University Press. 2008.

[17] Mehta V, Cooper JS. Review and analysis of PEM fuel cell design and manufacturing. *Journal of Power Sources*. 2003;114(1):32–53.

[18] Williams MC, Strakey JP, Singhal SC. US distributed generation fuel cell program. *Journal of Power Sources*. 2004;131(1-2):79–85.

[19] Steele BC, Heinzel A. Materials for fuel-cell technologies. In: *Materials For Sustainable Energy: A Collection of Peer-Reviewed Research and Review Articles from Nature Publishing Group*, pp. 224–231. World Scientific. 2011;.

[20] Teichmann D, Stark K, Müller K, Zöttl G, Wasserscheid P, Arlt W. Energy storage in residential and commercial buildings via Liquid Organic Hydrogen Carriers (LOHC). *Energy & Environmental Science*. 2012;5(10):9044–9054.

[21] Teichmann D, Arlt W, Wasserscheid P. Liquid organic hydrogen carriers as an efficient vector for the transport and storage of renewable energy. *International Journal of Hydrogen Energy*. 2012;37(23):18118–18132.

[22] Sakintuna B, Lamari-Darkrim F, Hirscher M. Metal hydride materials for solid hydrogen storage: a review. *International journal of hydrogen energy*. 2007;32(9):1121–1140.

[23] Nicoletti G, Arcuri N, Nicoletti G, Bruno R. A technical and environmental comparison between hydrogen and some fossil fuels. *Energy Conversion and Management*. 2015;89:205–213.

[24] Bhandari R, Trudewind CA, Zapp P. Life cycle assessment of hydrogen production via electrolysis–a review. *Journal of cleaner production*. 2014;85:151–163.

[25] Nørskov J, Chen J, Miranda R, Fitzsimmons T, Stack R. Sustainable Ammonia Synthesis–Exploring the scientific challenges associated with discovering alternative, sustainable processes for ammonia production. *Tech. rep.*, US DOE Office of Science. 2016.

[26] Trasatti S. Water electrolysis: who first? *Journal of Electroanalytical Chemistry*. 1999; 476(1):90–91.

[27] Jović V, Jović B, Lačnjevac U, Krstajić N, Zabinski P, Elezović N. Accelerated service life test of electrodeposited NiSn alloys as bifunctional catalysts for alkaline water electrolysis under industrial operating conditions. *Journal of Electroanalytical Chemistry*. 2018;819:16–25.

[28] Kreuter W, Hofmann H. Electrolysis: the important energy transformer in a world of sustainable energy. *International Journal of Hydrogen Energy*. 1998;23(8):661–666.

[29] Zeng K, Zhang D. Recent progress in alkaline water electrolysis for hydrogen production and applications. *Progress in Energy and Combustion Science*. 2010;36(3):307–326.

[30] Carmo M, Fritz DL, Mergel J, Stolten D. A comprehensive review on PEM water electrolysis. *International journal of hydrogen energy*. 2013;38(12):4901–4934.

[31] Vincent I, Bessarabov D. Low cost hydrogen production by anion exchange membrane electrolysis: a review. *Renewable and Sustainable Energy Reviews*. 2017;.

[32] Shapiro D, Duffy J, Kimble M, Pien M. Solar-powered regenerative PEM electrolyzer/fuel cell system. *Solar Energy*. 2005;79(5):544–550.

[33] Winter CJ. The hydrogen energy economy: An industry tycoon in sight? *International Journal of Hydrogen Energy*. 2011;20(36):12653–12654.

[34] Quaino P, Juarez F, Santos E, Schmickler W. Volcano plots in hydrogen electrocatalysis–uses and abuses. *Beilstein journal of nanotechnology*. 2014;5:846.

[35] Nørskov JK, Bligaard T, Logadottir A, Kitchin J, Chen JG, Pandelov S, Stimming U. Trends in the exchange current for hydrogen evolution. *Journal of the Electrochemical Society*. 2005; 152(3):J23–J26.

[36] Eftekhari A. Electrocatalysts for hydrogen evolution reaction. *International Journal of Hydrogen Energy*. 2017;42(16):11053–11077.

[37] Delahay P. Implications of the Kinetics of Ionic Dissociation with Regard to Some Electrochemical Processes—Application to Polarography. *Journal of the American Chemical Society*. 1952;74(14):3497–3500.

[38] Zheng Y, Jiao Y, Vasileff A, Qiao SZ. The Hydrogen Evolution Reaction in Alkaline Solution: From Theory, Single Crystal Models, to Practical Electrocatalysts. *Angewandte Chemie International Edition*. 2017;.

[39] Subbaraman R, Tripkovic D, Strmcnik D, Chang KC, Uchimura M, Paulikas AP, Stamenkovic V, Markovic NM. Enhancing hydrogen evolution activity in water splitting by tailoring Li+-Ni (OH) 2-Pt interfaces. *Science*. 2011;334(6060):1256–1260.

[40] Subbaraman R, Tripkovic D, Chang KC, Strmcnik D, Paulikas AP, Hirunsit P, Chan M, Greeley J, Stamenkovic V, Markovic NM. Trends in activity for the water electrolyser reactions on 3d M (Ni, Co, Fe, Mn) hydr (oxy) oxide catalysts. *Nature materials*. 2012;11(6):550.

[41] Hinnemann B, Moses PG, Bonde J, Jørgensen KP, Nielsen JH, Horch S, Chorkendorff I, Nørskov JK. Biomimetic hydrogen evolution: MoS2 nanoparticles as catalyst for hydrogen evolution. *Journal of the American Chemical Society*. 2005;127(15):5308–5309.

[42] Evans DJ, Pickett CJ. Chemistry and the hydrogenases. *Chemical Society Reviews*. 2003; 32(5):268–275.

[43] Lazar P, Otyepka M. Role of the edge properties in the hydrogen evolution reaction on MoS2. *Chemistry–A European Journal*. 2017;23(20):4863–4869.

[44] Xie J, Zhang H, Li S, Wang R, Sun X, Zhou M, Zhou J, Lou XW, Xie Y. Defect-rich MoS2 ultrathin nanosheets with additional active edge sites for enhanced electrocatalytic hydrogen evolution. *Advanced materials*. 2013;25(40):5807–5813.

[45] Lukowski MA, Daniel AS, Meng F, Forticaux A, Li L, Jin S. Enhanced hydrogen evolution catalysis from chemically exfoliated metallic MoS2 nanosheets. *Journal of the American Chemical Society*. 2013;135(28):10274–10277.

[46] Kong D, Cha JJ, Wang H, Lee HR, Cui Y. First-row transition metal dichalcogenide catalysts for hydrogen evolution reaction. *Energy & Environmental Science*. 2013;6(12):3553–3558.

[47] Faber MS, Lukowski MA, Ding Q, Kaiser NS, Jin S. Earth-abundant metal pyrites (FeS2, CoS2, NiS2, and their alloys) for highly efficient hydrogen evolution and polysulfide reduction electrocatalysis. *The Journal of Physical Chemistry C*. 2014;118(37):21347–21356.

[48] Wu Z, Fang B, Bonakdarpour A, Sun A, Wilkinson DP, Wang D. WS2 nanosheets as a highly efficient electrocatalyst for hydrogen evolution reaction. *Applied Catalysis B: Environmental*. 2012;125:59–66.

[49] Jasion D, Barforoush JM, Qiao Q, Zhu Y, Ren S, Leonard KC. Low-dimensional hyper-thin FeS2 nanostructures for efficient and stable hydrogen evolution electrocatalysis. *ACS Catalysis*. 2015;5(11):6653–6657.

[50] Dau H, Limberg C, Reier T, Risch M, Roggan S, Strasser P. The mechanism of water oxidation: from electrolysis via homogeneous to biological catalysis. *ChemCatChem*. 2010; 2(7):724–761.

[51] Hu JM, Zhang JQ, Cao CN. Oxygen evolution reaction on IrO2-based DSA® type electrodes: kinetics analysis of Tafel lines and EIS. *International Journal of Hydrogen Energy*. 2004; 29(8):791–797.

[52] Rossmeisl J, Qu ZW, Zhu H, Kroes GJ, Nørskov JK. Electrolysis of water on oxide surfaces. *Journal of Electroanalytical Chemistry*. 2007;607(1-2):83–89.

[53] Rossmeisl J, Logadottir A, Nørskov JK. Electrolysis of water on (oxidized) metal surfaces. *Chemical physics*. 2005;319(1-3):178–184.

[54] Lee Y, Suntivich J, May KJ, Perry EE, Shao-Horn Y. Synthesis and activities of rutile IrO2 and RuO2 nanoparticles for oxygen evolution in acid and alkaline solutions. *The journal of physical chemistry letters*. 2012;3(3):399–404.

[55] Burgess M, Hernández-Burgos K, Cheng KJ, Moore JS, Rodríguez-López J. Impact of electrolyte composition on the reactivity of a redox active polymer studied through surface interrogation and ion-sensitive scanning electrochemical microscopy. *Analyst*. 2016;141(12):3842–3850.

[56] Cherevko S, Geiger S, Kasian O, Kulyk N, Grote JP, Savan A, Shrestha BR, Merzlikin S, Breitbach B, Ludwig A, et al. Oxygen and hydrogen evolution reactions on Ru, RuO2, Ir, and IrO2 thin film electrodes in acidic and alkaline electrolytes: A comparative study on activity and stability. *Catalysis Today*. 2016;262:170–180.

[57] Trześniewski BJ, Diaz-Morales O, Vermaas DA, Longo A, Bras W, Koper MT, Smith WA. In situ observation of active oxygen species in Fe-containing Ni-based oxygen evolution catalysts: The effect of pH on electrochemical activity. *Journal of the American Chemical Society*. 2015;137(48):15112–15121.

[58] Gong M, Dai H. A mini review of NiFe-based materials as highly active oxygen evolution reaction electrocatalysts. *Nano Research*. 2015;8(1):23–39.

[59] Yin S, Tu W, Sheng Y, Du Y, Kraft M, Borgna A, Xu R. A Highly Efficient Oxygen Evolution Catalyst Consisting of Interconnected Nickel–Iron-Layered Double Hydroxide and Carbon Nanodomains. *Advanced Materials*. 2018;30(5):1705106.

[60] Louie MW, Bell AT. An investigation of thin-film Ni–Fe oxide catalysts for the electrochemical evolution of oxygen. *Journal of the American Chemical Society*. 2013;135(33):12329–12337.

[61] Hunter BM, Blakemore JD, Deimund M, Gray HB, Winkler JR, Müller AM. Highly active mixed-metal nanosheet water oxidation catalysts made by pulsed-laser ablation in liquids. *Journal of the American Chemical Society*. 2014;136(38):13118–13121.

[62] Barforoush JM, Jantz DT, Seuferling TE, Song KR, Cummings LC, Leonard KC. Microwave-assisted synthesis of a nanoamorphous (Ni 0.8, Fe 0.2) oxide oxygen-evolving electrocatalyst containing only "fast" sites. *Journal of Materials Chemistry A*. 2017;5(23):11661–11670.

[63] Friebel D, Louie MW, Bajdich M, Sanwald KE, Cai Y, Wise AM, Cheng MJ, Sokaras D, Weng TC, Alonso-Mori R, et al. Identification of highly active Fe sites in (Ni, Fe) OOH for electrocatalytic water splitting. *Journal of the American Chemical Society*. 2015;137(3):1305–1313.

[64] Ahn HS, Bard AJ. Surface Interrogation Scanning Electrochemical Microscopy of $Ni_{1-x}Fe_xOOH$ ($0 < x < 0.27$) Oxygen Evolving Catalyst: Kinetics of the "fast" Iron Sites. *J Am Chem Soc*. 2016;138(1):313–318.

[65] Barforoush JM, Seuferling TE, Jantz DT, Song KR, Leonard KC. Insights into the Active Electrocatalytic Areas of Layered Double Hydroxide and Amorphous Nickel–Iron Oxide Oxygen Evolution Electrocatalysts. *ACS Applied Energy Materials*. 2018;1(4):1415–1423.

[66] Zhang B, Zheng X, Voznyy O, Comin R, Bajdich M, García-Melchor M, Han L, Xu J, Liu M, Zheng L, García de Arquer1 FP, Dinh1 CT, Fan1 F, Yuan1 M, Yassitepe1 E, Chen N, Regier T, Liu P, Li Y, Luna1 PD, Janmohamed A, Xin HL, Yang H, Vojvodic A, Sargent EH. Homogeneously dispersed multimetal oxygen-evolving catalysts. *Science*. 2016;352(6283):333–337.

[67] Grubb W. Batteries with solid ion exchange electrolytes I. secondary cells employing metal electrodes. *Journal of the Electrochemical Society*. 1959;106(4):275–278.

[68] Millet P, Ngameni R, Grigoriev S, Mbemba N, Brisset F, Ranjbari A, Etievant C. PEM water electrolyzers: from electrocatalysis to stack development. *International Journal of hydrogen energy*. 2010;35(10):5043–5052.

[69] Zuo Z, Fu Y, Manthiram A. Novel blend membranes based on acid-base interactions for fuel cells. *Polymers*. 2012;4(4):1627–1644.

[70] Brey J, Muñoz D, Mesa V, Guerrero T. Use of Fuel Cells and Electrolyzers In Space Applications: From Energy Storage To Propulsion/Deorbitation. In: *E3S Web of Conferences*, vol. 16. EDP Sciences. 2017; p. 17004.

[71] Paidar M, Fateev V, Bouzek K. Membrane electrolysis—History, current status and perspective. *Electrochimica acta*. 2016;209:737–756.

[72] Davenport RJ, Schubert FH, Grigger DJ. Space water electrolysis: Space Station through advance missions. *troc*. 1991;91:37.

[73] Kanan MW, Nocera DG. In situ formation of an oxygen-evolving catalyst in neutral water containing phosphate and Co2+. *Science*. 2008;321(5892):1072–1075.

[74] McKone JR, Warren EL, Bierman MJ, Boettcher SW, Brunschwig BS, Lewis NS, Gray HB. Evaluation of Pt, Ni, and Ni–Mo electrocatalysts for hydrogen evolution on crystalline Si electrodes. *Energy & Environmental Science*. 2011;4(9):3573–3583.

[75] Leonard KC, Bard AJ. Pattern recognition correlating materials properties of the elements to their kinetics for the hydrogen evolution reaction. *Journal of the American Chemical Society*. 2013;135(42):15885–15889.

[76] McKone JR, Lewis NS, Gray HB. Will solar-driven water-splitting devices see the light of day? *Chemistry of Materials*. 2013;26(1):407–414.

[77] Lewis NS, Nocera DG. Powering the planet: Chemical challenges in solar energy utilization. *Proceedings of the National Academy of Sciences*. 2006;103(43):15729–15735.

[78] Gray H. Nat. Chem 2009, 1, 7.(b) Lewis, NS; Nocera. *Proc Natl Acad Sci USA*. 2006; 103:15729–15735.

[79] Yang J, Shin HS. Recent advances in layered transition metal dichalcogenides for hydrogen evolution reaction. *Journal of Materials Chemistry A*. 2014;2(17):5979–5985.

[80] Di Giovanni C, Wang WA, Nowak S, Greneche JM, Lecoq H, Mouton L, Giraud M, Tard C. Bioinspired iron sulfide nanoparticles for cheap and long-lived electrocatalytic molecular hydrogen evolution in neutral water. *Acs Catalysis*. 2014;4(2):681–687.

[81] Peng Z, Jia D, Al-Enizi AM, Elzatahry AA, Zheng G. From water oxidation to reduction: Homologous Ni–Co based nanowires as complementary water splitting electrocatalysts. *Advanced Energy Materials*. 2015;5(9):1402031.

[82] Li Y, Wang H, Xie L, Liang Y, Hong G, Dai H. MoS2 nanoparticles grown on graphene: an advanced catalyst for the hydrogen evolution reaction. *Journal of the American Chemical Society*. 2011;133(19):7296–7299.

[83] Yu Y, Huang SY, Li Y, Steinmann SN, Yang W, Cao L. Layer-dependent electrocatalysis of MoS2 for hydrogen evolution. *Nano letters*. 2014;14(2):553–558.

[84] Jaramillo TF, Jørgensen KP, Bonde J, Nielsen JH, Horch S, Chorkendorff I. Identification of active edge sites for electrochemical H2 evolution from MoS2 nanocatalysts. *science*. 2007; 317(5834):100–102.

[85] Wadia C, Alivisatos AP, Kammen DM. Materials availability expands the opportunity for large-scale photovoltaics deployment. *Environmental science & technology*. 2009;43(6):2072–2077.

[86] Macpherson HA, Stoldt CR. Iron pyrite nanocubes: size and shape considerations for photovoltaic application. *Acs Nano*. 2012;6(10):8940–8949.

[87] Bai Y, Yeom J, Yang M, Cha SH, Sun K, Kotov NA. Universal synthesis of single-phase pyrite FeS2 nanoparticles, nanowires, and nanosheets. *The Journal of Physical Chemistry C*. 2013;117(6):2567–2573.

[88] Kirkeminde A, Ruzicka BA, Wang R, Puna S, Zhao H, Ren S. Synthesis and optoelectronic properties of two-dimensional FeS2 nanoplates. *ACS applied materials & interfaces*. 2012; 4(3):1174–1177.

[89] Kirkeminde A, Gingrich P, Gong M, Cui H, Ren S. Iron sulfide ink for the growth of pyrite crystals. *Nanotechnology*. 2014;25(20):205603.

[90] Ennaoui A, Fiechter S, Tributsch H, Giersig M, Vogel R, Weller H. Photoelectrochemical energy conversion obtained with ultrathin organo-metallic-chemical-vapor-deposition layer of FeS2 (pyrite) on TiO2. *Journal of the Electrochemical Society*. 1992;139(9):2514–2518.

[91] Chatzitheodorou G, Fiechter S, Könenkamp R, Kunst M, Jaegermann W, Tributsch H. Thin photoactive FeS2 (pyrite) films. *Materials research bulletin*. 1986;21(12):1481–1487.

[92] Aricò A, Antonucci V, Antonucci P, Modica E, Ferrara S, Giordano N. Electrodeposition and characterization of iron sulphide thin films. *Materials Letters*. 1992;13(1):12–17.

[93] Rosso KM, Becker U, Hochella MF. Atomically resolved electronic structure of pyrite {100} surfaces: An experimental and theoretical investigation with implications for reactivity. *American Mineralogist*. 1999;84(10):1535–1548.

[94] Yu BB, Zhang X, Jiang Y, Liu J, Gu L, Hu JS, Wan LJ. Solvent-induced oriented attachment growth of air-stable phase-pure pyrite FeS2 nanocrystals. *Journal of the American Chemical Society*. 2015;137(6):2211–2214.

[95] Vogt H, Chattopadhyay T, Stolz H. Complete first-order Raman spectra of the pyrite structure compounds FeS2, MnS2 and SiP2. *Journal of Physics and Chemistry of Solids*. 1983; 44(9):869–873.

[96] Lutz H, Müller B. Lattice vibration spectra. LXVIII. Single-crystal Raman spectra of marcasite-type iron chalcogenides and pnictides, FeX 2 (X= S, Se, Te; P, As, Sb). *Physics and Chemistry of Minerals*. 1991;18(4):265–268.

[97] Costentin C, Canales JC, Haddou B, Saveant JM. Electrochemistry of acids on platinum. Application to the reduction of carbon dioxide in the presence of pyridinium ion in water. *Journal of the American Chemical Society*. 2013;135(47):17671–17674.

[98] Leonard KC, Bard AJ. The study of multireactional electrochemical interfaces via a tip generation/substrate collection mode of scanning electrochemical microscopy: the hydrogen evolution reaction for Mn in acidic solution. *Journal of the American Chemical Society*. 2013; 135(42):15890–15896.

[99] Bard AJ, Fan FRF, Pierce DT, Unwin PR, Wipf DO, Zhou F. Chemical imaging of surfaces with the scanning electrochemical microscope. *Science*. 1991;254(5028):68–74.

[100] Sun T, Yu Y, Zacher BJ, Mirkin MV. Scanning electrochemical microscopy of individual catalytic nanoparticles. *Angewandte Chemie International Edition*. 2014;53(51):14120–14123.

[101] Wilcoxon J, Newcomer P, Samara G. Strong quantum confinement effects in semiconductors: FeS2 nanoclusters. *Solid state communications*. 1996;98(6):581–585.

[102] Gong M, Kirkeminde A, Ren S. Symmetry-defying iron pyrite (FeS 2) nanocrystals through oriented attachment. *Scientific reports*. 2013;3:2092.

[103] Bard AJ, Fox MA. Artificial photosynthesis: solar splitting of water to hydrogen and oxygen. *Accounts of Chemical Research*. 1995;28(3):141–145.

[104] Gray HB. Powering the planet with solar fuel. *Nature chemistry*. 2009;1(1):7.

[105] McCrory CC, Jung S, Ferrer IM, Chatman SM, Peters JC, Jaramillo TF. Benchmarking hydrogen evolving reaction and oxygen evolving reaction electrocatalysts for solar water splitting devices. *Journal of the American Chemical Society*. 2015;137(13):4347–4357.

[106] Trasatti S. Electrocatalysis in the anodic evolution of oxygen and chlorine. *Electrochimica Acta*. 1984;29(11):1503–1512.

[107] Horkans J, Shafer M. An investigation of the electrochemistry of a series of metal dioxides with rutile-type structure: MoO2, WO 2, ReO2, RuO2, OsO2, and IrO2. *Journal of The Electrochemical Society*. 1977;124(8):1202–1207.

[108] Corrigan DA. The catalysis of the oxygen evolution reaction by iron impurities in thin film nickel oxide electrodes. *Journal of The Electrochemical Society*. 1987;134(2):377–384.

[109] Trotochaud L, Young SL, Ranney JK, Boettcher SW. Nickel–iron oxyhydroxide oxygen-evolution electrocatalysts: the role of intentional and incidental iron incorporation. *Journal of the American Chemical Society*. 2014;136(18):6744–6753.

[110] Bau JA, Luber EJ, Buriak JM. Oxygen evolution catalyzed by nickel–iron oxide nanocrystals with a nonequilibrium phase. *ACS applied materials & interfaces*. 2015;7(35):19755–19763.

[111] Guerrini E, Piozzini M, Castelli A, Colombo A, Trasatti S. Effect of FeO x on the electrocatalytic properties of NiCo 2 O 4 for O 2 evolution from alkaline solutions. *Journal of Solid State Electrochemistry*. 2008;12(4):363–373.

[112] Landon J, Demeter E, Inoglu N, Keturakis C, Wachs IE, Vasic R, Frenkel AI, Kitchin JR. Spectroscopic characterization of mixed Fe–Ni oxide electrocatalysts for the oxygen evolution reaction in alkaline electrolytes. *Acs Catalysis*. 2012;2(8):1793–1801.

[113] Swierk JR, Klaus S, Trotochaud L, Bell AT, Tilley TD. Electrochemical study of the energetics of the oxygen evolution reaction at nickel iron (oxy) hydroxide catalysts. *The Journal of Physical Chemistry C*. 2015;119(33):19022–19029.

[114] Zhang G, Cuharuc AS, Güell AG, Unwin PR. Electrochemistry at highly oriented pyrolytic graphite (HOPG): lower limit for the kinetics of outer-sphere redox processes and general implications for electron transfer models. *Physical Chemistry Chemical Physics*. 2015; 17(17):11827–11838.

[115] Hoang TT, Gewirth AA. High activity oxygen evolution reaction catalysts from additive-controlled electrodeposited Ni and NiFe films. *Acs Catalysis*. 2016;6(2):1159–1164.

[116] Hou Y, Lohe MR, Zhang J, Liu S, Zhuang X, Feng X. Vertically oriented cobalt selenide/NiFe layered-double-hydroxide nanosheets supported on exfoliated graphene foil: an efficient 3D electrode for overall water splitting. *Energy & Environmental Science*. 2016;9(2):478–483.

[117] Kim TW, Choi KS. Nanoporous BiVO4 photoanodes with dual-layer oxygen evolution catalysts for solar water splitting. *Science*. 2014;p. 1245026.

[118] Lu X, Zhao C. Electrodeposition of hierarchically structured three-dimensional nickel–iron electrodes for efficient oxygen evolution at high current densities. *Nature communications*. 2015;6:6616.

[119] Hou Y, Wen Z, Cui S, Feng X, Chen J. Strongly coupled ternary hybrid aerogels of N-deficient porous graphitic-C3N4 nanosheets/N-doped graphene/NiFe-layered double hydroxide for solar-driven photoelectrochemical water oxidation. *Nano letters*. 2016;16(4):2268–2277.

[120] Burke MS, Zou S, Enman LJ, Kellon JE, Gabor CA, Pledger E, Boettcher SW. Revised oxygen evolution reaction activity trends for first-row transition-metal (oxy) hydroxides in alkaline media. *The journal of physical chemistry letters*. 2015;6(18):3737–3742.

[121] Klaus S, Cai Y, Louie MW, Trotochaud L, Bell AT. Effects of Fe electrolyte impurities on Ni (OH) 2/NiOOH structure and oxygen evolution activity. *The Journal of Physical Chemistry C*. 2015;119(13):7243–7254.

[122] Trotochaud L, Ranney JK, Williams KN, Boettcher SW. Solution-cast metal oxide thin film electrocatalysts for oxygen evolution. *Journal of the American Chemical Society*. 2012; 134(41):17253–17261.

[123] Gong M, Li Y, Wang H, Liang Y, Wu JZ, Zhou J, Wang J, Regier T, Wei F, Dai H. An advanced Ni–Fe layered double hydroxide electrocatalyst for water oxidation. *Journal of the American Chemical Society*. 2013;135(23):8452–8455.

[124] Yu X, Zhang M, Yuan W, Shi G. A high-performance three-dimensional Ni–Fe layered double hydroxide/graphene electrode for water oxidation. *Journal of Materials Chemistry A*. 2015; 3(13):6921–6928.

[125] Long X, Li J, Xiao S, Yan K, Wang Z, Chen H, Yang S. A strongly coupled graphene and FeNi double hydroxide hybrid as an excellent electrocatalyst for the oxygen evolution reaction. *Angewandte Chemie*. 2014;126(29):7714–7718.

[126] Lu Z, Xu W, Zhu W, Yang Q, Lei X, Liu J, Li Y, Sun X, Duan X. Three-dimensional NiFe layered double hydroxide film for high-efficiency oxygen evolution reaction. *Chemical Communications*. 2014;50(49):6479–6482.

[127] Hunter BM, Hieringer W, Winkler J, Gray H, Müller A. Effect of interlayer anions on [NiFe]-LDH nanosheet water oxidation activity. *Energy & Environmental Science*. 2016;9(5):1734–1743.

[128] Smith RD, Berlinguette CP. Accounting for the dynamic oxidative behavior of nickel anodes. *Journal of the American Chemical Society*. 2016;138(5):1561–1567.

[129] McDonald TD, Bayer C, DeLee AM, Atchison E, Widrig D, Hutchens B, Leonard KC. Rapid Characterization of Multi-Metallic Electrocatalysts for the Water Splitting Reactions Utilizing Printed Microelectrodes on a Chip. *Journal of The Electrochemical Society*. 2016; 163(5):H359–H366.

[130] Ahn HS, Bard AJ. Surface interrogation of CoPi water oxidation catalyst by scanning electrochemical microscopy. *Journal of the American Chemical Society*. 2015;137(2):612–615.

[131] Park HS, Leonard KC, Bard AJ. Surface interrogation scanning electrochemical microscopy (SI-SECM) of photoelectrochemistry at a W/Mo-BiVO4 semiconductor electrode: quantification of hydroxyl radicals during water oxidation. *The Journal of Physical Chemistry C*. 2013;117(23):12093–12102.

[132] Arroyo-Curras N, Bard AJ. Iridium oxidation as observed by surface interrogation scanning electrochemical microscopy. *The Journal of Physical Chemistry C*. 2015;119(15):8147–8154.

[133] Rodriguez-Lopez J, Alpuche-Avilés MA, Bard AJ. Interrogation of surfaces for the quantification of adsorbed species on electrodes: oxygen on gold and platinum in neutral Media. *Journal of the American Chemical Society*. 2008;130(50):16985–16995.

[134] Smith RD, Prevot MS, Fagan RD, Trudel S, Berlinguette CP. Water oxidation catalysis: electrocatalytic response to metal stoichiometry in amorphous metal oxide films containing iron, cobalt, and nickel. *Journal of the American Chemical Society*. 2013;135(31):11580–11586.

[135] Wang L, Geng J, Wang W, Yuan C, Kuai L, Geng B. Facile synthesis of Fe/Ni bimetallic oxide solid-solution nanoparticles with superior electrocatalytic activity for oxygen evolution reaction. *Nano research*. 2015;8(12):3815–3822.

[136] Ullman AM, Brodsky CN, Li N, Zheng SL, Nocera DG. Probing edge site reactivity of oxidic cobalt water oxidation catalysts. *Journal of the American Chemical Society*. 2016; 138(12):4229–4236.

[137] Kanan MW, Surendranath Y, Nocera DG. Cobalt–phosphate oxygen-evolving compound. *Chemical Society Reviews*. 2009;38(1):109–114.

[138] Li W, Sheehan SW, He D, He Y, Yao X, Grimm RL, Brudvig GW, Wang D. Hematite-Based Solar Water Splitting in Acidic Solutions: Functionalization by Mono-and Multilayers of Iridium Oxygen-Evolution Catalysts. *Angewandte Chemie*. 2015;127(39):11590–11594.

[139] Blakemore JD, Schley ND, Olack GW, Incarvito CD, Brudvig GW, Crabtree RH. Anodic deposition of a robust iridium-based water-oxidation catalyst from organometallic precursors. *Chemical Science*. 2011;2(1):94–98.

[140] Masa J, Weide P, Peeters D, Sinev I, Xia W, Sun Z, Somsen C, Muhler M, Schuhmann W. Amorphous cobalt boride (Co2B) as a highly efficient nonprecious catalyst for electrochemical water splitting: oxygen and hydrogen evolution. *Advanced Energy Materials*. 2016; 6(6):1502313.

[141] Dahal N, Garcia S, Zhou J, Humphrey SM. Beneficial effects of microwave-assisted heating versus conventional heating in noble metal nanoparticle synthesis. *ACS nano*. 2012; 6(11):9433–9446.

[142] Katsuki H, Komarneni S. Microwave-Hydrothermal Synthesis of Monodispersed Nanophase α-Fe2O3. *Journal of the American Ceramic Society*. 2001;84(10):2313–2317.

[143] Kijima N, Yoshinaga M, Awaka J, Akimoto J. Microwave synthesis, characterization, and electrochemical properties of α-Fe2O3 nanoparticles. *Solid State Ionics*. 2011;192(1):293–297.

[144] Baghbanzadeh M, Carbone L, Cozzoli PD, Kappe CO. Microwave-assisted synthesis of colloidal inorganic nanocrystals. *Angewandte Chemie International Edition*. 2011;50(48):11312–11359.

[145] Leonard KC, Nam KM, Lee HC, Kang SH, Park HS, Bard AJ. ZnWO4/WO3 composite for improving photoelectrochemical water oxidation. *The Journal of Physical Chemistry C*. 2013;117(31):15901–15910.

[146] Machevsky ML, Anderson MA. Calorimetric acid-base titrations of aqueous goethite and rutile suspensions. *Langmuir*. 1986;2(5):583–587.

[147] Atkinson R, Posner A, Quirk J. Crystal nucleation in Fe (III) solutions and hydroxide gels. *Journal of Inorganic and Nuclear Chemistry*. 1968;30(9):2371–2381.

[148] Barforoush JM, McDonald TD, Desai TA, Widrig D, Bayer C, Brown MK, Cummings LC, Leonard KC. Intelligent Scanning Electrochemical Microscopy Tip and Substrate Control Utilizing Fuzzy Logic. *Electrochimica Acta*. 2016;190:713–719.

[149] Heuer J, Stubbins J. An XPS characterization of FeCO3 films from CO2 corrosion. *Corrosion Science*. 1999;41(7):1231–1243.

[150] Temesghen W, Sherwood P. Analytical utility of valence band X-ray photoelectron spectroscopy of iron and its oxides, with spectral interpretation by cluster and band structure calculations. *Analytical and bioanalytical chemistry*. 2002;373(7):601–608.

[151] McIntyre N, Zetaruk D. X-ray photoelectron spectroscopic studies of iron oxides. *Analytical Chemistry*. 1977;49(11):1521–1529.

[152] Bard AJ, Fox MA. Artificial photosynthesis: solar splitting of water to hydrogen and oxygen. *Acc Chem Res*. 1995;28(3):141–145.

[153] Walter MG, Warren EL, McKone JR, Boettcher SW, Mi QX, Santori EA, Lewis NS. Solar Water Splitting Cells. *Chem Rev*. 2010;110(11):6446–6473.
URL `<Go to ISI>://WOS:000284134300002`

[154] Gray HB. Powering the planet with solar fuel. *Nat Chem*. 2009;1(1):7–7.

[155] Man IC, Su H, Calle-Vallejo F, Hansen HA, Martínez JI, Inoglu NG, Kitchin J, Jaramillo TF, Nørskov JK, Rossmeisl J. Universality in oxygen evolution electrocatalysis on oxide surfaces. *ChemCatChem*. 2011;3(7):1159–1165.

[156] Dau H, Limberg C, Reier T, Risch M, Roggan S, Strasser P. The mechanism of water oxidation: from electrolysis via homogeneous to biological catalysis. *ChemCatChem*. 2010; 2(7):724–761.

[157] Kanan MW, Nocera DG. In situ formation of an oxygen-evolving catalyst in neutral water containing phosphate and Co^{2+}. *Science*. 2008;321(5892):1072–1075.

[158] Reier T, Oezaslan M, Strasser P. Electrocatalytic oxygen evolution reaction (OER) on Ru,

Ir, and Pt catalysts: a comparative study of nanoparticles and bulk materials. *ACS Catal.* 2012;2(8):1765–1772.

[159] Trasatti S. Electrocatalysis in the anodic evolution of oxygen and chlorine. *Electrochim Acta.* 1984;29(11):1503–1512.

[160] Horkans J, Shafer M. An investigation of the electrochemistry of a series of metal dioxides with rutile-type structure: MoO_2, WO_2, ReO_2, RuO_2, OsO_2, and IrO_2. *J Am Chem Soc.* 1977;124(8):1202–1207.

[161] Song F, Hu X. Exfoliation of layered double hydroxides for enhanced oxygen evolution catalysis. *Nat Commun.* 2014;5:1–9.

[162] Lu Z, Xu W, Zhu W, Yang Q, Lei X, Liu J, Li Y, Sun X, Duan X. Three-dimensional NiFe layered double hydroxide film for high-efficiency oxygen evolution reaction. *Chem Commun.* 2014;50(49):6479–6482.

[163] Gong M, Li Y, Wang H, Liang Y, Wu JZ, Zhou J, Wang J, Regier T, Wei F, Dai H. An advanced Ni–Fe layered double hydroxide electrocatalyst for water oxidation. *J Am Chem Soc.* 2013;135(23):8452–8455.

[164] Zhan T, Liu X, Lu S, Hou W. Nitrogen doped NiFe layered double hydroxide/reduced graphene oxide mesoporous nanosphere as an effective bifunctional electrocatalyst for oxygen reduction and evolution reactions. *Applied Catalysis B: Environmental.* 2017;205:551–558.

[165] Zhao D, Jiang K, Pi Y, Huang X. Superior Electrochemical Oxygen Evolution Enabled by Three-Dimensional Layered Double Hydroxide Nanosheet Superstructures. *ChemCatChem.* 2017;9(1):84–88.

[166] Swierk JR, Klaus S, Trotochaud L, Bell AT, Tilley TD. Electrochemical study of the energetics of the oxygen evolution reaction at nickel iron (oxy) hydroxide catalysts. *J Phys Chem C.* 2015;119(33):19022–19029.

[167] Hou Y, Lohe MR, Zhang J, Liu S, Zhuang X, Feng X. Vertically oriented cobalt selenide/NiFe layered-double-hydroxide nanosheets supported on exfoliated graphene foil: an efficient 3D electrode for overall water splitting. *Energy Environ Sci.* 2016;9(2):478–483.

[168] Hou Y, Wen Z, Cui S, Feng X, Chen J. Strongly Coupled Ternary Hybrid Aerogels of N-deficient Porous Graphitic-C_3N_4 Nanosheets/N-Doped Graphene/NiFe-Layered Double Hydroxide for Solar-Driven Photoelectrochemical Water Oxidation. *Nano Lett.* 2016;16(4):2268–2277.

[169] Burke MS, Zou S, Enman LJ, Kellon JE, Gabor CA, Pledger E, Boettcher SW. Revised oxygen evolution reaction activity trends for first-row transition-metal (oxy) hydroxides in alkaline media. *J Phys Chem Lett.* 2015;6(18):3737–3742.

[170] Klaus S, Cai Y, Louie MW, Trotochaud L, Bell AT. Effects of Fe electrolyte impurities on $Ni(OH)_2$/NiOOH structure and oxygen evolution activity. *J Phys Chem C.* 2015; 119(13):7243–7254.

[171] Hunter BM, Blakemore JD, Deimund M, Gray HB, Winkler JR, Müller AM. Highly active mixed-metal nanosheet water oxidation catalysts made by pulsed-laser ablation in liquids. *J Am Chem Soc.* 2014;136(38):13118–13121.

[172] Yu X, Zhang M, Yuan W, Shi G. A high-performance three-dimensional Ni–Fe layered double hydroxide/graphene electrode for water oxidation. *J Mater Chem A.* 2015;3(13):6921–6928.

[173] Long X, Li J, Xiao S, Yan K, Wang Z, Chen H, Yang S. A strongly coupled graphene and FeNi double hydroxide hybrid as an excellent electrocatalyst for the oxygen evolution reaction. *Angew Chem.* 2014;126(29):7714–7718.

[174] Hunter BM, Hieringer W, Winkler J, Gray H, Müller A. Effect of interlayer anions on [NiFe]-LDH nanosheet water oxidation activity. *Energy Environ Sci.* 2016;9(5):1734–1743.

[175] Barforoush JM, Jantz DT, Seuferling TE, Song KR, Cummings LC, Leonard KC. Microwave-assisted synthesis of a nanoamorphous ($Ni_{0.8}$,$Fe_{0.2}$) oxide oxygen-evolving electrocatalyst containing only "fast" sites. *Journal of Materials Chemistry A.* 2017;5(23):11661–11670.

[176] Candelaria SL, Bedford NM, Woehl TJ, Rentz NS, Showalter AR, Pylypenko S, Bunker BA, Lee S, Reinhart B, Ren Y, Ertem SP, Coughlin EB, Sather NA, Horan JL, Herring AM, Greenlee LF. Multi-component Fe–Ni hydroxide nanocatalyst for oxygen evolution and methanol oxidation reactions under alkaline conditions. *ACS Catalysis.* 2016;7(1):365–379.

[177] Greenlee LF, Acharya P, Nelson Z. Compositional Optimization of Alloy FexNiy (OH) 2 Nanoparticles for Alkaline Electrochemical Oxygen Evolution. *ECS Transactions*. 2017; 77(9):25–38.

[178] Wang Q, O'Hare D. Recent advances in the synthesis and application of layered double hydroxide (LDH) nanosheets. *Chem Rev*. 2012;112(7):4124–4155.

[179] Khan AI, O'Hare D. Intercalation chemistry of layered double hydroxides: recent developments and applications. *J Mater Chem*. 2002;12(11):3191–3198.

[180] Miyata S. The syntheses of hydrotalcite-like compounds and their structures and physicochemical properties I: The systems Mg^{2+}-Al^{3+}-NO_3^-, Mg^{2+}-Al^{3+}-Cl^-, Mg^{2+}-Al^{3+}-ClO_4^-, Ni^{2+}-Al^{3+}-Cl^- and Zn^{2+}-Al^{3+}-Cl^-. *Clays Clay Miner*. 1975;23:369–375.

[181] Brindley G, Kikkawa S. Thermal behavior of hydrotalcite and of anion-exchanged forms of hydrotalcite. *Clays Clay Miner*. 1980;28(2):87–91.

[182] Pesic L, Salipurovic S, Markovic V, Vucelic D, Kagunya W, Jones W. Thermal characteristics of a synthetic hydrotalcite-like material. *J Mater Chem*. 1992;2(10):1069–1073.

[183] Wehrens-Dijksma M, Notten P. Electrochemical Quartz Microbalance characterization of $Ni(OH)_2$-based thin film electrodes. *Electrochimica Acta*. 2006;51(18):3609–3621.

[184] Gerken JB, McAlpin JG, Chen JY, Rigsby ML, Casey WH, Britt RD, Stahl SS. Electrochemical water oxidation with cobalt-based electrocatalysts from pH 0–14: the thermodynamic basis for catalyst structure, stability, and activity. *J Am Chem Soc*. 2011;133(36):14431–14442.

[185] Morishita M, Ochiai S, Kakeya T, Ozaki T, Kawabe Y, Watada M, Tanase S, Sakai T. Phase Transformation in the Charge-Discharge Process and the Structural Analysis by Synchrotron XAFS and XRD for Nickel Hydroxide Electrode. *Electrochemistry*. 2008;76(11):802–807.

[186] Zhang Y, Cui B, Zhao C, Lin H, Li J. Co–Ni layered double hydroxides for water oxidation in neutral electrolyte. *Phys Chem Chem Phys*. 2013;15(19):7363–7369.

[187] Marcelin G, Stockhausen N, Post J, Schutz A. Dynamics and ordering of intercalated water in layered metal hydroxides. *J Phys Chem*. 1989;93(11):4646–4650.

[188] Lukowski MA, Daniel AS, Meng F, Forticaux A, Li L, Jin S. Enhanced hydrogen evolution catalysis from chemically exfoliated metallic MoS_2 nanosheets. *J Am Chem Soc*. 2013; 135(28):10274–10277.

[189] Li Y, Wang H, Xie L, Liang Y, Hong G, Dai H. MoS_2 nanoparticles grown on graphene: an advanced catalyst for the hydrogen evolution reaction. *Journal of the American Chemical Society*. 2011;133(19):7296–7299.

[190] Jasion D, Barforoush JM, Qiao Q, Zhu Y, Ren S, Leonard KC. Low-dimensional hyperthin FeS_2 nanostructures for efficient and stable hydrogen evolution electrocatalysis. *ACS Catalysis*. 2015;5(11):6653–6657.

[191] Im H, Pawar SM, Pawar B, Hou B, Kim J, Talha AA, Chavan HS, Jo Y, Cho S, Inamdar A, Gunjakar JL, Kim H, Cha S, Im H. Self-assembled Two-dimensional Copper Oxide Nanosheet Bundles as an efficient Oxygen Evolution Reaction (OER) electrocatalyst for water splitting application. *Journal of Materials Chemistry A*. 2017;5(25):12747–12751.

[192] Lightcap IV, Kosel TH, Kamat PV. Anchoring semiconductor and metal nanoparticles on a two-dimensional catalyst mat. Storing and shuttling electrons with reduced graphene oxide. *Nano letters*. 2010;10(2):577–583.

[193] Yang J, Voiry D, Ahn SJ, Kang D, Kim AY, Chhowalla M, Shin HS. Two-Dimensional Hybrid Nanosheets of Tungsten Disulfide and Reduced Graphene Oxide as Catalysts for Enhanced Hydrogen Evolution. *Angewandte Chemie International Edition*. 2013;52(51):13751–13754.

[194] Batchellor AS, Boettcher SW. Pulse-electrodeposited Ni–Fe (oxy) hydroxide oxygen evolution electrocatalysts with high geometric and intrinsic activities at large mass loadings. *ACS Catal*. 2015;5(11):6680–6689.

[195] Stevens MB, Trang CD, Enman LJ, Deng J, Boettcher SW. Reactive Fe-sites in Ni/Fe (oxy) hydroxide are responsible for exceptional oxygen electrocatalysis activity. *Journal of the American Chemical Society*. 2017;139(33):11361–11364.

[196] Burke MS, Kast MG, Trotochaud L, Smith AM, Boettcher SW. Cobalt–iron (oxy) hydroxide

oxygen evolution electrocatalysts: the role of structure and composition on activity, stability, and mechanism. *Journal of the American Chemical Society*. 2015;137(10):3638–3648.

[197] McCrory CC, Jung S, Peters JC, Jaramillo TF. Benchmarking heterogeneous electrocatalysts for the oxygen evolution reaction. *Journal of the American Chemical Society*. 2013; 135(45):16977–16987.

[198] McCrory CC, Jung S, Ferrer IM, Chatman SM, Peters JC, Jaramillo TF. Benchmarking hydrogen evolving reaction and oxygen evolving reaction electrocatalysts for solar water splitting devices. *J Am Chem Soc*. 2015;137(13):4347–4357.

[199] Trotochaud L, Young SL, Ranney JK, Boettcher SW. Nickel–iron oxyhydroxide oxygen-evolution electrocatalysts: The role of intentional and incidental iron incorporation. *J Am Chem Soc*. 2014;136(18):6744–6753.

[200] Trasatti S, Petrii O. Real surface area measurements in electrochemistry. *Journal of Electroanalytical Chemistry*. 1992;327(1-2):353–376.

[201] Bockris JO, Otagawa T. The electrocatalysis of oxygen evolution on perovskites. *Journal of the Electrochemical Society*. 1984;131(2):290–302.

[202] Rüetschi P, Delahay P. Influence of electrode material on oxygen overvoltage: a theoretical analysis. *The Journal of Chemical Physics*. 1955;23(3):556–560.

[203] Ahn HS, Bard AJ. Surface Interrogation of CoPi Water Oxidation Catalyst by Scanning Electrochemical Microscopy. *J Am Chem Soc*. 2015;137(2):612–615.

[204] Arroyo-Currás N, Bard AJ. Iridium Oxidation as Observed by Surface Interrogation Scanning Electrochemical Microscopy. *J Phys Chem C*. 2015;119(15):8147–8154.

[205] Rodríguez-López J, Alpuche-Avilés MA, Bard AJ. Interrogation of surfaces for the quantification of adsorbed species on electrodes: oxygen on gold and platinum in neutral Media. *J Am Chem Soc*. 2008;130(50):16985–16995.

[206] Park HS, Leonard KC, Bard AJ. Surface interrogation scanning electrochemical microscopy

(SI-SECM) of photoelectrochemistry at a W/Mo-$BiVO_4$ semiconductor electrode: quantification of hydroxyl radicals during water oxidation. *J Phys Chem C*. 2013;117(23):12093–12102.

[207] Barforoush JM, McDonald TD, Desai TA, Widrig D, Bayer C, Brown MK, Cummings LC, Leonard KC. Intelligent Scanning Electrochemical Microscopy Tip and Substrate Control Utilizing Fuzzy Logic. *Electrochimica Acta*. 2016;190:713–719.

[208] Zigah D, Rodríguez-López J, Bard AJ. Quantification of photoelectrogenerated hydroxyl radical on TiO_2 by surface interrogation scanning electrochemical microscopy. *Physical Chemistry Chemical Physics*. 2012;14(37):12764–12772.

[209] Minguzzi A, Alpuche-Aviles MA, López JR, Rondinini S, Bard AJ. Screening of oxygen evolution electrocatalysts by scanning electrochemical microscopy using a shielded tip approach. *Analytical chemistry*. 2008;80(11):4055–4064.

[210] Gossage ZT, Schorr NB, Hernández-Burgos K, Hui J, Simpson BH, Montoto EC, Rodríguez-López J. Interrogating Charge Storage on Redox Active Colloids via Combined Raman Spectroscopy and Scanning Electrochemical Microscopy. *Langmuir*. 2017;33(37):9455–9463.

[211] Simpson B, Rodríguez-López J. Emerging techniques for the in situ analysis of reaction intermediates on photo-electrochemical interfaces. *Analytical Methods*. 2015;7(17):7029–7041.

[212] Ahn HS, Bard AJ. Surface Interrogation Scanning Electrochemical Microscopy of $Ni_{1-x}Fe_xOOH$ ($0 < x < 0.27$) Oxygen Evolving Catalyst: Kinetics of the "fast" Iron Sites. *J Am Chem Soc*. 2016;138(1):313–318.

[213] Kim JY, Ahn HS, Bard AJ. Surface Interrogation Scanning Electrochemical Microscopy for a Photoelectrochemical Reaction–Water Oxidation on a Hematite Surface. *Analytical chemistry*. 2018;.

[214] Krumov MR, Simpson BH, Counihan MJ, Rodriguez-Lopez J. In Situ Quantification of Surface Intermediates and Correlation to Discharge Products on Hematite Photoanodes using a Combined Scanning Electrochemical Microscopy Approach. *Analytical chemistry*. 2018;.

[215] Trotochaud L, Ranney JK, Williams KN, Boettcher SW. Solution-cast metal oxide thin film electrocatalysts for oxygen evolution. *J Am Chem Soc*. 2012;134(41):17253–17261.

[216] Hu F, Zhu S, Chen S, Li Y, Ma L, Wu T, Zhang Y, Wang C, Liu C, Yang X, Song L, Yang X, Xiong Y. Amorphous Metallic NiFeP: A Conductive Bulk Material Achieving High Activity for Oxygen Evolution Reaction in Both Alkaline and Acidic Media. *Advanced Materials*. 2017; 29(32).

[217] Fan J, Chen Z, Shi H, Zhao G. In situ grown, self-supported iron–cobalt–nickel alloy amorphous oxide nanosheets with low overpotential toward water oxidation. *Chemical Communications*. 2016;52(23):4290–4293.

[218] Dong B, Zhao X, Han GQ, Li X, Shang X, Liu YR, Hu WH, Chai YM, Zhao H, Liu CG. Two-step synthesis of binary Ni–Fe sulfides supported on nickel foam as highly efficient electrocatalysts for the oxygen evolution reaction. *Journal of Materials Chemistry A*. 2016; 4(35):13499–13508.

[219] Yang Y, Zhuang L, Lin R, Li M, Xu X, Rufford TE, Zhu Z. A facile method to synthesize boron-doped Ni/Fe alloy nano-chains as electrocatalyst for water oxidation. *Journal of Power Sources*. 2017;349:68–74.

[220] Smith RD, Prévot MS, Fagan RD, Trudel S, Berlinguette CP. Water oxidation catalysis: electrocatalytic response to metal stoichiometry in amorphous metal oxide films containing iron, cobalt, and nickel. *Journal of the American Chemical Society*. 2013;135(31):11580–11586.

[221] Wang L, Geng J, Wang W, Yuan C, Kuai L, Geng B. Facile synthesis of Fe/Ni bimetallic oxide solid-solution nanoparticles with superior electrocatalytic activity for oxygen evolution reaction. *Nano Research*. 2015;8(12):3815–3822.

[222] Morales-Guio CG, Mayer MT, Yella A, Tilley SD, Gratzel M, Hu X. An optically transparent iron nickel oxide catalyst for solar water splitting. *Journal of the American Chemical Society*. 2015;137(31):9927–9936.

[223] Smith RD, Prévot MS, Fagan RD, Zhang Z, Sedach PA, Siu MKJ, Trudel S, Berlinguette CP. Photochemical route for accessing amorphous metal oxide materials for water oxidation catalysis. *Science*. 2013;p. 1233638.

[224] Smith RD, Berlinguette CP. Accounting for the dynamic oxidative behavior of nickel anodes. *Journal of the American Chemical Society*. 2016;138(5):1561–1567.

[225] Bergmann A, Martinez-Moreno E, Teschner D, Chernev P, Gliech M, De Araújo JF, Reier T, Dau H, Strasser P. Reversible amorphization and the catalytically active state of crystalline Co_3O_4 during oxygen evolution. *Nature communications*. 2015;6.

[226] Ullman AM, Brodsky CN, Li N, Zheng SL, Nocera DG. Probing edge site reactivity of oxidic cobalt water oxidation catalysts. *J Am Chem Soc*. 2016;138(12):4229–4236.

[227] Kanan MW, Surendranath Y, Nocera DG. Cobalt–phosphate oxygen-evolving compound. *Chemical Society Reviews*. 2009;38(1):109–114.

[228] Li W, Sheehan SW, He D, He Y, Yao X, Grimm RL, Brudvig GW, Wang D. Hematite-Based Solar Water Splitting in Acidic Solutions: Functionalization by Mono-and Multilayers of Iridium Oxygen-Evolution Catalysts. *Angewandte Chemie International Edition*. 2015; 54(39):11428–11432.

[229] Blakemore JD, Schley ND, Olack GW, Incarvito CD, Brudvig GW, Crabtree RH. Anodic deposition of a robust iridium-based water-oxidation catalyst from organometallic precursors. *Chemical Science*. 2011;2(1):94–98.

[230] Masa J, Weide P, Peeters D, Sinev I, Xia W, Sun Z, Somsen C, Muhler M, Schuhmann W. Amorphous cobalt boride (Co_2B) as a highly efficient nonprecious catalyst for electrochemical water splitting: Oxygen and hydrogen evolution. *Advanced Energy Materials*. 2016;6(6).

[231] Zhang B, Zheng X, Voznyy O, Comin R, Bajdich M, García-Melchor M, Han L, Xu J, Liu M, Zheng L, García de Arquer1 FP, Dinh1 CT, Fan1 F, Yuan1 M, Yassitepe1 E, Chen N, Regier T, Liu P, Li Y, Luna1 PD, Janmohamed A, Xin HL, Yang H, Vojvodic A, Sargent EH. Homogeneously dispersed multimetal oxygen-evolving catalysts. *Science*. 2016;352(6283):333–337.

[232] Friebel D, Louie MW, Bajdich M, Sanwald KE, Cai Y, Wise AM, Cheng MJ, Sokaras D, Weng TC, Alonso-Mori R, Davis RC, Bargar JR, Nørskov JK, Nilsson A, Bell AT. Identification

of highly active Fe sites in (Ni, Fe) OOH for electrocatalytic water splitting. *Journal of the American Chemical Society*. 2015;137(3):1305–1313.

[233] Rodriguez-Lopez J, Alpuche-Avilés MA, Bard AJ. Interrogation of surfaces for the quantification of adsorbed species on electrodes: oxygen on gold and platinum in neutral Media. *Journal of the American Chemical Society*. 2008;130(50):16985–16995.

[234] Mefford JT, Rong X, Abakumov AM, Hardin WG, Dai S, Kolpak AM, Johnston KP, Stevenson KJ. Water electrolysis on $La_{1-x}Sr_xCoO_{3-\delta}$ perovskite electrocatalysts. *Nature communications*. 2016;7:11053.

[235] McEwen RS. Crystallographic studies on nickel hydroxide and the higher nickel oxides. *J Phys Chem*. 1971;75(12):1782–1789.
URL `http://dx.doi.org/10.1021/j100681a004`

[236] Tessier C, Haumesser P, Bernard P, Delmas C. The structure of $Ni(OH)_2$: from the ideal material to the electrochemically active one. *J Am Chem Soc*. 1999;146(6):2059–2067.

[237] Zhou F, Unwin PR, Bard AJ. Scanning electrochemical microscopy. 16. Study of second-order homogeneous chemical reactions via the feedback and generation/collection modes. *The Journal of Physical Chemistry*. 1992;96(12):4917–4924.

[238] Cao F, Kim J, Bard AJ. Detection of the short-lived cation radical intermediate in the electrochemical oxidation of N, N-dimethylaniline by scanning electrochemical microscopy. *Journal of the American Chemical Society*. 2014;136(52):18163–18169.

[239] Chang J, Bard AJ. Detection of the Sn (III) intermediate and the mechanism of the Sn (IV)/Sn (II) electroreduction reaction in bromide media by cyclic voltammetry and scanning electrochemical microscopy. *Journal of the American Chemical Society*. 2013;136(1):311–320.

[240] Sun Y, Liu C, Grauer DC, Yano J, Long JR, Yang P, Chang CJ. Electrodeposited cobalt-sulfide catalyst for electrochemical and photoelectrochemical hydrogen generation from water. *Journal of the American Chemical Society*. 2013;135(47):17699–17702.

[241] Noël JM, Velmurugan J, Gökmeşe E, Mirkin MV. Fabrication, characterization, and chemical etching of Ag nanoelectrodes. *Journal of Solid State Electrochemistry*. 2013;17(2):385–389.

[242] Hu K, Gao Y, Wang Y, Yu Y, Zhao X, Rotenberg SA, Gökmeşe E, Mirkin MV, Friedman G, Gogotsi Y. Platinized carbon nanoelectrodes as potentiometric and amperometric SECM probes. *Journal of Solid State Electrochemistry*. 2013;17(12):2971–2977.

[243] Kim J, Izadyar A, Nioradze N, Amemiya S. Nanoscale mechanism of molecular transport through the nuclear pore complex as studied by scanning electrochemical microscopy. *Journal of the American Chemical Society*. 2013;135(6):2321–2329.

[244] Lee C, Kwak J, Bard AJ. Application of scanning electrochemical microscopy to biological samples. *Proceedings of the National Academy of Sciences*. 1990;87(5):1740–1743.

[245] Kim J, Connell JL, Whiteley M, Bard AJ. Development of a versatile in vitro platform for studying biological systems using micro-3D printing and scanning electrochemical microscopy. *Analytical chemistry*. 2014;86(24):12327–12333.

[246] Connell JL, Kim J, Shear JB, Bard AJ, Whiteley M. Real-time monitoring of quorum sensing in 3D-printed bacterial aggregates using scanning electrochemical microscopy. *Proceedings of the National Academy of Sciences*. 2014;111(51):18255–18260.

[247] Minguzzi A, Alpuche-Aviles MA, López JR, Rondinini S, Bard AJ. Screening of oxygen evolution electrocatalysts by scanning electrochemical microscopy using a shielded tip approach. *Analytical chemistry*. 2008;80(11):4055–4064.

[248] Fernández JL, Walsh DA, Bard AJ. Thermodynamic guidelines for the design of bimetallic catalysts for oxygen electroreduction and rapid screening by scanning electrochemical microscopy. M- Co (M: Pd, Ag, Au). *Journal of the American Chemical Society*. 2005; 127(1):357–365.

[249] Lee J, Ye H, Pan S, Bard AJ. Screening of photocatalysts by scanning electrochemical microscopy. *Analytical chemistry*. 2008;80(19):7445–7450.

[250] Rodriguez-Lopez J, Bard AJ. Scanning electrochemical microscopy: surface interrogation of adsorbed hydrogen and the open circuit catalytic decomposition of formic acid at platinum. *Journal of the American Chemical Society*. 2010;132(14):5121–5129.

[251] Zhou M, Yu Y, Hu K, Mirkin MV. Nanoelectrochemical approach to detecting short-lived intermediates of electrocatalytic oxygen reduction. *Journal of the American Chemical Society*. 2015;137(20):6517–6523.

[252] Rodriguez-Lopez J, Minguzzi A, Bard AJ. Reaction of various reductants with oxide films on Pt electrodes as studied by the surface interrogation mode of scanning electrochemical microscopy (SI-SECM): Possible validity of a Marcus relationship. *The Journal of Physical Chemistry C*. 2010;114(43):18645–18655.

[253] Shen M, Ishimatsu R, Kim J, Amemiya S. Quantitative imaging of ion transport through single nanopores by high-resolution scanning electrochemical microscopy. *Journal of the American Chemical Society*. 2012;134(24):9856–9859.

[254] Aaronson BD, Lai SC, Unwin PR. Spatially resolved electrochemistry in ionic liquids: surface structure effects on triiodide reduction at platinum electrodes. *Langmuir*. 2014;30(7):1915–1919.

[255] Chen CH, Meadows KE, Cuharuc A, Lai SC, Unwin PR. High resolution mapping of oxygen reduction reaction kinetics at polycrystalline platinum electrodes. *Physical Chemistry Chemical Physics*. 2014;16(34):18545–18552.

[256] Boika A, Bard AJ. Electrophoretic migration and particle collisions in scanning electrochemical microscopy. *Analytical chemistry*. 2014;86(23):11666–11672.

[257] Bard AJ, Mirkin MV. *Scanning electrochemical microscopy*. CRC Press. 2012.

[258] Amemiya S, Bard AJ, Fan FRF, Mirkin MV, Unwin PR. Scanning electrochemical microscopy. *Annu Rev Anal Chem*. 2008;1:95–131.

[259] Nioradze N, Chen R, Kurapati N, Khvataeva-Domanov A, Mabic S, Amemiya S. Organic contamination of highly oriented pyrolytic graphite as studied by scanning electrochemical microscopy. *Analytical chemistry*. 2015;87(9):4836–4843.

[260] guell AG, Meadows KE, Dudin PV, Ebejer N, Macpherson JV, Unwin PR. Mapping nanoscale electrochemistry of individual single-walled carbon nanotubes. *Nano letters*. 2013;14(1):220–224.

[261] Ebejer N, Güell AG, Lai SC, McKelvey K, Snowden ME, Unwin PR. Scanning electrochemical cell microscopy: a versatile technique for nanoscale electrochemistry and functional imaging. *Annual Review of Analytical Chemistry*. 2013;6:329–351.

[262] Chen CH, Jacobse L, McKelvey K, Lai SC, Koper MT, Unwin PR. Voltammetric scanning electrochemical cell microscopy: dynamic imaging of hydrazine electro-oxidation on platinum electrodes. *Analytical chemistry*. 2015;87(11):5782–5789.

[263] guell AG, Cuharuc AS, Kim YR, Zhang G, Tan Sy, Ebejer N, Unwin PR. Redox-dependent spatially resolved electrochemistry at graphene and graphite step edges. *ACS nano*. 2015; 9(4):3558–3571.

[264] Byers JC, guell AG, Unwin PR. Nanoscale electrocatalysis: visualizing oxygen reduction at pristine, kinked, and oxidized sites on individual carbon nanotubes. *Journal of the American Chemical Society*. 2014;136(32):11252–11255.

[265] Miller TS, Macpherson JV, Unwin PR. Electrochemical activation of pristine single walled carbon nanotubes: impact on oxygen reduction and other surface sensitive redox processes. *Physical Chemistry Chemical Physics*. 2014;16(21):9966–9973.

[266] Zhang G, Kirkman PM, Patel AN, Cuharuc AS, McKelvey K, Unwin PR. Molecular functionalization of graphite surfaces: basal plane versus step edge electrochemical activity. *Journal of the American Chemical Society*. 2014;136(32):11444–11451.

[267] Wipf DO, Bard AJ, Tallman DE. Scanning electrochemical microscopy. 21. Constant-current imaging with an autoswitching controller. *Analytical Chemistry*. 1993;65(10):1373–1377.

[268] Fan FRF, Bard AJ. Imaging of biological macromolecules on mica in humid air by scanning electrochemical microscopy. *Proceedings of the National Academy of Sciences*. 1999; 96(25):14222–14227.

[269] Ballesteros Katemann B, Schulte A, Schuhmann W. Constant-Distance Mode Scanning Electrochemical Microscopy (SECM)—Part I: Adaptation of a Non-Optical Shear-Force-Based Positioning Mode for SECM Tips. *Chemistry–A European Journal*. 2003;9(9):2025–2033.

[270] Etienne M, Schulte A, Schuhmann W. High resolution constant-distance mode alternating current scanning electrochemical microscopy (AC-SECM). *Electrochemistry communications*. 2004;6(3):288–293.

[271] Kurulugama RT, Wipf DO, Takacs SA, Pongmayteegul S, Garris PA, Baur JE. Scanning electrochemical microscopy of model neurons: constant distance imaging. *Analytical chemistry*. 2005;77(4):1111–1117.

[272] Macpherson JV, Unwin PR. Combined scanning electrochemical- atomic force microscopy. *Analytical Chemistry*. 2000;72(2):276–285.

[273] Gardner CE, Macpherson JV. Peer reviewed: Atomic force microscopy probes go electrochemical. 2002.

[274] Wain AJ, Pollard AJ, Richter C. High-resolution electrochemical and topographical imaging using batch-fabricated cantilever probes. *Analytical chemistry*. 2014;86(10):5143–5149.

[275] Eifert A, Mizaikoff B, Kranz C. Advanced fabrication process for combined atomic force-scanning electrochemical microscopy (AFM-SECM) probes. *Micron*. 2015;68:27–35.

[276] Takahashi Y, Shevchuk AI, Novak P, Murakami Y, Shiku H, Korchev YE, Matsue T. Simultaneous noncontact topography and electrochemical imaging by SECM/SICM featuring ion current feedback regulation. *Journal of the American Chemical Society*. 2010;132(29):10118–10126.

[277] Ludwig M, Kranz C, Schuhmann W, Gaub HE. Topography feedback mechanism for the scanning electrochemical microscope based on hydrodynamic forces between tip and sample. *Review of scientific instruments*. 1995;66(4):2857–2860.

[278] Danis L, Snowden ME, Tefashe UM, Heinemann CN, Mauzeroll J. Development of nano-disc electrodes for application as shear force sensitive electrochemical probes. *Electrochimica Acta*. 2014;136:121–129.

[279] Chang J, Leonard KC, Cho SK, Bard AJ. Examining Ultramicroelectrodes for Scanning Electrochemical Microscopy by White Light Vertical Scanning Interferometry and Filling Recessed Tips by Electrodeposition of Gold. *Analytical chemistry*. 2012;84(11):5159–5163.

[280] Zigah D, Rodríguez-López J, Bard AJ. Quantification of photoelectrogenerated hydroxyl radical on TiO 2 by surface interrogation scanning electrochemical microscopy. *Physical Chemistry Chemical Physics*. 2012;14(37):12764–12772.

[281] Bose BK. Expert system, fuzzy logic, and neural network applications in power electronics and motion control. *Proceedings of the IEEE*. 1994;82(8):1303–1323.

[282] Sun P, Mirkin MV. Kinetics of electron-transfer reactions at nanoelectrodes. *Analytical chemistry*. 2006;78(18):6526–6534.

[283] Durst J, Siebel A, Simon C, Hasche F, Herranz J, Gasteiger H. New insights into the electrochemical hydrogen oxidation and evolution reaction mechanism. *Energy & Environmental Science*. 2014;7(7):2255–2260.

[284] Durst J, Simon C, Hasché F, Gasteiger H. Hydrogen Oxidation and Evolution Reaction Kinetics on Carbon Supported Pt, Ir, Rh, and Pd Electrocatalysts in Acidic Media. *Journal of The Electrochemical Society*. 2010;157(11):B1529–B1536.

[285] Sheng W, Gasteiger HA, Shao-Horn Y. Hydrogen oxidation and evolution reaction kinetics on platinum: acid vs alkaline electrolytes. *Journal of The Electrochemical Society*. 2010; 157(11):B1529–B1536.

[286] Deng J, Ren P, Deng D, Yu L, Yang F, Bao X. Highly active and durable non-precious-metal catalysts encapsulated in carbon nanotubes for hydrogen evolution reaction. *Energy & Environmental Science*. 2014;7(6):1919–1923.

[287] Kibsgaard J, Jaramillo TF. Molybdenum Phosphosulfide: An Active, Acid-Stable, Earth-Abundant Catalyst for the Hydrogen Evolution Reaction. *Angewandte Chemie International Edition*. 2014;53(52):14433–14437.

[288] Feng LL, Yu G, Wu Y, Li GD, Li H, Sun Y, Asefa T, Chen W, Zou X. High-index faceted Ni3S2 nanosheet arrays as highly active and ultrastable electrocatalysts for water splitting. *Journal of the American Chemical Society*. 2015;137(44):14023–14026.

[289] Chia X, Eng AYS, Ambrosi A, Tan SM, Pumera M. Electrochemistry of nanostructured layered transition-metal dichalcogenides. *Chemical reviews*. 2015;115(21):11941–11966.

[290] Miao J, Xiao FX, Yang HB, Khoo SY, Chen J, Fan Z, Hsu YY, Chen HM, Zhang H, Liu B. Hierarchical Ni-Mo-S nanosheets on carbon fiber cloth: A flexible electrode for efficient hydrogen generation in neutral electrolyte. *Science Advances*. 2015;1(7):e1500259.

[291] Burke LD, Murphy OJ, O'Neill JF, Venkatesan S. The oxygen electrode. Part 8.—Oxygen evolution at ruthenium dioxide anodes. *Journal of the Chemical Society, Faraday Transactions 1: Physical Chemistry in Condensed Phases*. 1977;73:1659–1671.

[292] Dionigi F, Strasser P. NiFe-Based (Oxy) hydroxide Catalysts for Oxygen Evolution Reaction in Non-Acidic Electrolytes. *Advanced Energy Materials*. 2016;6(23).

[293] Hong WT, Risch M, Stoerzinger KA, Grimaud A, Suntivich J, Shao-Horn Y. Toward the rational design of non-precious transition metal oxides for oxygen electrocatalysis. *Energy & Environmental Science*. 2015;8(5):1404–1427.

[294] Grigoriev S, Millet P, Fateev V. Evaluation of carbon-supported Pt and Pd nanoparticles for the hydrogen evolution reaction in PEM water electrolysers. *Journal of Power Sources*. 2008; 177(2):281–285.

[295] Grigoriev S, Mamat M, Dzhus K, Walker G, Millet P. Platinum and palladium nano-particles supported by graphitic nano-fibers as catalysts for PEM water electrolysis. *International Journal of hydrogen energy*. 2011;36(6):4143–4147.

[296] Lettenmeier P, Wang R, Abouatallah R, Saruhan B, Freitag O, Gazdzicki P, Morawietz T, Hiesgen R, Gago A, Friedrich K. Low-cost and durable bipolar plates for proton exchange membrane electrolyzers. *Scientific Reports*. 2017;7:44035.

[297] Esposito DV. Membraneless electrolyzers for low-cost hydrogen production in a renewable energy future. *Joule*. 2017;.

[298] Schröder V, Emonts B, Janßen H, Schulze HP. Explosion limits of hydrogen/oxygen mixtures at initial pressures up to 200 bar. *Chemical Engineering & Technology: Industrial Chemistry-Plant Equipment-Process Engineering-Biotechnology*. 2004;27(8):847–851.